Experimental Investigation of Effect of Windshield Barriers on the Aerodynamic Properties of the Multi-box Bridge Decks

by

Xi Chen

A thesis submitted to the Faculty of Graduate and Postdoctoral Studies in partial fulfilment of the requirements for the degree of

Masters of Applied Science

In

Civil Engineering

uOttawa

Department of Civil Engineering

University of Ottawa

Ottawa, Canada

June 2015

Acknowledgements

I would like to express my deepest appreciation to Dr. Elena Dragomirescu for her untiring and sincere teachings. She patiently guided me from choosing the topic to submitting the thesis.

I'm also grateful to Dr. Muslim Majid for the advices and assistance when I was preparing the experiments. Thanks to Dr. Bas Baskaran and Mr. Steve Ko who lend the equipment needed for the experiment. Particular I am thankful to Mr. Vincent Ferraro, Mr. Un Yong Jeong, Mr. Dave Menard and Mr. Ryan Rosborough for making available the wind tunnel facility used in this experiment and for modifying the experimental model and technique support.

My deepest thanks go to Fan Feng, Zhida Wang, Songyu Cao, Xiangwen Zuo and all my friends for their various kinds of helps during the experiment procedure.

Finally, I would like to acknowledge with gratitude, the support and love from my family and my girlfriend. Their understanding and unwavering support kept me going and helped me overcoming difficulties.

Abstract

With the development of aerodynamic investigation methods, long-span bridge projects gradually became more open to adopt challenging geometric optimizations and countermeasure implementations. Thus the bridge girder decks improved as well, changing from the compact box-deck girders shapes, to twin-box and multi-box deck sections. The objectives of the current research are first to experimentally investigate the aerodynamic properties of a new type of bridge deck with multiple-decks consisting of two side decks for traffic lanes and two middle decks for railway traffic. Secondly, the aerodynamic effect of the windshield barriers with two different heights (30 mm and 50 mm) was experimentally analyzed for the multiple-deck bridge deck model. Finally, the Iterative Least Squares (ILS) method was used for extracting the eight flutter derivatives of this new type of deck section model. Furthermore, a detailed comparison of the aerodynamic characteristics between the current research model and other types of box girder bridges was carried out for identifying the similarities and discrepancies in the overall aerodynamic performance of the bridge deck. A wind tunnel facility was used for testing the force coefficients and the flutter derivatives for the multi-box deck model for wind speeds in the range of 0.8 m/s to 11.0 m/s. In total, 301 test cases for 7 different attack angles ($\pm 6°$, $\pm 4°$, $\pm 2°$, $0°$) and two different windshield heights (30 mm and 50 mm) were carried out, as part of this research.

Contents

List of Figures

List of Tables

Nomenclature

ILS	Iterative Least Squares
VIV	Vortex-induced vibration
DVM	Discrete vortex method
DOF	Degree-of-freedom
LCO	Limit cycle oscillation
CFD	Computational fluid dynamics
LES	Large eddy simulation
ABS	Acrylonitrile Butadiene Styrene
NRC	National Research Council Canada
RPM	Revolutions per minute
FFT	Fast Fourier Transform
M'	Aerodynamic moment per unit length (kN)
U	Fluid velocity (m/s)
K	Reduced frequency (Hz)
B	Width of the cross-section (m)
α	angle of attack (rad or degree)
C(K)	Theodorsen's circulation function
F(K)	Real part of Theodorsen's circulation function
G(K)	Imaginary part of Theodorsen's circulation function
L	Characteristic linear dimension of the structure (m)
L_{se}	Self-excited aerodynamic lift force (N)
M_{se}	Self-excited aerodynamic moment (N · mm)

$[M]$	System mass matrix (kg)
$[C]$	System damping matrix
$[K]$	System Stiffness matrix
$[\mathrm{C}^{\mathrm{eff}}]$	Aeroelastically effective damping matrix
$[\mathrm{K}^{\mathrm{eff}}]$	Aeroelastically effective stiffness matrix
$[\mathrm{C}^{\mathrm{mech}}]$	Mechanical damping matrix
$[\mathrm{K}^{\mathrm{mech}}]$	Mechanical stiffness matrix
Re	Reynolds number
Ma	Mach number
Eu	Euler number
ρ	Air density (kg/m^3)
H_i^* A_i^* P_i^*	Flutter derivatives
$\mathrm{C_L}$	Aerodynamic lift coefficient
$\mathrm{C_D}$	Aerodynamic drag coefficient
ω_h	Circular frequency in vertical direction (Hz)
ω_α	Circular frequency in torsional direction (Hz)
$\mathrm{f_h}$	First natural frequency in vertical direction (Hz)
f_α	First natural frequency in torsional direction (Hz)
ε	Frequency ratio
m	Mass (kg)
I	Mass moment of inertia ($\mathrm{kg \cdot m^4}$)
ξ_h	Damping in vertical direction
ξ_α	Damping in torsional direction
$\mathrm{K_{sp}}$	Equivalent stiffness of spring

K_{tsp}	Equivalent stiffness of spring in the top
K_{bsp}	Equivalent stiffness of spring in the bottom
K_h	System stiffness in the vertical direction
K_α	System stiffness in the torsional direction
F_h	Force in the spring (N)
M_α	Moment produced by forces in springs ($N \cdot mm$)
Δl	Extension of the spring (mm)
r	Distance from the measuring point to the midpoint of the transverse bar (mm)

Chapter 1: Introduction

1.1 Background of the bridge aerodynamics

In November 1940, Tacoma Narrows Bridge, the third-longest suspension bridge at the time of its construction (after the Golden Gate Bridge and the George Washington Bridge) dramatically collapsed into the Puget Sound River due to wind effect [1]. This collapse is nowadays perceived as the most well-known bridge failure caused by lateral wind-induced vibrations, and it had a lasting effect on the advances recorded in the field of bridge engineering. Also this failure was presented as an example of elementary forced resonance with the wind speed providing an external periodic loading with a frequency that matched the bridge's natural frequency, although the actual cause of this failure was aeroelastic flutter [2]. This failure boosted research related to aerodynamics of slender structures, and such studies had a significant influence on the design of the world's great long-span bridges built since 1940 [3].

In the early 1960s, actual bridge tests, particularly those tests for simple single-span bridges, were undertaken to study the wind-induced vibrations, and to investigate the aerodynamic parameters of bridges [4]. Meanwhile, wind tunnel bridge model testing techniques were developed in order to further clarifying the aerodynamic characteristics and vertical and torsional motions of bridges subjected to different wind loading conditions in the laboratory. In addition, simplified beams and dynamic force analytical models were gradually applied to the finite element models of long-span bridges for performing the wind-vibration study. Later, much of the analytical work was performed for the vehicles-bridge interaction models to describe the bridge vibrations as computers became more available [4]. During the same period, actual field tests began on more complicated bridges such as continuous bridges.

Nowadays, bridge vibration studies cover almost all categories of bridges, such as suspension bridges, cable-stayed bridges, curved bridges, prestressed concrete bridges, high-speed transit structure bridges, etc. [5]. Analytical studies and computer models were used to handle parametrical studies such as accelerations and decelerations of vehicles, surface roughness of the bridge deck, seismic forces acting on the abutment, bridge aerodynamic parameters and multi-vehicle loading [6].

1.2 Wind-induced bridge vibrations and bridge aerodynamic instability

Bridge vibrations are mainly caused when the structure responds to dynamic loadings of increased amplitudes and with frequency components of the loading oscillations, exciting some of the structural frequencies of vibration. In other words, this means that if a structure begins to vibrate beyond serviceability limits, it is liable to fail mechanically, which can quickly lead to its total destruction. If these vibrations occur at a system’s resonance frequency, then oscillations will generate kinetic energies stored in the structural elements of the bridge. If the stored energy exceeds the load limit of the structure, the self-excited motion of such structure will be generated and due to both the external loading and the self-excited motion, the structural integrity of the bridge would be affected, which may cause the destruction of the bridge.

Aerodynamic instability is an unstable state caused by oscillations of a structure that are generated by spontaneous and periodic fluctuations in the flow, particularly in the wake of the structure [6]. Structures produce a response under the dynamic wind forces. In general, because of the existence of the structural damping, the response reaches the maximum value but tends to be damped, which forms a kind of back-and-forth vibration known as "beats" [7]. Nevertheless, wind forces can produce

negative damping components, when the velocity of wind reaches a certain critical value, the aerodynamic negative damping would become higher than the positive structural damping, and the wind-induced motion becomes more violent without stabilizing until the destruction is reached, which is known as the aerodynamic instability. As a whole, the aerodynamic instability of long-span bridges associated with the vibrations induced by wind can be categorized into four types: vortex-induced vibrations, buffeting vibrations, galloping instability and flutter instability; among them, vibration response of flutter and buffeting are divergent, which may cause destruction of the whole bridge [7]. The current research will focus on determining the flutter occurrence conditions for a bridge deck with multiple-box configuration, as it will be presented in the following sections and chapters.

1.3 Box girder bridges and windshield barriers

A bridge with main beams consisting of girders in the shape of a hollow box or multiple hollow boxes is called a box girder bridge. Normally, the geometric cross-section shape of the box girder bridges is rectangular or trapezoidal, and the construction material includes various kinds of concrete and steel. Compared to a classic I-beam bridge, the advantages of box girder bridges are as follows: (1) the box girder can carry more load than the I-beam section with equal height; and (2) the shape of the box girder is better for resisting torsional moment induced by wind. However, disadvantages also exist; for example, the box girder bridges are more expensive to construct and are more difficult to maintain, mainly because of the confined space inside the box girder that needs to be accessed [8]. With the development of the transportation industry, the single box girder bridge cannot fulfill the requirement of a rapid increase in bridge span length, thus the twin box girder bridge has been introduced, such as the Tsing Ma Bridge and the Stonecutters Bridge.

These twin box girder bridges take the geometrical form of a single box, but their aeroelastic properties present better stabilization for the critical flutter wind speed, which indicates that the twin-box girder can be applied for long-span bridges with a main span of up to 1,500 m and higher [9]. The Xihoumen Bridge (China), the second-longest bridge ranked by the length of the middle span, is a twin-box girder bridge with a central span of 1,650 m. Only the Akashi-Kaikyo Bridge with a central span of 1991 m in Japan had a longer span when the Xihoumen Bridge opened to the public in 2009. Nonetheless, several other bridges, including some new types of bridges such as the Strait of Messina Bridge, which is a three-box girder bridge, were designed or are under construction, and the central span length will also be larger than that of the Akashi-Kaikyo Bridge and the Xihoumen Bridge.

The present design of bridge structures does not only consider the basic bridge safety but also pays more attention to improving the functionality of the bridge decks. The traffic suffering from large lateral wind force might encounter some security problems such as vehicle sideslip or roll, which affect the driving security of vehicles. Automobiles collisions caused by lateral wind speeds have been reported sometimes, and the driving security affected by the high lateral wind speeds also needs to be considered. Thus, improving the functionality of the bridges became an urgent problem which needs a practical and immediate solution; for example, for long span bridges, the traffic should be controlled when the wind speed on the deck reaches 24 m/s [10].

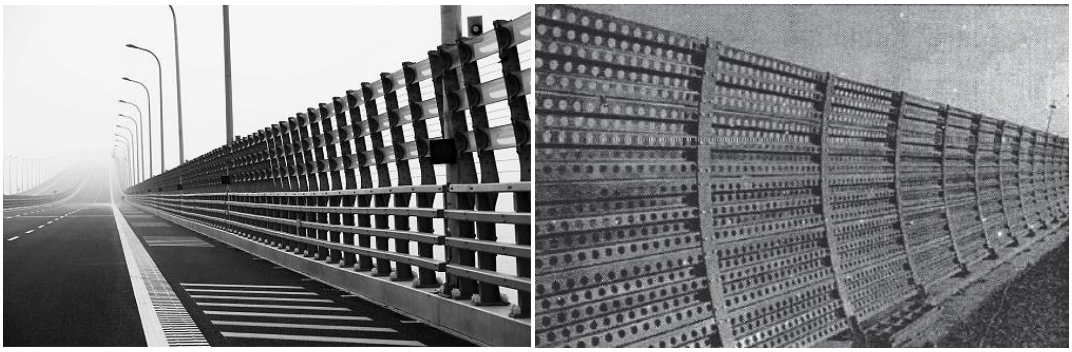

Figure 1.1 Types of windshield: (a) strip windshield barrier and (b) slab windshield barrier [10]

Windshield barrier is an additional structure for the bridge. It is set on both sides of the bridge decks and is used to decrease the incoming lateral wind speed, thus preventing the vehicles' rollover and ensuring driving security under high lateral wind force. According to different geometrical forms, the windshield barriers are divided into strip windshield barrier and slab windshield barrier [10]. The slab windshield barriers are made by assemblies of columns and perforated plates with small porosity (Fig 1.1 (b)). Long-span bridges, especially the bridges built over the sea, are exposed to strong wind loads, and for this reason they usually need to adopt the strip windshield which are made of columns and strips with large porosity (Fig 1.1 (a)). The function of the columns is to support the windshield barriers and the strips are used as windshields for this type of strip windshield barriers. The sheltering efficiency can be changed by adjusting the width of the barrier strips, the space between them and the dimensions of the strips.

1.4 Research motivation

For over-passing the main span limitations and reaching lengths of 2,000 m and more, improving the aerodynamic properties by adopting new geometric shapes for the bridge decks is required. As mentioned in section 1.3, the box girder bridge allows for a larger increase of the span length, when compared with the I-beam bridge deck, because the shape of the box girders can offer better resistance to torsion, and the two webs of the box girder allow larger and stronger flanges. However, a single box girder cannot satisfy the ever-growing transportation industry; the width and length of the main span needs to be increased. Therefore, bridge decks have evolved from traditional single-box bridge decks to twin-box bridge decks, with the increase in the main span lengths; for example, from 344 m for the Jindo Bridge with a single-box deck, the main span increased to 1,650 m for the Xihoumen Bridge which has a twin-box deck [10]. Due to the good efficiency for high wind speeds, the number of twin-box girder bridges with long spans, which have been constructed in recent years has increased, including the Yi Sun-Sin Bridge (2012, Korea) [11] with a main span of 1,545 m, the Tsing Ma Bridge (1997, China) [12] with a main span of 1,377 m, the Stonecutters Bridge (2009, China) [13] with a main span of 1018 m, etc. However, the main spans of these bridges never exceeded 2,000 m, and as an engineering challenge of crossing wide rivers and sea straits, some proposals of multiple box girder bridges with super-long spans have been designed such as the Strait of Messina Bridge [14] with a proposed main span of 3,300 m, the Qiongzhou Strait Bridge [16] with a proposed main span of 2,800 m, the Limit Span Scheme Bridge [17] with a proposed main span of 5,000 m, the Gibraltar Strait I Bridge [18] with a proposed main span of 3,500 m, etc. The data and the information regarding the main wind-induced instability problem and the type of the wind shields proposed for some of the bridges with super-long spans are presented in Table 1.1:

Table 1.1 Super-long span suspension bridges proposed in the world [19]

Span Order	Bridge Name	Main Span	Girder Type	Wind-induced Instability	Barrier Type	Year of Design
1	Bali Strait	2,100 m	Single Box	Flutter	Strip	2001
2	Tokyo Bay	2,300 m	Single Box	Flutter	Strip	1998
3	Qiongzhou Strait	2,800 m	Twin Box	Flutter	Strip	2002
4	Sunda Strait	3,000 m	Triple Box	Flutter	Strip	1997
5	Messina Strait	3,300 m	Triple Box	Flutter	Strip	1993
6	Gibraltar Strait I	3,500 m	Twin Box	Flutter	Strip	1991
7	Gibraltar Strait II	5,000 m	Triple Box	Flutter	Strip	1991
8	Limit Span Scheme	5,000 m	Twin Box	Flutter	Strip	2003

As a result of the increment of span length, besides the single-box girder bridge, the twin-box girder bridge and triple-box girder bridges have been considered to improve aerodynamic stability against strong winds. Flutter instability is estimated to be the main wind-induced problem, as it can be seen in Table 1.1. If the aerodynamic instability, especially the flutter, for super-long span bridges can be overcome, bridges with main spans of 5,000 m or even over 5,000 m can be reached by creating new structural shapes of bridge decks.

As mentioned in section 1.3, the super-long span bridges sensitive to wind loads need to be constructed with windshield barriers, and all the proposed super-long span bridges in the Table 1.1 have strip windshield barriers. According to the research outcomes presented by Nieto et al. [20] and Meng [21], the windshield barriers (breaks) play an important role in the aerodynamic properties of long-span bridge decks, and this structural element should be an inseparable part for an actual bridge deck or the sectional deck model used in experiments. The height of the windshield

barrier is an important factor for preventing vehicles overturning on their side, when subjected to high lateral wind speeds. Moreover, the height of the windshield barriers has direct effect on the aerodynamic parameters of the bridge deck itself, such as the static aerodynamic coefficients and the flutter derivatives. However, current research related to windshield barrier effects on multi-deck bridges concentrated only on the static aerodynamic coefficients, and few studies have been performed for determining the optimum flutter derivatives for different heights of the windshield barriers.

In order to investigate the multi-deck bridge and windshield barrier effect at the same time, a concept of a novel type of bridge deck consisting of four individual decks that are two side decks for traffic lanes and two middle decks for railways, named the Megane Bridge Deck, has been proposed for improving the aerodynamic stability for the super-long span. In order to prepare the Megane Bridge Deck for construction, the final configuration, including the windshield barriers must be implemented and the recommendations for the aerodynamic characteristics should be formulated.

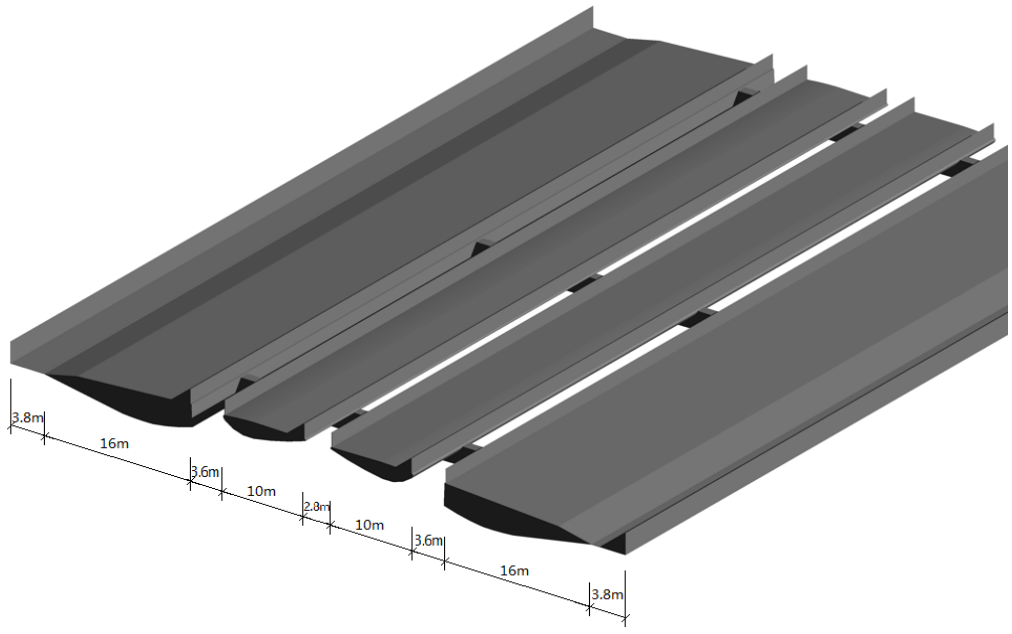

Figure 1.2 Geometrical dimensions of the Megane Bridge Deck

The real Megane Bridge multiple-box sectional deck, consisting of two 10 m width airfoil decks for railway in the middle and two 16 m airfoil decks for the traffic on either side, has a total dimension of 69.6 m wide including the 3.8 m sidewalk lane on both edges of the deck, as shown in Fig. 1.2. The depth of the railway and traffic box-decks is 3.0 m and 2.0 m, respectively; the width of the gap between the two railway decks is 2.8 m and the width of the deck between the railway and traffic decks is 3.6 m.

The experimental and CFD research performed by Wang [15] for determining the aerodynamic characteristics for the simplified Megane Bridge deck, consisting in the bare multi-box deck shape model without windshield barriers and sidewalks, showed a good performance of this geometrical configuration.

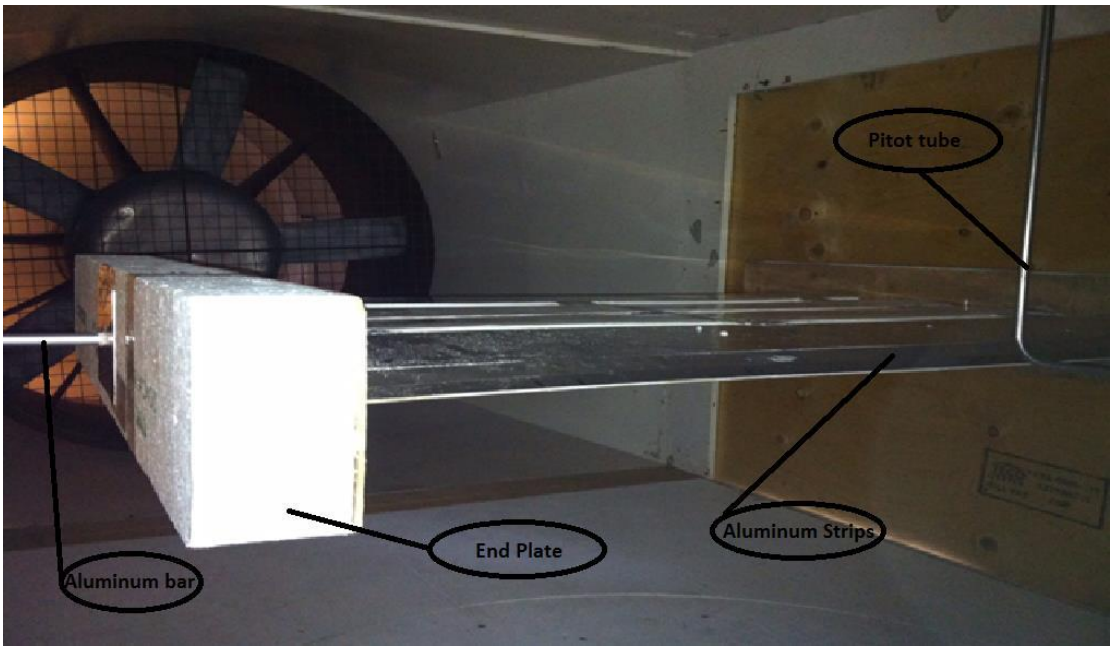

Figure 1.3 Simplified model of Megane Bridge deck [15]

However the bridge cannot be constructed without the wind shields and barriers, and these two structural elements should be inseparable parts for an actual bridge deck. Therefore, the aerodynamic properties of the Megane Bridge deck model, including

the windshields and barriers, should be determined, in order to ensure the possibility of construction for such a multi-box deck. In addition, the flutter derivatives of multi-box bridge decks are currently available only for the angle of attack of 0 °[15], however the most vulnerable cases for bridge decks are registered at ±4 °to ±8 °cases. Therefore, the main objective of the current research is building the complete bridge sectional model of the Megane Bridge deck with windshield barriers and sidewalks, then obtaining the aerodynamic properties of the model. Also identifying the static force coefficients and the flutter derivatives of the Megane Bridge sectional model under different attack angles, and different wind speeds will be performed. In order to achieve the best aerodynamic performance given by the multiple-box configuration of the deck and by the windshield barrier configuration, researching on the aerodynamic properties conferred by different heights of windshield barriers became a major contribution of the current research.

1.6 Research objectives

In order to determine the aerodynamic properties of the Megane Bridge multi-box deck model, two types of wind tunnel experiments were chosen for identifying the static force coefficients and the flutter derivatives respectively. The 2.1 m wide by 1.8 m high and 27.0 m long wind tunnel facility of the wind engineering company Gradient Wind Engineering Inc. was used for carrying out these tests. Moreover, well-organized experimental steps need to be performed as follows:

Through the experimental and analytical work carried out in this project, the current research aims at accomplishing three main objectives. The first objective is to build a proper bridge deck model with windshield barriers which respects all the aerodynamic similarity conditions. The second objective achievable from the static wind tunnel experiments is to determine the static drag and lift coefficients for applying the Den

Hartog criterion and for verifying if the current model would encounter the galloping instability. Also from the dynamic experiments the vertical and torsional vibrations for all the wind speeds allowable in the wind tunnel will be determined. As a third objective, based on the dynamic response obtained from the wind tunnel experiments, the ILS analytical method can be employed and the flutter derivatives for different angles of attack and for different wind speeds can be determined. Thus a full characterization of the aerodynamic characteristics of the Megane Bridge deck can be concluded. The final outcome of this research, is recommending the windshield barriers height with best aerodynamic performance, necessary for preparing the Megane Bridge deck for the potential construction stage.

Moreover, in order to obtain very good results, a systematic preparation of the wind tunnel experiment, can be conducted if the following experimental steps are carried out:

1. To measure the static aerodynamic coefficients, the bridge sectional model is fixed in the wind tunnel by the force balances installed into the wooden plate system during static tests. The lift and drag forces are measured by the force balances and are recorded by the data acquisition system under different attack angles and wind speeds. In total, 21 cases were carried out for the static coefficient tests with the testing cases of attack angles being in the range of -6 ° to 6 ° (in steps of 2 °) and wind speeds of 8 m/s, 9 m/s and 10 m/s. The results obtained from the wind tunnel experiments are then used in the related quasi-steady wind load formulation presented by Simiu and Scanlan [22], to obtain the static force coefficients C_D and C_L. Thereafter, the results of C_D and C_L of the Megane Bridge multiple-deck without windshield barrier and other kinds of box deck bridges are used for comparison with those of the current model.

2. To measure the vibration amplitudes and flutter derivatives, the bridge model is

suspended by eight springs of the spring suspension system, in which two springs were on the top and two springs were on the bottom of the transverse bar for each side. The displacement sensors are stuck on the wooden plate to measure the distances from the two measuring points to the transverse bar, which was varied with the vibration under smooth wind flow. Average amplitudes of vertical displacement and rotational angle need to be calculated for each in order to determine the vibration effect produced by different heights of windshield barriers in the edge. By using the system identification method — the Iterative Least Squares (ILS) method — the flutter derivatives of the sectional model can be extracted under different wind speeds and attack angles. Similarly, as the static coefficient tests, results of the flutter derivatives of the Theodorsen's thin plate theory, the Megane Bridge without windshield barrier case and other kinds of box girder bridges are used as comparison with the current model. In total, there are 280 cases for dynamic tests including 140 cases on 30 mm high windshield barrier and 140 cases on 50 mm high windshield barrier. The testing attack angles will increase from 0.8 m/s to 3.0 m/s in 0.2 m/s increment and then increase from 3.0 m/s to 11.0 m/s in increment of 1.0 m/s.

1.7 Thesis layout

The background, the introduction, the research motivation and objectives related to the Megane Bridge multi-box deck aerodynamic performance has been presented in Chapter 1. Some of the detailed background for the aerodynamic instability of bridge decks and various types of windshield barriers, the basic theoretical concepts of the analyzed methods, the evaluation of different kinds of bridge decks and the relevant deck shapes will be presented in Chapter 2, along with the Iterative Least Squares (ILS) method employed for determining the flutter derivatives from the performed wind tunnel experiments.

In Chapter 3, the model-making process and the presentation of the geometric shape of the Megane Bridge multi-box deck are presented. The experimental setup and testing procedures for the static force coefficients and for the flutter derivatives are then introduced in detail. A case for calibration of the free vibration test is then shown.

The results obtained for the static force coefficient tests and for the free vibration tests have been measured and these are discussed in Chapter 4. The amplitudes of vibration motions have been measured and are compared for different angles of attack and wind speeds in Chapter 4. Also, the results of the static force coefficients of the Megane Bridge without windshield barriers and for other kinds of box deck bridges were collected for comparison with the results obtained for the current model. For the flutter derivatives, the data referenced from Theodorsen's thin plate theory, the Megane Bridge without windshield barrier case and other kinds of box deck bridge cases were used for comparison with the flutter derivatives of the current model.

Conclusions derived from the experimentally obtained results and from the numerically estimated flutter derivatives are summarized in Chapter 5, followed by the recommendations for future work.

Chapter 2 Literature Review

2.1 Divergent vibrations phenomenon

For an airplane or streamline bridge deck under smooth wind flow, two static aeroelastic effects (vertical and torsional vibrations) may occur simultaneously, which is referred to as the aeroelastic coupling effect [23]. When the slope of the airfoil wind-induced response gradually increases until very high amplitude, the phenomenon called divergence occurs, causing the structural instability to occur.

A detailed explanation of divergence is presented by Hodges and Pierce [24], which mentions that the divergence occurs when a lifting surface deflects under aerodynamic load, so that when the applied load increases, the twisting effect on the structure increases as well. Vibration of the structure affected by the gradually increasing load can eventually reach the divergent point. In other words, divergence can be understood as a simple property of the differential equations governing the structure deflection [24]. The uncoupled torsional equation of motion for modelling the airplane wing or streamline as an isotropic Euler-Bernoulli beam can be expressed as:

$$GJ\frac{d^2\theta}{dy^2} = -M' \tag{2.1}$$

where y is the spanwise dimension, θ is the elastic twist of the beam, GJ is the torsinal stiffness of the beam, L is the beam length and M' is the aerodynamic moment per unit length, which can be expressed by free-stream fluid velocity U and initial angle of attack α_0. By substituting a parameter $\lambda^2 = C/(GJ)$, Eq. 2.1 can be rewritten as an ordinary differential equation of the form:

$$\frac{d^2\theta}{dy^2} + \lambda^2\theta = -\lambda^2\alpha_0 \tag{2.2}$$

After substituting the boundary conditions, $\theta\big|_{y=0} = \left.\frac{d\theta}{dy}\right|_{y=L} = 0$, for a clamped-free beam, the yielded solution is:

$$\theta = \alpha_0[\tan(\lambda L)\sin(\lambda L) + \cos(\lambda y) - 1] \tag{2.3}$$

As seen from Eq. 2.3, when $\lambda L = n/2 + n\pi$, the item $\tan(\lambda L)$ is infinite. This will correspond to a single value of free-stream velocity U for the torsional divergence speed. Therefore, for some boundary conditions and wind speeds implemented in a wind tunnel, it is possible to obtain the divergence phenomenon [24].

2.2 Aerodynamic instability

As mentioned in Chapter 1, aerodynamic instability induced by wind can be categorized into four aspects: vortex-induced vibration, buffeting vibration, galloping instability and flutter instability; among them, vibration response of flutter and buffeting are divergent; the divergent vibrations gradually increase until the entire bridge deck is losing its structural stability.

2.2.1 Vortex vibration

When the cross section of the bluff body is immersed in uniform flow, shedding of the periodic vortices downstream the body will induce a periodic aerodynamic force, the vortex-excited force. When the flow-around an object is a system of vibration, the periodic vortex-induced force behind the object will produce vortex-induced vibration

of the entire structural system. In addition, the vortex-excited resonance happens while vortex shedding frequency is equal to the natural frequency of the structure. Vortex-induced vibration (VIV) is not a hazardous divergent vibration because this is attenuated with the next increase on wind speed; the amplitude of vortex-induced vibration could be kept in an acceptable range by increasing the damping value or by using an appropriate correcting rectifying device [25].

In fluid dynamics, vortex-induced vibrations are the motions induced on bodies interacting with an external fluid flow, produced by periodical irregularities on this flow. One of the classical open-flow problems concerns the flow around a circular cylinder, or more generally, a bluff body. At very low Reynolds numbers (based on the diameter of the circular member), the streamlines of the resulting flow is are symmetric as expected from potential energy theory. However, as the Reynolds number is increased, the flow becomes asymmetric and the so-called Kármán vortex street (Figure 2.2.1) occurs [26].

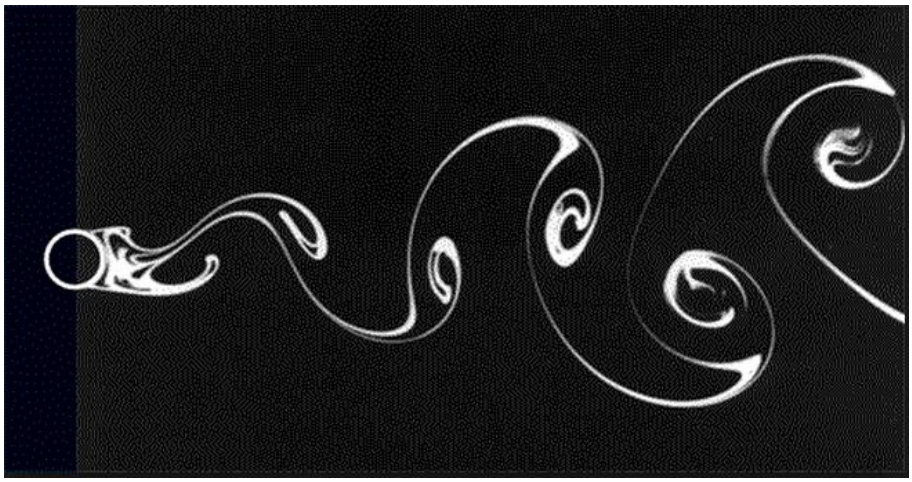

Figure 2.2.1 Karman vortex street created by a cylindrical object [27]

During past decades, both numerical and experimental studies have focused on understanding the dynamics of the VIV vibration of bluff bodies, including bridge decks. The fundamental reason is that VIV is not a small perturbation superimposed

on a mean steady motion, but it is an inherently nonlinear, self-governed or self-regulated multi-degree-of-freedom phenomenon. Also, for higher Re number, the unsteady flow characteristics are manifested by the existence of two unsteady shear layers and large-scale vortices structures [28].

For example, the wind tunnel results obtained for rectangular prisms with various aspect ratios (length to width ratio) presented by Nakamura and Mizota [29] show that, for the aspect ratios of 1:1 to 1:2, the boundary layers separate at the two front edges, under the attack angle of 0 °, however, for the aspect ratio of 1:4, the separated shear layers reattach to the object, frpm the sides of the prisms. They suggested that experimental research for other structures should be under taken at comparatively smaller aspect ratio of the length to width, which can reduce the vortex-induced forces. Bishop [30] summarized a number of experiments in order to establish the basic concepts for numerical models. The systematical results of the stationary circular cylinder and fluctuating static force coefficients were presented. Other reviews [31][32][33] summarized the development of the VIV vibrations and presented the detailed properties for these vibrations.

2.2.2 Galloping instability

Galloping is a kind of self-excited oscillation of a single degree of freedom system. Galloping oscillation usually happens for a slender structure with a specified cross-section, and is divided into two types: the cross-flow galloping and the wake galloping. Cross-flow galloping is a divergent self-excited vibration due to the negative slope of the lift coefficient or torsional moment. Wake galloping is a type of vibration which happens when the structure is in the wake flow of the previous structure, and this is influenced by the turbulent wake generated behind the previous structure.

Galloping instability happening at high wind speeds has two main parts: one is the vertical vibration influencing the bridge deck, and the other is the across-wind vibration (Figure 2.2.2) in the horizontal direction, which has a great effect on the towers [34].

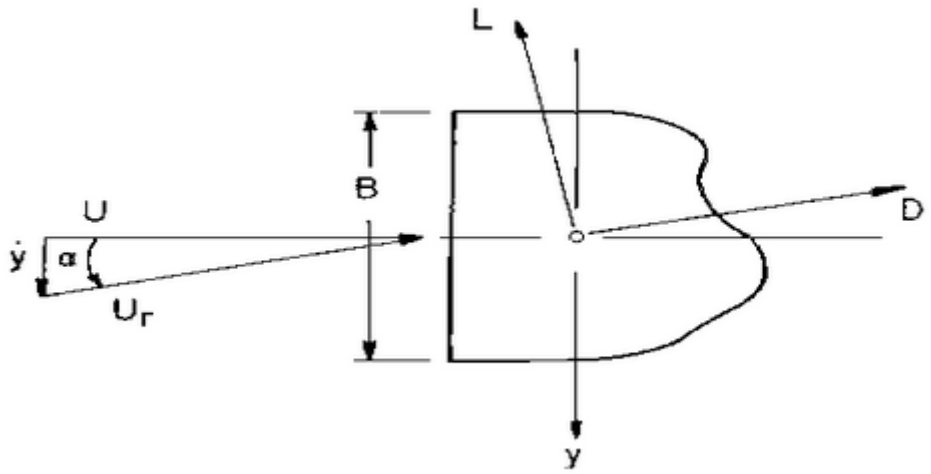

Figure 2.2.2 Across-wind galloping: Lift and drag forces (induced by wind) on a bluff body [34]

Particularly, for slender structures of nearly constant cross-section caused by wind-induced excitation, transverse galloping may happen as a dynamic instability. According to an explanation given by Glauert [35], if the negative slope of the lift coefficient becomes higher than the vertical coordinate of the drag coefficient, then transverse galloping occurs. Den Hartog [36] proposed the well-known Den Hartog stability criterion for evaluating the potential susceptibility of a structure under galloping. The corresponding Den Hartog formulation is related to the static aerodynamic coefficients of the structures, which can be obtained from wind tunnel experiments. Both static and dynamic wind tunnel tests were carried out to evaluate which one is better for galloping analyses; as a result, there were no big differences between the two methods [37]. Several experiments on different kinds of cross-sections of the bridge deck have been performed for verifying the galloping

instability, most of which were focused on the cross-sections with rectangular shapes [38]. However, galloping phenomenon can also occur for bodies of other cross-sections shapes. Alonso and Meseguer performed the galloping analyses on other two degree-of-freedom bodies with various cross-sections such as triangular shape, biconvex shape and rhomboidal shape [39][40].

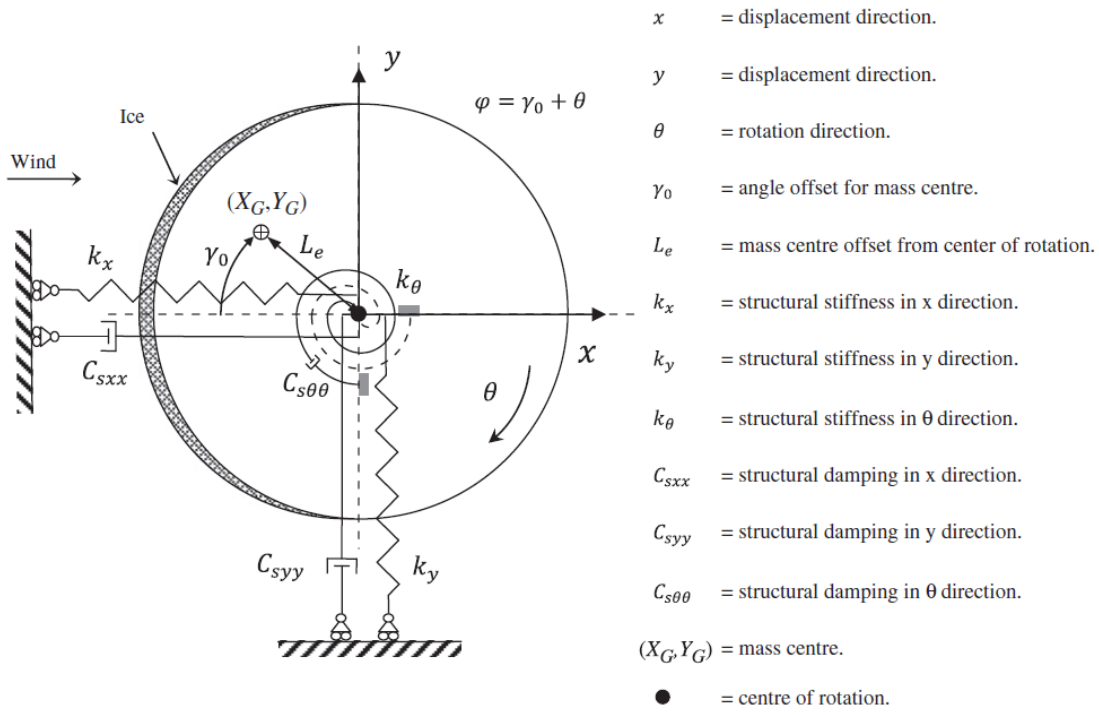

Figure 2.2.3 Definition of 3-dof section-based dynamic system [41]

By using the proven two degree-of-freedom model, Gjelstrup and Georgakis (2011) [41] proposed the onset of bluff body galloping instability in a three degree-of-freedom model (Fig 2.2.3) based on quasi-steady theory. The conclusion obtained in the research shows that the proposed three degree-of-freedom model is capable of estimating instabilities due to negative aerodynamic damping, while the results of the same model but with two degree-of-freedom presented by Macdonald and Larose [42] shows good agreement with the 3-DOF one.

2.2.3 Flutter instability

Flutter is a kind of self-excited aeroelastic phenomenon and occurs by the interaction of three types of forces: aerodynamic force, elastic force and inertia force. The vibration of a structure system absorbs the energy from the wind flow to offset the decaying trend resulting from the structure damping under a specified frequency and phase. When the positive structure damping reaches the zero net damping point or decreases further, a self-oscillation phenomenon occurs, and the corresponding amplitudes for deflection, rotational or torsional angle increases quickly until the structure breaks up. According to the decreasing speed of the net damping value, flutter is classified as two types: hard flutter (net damping decreases immediately to zero damping) and soft flutter (net damping decreases gradually to zero damping). For the majority of bridges, hard flutter phenomenon is commonly exhibited with modal damping decreasing rapidly as wind velocity increases [43].

Several methods have been proposed for flutter instability. Hodges and Pierce [24] presented three methods of predicting flutter for linear structures: the p-method, the k-method and the p-k method. For nonlinear systems, the nonlinear beam theory and the ONERA aerodynamic stall model were used for investigating the effects of nonlinearity on flutter, where a limit cycle oscillation (LCO) was used and the critical of flutter wind speed could be determined [44].

For a long-span cable-supported bridge, aerodynamic stability will not be affected by the buffeting forces when flutter occurs, and the predominant forces acting on the bridge are the self-excited forces. The governing equation of motion can be expressed as [22]

$$M\ddot{X} + C\dot{X} + KX = F_{se} \tag{2.4}$$

where *M*, *C* and *K* are the structural mass, damping and stiffness matrix, respectively; X is the nodal displacement matrix, $\dot{X}$ is the nodal velocity matrix and $\ddot{X}$ is the acceleration matrix; F_{se} represents the nodal equivalent self-excited force matrix. For a 2-DOF, F_{se} is the lift force and the rotational moment, while, for a 3 DOF linear dynamic system, F_{se} is the lift force, the drag force and the rotational moment. For the 2-DOF system, the F_{se} can be expressed as:

$$L_{\text{se}} = m(\ddot{h} + a\ddot{\alpha} + 2\zeta_h \omega_h \dot{h} + \omega_h^2 h) \tag{2.5}$$

$$M_{\text{se}} = I(\frac{a}{r_g^2}\ddot{h} + \ddot{\alpha} + 2\zeta_\alpha \omega_\alpha \dot{\alpha} + \omega_\alpha^2 \alpha) \tag{2.6}$$

where *m* is the mass of the modal system, *I* is the mass moment of inertia of the modal system, r_g is the radius of gyration of the body about the centre of the rotation, ζ_h and ζ_a are the mechanical damping ratios-to-critical in bending and torsion, respectively. ω_h and ω_a are the natural and circular frequencies, L_{se} is the self-excited aerodynamic lift force and M_{se} is the self-excited aerodynamic moment. In order to find the linear solution of Eq. 2.5 and 2.6, Theodorsen proposed the Theodorsen's circulation function to simplify the formula of aerodynamic self-excited forces [45]:

$$C(K) = F(K) + i \cdot G(K) \tag{2.7}$$

where $F(K)$ is the real part of the Theodorsen function $C(K)$, $G(K)$ is the imaginary part of $C(K)$ and K is the relevant frequency. The values of $F(K)$ and $G(K)$ vary with $1/K$ as shown in Figure 2.2.4.

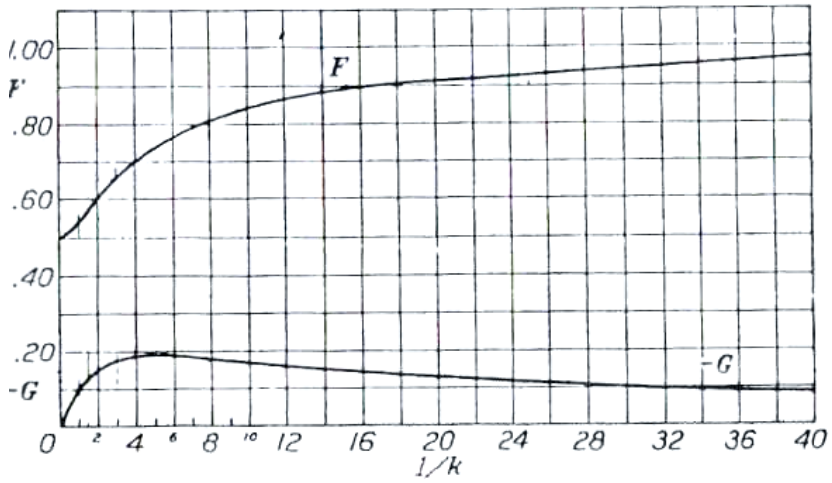

Figure 2.2.4 Values of $F(K)$ and G(K) varied with increment of 1/k [46]

The real and imaginary parts of $C(K)$ can be presented as [46]:

$$F(K)=\frac{0.500502\cdot K^3+0.512607\cdot K^2+0.210400\cdot K+0.021573}{K^3+1.035378\cdot K^2+0.251239\cdot K+0.021508} \tag{2.8}$$

$$G(K)=-\frac{0.000146\cdot K^3+0.122397\cdot K^2+0.327214\cdot K+0.001995}{K^3+2.481481\cdot K^2+0.934530\cdot K+0.089318} \tag{2.9}$$

After substituting the Theodorsen 's circulation function, Eq. (2.4) and (2.5) can be written as:

$$L_{se}=2\pi b\rho U^2\{(F+iG)[\alpha_0+\frac{i}{b}Kh_0+(\frac{1}{2}-a)iK\alpha_0]-\frac{1}{2}k^2(\frac{h_0}{b}-a\alpha_0)+\frac{1}{2}iK\alpha_0)\}e^{ikr} \tag{2.10}$$

$$M_{se}=2\pi b^2\rho U^2\{(\frac{1}{2}+a)(F+iG)[\alpha_0+\frac{i}{b}Kh_0+(\frac{1}{2}-a)iK\alpha_0]-\frac{1}{2}K^2a(\frac{h_0}{b}-a\alpha_0)+(\frac{1}{2}-a)iK\alpha_0+\frac{K^2}{8}\alpha_0)\}e^{ikr} \tag{2.11}$$

where U is the average speed of the wind flow, ρ is the air density, a is the distance from the midpoint of the plate to the point of rotation, b is the width of model, α_0 is

the rotational angle, h_0 is the vertical displacement and K is the reduced frequency. After the formula presented by Theodorsen was successfully applied on the aerodynamic forces on airfoil, the attempt of applying the theory on bridge decks was made [47], but the results showed the Theodorsen theory cannot accurately predict the aerodynamic forces of the bluff body. In 1971, Scanlan and Tomoko [48] introduced the concepts of flutter derivatives to express the aerodynamic self-excited forces in a brand-new way. For a 2-DOF system, the aerodynamic self-excited forces for lift and moment are expressed as:

$$L_{ae} = \frac{1}{2}\rho U^2 B\left[KH_1^*(K)\frac{\dot{h}}{U} + KH_2^*(K)\frac{B\dot{\alpha}}{U} + K^2 H_3^*(K)\alpha + K^2 H_4^*(K)\frac{h}{B}\right] \quad (2.12)$$

$$M_{ae} = \frac{1}{2}\rho U^2 B^2\left[KA_1^*(K)\frac{\dot{h}}{U} + KA_2^*(K)\frac{B\dot{\alpha}}{U} + K^2 A_3^*(K)\alpha + K^2 A_4^*(K)\frac{h}{B}\right] \quad (2.13)$$

where B is the deck width of the experimental model, H_i^* and A_i^* (i=1,2,3,4) are the flutter derivatives in terms of non-dimensional factor. The reduced frequency K is defined as:

$$K = \frac{\omega B}{U} \quad (2.14)$$

Nowadays, using flutter derivatives to express the aerodynamic self-excited forces is very common because only the real number appears in the formula, which is easier for calculating relevant parameters for a gradually complicated system. As for the 3-DOF system, the flutter derivatives change from H_i^* and A_i^* (i=1,2,3,4) to H_i^* ,P_i^* and A_i^* (i=1,2,3,4). These flutter derivatives can only be obtained through the system identification method, which will be introduced in Chapter 3.

2.2.4 Buffeting instability

The concepts of flutter, galloping and vortex-induced vibrations, are developed according to uniform flow assumptions, as discussed above. Buffeting vibration is a high-frequency instability caused by the airflow separation or by the random oscillations of one object influencing the motion of another. It is also caused by a random forced vibration due to fluctuating force acting on the object. Thus, according to different phenomena associated with the turbulence in the fluctuating wind, buffeting can be divided into three categories. The first is produced by the turbulence in the flow itself, the second is caused by the fluctuations of the characteristic turbulence in boundary layer, and the third is induced by the wake flow of the upper structure. Similar to the vortex vibration, buffeting is a finite amplitude vibration. The buffeting vibrations will induce local fatigue of the structure or can make individuals uncomfortable at higher levels buffeting can even affect the security of high-speed driving, but usually will not bring destructive damage to the bridge structures[49].

The analysis of buffeting response can be treated by the frequency-domain and time-domain approaches. The frequency domain method includes quasi-steady buffeting forces, turbulence modelling (power spectral density) and the spectral analysis method (correction functions). But the frequency domain methods can only apply to linear analysis, while time domain methods such as the quasi-steady buffeting model, time-history turbulence simulation and time-history analysis can satisfy both linear and non-linear situations. Since the 1920s, time domain buffeting response analysis was introduced and the relationship of unsteady aerodynamic lift forces on angle of attack and force coefficient were expressed under the form of polynomial one on the Laplace variable [50]. Unsteady aerodynamic response of airfoil under uniform gust of airfoil was solved first by developing the Wagner's [51] problem, after which Sears [52] developed a solution for vertical gust in 1941. A

framework method for buffeting analysis of bridge structures was firstly introduced by Davenport [53], which combined spectrum analysis and statistical computation in the modal space. Davenport also invented the so-called joint acceptance function, but only the single mode-based response prediction has been taken into consideration; cross-coupling between modes was neglected.

However, coupled buffeting must be considered for three reasons: first, turbulence or unsteady wind is the nature of wind; second, flutter and buffeting potentially occur simultaneously in high wind velocities; and third, aerodynamic forces by the quasi-steady theory is able to predict the bi-modal pressure probability distribution seen at laps under vortex.

2.3 Aeroelastic investigations of long-span bridges and windshield barriers

2.3.1 Similarity principles in wind tunnel experiments

Currently, wind tunnel testing is considered as an effective tool for studying the aerodynamic characteristics of bridges, airplanes or other structures exposed to wind flow. The wind tunnel experimental conditions should follow the similarity principles applicable to the flow and to the tested structural models. According to the specificity of aerodynamic characteristics, not only the geometric shape, mass, mass moment of inertia and elastic properties must be scaled, but also some of the following prerequisite need to be considered before carrying out wind tunnel experiments:

1.Geometric similarity of flow distribution

For aerodynamic research on long-span bridges, the boundary layer in the wind tunnel

should be under similar conditions as the actual one; the ratio of turbulence scale between the model and prototype can be calculated as:

$$L_m / L_s = \frac{\eta_m (\sqrt{\bar{u}_1^2} / \nu_1)_m}{\eta_s (\sqrt{\bar{u}_1^2} / \nu_1)_s} \tag{2.15}$$

where L_m/L_s is the ratio of turbulence scale between the model and prototype; η_m/η_s is the ratio of eddy scale between the model and prototype; $\sqrt{\bar{u}_1^2}$ (m/s) is the root-mean square value of vertical turbulent wind velocity; and ν_1 (m/s) is Kolmogorov velocity.

2. Kinematic similarity of flow

Kinematic similarity requires flow velocity on each node in the model should keep the same ratio of velocity and distribution of non-dimensionless turbulent value $\sqrt{\overline{u^2}}/U$ (U is the velocity at the top of the boundary layer) must be the same between the model and actual bridge.

3. Reynolds number Re

Reynolds number is the ratio between inertial and gravitational force, which is presented as the similarity principle of flow affected by fluid viscosity. All the physical quantities related to flow, such as drag force, lift force, etc., are related to the value of Re.

$$\mathrm{Re} = \frac{F_i}{F_v} = \frac{\rho v^2 l^2}{\mu v l} = \frac{\rho v l}{\mu} \tag{2.16}$$

where ρ is the air density, v is the flow speed, μ is the fluid viscosity and l is the characteristic length of the structure.

4.Mach number Ma

Mach number is the ratio between inertial and elastic force, which is presented as the similarity principle of flow effected by gassy compressibility. For low speed ($Ma < 0.4$) fluid, gassy compressibility can be neglected, while for flow with comparatively high speed ($Ma \geq 0.4$), the corresponding gassy compressibility should be considered.

$$Ma^2 = \frac{F_i}{F_c} = \frac{\rho v^2 l^2}{pl^2} = \frac{v^2}{p/\rho} = \frac{v^2}{a^2} \tag{2.17}$$

$$Ma = \frac{v}{a} \tag{2.18}$$

where a is velocity of sound.

5. Euler number Eu

Euler number is the ratio between pressure force and inertial force, which is presented as the similarity principle of flow effected by momentum loss. The value of Eu is related to the pressure or intensity of pressure

$$Eu = \frac{F_p}{F_i} = \frac{\rho l^2}{pv^2 l^2} = \frac{p^2}{\rho v^2} \tag{2.19}$$

Except for the above frequently used similarity principles, some wind tunnel experiments need consider other similarity principles like Prandtl number Pr , Nusselt number Nu, Lagrange number La, Strouhal number Sr, etc. For an investigation of aerodynamic properties, geometric similarity of flow distribution and kinematic similarity of flow are the main similarity principles for wind tunnel experiments on bridges.

2.3.2 Types of wind tunnel tests

The wind-induced dynamic and static parameters, such as flutter derivatives and aerodynamic force coefficients can be converted from wind tunnel tests results by using related similarity calculation methods. Usually the stability of bridge decks can be proved by performing sectional model tests which are less expensive comparing with other aerodynamic full-scale tests necessary for the stability verification methods. In other conditions, choosing different types of wind tunnel tests, mostly depends on the economic and the time frame requirements for the construction project. Simiu and Scanlan [22] summarized different types of wind tunnel tests for bridge structures and explained them briefly.

1. Full bridge aeroelastic model test: The full bridge aeroelastic test is performed on a scaled-down model of real bridge structure. This type of models are not only satisfying the reduced geometric similarity aspect, but also are satisfying the similarity conditions of mass, mass moment of inertia, damping, modal frequency and vibration modes.

2. Three-dimensional partial test: The three-dimensional partial wind tunnel test is carried out in order to simplify the full bridge aeroelastic model and to reduce the expenditure for the bridge modeling. This type of models still follow the similarity rules which includes the mass, mass moment of inertia, damping, modal frequency and vibration modes, but they only build the main span of the bridge or half of the whole bridge usually due to considerations of cost or dimensions.

3. Sectional model test: The sectional model test cost comparatively less than the full bridge aeroelastic model and three-dimensional partial model test. This type of test is employing usually only a segment of the deck, cable, or other part of the bridge, which is supported by a spring system or is connected to a force-balance system for

allowing the wind-induced motions of the model and for measuring the aerodynamic force coefficients, respectively. Because of the low cost of the bridge model, the scales of the model can be relatively high, compared with the other two types of models, as more than 1/80 scale can be employed, which is considered to have an effect on the accuracy and reliability of the results more reliable and less inaccurate. The small scale models also reduce the difference of results between the section models and the full bridge models. In addition, for this type of models, the aeroelastic parameters can be simply calculated by comprehensive methods such as Ibrahim Time Domain (ITD) method, Modified Ibrahim Time Domain (MITD) method, Iterative Least Square (ILS) method, Gradient Declining Algorithm, etc.

2.3.3 Bridge aerodynamics of different deck shapes

One of the most effective factors of bridge aerodynamic properties is the shape of the bridge deck or the geometry of the cross-section. Streamline shapes provide a relatively high stability against wind, such as the airplane wing, on which no turbulence is created by the wind and the boundary layers show no separation. However, currently developed long-span suspension bridges — like the single box deck bridge, the Great Belt Bridge [54]; and the twin-box girder bridge, the Stonecutters Bridge [55] — took the trapezoidal deck shape as their decks. Although the rhombus or the trapezoidal shape has better aerodynamic stability than the rectangular or square shape [56], wind-induced phenomenon like flutter or vortex shedding might affect the aerodynamic behaviours of the bridge. Therefore, in order to fulfill the requirement of longer bridge spans, it is necessary to investigate aerodynamic characteristics effected by different shapes of bridge decks.

More than 16 types of trapezoidal box sections were tested for the design of the Great Belt East Bridge, under smooth or turbulent flow for establishing the influence of

deck depth, edge configuration and side wall slopes by Larson (1993) [57] (Figure 2.3.1).

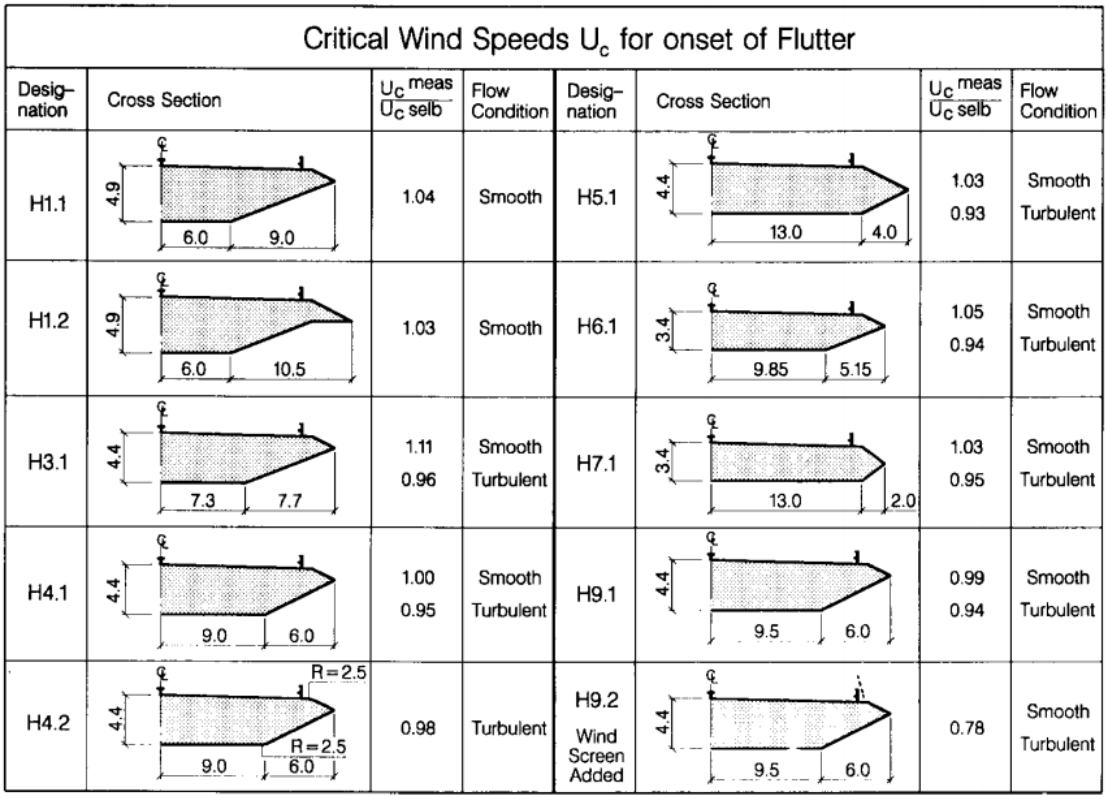

Figure 2.3.1 Critical wind speed for onset of aerodynamic instability for selected girder cross-sections performed in smooth and turbulent flow at 0° [57]

Flutter was identified as the conclusive factor for aerodynamic stability of the trapezoidal deck shape of the Great Belt East Bridge. Parts of the prominent cases are shown in Figure 2.3.1; case H 3.1 presents a comparatively high stability among all the cases. Later, the discrete vortex method (DVM) was used on five specified bridge decks to obtain the flow field and calculate the flutter derivatives [58]. Silva and Tarini (1998) found results obtained through the finite difference method and the finite element method are in agreement with those from the wind tunnel [59]. Based on those cases, Wang (2009) expanded more types of bridge shapes about rostra with different widths and acutance on the Nanjing Yangtze 4th Bridge [60]. The results obtained from the comparison between the cases shown in Fig. 2.3.2 concluded that

wider and acutance section rostra has a stronger aerodynamic stability of the girder, but the width of the girder can't exceed 3 m. Moreover, flutter critical wind speed increases as the web slope decreases.

case	Type of the section rostra		Flutter critical wind speed（m/s）		
			+3°	−3°	−3°
1		width：1.9m	51.5	>69.6	>70.6
2		width：2.1m	53.7	>70.7	>70.3
3		width：2.3m	54.6	>71.2	>70.5
4	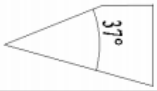	width：2.5m	56.7	>70.8	>71.2
5		width：2.7m	58.6	>71.5	>75.2
6	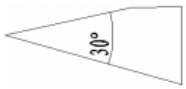	width：3.0m	63.4	>72.5	>70.9
7		width：3.3m	59.3	>71.3	>72.8

Figure 2.3.2 Critical wind speed for selected cross-sections performed in smooth flow at 0° [60]

They also found a small dead wake region appears when the slope of the inclined web is decreased to 15 ° and the flow along the bottom plate stays mainly attached to the web, which means it is not easy to format large vortices. As the wind speed increases to the critical flutter wind speed, the opposite vortices reduce and the girder cannot be provided with efficient excitation. In addition, for some scaled models, vortex shedding vibration may not happen or cannot be observed. Different width, height and rostra slope of the same kind of bridge deck show a different but similar trend in terms of aerodynamic characteristics. For different types of girders as closed box girder and plate girder as shown in Figure 2.3.3, Lin et al. (2005) [56] performed the

related experimental research on bridge aerodynamics, and calculated the flutter derivatives and critical flutter wind speed of different geometric cases.

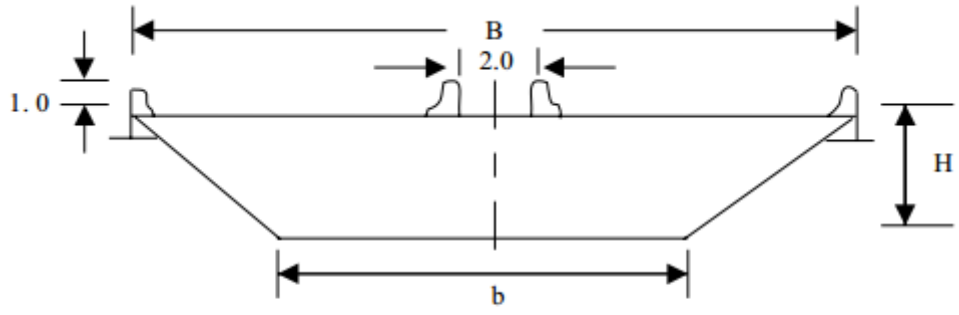

Model	1–1	1–2	1–3	1–4
H(cm)	1.75	2.4	3.2	5
b(cm)	27.7	25.4	21.8	15.4

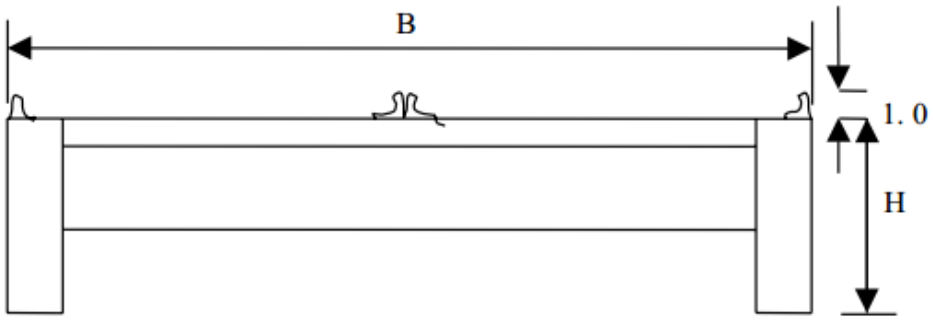

Model	2–1	2–2	2–3	2–4
H(cm)	1.5	2	3	5

Figure 2.3.3 Geometry (closed box girder and plate girder) of section models [56]

After analyzing the flutter and buffeting, it could be concluded that the closed box girder deck has a much higher critical flutter wind speed than the plate girder deck, which means that the closed box girder is a better aerodynamically stable deck shape. Furthermore, the box girder bridge shows better aerodynamic stability in turbulent flow than smooth flow when compared with the behaviour in smooth flow [56].

Based on the research performed on the single box bridge deck, twin deck section was proposed. As an example, Ge and Xiang (2009) compared the static coefficients of the

single box deck and twin box deck by using the data of the Great Belt Bridge and the Stonecutters Bridge, respectively, to show the advantages of using the twin bridge deck section. The results show that the critical wind speed of the twin box shape is much higher than that of the single box deck configuration [9]. Additionally, the aerodynamic interference effects on the flutter stability of twin decks was done by the wind tunnel experiment [61]. As a result, it was concluded that aerodynamic interference effects on flutter and vortex shedding have an assignable influence on the aerodynamic stability design of twin-deck bridges. In order to explore the vortices and turbulent flow around the twin box girder, a number of twin deck models with different gap ratios in the range of 0.85 to 3.40 were tested in the wind tunnel by Chen et al. (2014) [62]. The measurement results indicate that the gap ratio is an important factor which can influence the formation of vortices and turbulent flow, while the cross-beams have the function of reducing the pressure fluctuation and weakening the vortex shedding. When the gap ratios increase from a small range (0.85 and 1.70) to a large range (2.55 and 3.4), the increasing slope of lift coefficient C_D is mainly induced by the intense negative region of the mean pressure coefficients. And the mean pressure coefficients can also affect the drag coefficient C_L. From the above results, the shape of the box deck, no matter if it is a twin-box shape or single-box shape, is a main factor affecting the aerodynamic properties of bridges.

In terms of general bridge design with very long spans, achieving a low dead weight becomes a paramount consideration thus bridges should adopt lighter deck structures with minimal surfacing and fitting weights [63]. The Strait of Messina Bridge as shown in Figure 2.3.4, which is a triple-box-deck suspension bridge with a main span of 3,300 m, was proposed as a challening step forward in bridge engineering. For such a long-span structure, this bridge is very sensitive to wind flow, and aerodynamic stability is the governing factor among the design procedures.

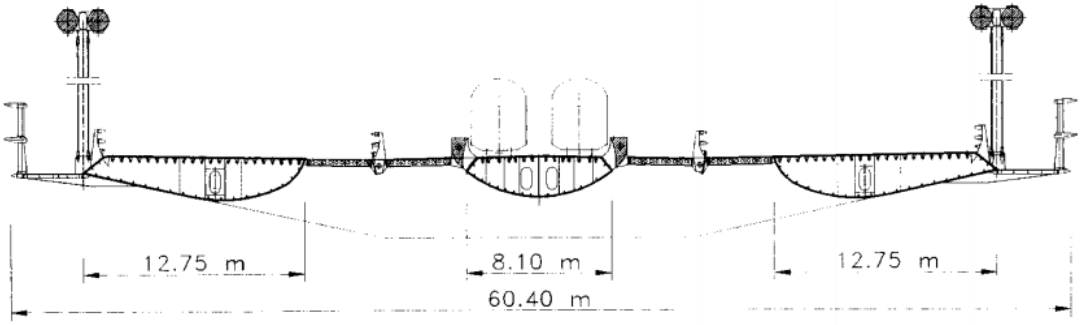

Figure 2.3.4 Cross-section of the Messina Strait Bridge deck[63]

Since the 1990s, numerical and experimental research has been achieved on the Messina Straits Bridge. Brancaleoni and Diana (1993) [63] firstly introduced the triple box shape, and obtained some basic static and dynamic properties by using wind tunnel tests on the 1:30 and 1:87 sectional model. As seen in Fig 2.3.5, compared with the single-deck bridge: the Humber Bridge (Figure 2.3.6), lift and moment derivatives are positive but values of the Messina Strait Bridge are much lower than those of the Humber Bridge because the triple box deck allows for a higher value of critical flutter speed. For the same 3,300 m span length, the triple box bridge with windshield barriers allows for 90 m/s critical flutter velocity, while the single box bridge only allows for 40 m/s.

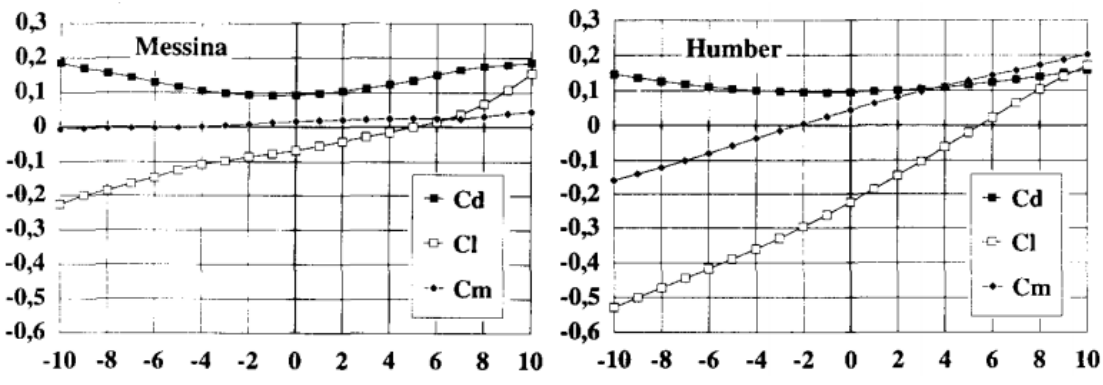

Figure 2.3.5 Drag, lift and pitch coefficient for the Messina Strait Bridge and the Humber Bridge [63]

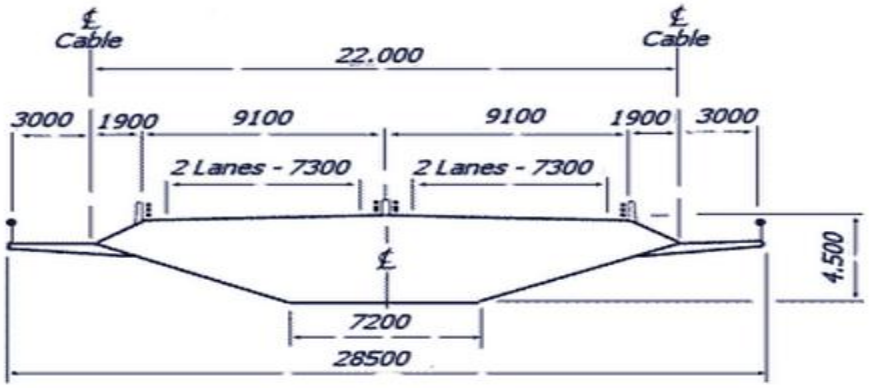

Figure 2.3.6 Cross-section of the Humber Bridge [63]

Later in 1995, Diana et al. built a full aeroelastic model of the Messina Strait Bridge (Figure 2.3.7) to verify the aerodynamic behaviour of this bridge and performed numerical tests numerically and experimentally investigationsy on the models scaled 1:30 and 1:250, respectively [64]. Results of static aerodynamic force coefficients are shown in Figure 2.10; all three parameters show good agreement with the sectional model results by Brancaleoni and Diana [63].

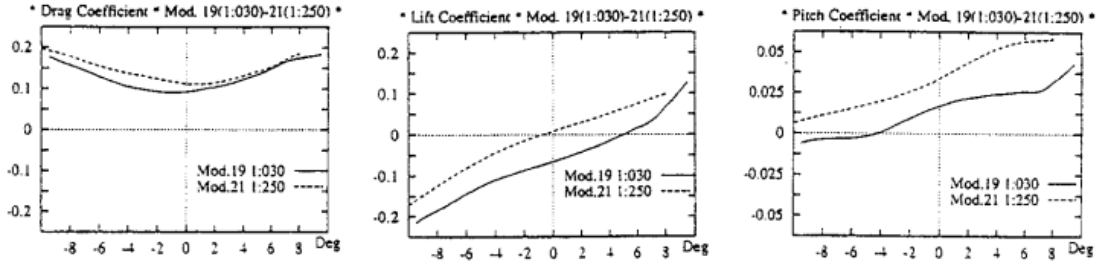

Figure 2.3.7 Drag, lift and pitch coefficient for Messina Bridge [64]

In addition, in order to investigate the flutter phenomenon on the three-deck bridge, free vibration experiments were carried out under smooth and turbulent flow to get the damping ratios and natural frequencies. The results indicate the flutter instability is well beyond wind speed of 62 m/s, and the turbulence of the flow plays a minor role in the determination of flutter instability.

The advantages of the triple box deck have been presented above, but some shortcomings still exist. Compared with the size, the Messina Strait Bridge is lightweight, but a large amount of steel used is only for fatigue resistance and the design is far from being perfect aesthetically [65]. That said, if the Messina Strait Bridge can be constructed successfully, the limitations in terms of bridge span will be pushed ever further.

2.3.4 Static aerodynamic coefficients effected by windshield barriers

Setup of windshield barriers can effectively improve the driving security under lateral wind; it also affects the bridge aerodynamic characteristics. In addition, the shape of the windshield barrier and the installation position also affects the reducing consequence of lateral wind speed and bridge aerodynamic characteristics. Hence, only through optimizing windshield barriers is the wind sheltering ability able to be brought into play, and at the same time, the resistance can be guaranteed. Recently, research has adopted several methods such as the standard k-ϵ model, RNG k-ϵ model, discrete vortex method and LES to simulate flow around a square cylinder [66][67]. The results showed that the standard k-ϵ model was not able to express the complicated characteristics of separation and reattachment of the flow reasonably when simulating flow around blunt body.

According to the numerical simulation on the Xiangshangang Bridge by Zhou and Zhu (2000) [68], it was indicated that the unsteady problem of flow around the cross-section of the bridge has successfully been simulated through the RNG k-ϵ turbulence model. The sheltering efficiency of the windshield barrier is bound up with the porosity value, attack angle of incoming wind and windshield barrier height. Meanwhile, they also took a composite pylon of cable-stayed bridge with a 688 m main span as shown in Figure 2.3.8. Different types of windshield barriers and

different corresponding installation positions have been considered as the impact factors of the bridge aerodynamic characteristics through the wind tunnel experiment [69].

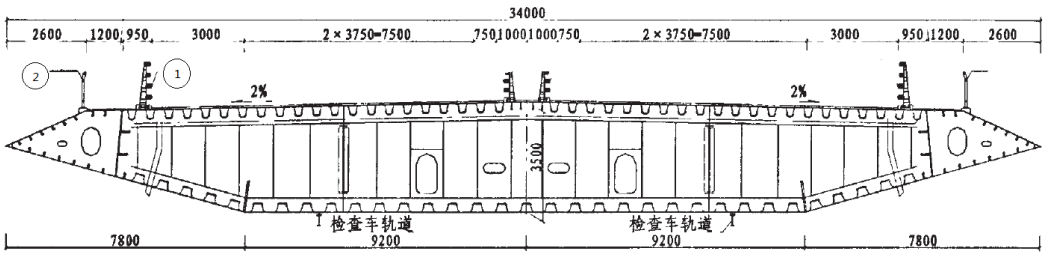

Figure 2.3.8 Deck cross-section figuration of the cable-stayed bridge [69]

In order not to take additional travel space, there are two positions to set up the windshield barrier: 1) the crash barrier; and 2) the maintaining barrier. The combination of the windshield barrier with the crash barrier or the maintaining barrier can save material and space. Six windshield barriers for different kinds or porosities were designed as follows:

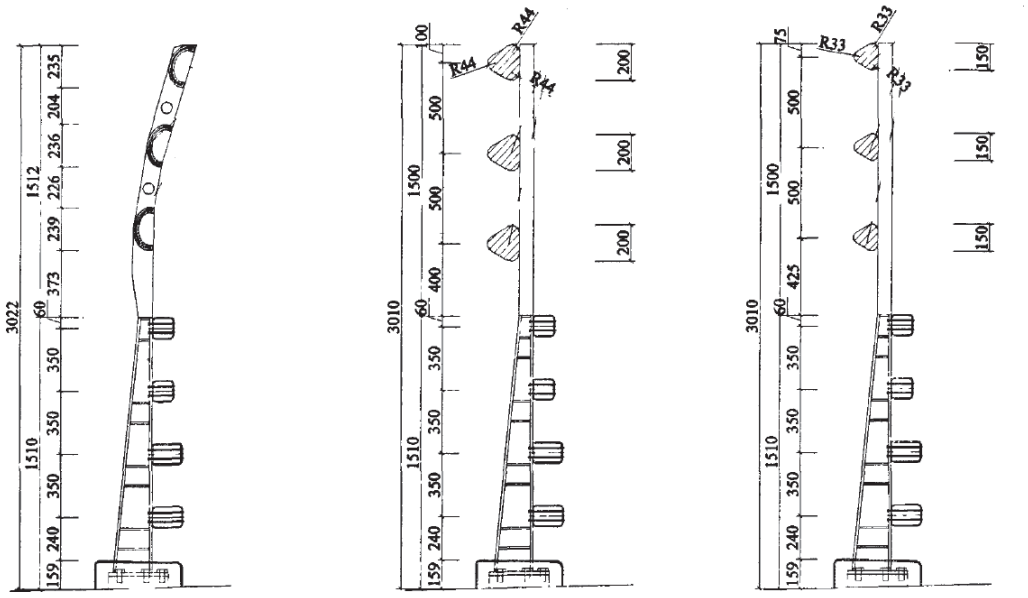

A B C

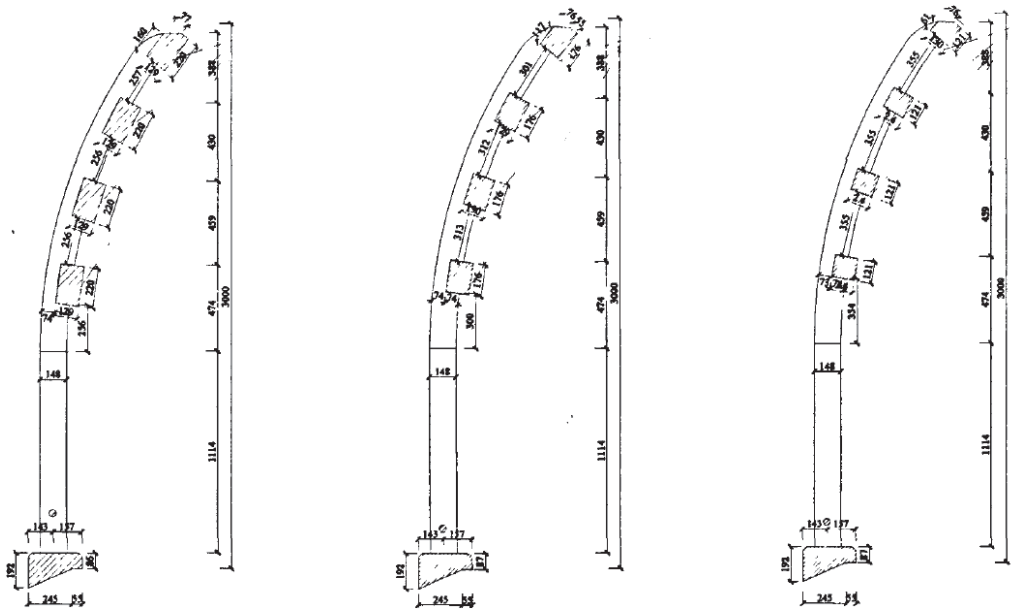

D E F

Figure 2.3.9 Six types of curved windshield barriers [69]

As shown in Figure 2.3.9, the six kinds of windshield barriers, each of 3.0 m height and 0.12 m width are: A) 50% porosity semielliptical windshield barrier; B) 60% porosity triangular windshield barrier; C) 70% porosity triangular windshield barrier. The installation position at the crash barrier: D) 50% porosity curved windshield barrier; E) 60% porosity curved windshield barrier; F) 60% porosity curved windshield barrier. The research has also been carried on CFD analysis to obtain the reduction factor of the wind speed and the drag coefficient C_D. The analysis result shows that the reduction factor for the wind speed gradually decreases from the upper side to the lower side; therefore, windshield barrier should be better set up in the maintaining barrier place, which has a longer distance to the bridge lanes. For the different windshield barriers in the same place, the reduction factor of the wind speed is inversely proportional to the drag coefficient of the main beam cross-section. Considered the limitation for the static wind requirement, the 60% porosity curved windshield barrier is determined to be the final scheme. Not every bridge should select the 60% porosity as their windshield barrier; for example, 50% porosity was

chosen to be the best option on a twin box girder bridge [20], but the porosity of the windshield barriers was proved to be the main factor affecting the wind sheltering effect, and the rectangular railing had the best sheltering efficiency [66]. By investigating a train-bridge system, results obtained from wind tunnel experiments concluded that the height of the windshield barrier is also an effective factor for improving the wind sheltering effect; furthermore, different heights of windshield barriers affects differently the aerodynamic property of the entire whole bridge system [71].

Windshield barriers influence not only the wind velocity and the flow formations on the surface of bridge decks, they also have an influence on aerodynamic properties of the entire bridge. Nieto and Hernandez (2012) investigated a cable-stayed bridge deck by conducting CFD simulations, and four different deck cross-sections were compared in terms of aerodynamic force coefficients [20].

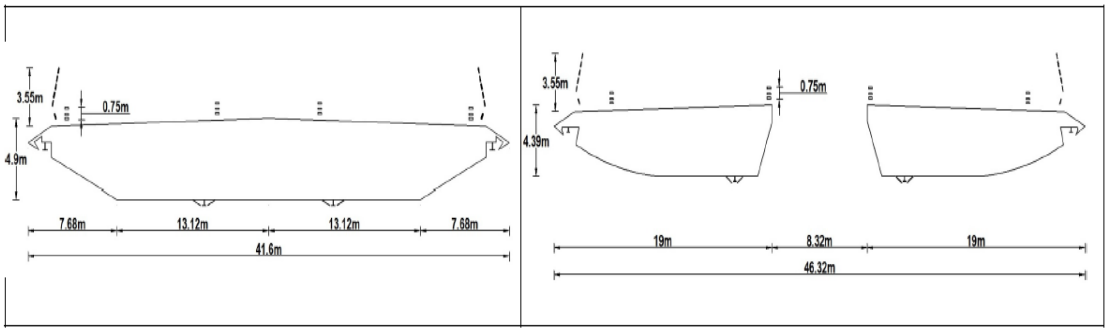

Figure 2.3.10 Geometry of the bridge deck types [20]

A single box girder with windshield barriers on the right side and a twin box girder with windshield barriers on the left side are shown in Figure 2.3.10. The single box girder and twin box girder without windshield barrier cross-sections were added to this study for comparison. For the single box girder considered for the design of the Great Belt Bridge, as shown in Figure 2.3.11, installation of windshield barriers causes the drag coefficient increasing greatly, shifting down the lift coefficients while

the same slope trends and gradually decreasing slope of moment coefficient were noticed.

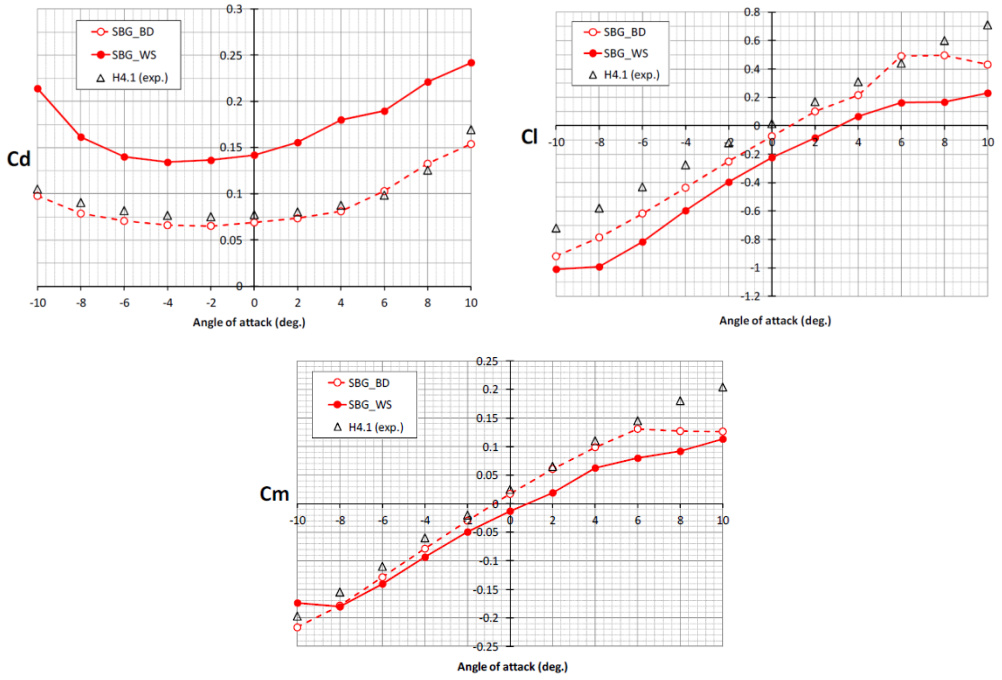

Figure 2.3.11 Force coefficients of the single box girder with and without windshield barriers [20]

For the twin box girder bridge, as shown in Figure 2.3.12, windshield barriers cause a parabolic shape on the drag coefficient and decreases the slope of lift coefficient for the positive attack angles. As for the moment coefficient, the obvious decrement happens for the range of all attack angles investigated.

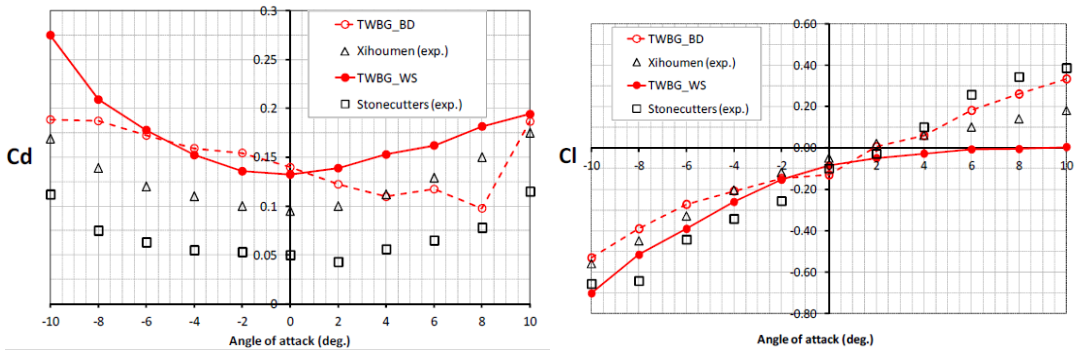

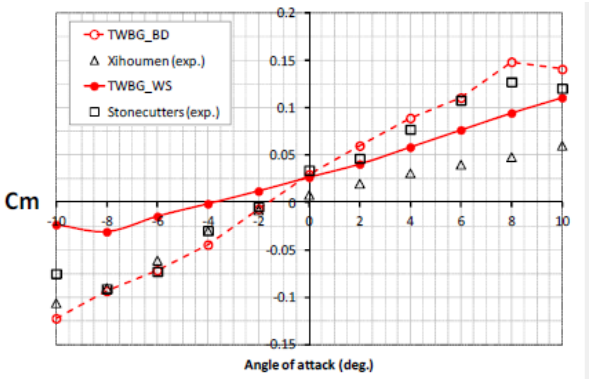

Figure 2.3.12 Force coefficients of the twin box girder with and without windshield barriers [20]

Guo and Wang (2015) [71] summarized the aerodynamic effect of windshield barriers on a train-bridge system, and they concluded that the windshield barriers are helpful for the sheltering effect on vehicles driving on the bridge; the side-force and rolling moment coefficients of the vehicle can be reduced with more than 70%. Similarly, windshield barriers show a negative influence on the bridge deck response and the drag and moment forces on the deck increase remarkably because the windshield barriers enlarge the windward nominal area between the windshield barriers.

2.3.5 Aerodynamic flutter derivatives effected by windshield barriers

Long-span bridge sectional models used for wind tunnel experiments are usually built with windshield barriers, because windshield barriers have a remarkable effect on the aerodynamic characteristics, such as the flutter derivatives. Flutter derivatives are critical parameters for bridge flutter and buffeting analyses. These parameters cannot be directly extracted from the initial experiment results that are obtained under smooth flow. The data recorded in these tests should be converted to displacement time history figures or overturn moment time history figures, then by using proper system identification methods, the relevant parameters should be extracted.

Different methods for extraction of flutter derivatives have been presented for determining the linear formulation of expressing the aerodynamic drag and lift forces and moment [7]. Among all the studies discussed, the simple linear formulations presented by Simiu and Scanlan [48] have been widely adopted by most bridge engineers who need to design for the wind effect aspect; Therefore these formulations have already become the standard method for expressing the aerodynamic flutter forces on bridge decks. The aerodynamic self-excited forces for lift and moment are expressed as per Eq. 2.12 and Eq. 2.13.

In both the wind tunnel test and in actual situations, bridges or bridge models respond to wind load with vibrations on the vertical and rotational directions with the bending frequency ω_h and the torsional frequency ω_α. As a result, the oscillation in these two directions may be coupled and the model can oscillate as a coupled motion. The question then arises whether the bending frequency ω_h or the torsion frequency ω_α should be substituted in the Eq. 2.12 and Eq. 2.13. For a complete consideration of the self-excited flutter forces, the bending frequency and the frequency are both substituted as:

$$L_{ae} = \frac{1}{2}\rho U^2 B\left[K_h H_1^*(K_h)\frac{\dot{h}}{U} + K_h H_2^*(K_h)\frac{B\dot{\alpha}}{U} + K_h^2 H_3^*(K_h)\alpha + K_h^2 H_4^*(K_h)\frac{h}{B}\right]$$

$$+\frac{1}{2}\rho U^2 B\left[K_\alpha H_1^*(K_\alpha)\frac{\dot{h}}{U} + K_\alpha H_2^*(K_\alpha)\frac{B\dot{\alpha}}{U} + K_\alpha^2 H_3^*(K_\alpha)\alpha + K_\alpha^2 H_4^*(K_\alpha)\frac{h}{B}\right] \quad (2.20)$$

$$M_{ae} = \frac{1}{2}\rho U^2 B^2\left[K_h A_1^*(K_h)\frac{\dot{h}}{U} + K_h A_2^*(K_h)\frac{B\dot{\alpha}}{U} + K_h^2 A_3^*(K_h)\alpha + K_h^2 A_4^*(K_h)\frac{h}{B}\right]$$

$$+\frac{1}{2}\rho U^2 B^2\left[K_\alpha A_1^*(K_\alpha)\frac{\dot{h}}{U} + K_\alpha A_2^*(K_\alpha)\frac{B\dot{\alpha}}{U} + K_\alpha^2 A_3^*(K_\alpha)\alpha + K_\alpha^2 A_4^*(K_\alpha)\frac{h}{B}\right] \quad (2.21)$$

The completed formulations of flutter forces include a total 16 flutter derivatives, which are $H_i^*(K_h)$, $H_i^*(K_\alpha)$, $A_i^*(K_h)$ and $A_i^*(K_h)$ (i =1,2,3,4) according to Equations 2.20 and 2.21. Among them, $H_i^*(K_h)$ and $H_i^*(K_\alpha)$ (i=1,2,3,4) are for calculating the aerodynamic lift force L_{ae} and $A_i^*(K_h)$ (i=1,2,3,4) are for obtaining the aerodynamic moment M_{ae}. Nonetheless, any kind of system identification method could only identify eight flutter derivatives or eight unknown parameters; in other words, the uniqueness question should be solved before adapting the system identification method.

Iwamoto and Fujino [73] performed an investigation on identifying the effect of coupling between the bending and rotation motions when a bridge section model suffers smooth wind flow in the wind tunnel. As the results show, the coupling between the two-direction motions was found to be weak because the power of bending motion and the rotation motion cannot reach the comparatively bigger value at the same time, thus they don't behave in the same manner. Said another way, the algebras including α and $\dot{\alpha}$ related with ω_h and the algebras including h and $\dot{h}$ related with ω_α can be neglected. As a result, the 16 flutter derivatives are reduced to 8; the system identification method can be used to identify the 8 unknown parameters. The simplified equations are shown below:

$$L_{ae} = \frac{1}{2}\rho U^2 B\left[K_h H_1^*(K_h)\frac{\dot{h}}{U} + K_\alpha H_2^*(K_\alpha)\frac{B\dot{\alpha}}{U} + K_\alpha^2 H_3^*(K_\alpha)\alpha + K_h^2 H_4^*(K_h)\frac{h}{B}\right] \quad (2.22)$$

$$M_{ae} = \frac{1}{2}\rho U^2 B^2\left[K_h A_1^*(K_h)\frac{\dot{h}}{U} + K_\alpha A_2^*(K_\alpha)\frac{B\dot{\alpha}}{U} + K_\alpha^2 A_3^*(K_\alpha)\alpha + K_h^2 A_4^*(K_h)\frac{h}{B}\right] \quad (2.23)$$

It's easy to see that the flutter derivatives H_1^*, H_4^*, A_1^* and A_4^* are in the terms

with ω_h, which means those four flutter derivatives are concerned with bending motions. The situation is similar for the other 4 flutter derivatives H_2^*, H_3^*, A_2^* and A_3^*, they should be obtained through the torsional motions [74]. Here, H_1^*, H_4^*, A_1^* and A_4^* are called direct-flutter derivatives because they can be identified by analyzing a single-degree-of-freedom model system. H_2^*, H_3^*, A_2^* and A_3^* are called cross-flutter derivatives, which only exist in a two-degree-of-freedom model system with the coupled motion, and they can only be obtained through the effect of the motion of the other degree of freedom.

The flutter motion equation of a two-degree-of-freedom bridge sectional model under smooth wind flow can be written as [75]:

$$M\ddot{X} + C\dot{X} + KX = F_{ae} \tag{2.24}$$

where M is the structural mass matrix, C is the structural damping matrix, K is the structural stiffness matrix and F_{se} is the structural aerodynamic self-excited force matrix acting on node. $\ddot{X}$, $\dot{X}$ and X are, respectively, the acceleration matrix, velocity matrix and displacement matrix of the node.

After substituting the relevant parameters, flutter motion equation per unit length can be rewritten as follows:

$$m(\ddot{h} + 2\zeta_h\omega_h\dot{h} + \omega_h^2 h) = L_{se} \tag{2.25}$$

$$I(\ddot{\alpha} + 2\zeta_\alpha\omega_\alpha\dot{\alpha} + \omega_\alpha^2\alpha) = M_{se} \tag{2.26}$$

where m is the model mass, I is the mass moment of inertia, ζ_h is the

mechanical bending damping ratio, ζ_α is the mechanical torsion damping ratio, ω_h is the natural frequency of bending, ω_α is the natural frequency of torsion, L_{se} is the self-excited lift force, M_{se} is the self-excited moment, $\ddot{h}$, $\dot{h}$ and h are the acceleration, velocity and displacement in the vertical direction, respectively, $\ddot{\alpha}$, $\dot{\alpha}$ and α are the angular acceleration, angular velocity and angle in the rotational direction, respectively. Eq. 2.27 can be expressed as matrix format:

$$[M][\ddot{X}]+[C][\dot{X}]+[K][X]=[F_{ae}] \tag{2.27}$$

where, $[M]=\begin{bmatrix} m & 0 \\ 0 & I \end{bmatrix}$, $[C]=\begin{bmatrix} C_h & 0 \\ 0 & C_\alpha \end{bmatrix}$, $[K]=\begin{bmatrix} K_h & 0 \\ 0 & K_\alpha \end{bmatrix}$, $[F_{ae}]=\begin{bmatrix} L_{ae} \\ M_{ae} \end{bmatrix}$. In order to simplify the above equation, both sides of Eq.2.30 are divided by $[M]$:

$$[\ddot{X}]+[M]^{-1}[C][\dot{X}]+[M]^{-1}[K][X]=[M]^{-1}[F_{ae}] \tag{2.28}$$

where, $[X]=\{h \quad \alpha\}^T$, $[M]^{-1}[C]=\begin{bmatrix} 2\zeta_h\omega_h & 0 \\ 0 & 2\zeta_\alpha\omega_\alpha \end{bmatrix}$, $[M]^{-1}[K]=\begin{bmatrix} \omega_h^2 & 0 \\ 0 & \omega_\alpha^2 \end{bmatrix}$, $[M]^{-1}[F_{ae}]=\begin{bmatrix} L_{ae} \\ M_{ae} \end{bmatrix}$.

And the aeroelastic self-excited force F_{ae} can also be expressed as the matrix format:

$$[F_{ae}]=\begin{bmatrix} L_{ae} \\ M_{ae} \end{bmatrix}=\begin{bmatrix} \frac{1}{2}\rho U^2 B & 0 \\ 0 & \frac{1}{2}\rho U^2 B \end{bmatrix}\begin{bmatrix} \frac{KH_1^*}{U} & \frac{KH_2^*B}{U} & K^2H_3^* & \frac{K^2H_4^*}{B} \\ \frac{KA_1^*}{U} & \frac{KA_2^*B}{U} & K^2A_3^* & \frac{K^2A_4^*}{B} \end{bmatrix}\begin{bmatrix} \dot{h} \\ \dot{\alpha} \\ h \\ \alpha \end{bmatrix} \tag{2.29}$$

where ρ is the air density, U is the mean wind velocity, B is the width of the

model and K is the reduced frequency. Substituting Eq. 2.32 into Eq. 2.31 and bringing the right side item to the left side, the modified free-vibration motion equation can be obtained:

$$\left[\ddot{X}\right]+\left[C^{eff}\right]\left[\dot{X}\right]+\left[K^{eff}\right]\left[X\right]=0 \tag{2.30}$$

where $[C^{eff}]$ and $[K^{eff}]$ represent for the aeroelastically effective damping and stiffness matrices of the system, respectively. And $[C^{mech}]$ and $[K^{mech}]$ are set as the mechanical damping and stiffness matrices under zero wind velocity condition. Therefore, the effective damping and stiffness matrices can be written in terms of the mechanical damping and stiffness matrices [76] as:

$$\left[C^{eff}\right]=\begin{bmatrix} C_{11}^{mech}-\dfrac{\rho B^2\omega_h}{2m}H_1^* & C_{12}^{mech}-\dfrac{\rho B^3\omega_\alpha}{2m}H_2^* \\ C_{21}^{mech}-\dfrac{\rho B^3\omega_h}{2I}A_1^* & C_{22}^{mech}-\dfrac{\rho B^4\omega_\alpha}{2I}A_2^* \end{bmatrix} \tag{2.31}$$

$$\left[K^{eff}\right]=\begin{bmatrix} K_{11}^{mech}-\dfrac{\rho B^2\omega_h^2}{2m}H_4^* & K_{12}^{mech}-\dfrac{\rho B^3\omega_\alpha^2}{2m}H_3^* \\ K_{21}^{mech}-\dfrac{\rho B^3\omega_h^2}{2I}A_4^* & K_{22}^{mech}-\dfrac{\rho B^4\omega_\alpha^2}{2I}A_3^* \end{bmatrix} \tag{2.32}$$

As seen from Eq. 2.31 and Eq. 2.32, the expression formula for each flutter derivative obtained by splitting the elements in matrices $[C^{eff}]$ and $[K^{eff}]$ can be written as:

$$H_1^*(K)=-\frac{2m}{\rho B^2\omega_h}(C_{11}^{eff}-C_{11}^{mech})$$

$$H_2^*(K)=-\frac{2m}{\rho B^3\omega_\alpha}(C_{12}^{eff}-C_{12}^{mech})$$

$$H_3^*(K)=-\frac{2m}{\rho B^3\omega_\alpha^2}(K_{12}^{eff}-K_{12}^{mech})$$

$$
\begin{aligned}
H_4^*(K) &= -\frac{2m}{\rho B^2 \omega_h^2}(K_{11}^{eff} - K_{11}^{mech}) \\
A_1^*(K) &= -\frac{2I}{\rho B^3 \omega_h}(C_{21}^{eff} - C_{21}^{mech}) \\
A_2^*(K) &= -\frac{2I}{\rho B^4 \omega_\alpha}(C_{22}^{eff} - C_{22}^{mech}) \\
A_3^*(K) &= -\frac{2I}{\rho B^4 \omega_\alpha^2}(K_{22}^{eff} - K_{22}^{mech}) \\
A_4^*(K) &= -\frac{2I}{\rho B^3 \omega_h^2}(K_{21}^{eff} - K_{21}^{mech})
\end{aligned} \tag{2.33}
$$

As Eq. 2.33 shows, the parameters that are known or can be easily obtained are the air density ρ, the mass m, the mass moment of inertia I, the circular natural frequencies ω_h, ω_α for the bending motion and torsion motion, respectively. The only unknown parameters are the aeroelastically effective damping and the stiffness matrices.

At present, various system identification methods have been investigated to identify the unknown system parameters according to different forms of data obtained from the wind tunnel experiments [3][23][77]. Nonetheless, not all the system identification methods can be used on any system. A nonlinear behaviour subjected to unknown dynamic loads or some kind of strong ground motions is really a challenge for system identification methods. At this point, a multi-paradigm approach may choose to be the most effective strategy for large structures subjected to dynamic loading [77]. But for a classic dynamic wind tunnel test, the system is simple and convenient to extract the relevant parameters by using comparatively uncomplicated methods, such as the Ibrahim Time Domain (ITD) method, the Modified Ibrahim Time Domain (MITD) method, the First-Order Reliability (FOR) method, Iterative Least Squares (ILS),etc.

For the latest research on aerodynamic instability of multi-box girder bridge with windshield barriers, Baldomir et al. (2013) [78] derived the values of flutter derivatives of the Messina Strait Bridge experimentally (Fig. 2.3.13) and numerically.

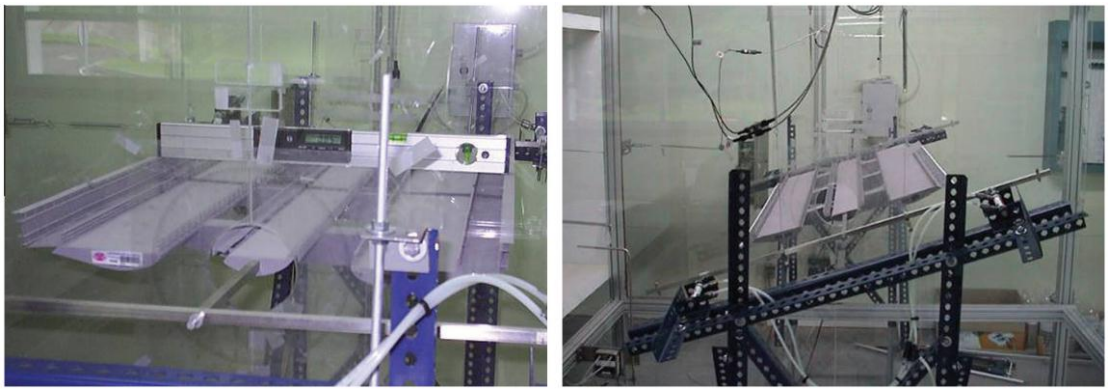

Figure 2.3.13 Wind tunnel testing of Messina Bridge deck [78]

They use the first-order reliability method to find that the most influential flutter derivatives on the structural safety are those related to the aeroelastic forces with the deck torsional degree of freedom. As shown in Figure 2.3.13, flutter derivatives of type A^*, especially A_2^* and A_3^*, have more influence than the others on the structural safety when the reduced velocity increases.

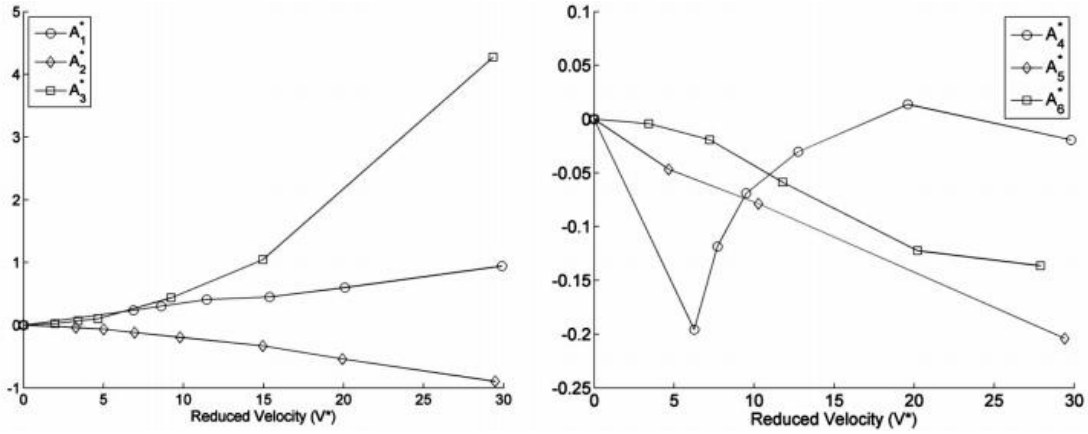

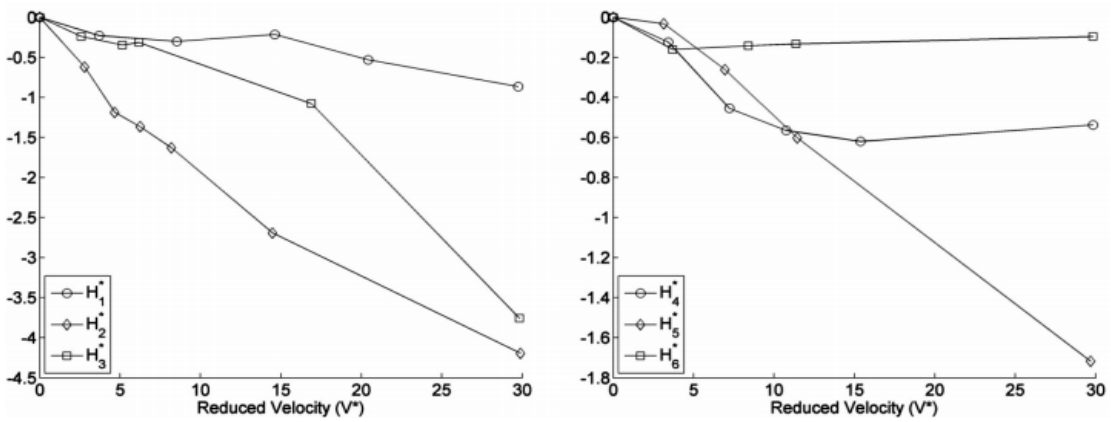

Figure 2.3.14 Wind tunnel testing of the sectional model of the Messina Strait Bridge [78]

Under wind speed from 3 m/s to 10 m/s, Yang et al. (2010) [79] used the MITD method to extract eight flutter derivatives on 2-DOF bridge sectional model system with windshield barriers as shown in Fig 2.3.15.

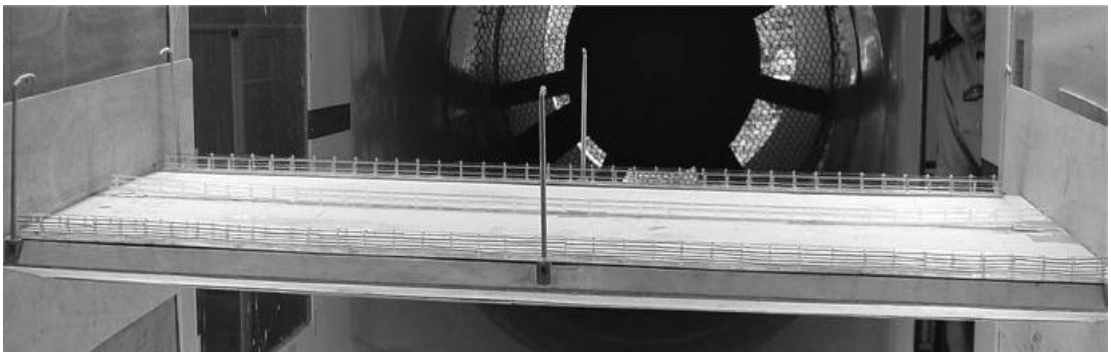

Figure 2.3.15 Wind tunnel testing of a twin-deck sectional model [79]

By comparison with results obtained from the numerical study, it can be concluded that, except for A_1^* (values of experimental A_1^* fluctuates around the numerical curve, the fitted curve of the experimental one is similar as the numerical results), the other seven flutter derivatives show good agreement as it can be seen in Fig. 2.3.16.

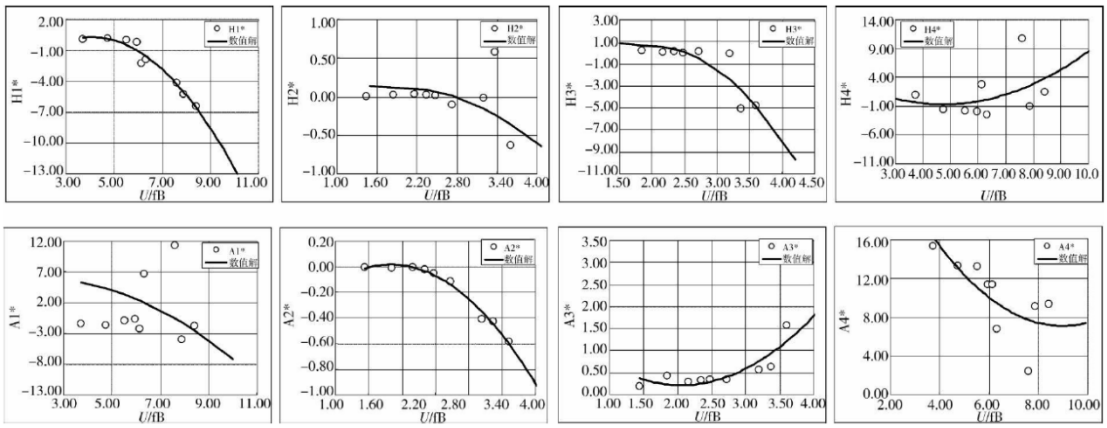

Figure 2.3.16 MITD experimental and numerical results of a twin deck model [78]

2.3.6 Identification of the aerodynamic flutter derivatives by ILS

A new system identification approach, Iterative Least Squares (ILS), was developed by A.G. Chowdhury and P.P. Sarkar [80] in 2003. The ILS method is able to extract 18 flutter derivatives for a three-degree-of-freedom system from free vibration displacement time-histories obtained from a bridge deck section model tested in a wind tunnel. As the research results show, the ILS method is better for extracting flutter derivatives for a one- and two-DOF structural system than for a three-DOF one. The ILS method is able to generate good parameter estimates for one- and two-DOF systems with a high noise-to-signal ratio, but only a moderate noise-to-signal ratio for the three-DOF system. Compared with other system identification methods, the ILS method shows the following advantages [80]: (1) extracting flutter derivatives for a combination of different DOF cases can simply be calculated by a single computer program; (2) instead of calculating the eigenvalue and eigenvectors, system stiffness and damping matrices are able to be calculated from the free-vibration displacement time histories directly; and (3) the parameters identified have good accuracy, which has been proved numerically and experimentally.

For a 2-DOF system under free vibrating condition, characterised by Eq.2.33 can be

represented as the state-space model:

$$[\dot{Y}] = [A][Y] \tag{2.37}$$

where,

$$[Y] = \begin{bmatrix} X \\ \dot{X} \end{bmatrix},\ [\dot{Y}] = \begin{bmatrix} \dot{X} \\ \ddot{X} \end{bmatrix},\ [A] = \begin{bmatrix} 0 & I \\ -[K^{eff}] & -[C^{eff}] \end{bmatrix}$$

The dimension of matrix A is 2n x 2n, where n is the number of degrees of freedom. I is the identity matrix. Obviously, if the series data of acceleration $\ddot{X}$, the velocity $\dot{X}$ and the displacement X can be obtained in a discrete-time system, the A matrix can be identified; in other words, the aeroelastically stiffness and damping matrices $[K^{eff}]$ and $[C^{eff}]$ can be extracted.

The data recorded from wind tunnel tests always include noise interference. In order to eliminate the noise effect, a computer program was prepared to set a low pass digital Butterworth filter for the recorded data, which is designed to make the frequency response as flat as possible in the passband. The cut-off frequency for each case was obtained through the Fast Fourier Transform (FFT) code built in MATLAB when the dynamic system is under wind-off condition. The detailed procedure for the ILS approach is shown as the following algorithm (Figure 2.3.17):

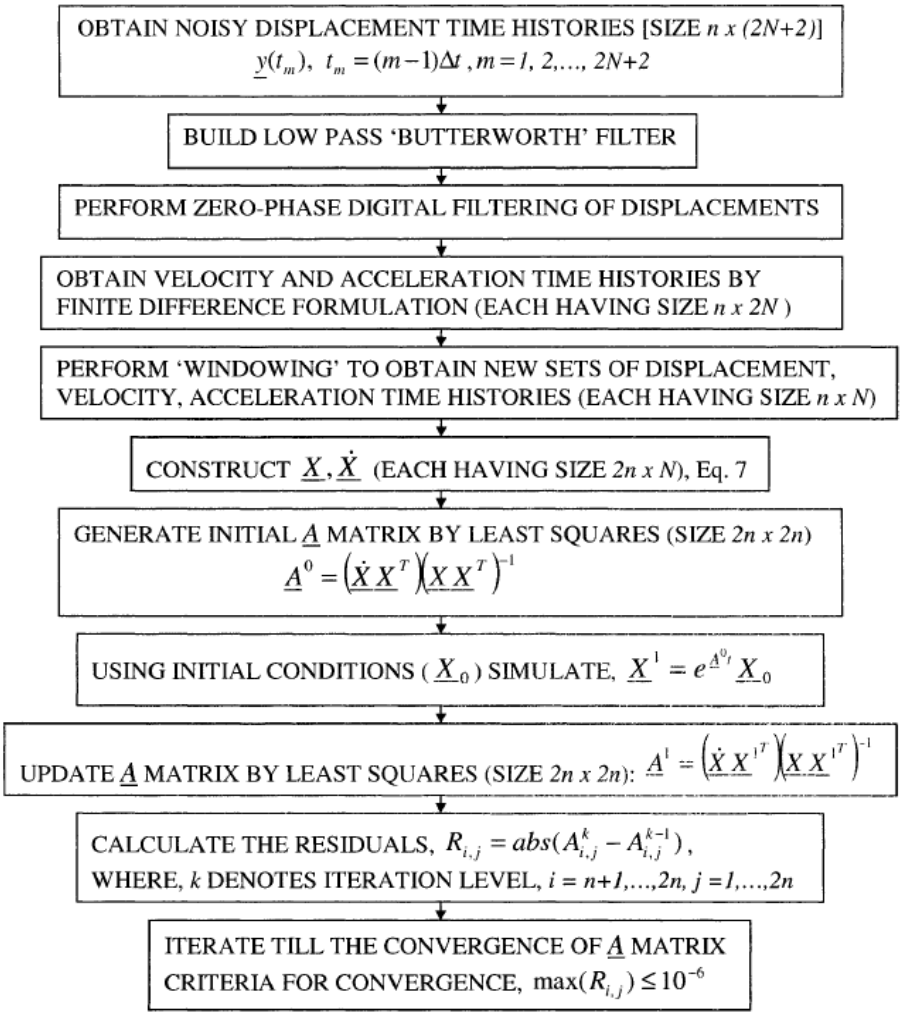

Figure 2.3.17 MATLAB code algorithm for ILS [80]

Considering the large amounts of cases in the current research, the ILS method is appropriate and convenient for extracting the eight flutter derivatives through the results obtained from the current wind tunnel experiment. The algorithm process is used for every wind tunnel dynamic test from -6° to 6°, and from minimum wind speed 0.8 m/s to 11.0 m/s. The measuring interval for the low wind speed range from 0.8 m/s to 3.0 m/s was determined to be 0.2 m/s, because there might be some differences for the stiffness and damping matrices if the vortex-induced vibration. The minimum interval for changing the wind speeds was 0.2 m/s. After all the A matrices have been obtained through MATLAB, the flutter derivatives for each case was able to be extracted by using Eq. 2.33.

Chapter 3 Experimental Program

In general, the aerodynamic experiments can be divided into two categories, field testing and wind tunnel experiments. A number of initial tests in bridge aerodynamics commenced with the testing and monitoring of the actual bridge deck, which helped researchers identify the most relevant structural characteristics of the bridge deck and their variation in time. Whereas the field testing can be performed on short or long span bridges, this consumes much time, and material resources to measure some specific cases required for the aerodynamic analysis. By contrast, adopting wind tunnel testing, enables wind engineers and researchers to perform aerodynamic studies which are effective and inexpensive, compared with the field testing. Nowadays, bridge designers and researchers usually obtain the aerodynamic parameters for the bridge deck they need to construct based on wind tunnel experiment results [11]. Wind tunnel tests are not only adopted for the bridge deck structures, but also they can be carried out for cables, hangers, towers and other structural elements of the bridges. Different parts of the bridges have different kinds of wind tunnel tests, but they are all designed for investigating the aeroelastic parameters of the tested structures. Wind tunnel tests are conducted based on the similarity principles for solid objects to better simulate the behavior of the actual bridge under controllable wind speed profile produced by powerful fan systems. Wind tunnel test methods for determining the flutter derivatives of the bridge decks involve mainly free vibration method and forced vibration method [19]. Free vibration method has been widely broadly applied for recently. The results for the free vibration method are extracted from the wind tunnel experiments results for a two-degree motion and they are calculated by ILS method, as described in detail in section 2.3.4. Due to potential uncertainties, every experiment case does not lead to the exact same results even if these are performed under the same experimental situation. Hence, the

experimental preparation set-up should firstly consider decreasing the random errors, such as noise level, data processing algorithm and technical and instrumentation operation effect. It is significant to use appropriate design for the bridge section model system, and the multiple-repeat tests in order to obtain accurate calibrations for the reliable force coefficients and data of flutter derivatives. Moreover, sensors and data acquisition system should have a low level of noise and other detailed experimental set-ups design like the positions of springs which need to be installed with a smallest possible error, thus making the aeroelastic experimental results more accurate.

3.1 Experimental set-up of sectional model

Preparation of the experimental set-up is more important than the experiment itself to some extent. More precisely the experimental set-up reduces the errors between different experimental steps and the floating values of the experimental results. Because the aerodynamic shape of the individual decks of the Megane Bridge deck is very sensitive, the original sectional model of the bridge deck was 3D-printed, based on an accurate AutoCAD model, by using a professional model printing company in Toronto, in the same time, the bridge windshield barriers were printed by the Print Shop of Algonquin College. Acrylonitrile Butadiene Styrene (ABS) material which has appropriate stiffness and robustness for the wind tunnel testing model was chosen as the 3D-printing material. Professional technicians from the Gradient Wind Engineering Inc. designed and constructed the connecting pieces and the end plates for the bridge deck sectional model after all the 3D printing pieces have been assembled. The deformation sensors and the force balances were borrowed from the National Research Council Canada (NRCC). All the other parts, including the cables and the data acquisition system were provided by the Structure Lab and the Mechanical Shop of the University of Ottawa. A medium size wind tunnel of a testing

section of 2.1 m wide by 1.8 m high, which is suitable for the testing process, was provided by Gradient Wind Engineering Inc..

3.1.1 Dimensioning testing conditions of the Megane Bridge deck

Before programming all the steps of the experimental set-up, some dimensions and parameters should be assumed in order to satisfy the requirements of the wind tunnel experimental procedure. The approximate dimensions of the sectional bridge deck model are 0.9 m wide by 1.0 m long with 7.9 kg mass.

The formation of the new type of multi-box bridge deck named Megane Bridge deck is similar to some extended to the concept used for the Messina Strait Bridge, which was proposed as the first bridge deck in the world with two gaps and three box girders. The multiple-deck sectional model for the Megane Bridge, consisting of two airfoil decks of 125 mm width for railway in the middle and two 200 mm wide airfoil decks for the traffic on either side of the deck, thus the bridge model has a total dimension of 870 mm wide including 47.5 mm wide pedestrian and bicycle lanes on either edge, as shown in Fig. 3.1.1. The depth for the railway decks and traffic decks were 37.5 mm and 25 mm respectively, with the gap width between the two railway decks and the width between the railway and the traffic decks of 35 mm and 45 mm respectively. The six windshield barriers in the middle of the model, represented by the red ellipse in Fig. 3.1.1 and in detail in Fig. 3.1.2, were designed as rectangular shape with 20 mm height and 50% porosity; the other two windshield barriers, on the edge of the model, represented in blue rhombus in Fig. 3.1.3 and in detail in Fig. 3.1.4, were designed as the same rectangular shape and porosity of 50%, but replaceable in order to conveniently change the windshield models from the 30 mm high model to the 50 mm high model.

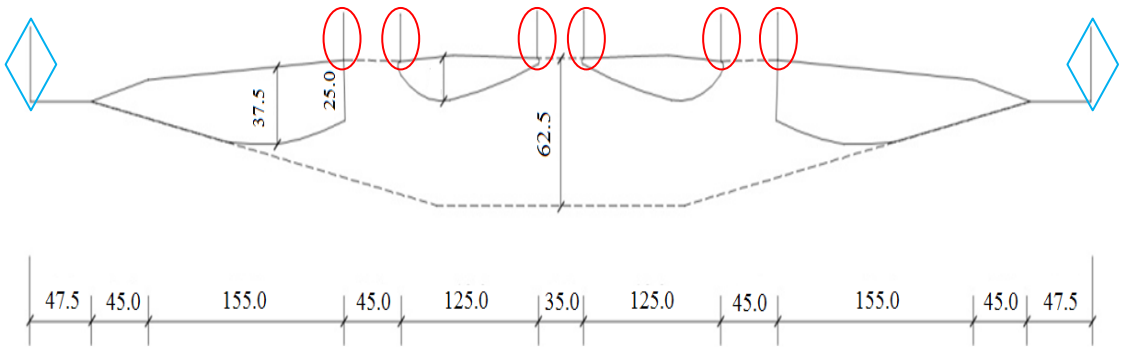

Figure 3.1.1 Cross-section of the Megane Bridge deck (unit: mm)

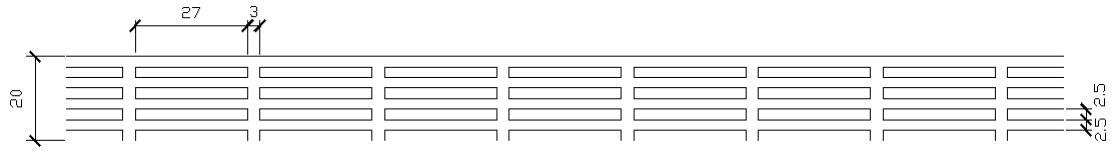

Figure 3.1.2 1:80 AutoCAD model of the 1.6 m (20 mm for model height) high windshield barrier (unit: mm)

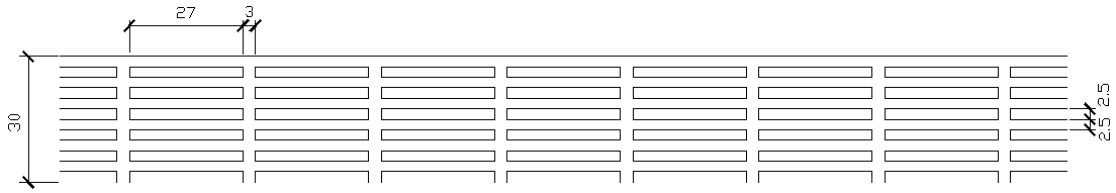

Figure 3.1.3 1:80 AutoCAD model of the 2.4 m (30 mm for model height) high windshield barrier (unit: mm)

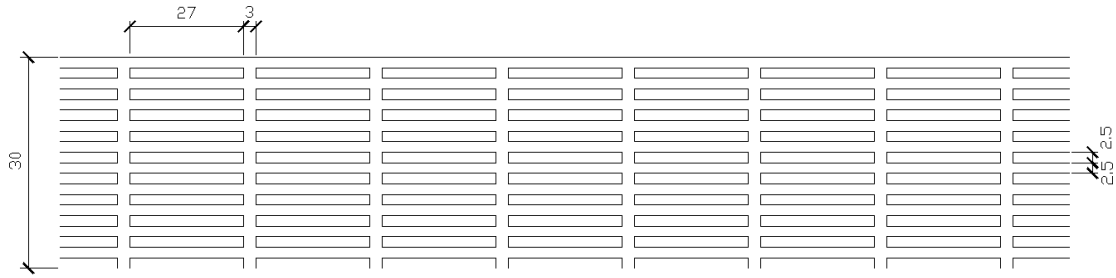

Figure 3.1.4 1:80 AutoCAD model of 4.0 m (50 mm for model height) high windshield barrier (unit: mm)

However, the design of the proposed Megane Bridge deck reached only the model configuration stage, and the bridge construction is not yet scheduled, therefore the corresponding mass, mass moment of inertia and the natural frequency of the prototype deck have not been finalized yet. Therefore, the parameters related to the similarity and scaling procedure between the prototype bridge deck structure and the bridge deck model used in the wind tunnel do not have considerable constraints, but should be within the limits of the existing structural bridge parameters. In the current study, the scaling ratio for the experimental model was set as 1:80, in order to fit the dimensions of the wind tunnel facility at the Gradient Wind Engineering Inc.. Thus, the dimensions of the experimental model dimensions were set to 1000 mm length and 870 mm width, according to the measuring section for the current wind tunnel (Fig. 3.1.5). The four individual experimental deck models were connected by three cross girder spanning with 45 mm gap to each box deck. Initially, the entire bridge deck shells, sidewalks and geometries of windshield barriers were made by SolidWorks models (Fig. 3.1.6 to Fig. 3.1.9) and then these were created by 3D printing (Fig. 3.1.10 to Fig. 3.1.12). By using the electric heating cutting machine, solid low density foam cores (Fig. 3.1.13) were cut following the same geometry shapes of the bridge deck shells, and were inserted in the four individual bridge deck shells. Considering that the wind load will approach the model from the lateral side, the surface of the bridge deck should be smooth, as much as possible, therefore aircraft grade 7075 aluminum sheets were used to cover the 3D printed surface of the bridge deck model. Also this will add rigidity to the 3D printed model. The bottom sides of the three cross-girders were plated by small pieces of wood as shown in Fig. 3.1.14.

Figure 3.1.5 Measuring section for the current wind tunnel at the Gradient Wind Engineering Inc.

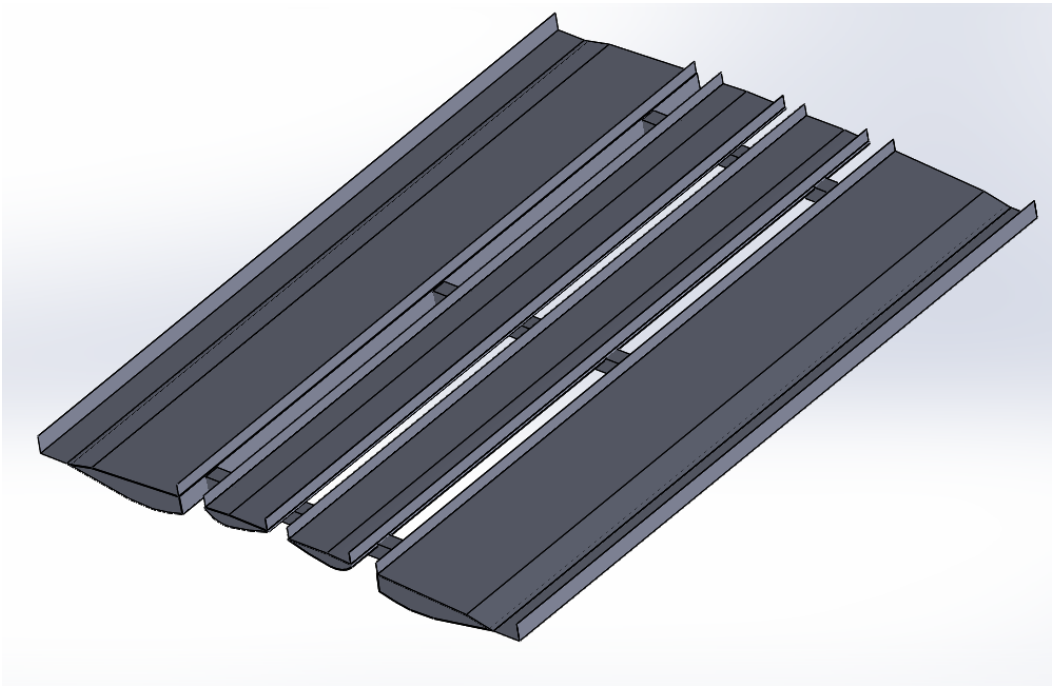

Figure 3.1.6 SolidWorks model of the Megane Bridge decks with cross girders

Figure 3.1.7 SolidWorks model of the windshield barrier with 20 mm height

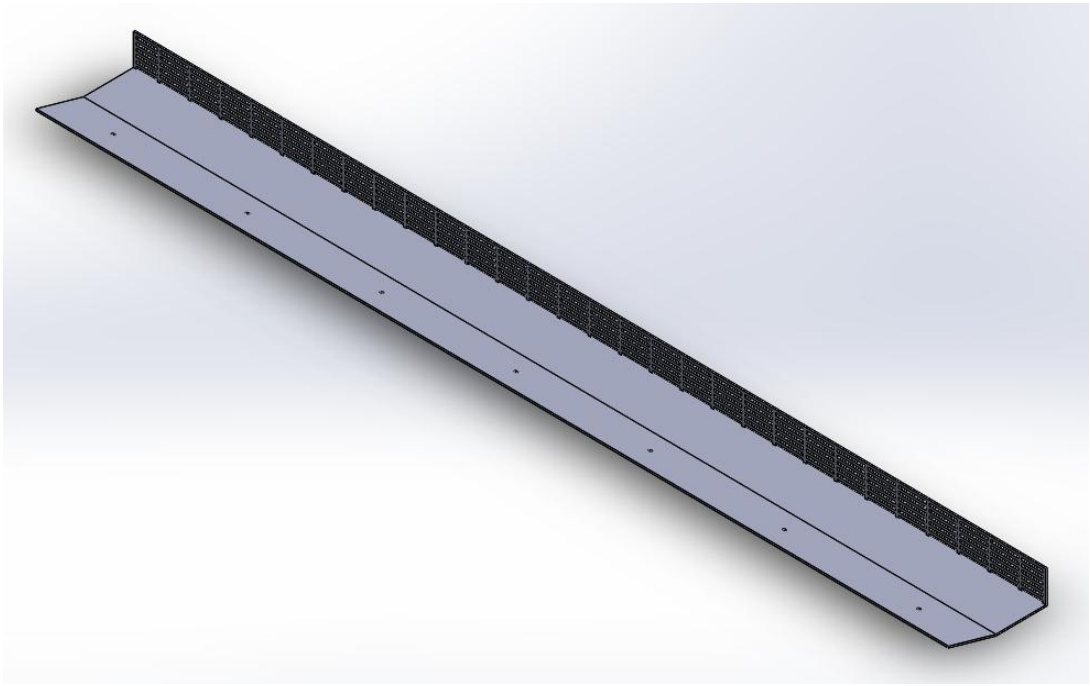

Figure 3.1.8 SolidWorks model of the 30 mm high windshield barrier with sidewalk

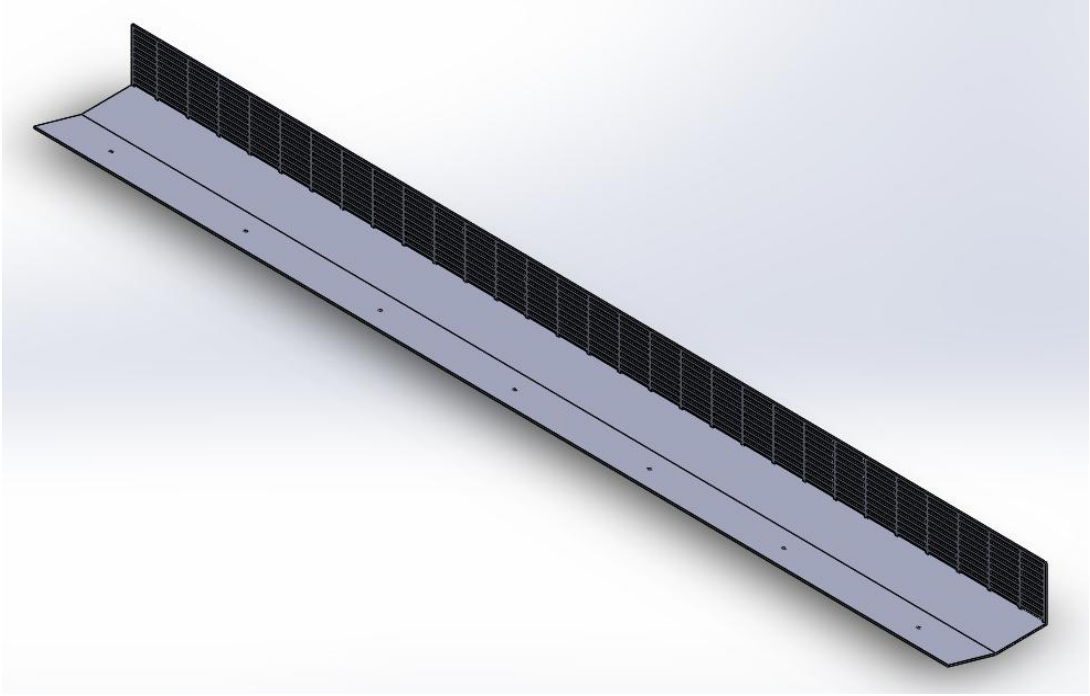

Figure 3.1.9 SolidWorks model of the 50 mm high windshield barrier with sidewalk

Figure 3.1.10 3D-printing model of the four individual bridge deck shells

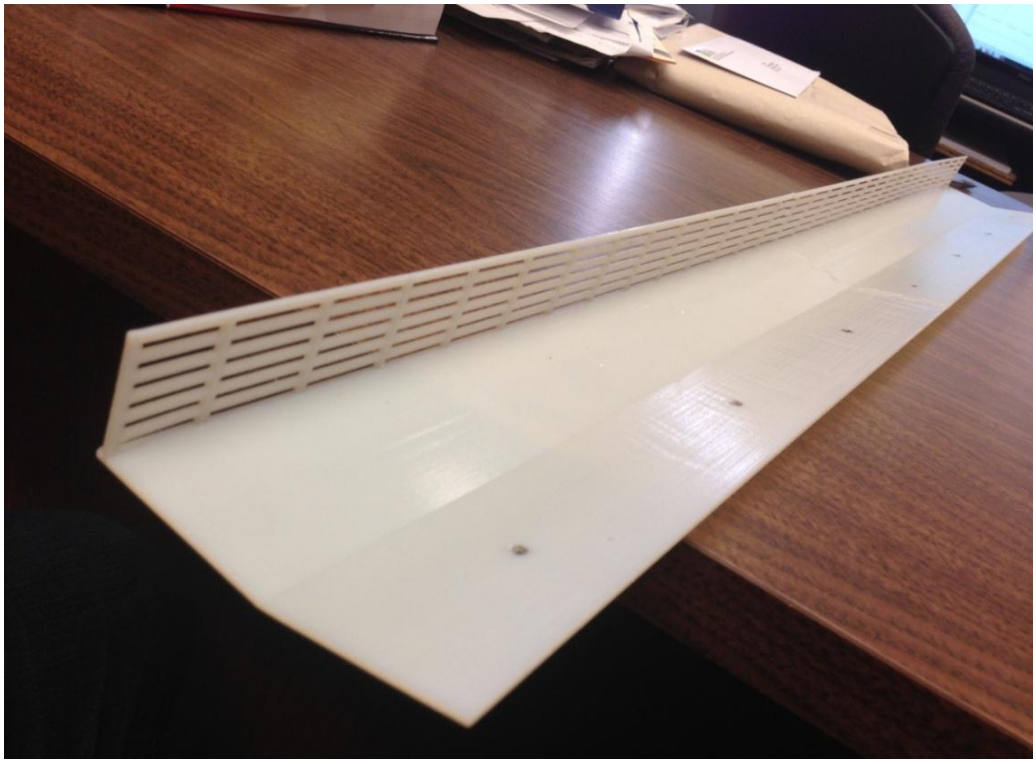

Figure 3.1.11 3D-printing model of the 30 mm high windshield barrier with sidewalk

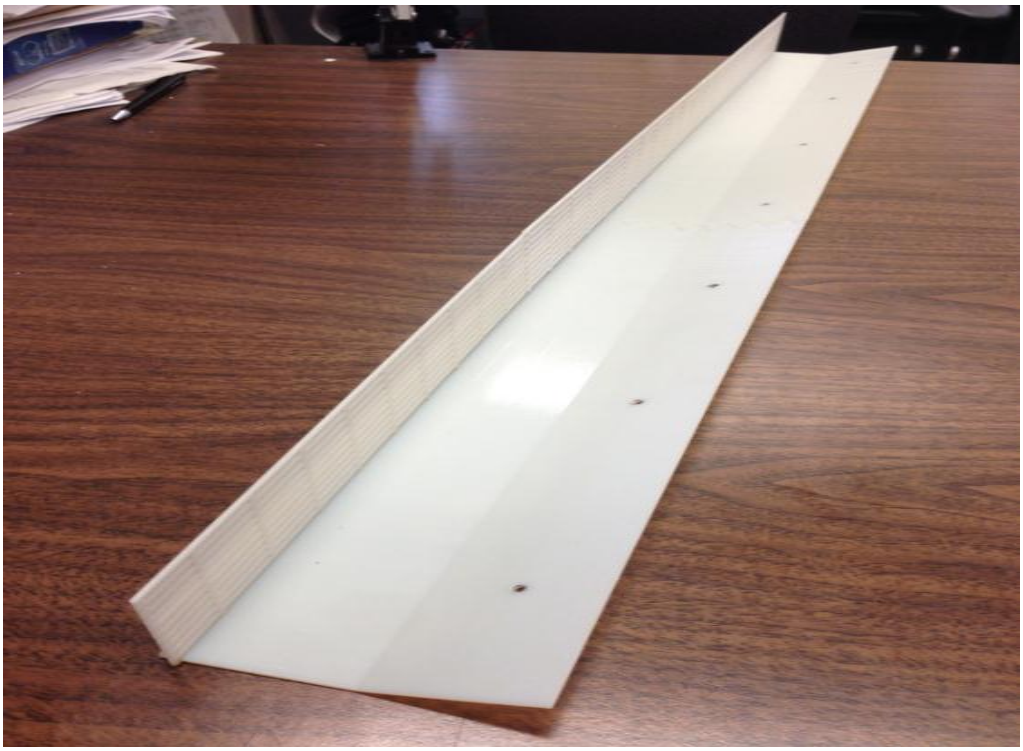

Figure 3.1.12 3D-printing model of the 50 mm high windshield barrier with sidewalk

Figure 3.1.13 Solid low density foam core used for inside of the four individual bridge deck shells

Figure 3.1.14 Bottom side of cross girders covered by small pieces of wood

The Megane Bridge deck section model has four box parts which were the connected at the extremities to two elliptical aluminum end plates, for restraining a potential individual motion of the boxes, which would interfere with the overall bridge deck dynamic behavior and thus makes the experimental model system more rigid and stable. Also installing end plates to the ends of the bridge deck models, is a well-known technique for avoiding the effect of the wind tunnel lateral wall .In addition, the aluminum end plates, with smooth elliptical shape, as shown in Fig 3.1.16, have a function of reducing turbulence flow near the two end sides, which

helps measuring the data with more accuracy. Considering that the windshield barriers on the edge of the model should be replaceable for different heights, they (red circles in Fig 3.1.15) were installed on the deck by demountable bolts, and the rest of the windshield barriers used in the middle of the deck (yellow circles in Fig 3.1.15) were fixed on the bridge deck surfaces by permanent adhesive. A fixed stainless steel Pitot tube was mounted directly on the ceiling of the wind tunnel and was placed in front of the section test model, to measure the incoming wind speeds which were measured by the speed controller monitor (Fig 3.1.17).

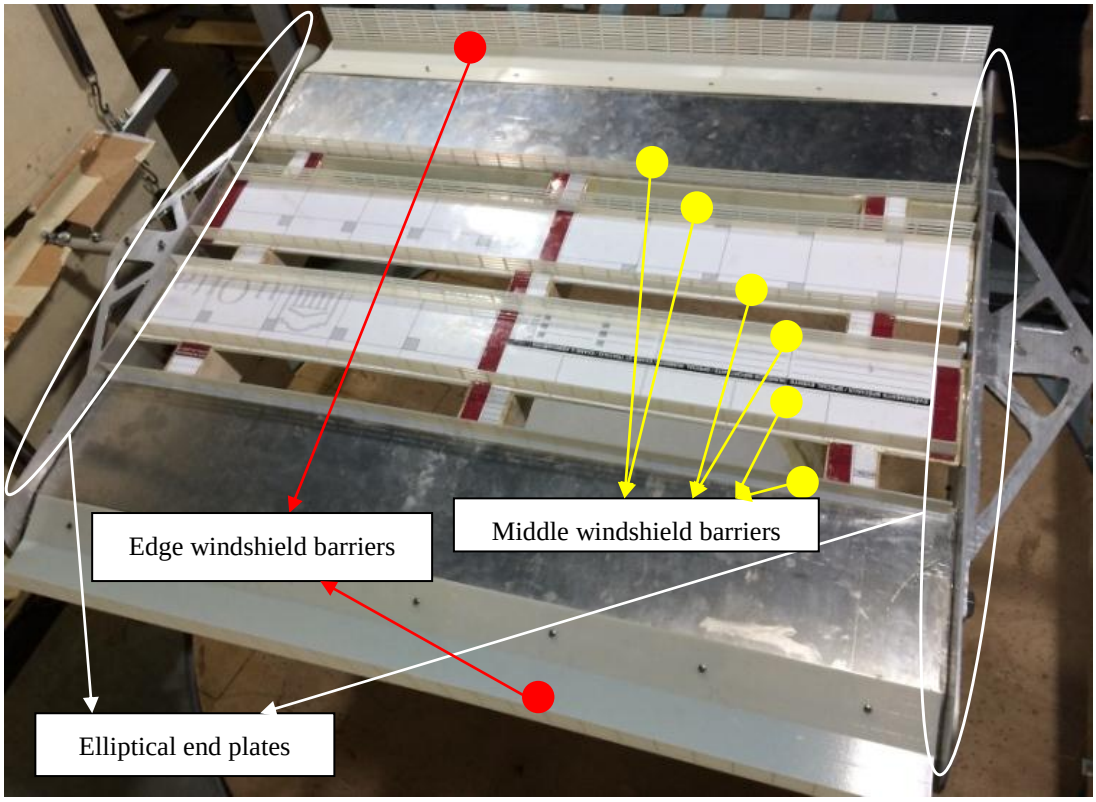

Figure 3.1.15 Oblique view of the sectional model

Figure 3.1.16 Elliptical aluminum end plate with connecting frame

Figure 3.1.17 Wind speed controller

3.1.2 Static test (force coefficients test)

The static test as shown in Fig. 3.1.18 aimed to identify the lift and drag force coefficients of the four-box girder bridge deck model tested in wind tunnel experiment. The two longitudinal bars of the bridge deck model system were fixed in the middle of end plates by steel connecting frames attached on the end plates (Fig. 3.1.19), the customized force balances were attached at the ends of the longitudinal bar, on both sides of the model: one for measuring the lift coefficients and the other for measuring the drag coefficients. The force balance measures the strain variation of the connected steel bar, and the measured data can be recorded by the computerized data acquisition system by the aid of StrainSmart software which provides the output for the time history files. With the variational vibration motion of the bridge sectional

model under different wind speeds, the average measured values can be obtained and then can be calibrated by the related formula to obtain the correct values, which were used for calculating the lift and drag force coefficients of the sectional deck model. After several attempts, wooden plates (Fig. 3.1.20) were chosen as the intermediate objects between the bridge deck models and the supporting system, which would eliminate completely the vibration motion of the bridge model, required for the static test. Thus, it was much easier to fix the force balance on wooden plates and to adjust the rotational angles of the wooden plates with accuracy for changing the angle of attack between the wind direction and the horizontal axis of the model. The wooden plates were clamped on a supporting system consisting of a 1.6 m high steel frame of 60 kg weight, approximately 8 times heavier than the weight of the bridge model. By fixing the pair of steel frames on the floor of the wind tunnel, the small oscillations interference coming from the heavy steel frame can be avoided.

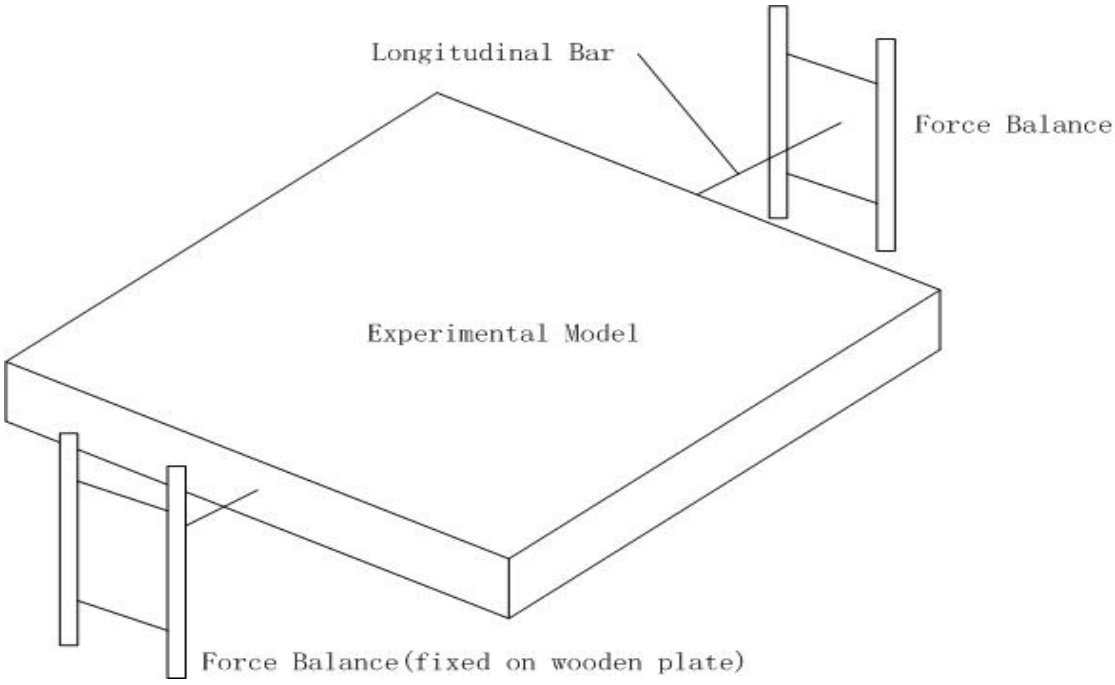

Figure 3.1.18 Schematic diagram of static test

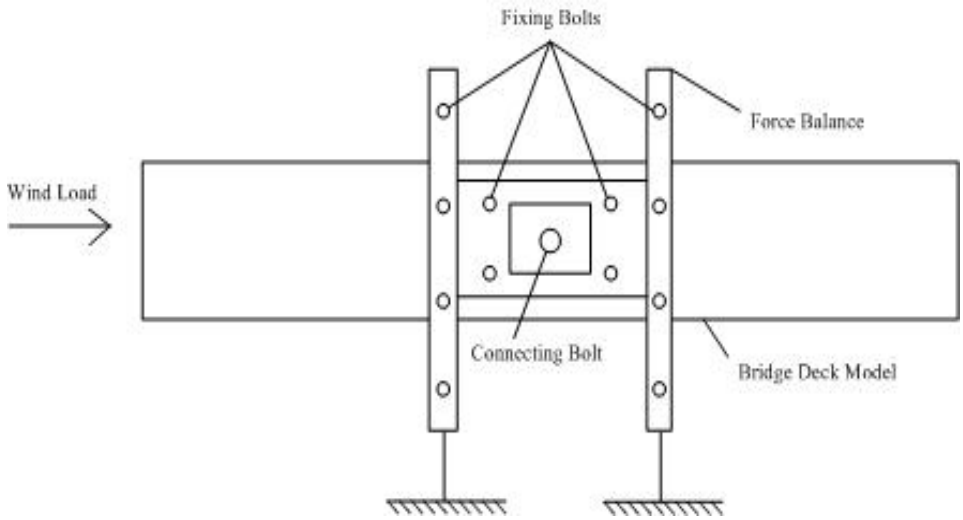

Figure 3.1.19 Supporting system of static test

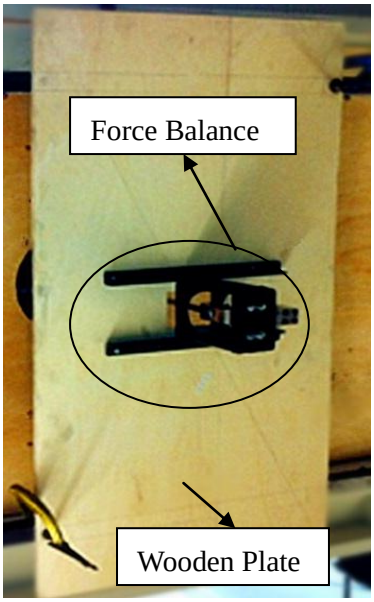

Figure 3.1.20 Force balance fixed on the wooden plate

Static tests were performed for wind speeds of 8 m/s to 10 m/s, and for angles of attack of -6° to 6°. The negative sign of the angles of attack is defined as shown in Figure 3.1.21.As other studies pointed out (Wang, 2015), beyond wind speed of 7 m/s, the lift and drag coefficients are not significantly influenced by the increase of the wind speed.

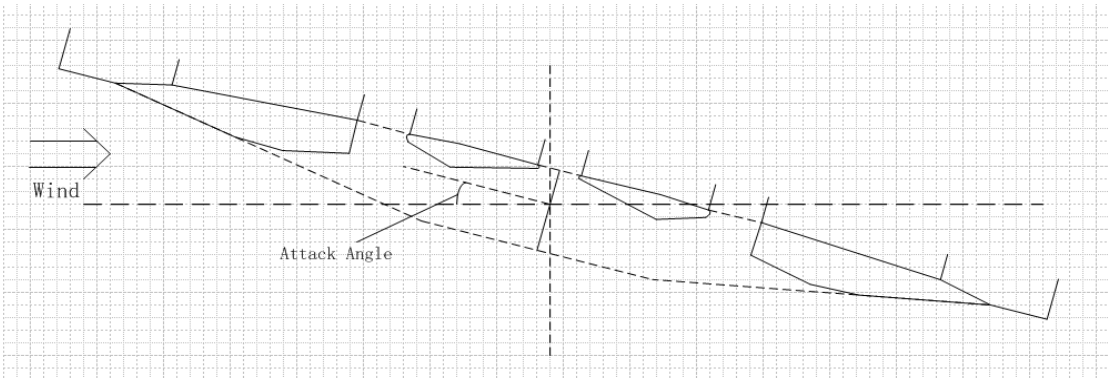

Figure 3.1.21 The experimental model rotates under negative attack angle

3.1.3 Dynamic test (free vibration test)

When the dynamic test was carried out, the experimental model was allowed to vibrate freely, therefore a spring suspension system was required to be installed for obtaining the vibration amplitudes and the flutter derivatives. The dynamic test aimed at measuring the vertical and torsional vibrations of the bridge deck model under different wind speeds and also at determining the flutter derivatives for different wind speeds and various angles of attack. Therefore the experimental setting for the bridge deck model was modified after finishing the static test, thus, for performing the dynamic test, a transverse bar was fixed to the longitudinal bar connected to the end plates, and this was suspended by four springs, two for the upper side of the model and two for the lower side of the model, on each side, as shown in Figure 3.1.22. Two displacement sensors were installed on the upper edge of the fixed wooden plate of the wind tunnel, with an equivalent distance to the mid-point of the transverse bar of 200 mm (Fig 3.1.23). The two displacement sensors can measure the corresponding vertical displacements and the rotation angles of the middle point was calculated by the use of some relevant formulas, as explained in detail below. The wind speed time history was also recorded by the Pitot tube and through the data acquisition system in the order of 0.1 m/s magnitude, thus wind speed data could be accurately observed. The dynamic testing system was supported by 8 equivalent springs (K_{sp}), which were

chosen in terms of the stiffness value of the entire bridge section model system. The vertical stiffness K_h of the springs suspension system can be calculated as $K_{tsp} + K_{bsp}$ and the torsional stiffness K_α of the system depends on the distance between the springs.

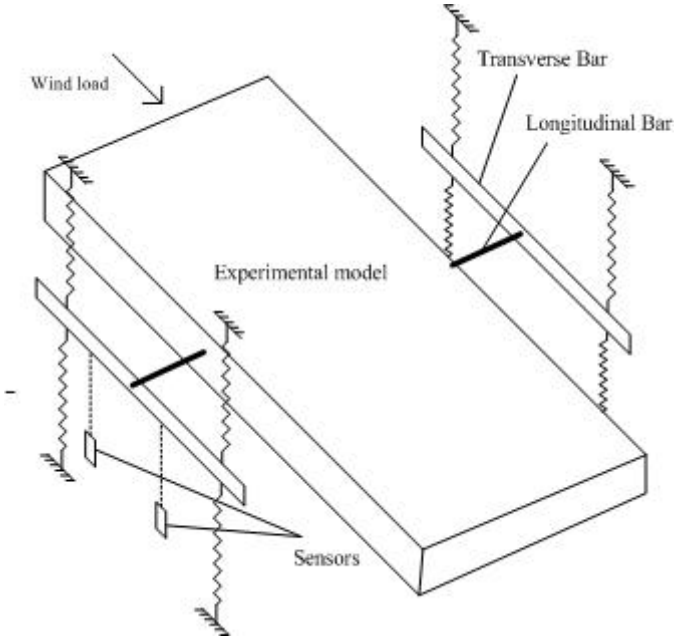

Figure 3.1.22 Schematic diagram of dynamic test

Figure 3.1.23 Springs suspension system

Finally dynamic tests as shown in Fig 3.1.24 were performed for wind speeds between 0.8 m/s and 11 m/s ,increasing in steps of 0.2 m/s, then from 3 m/s until 11 m/s, increasing the wind speed in higher steps of 1 m/s. Also for each wind speed tests were performed for -6°, -4°, -2°, 0°, 2°, 4°, 6° angles of attack, totaling a number of 280 test cases were performed.

Figure 3.1.24 Setup for the dynamic test in the wind tunnel

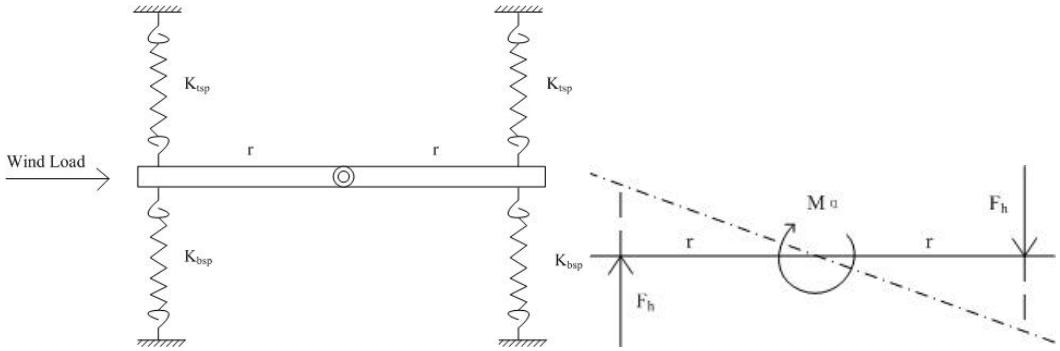

Figure 3.1.25 Stiffness details for the supporting system of the dynamic test

The overturning moment M_α around the midpoint of the transverse bar and the vertical force F_h represented in Figure 3.1.25 can be calculated as follows [21]:

$$F_h = (K_{\text{tsp}} + K_{bsp})\Delta l \tag{3.1}$$

$$M_\alpha = 2 \cdot F_{\text{h}} \cdot \Delta l = 2(K_{\text{tsp}} + K_{bsp})\Delta l \cdot r \tag{3.2}$$

where Δl is the changed length of the spring, *r* is the distance between the spring and the mid-point of the transverse bar.

Substituting $\Delta l = r \tan\alpha$ into Eq. 3.1 and Eq. 3.2 on the two sides,

$$F_h = 2 \times 2 \cdot (K_{\text{tsp}} + K_{bsp}) \cdot \text{r} \cdot \tan\alpha \approx 4(K_{\text{tsp}} + K_{bsp}) \cdot r \cdot \alpha = K_h \cdot r \cdot \alpha \tag{3.3}$$

$$M_\alpha = 2 \times 2 \cdot (K_{\text{tsp}} + K_{bsp}) \cdot r^2 \cdot \tan\alpha \approx 2(K_{\text{tsp}} + K_{bsp}) \cdot r^2 \cdot \alpha = K_\alpha \cdot \alpha \tag{3.4}$$

$$\Rightarrow K_\alpha = 4(K_{tsp} + K_{bsp})r^2, K_h = 4(K_{tsp} + K_{bsp}) \tag{3.5}$$

$$\Rightarrow K_\alpha = K_{\text{h}} \cdot r^2 \tag{3.6}$$

The distance *r* can be obtained from the following equations

$$K_{\text{h}} = m \cdot \omega_h^2; K_\alpha = I \cdot \omega_\alpha^2; r = \sqrt{K_\alpha / K_h} = \varepsilon^2 \cdot I / m = 0.227\text{m} \tag{3.7}$$

Due to the dimensions limitations of the wind tunnel facility, the distance *r* was set as 240 mm in the current experiment. The calculation method for the torsional and vertical stiffness, K_α and K_{h}, is based on the condition that all the springs are under tension at all the times, regardless of the vibration modes which will be encountered. The stiffness value of the springs should be suitable for such situation, otherwise the vibration amplitude is not notable and cannot be observed or the vibration amplitude might be too big to be in the elasticity limits of springs, which might suffer a plastic deformation. Here, the springs on the top side of the model have an elastic constant of

440 N/m and the springs on the bottom side of the model have an elastic constant of 240 N/m, resulting in a total elastic constant of the entire bridge springs suspension system of 680 N/m.

Because the wind tunnel test section has windows only on one side, all the experimental setup, including the model, the springs, and the supporting frames, were placed inside the test section of the wind tunnel. Due to the relatively high weight of the supporting frames, which were fixed on the floor of the wind tunnel as well, the slight vibration of the supporting frames was diminished and thus it did not affect the motion of the experimental deck model.

3.2 Calibration for the free vibration test

3.2.1 Data filtering

The data recorded from the wind tunnel tests are always affected by noise signal interference. In order to eliminate the noise effect, a computer code was prepared to set a low pass digital Butterworth filter, which is designed to make the frequency response as flat as possible in the passband [80]. The cut-off frequency for each case was obtained through the Fast Fourier Transform (FFT) which was applied through a code built in MATLAB, when the dynamic system is under zero wind (wind-off) condition. For example, the actual displacement and rotational angle time histories and the filtered displacement and angle time histories are shown in Figures 3.2.1 and 3.2.2, as follows:

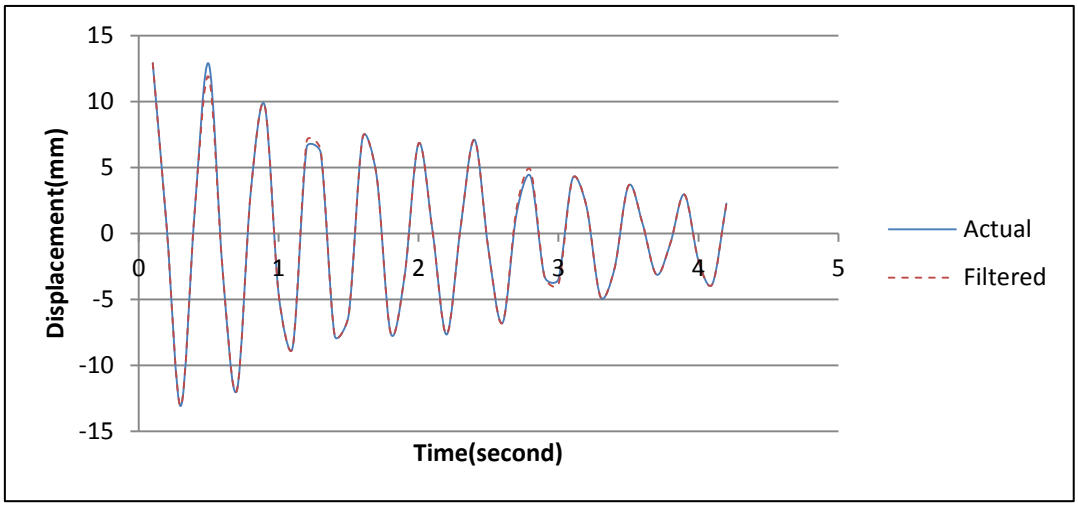

Figure 3.2.1 Filtered and actual free vibrations displacement for the 30 mm high windshield barrier (wind-off condition)

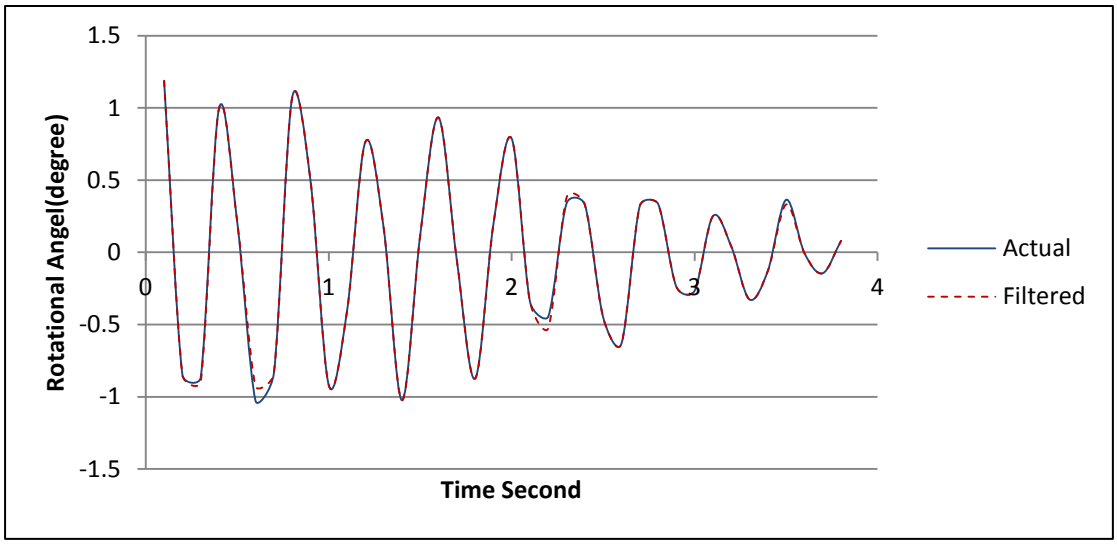

Figure 3.2.2 Filtered and actual free vibrations of rotational angle for the 30 mm high windshield barrier (wind-off condition)

It can be seen from the Fig. 3.2.1 and Fig. 3.2.2 that the actual and filtered time history curve for both vertical displacements and rotation angles are almost the same, which proves that the noise for the dynamic system would not affect significantly the results obtained from the wind tunnel test. Although the interference produced by the noise signal is comparatively low for wind-off conditions, all the data should be filtered with the low-pass digital Butterworth filter in order to avoid unpredictable

error for high frequency noise. The data of the treated output time history was used for generating the corresponding acceleration and velocity time histories by finite difference formula. Also, some basic parameters for the tested bridge deck section model have been calculated by extracting the data from free vibration test, such as: the first natural frequency in vertical direction: f_{h}=1.398 Hz, the first natural frequency in torsional direction: f_{α}=1.982 Hz, the frequency ratio: $\varepsilon = f_{\alpha}/f_{\mathrm{h}} = 1.409$, the damping ratio in vertical direction: $\xi_{\mathrm{h}} = 0.0113$, the damping ratio in torsional direction: $\xi_{\alpha} = 0.0132$. The first natural frequency of the actual Megane Bridge is not determined yet, because the bridge was not yet constructed, however, the frequency of similar bridges are of the order of 0.1 Hz or lower for those bridges with the main span of the order of one thousand meters or longer [63]; therefore, if the similarity condition presented in Eq. 2.16 is considered, then the ratio between the wind speed in the wind tunnel and actual wind speed is estimated over 1:10. Thus, for the maximum wind speed tested in the current wind tunnel experiment of 11 m/s, the corresponding actual wind speed is over 110 m/s.

3.2.2 Calibration to "zero average line"

As mentioned in 3.1.4, the two displacement sensors were placed on the upper edge of the wooden plate to measure the vertical displacements at the two sides of the transversal bar, which, being connected to the bridge deck model, it encounters the same motion as the model, under the effect of wind. The two set of displacement data, incoming from the two sensors, were transmitted to the data acquisition system (the Inter Technology System 5000) and were processed with the software StrainSmart, then the time history data was outputted as excel files. The initial data obtained directly from the two displacement sensors needed to be calibrated first, because different test cases would yield oscillations around different starting points, and then the plots of the time history displacement were used for calculating the actual

magnitudes of displacements and rotational angles of the bridge deck model. Finally, the vertical displacement at the center of the experimental model and the torsional angle of the corresponding vibration were obtained. Considering the structure of the experimental model setup, the center of the bridge deck model should have the same vibration motion as the mid-point of the transversal bar. A free vibration test was carried out to check whether this assumption was correct, and the results are shown in Figure 3.2.3.

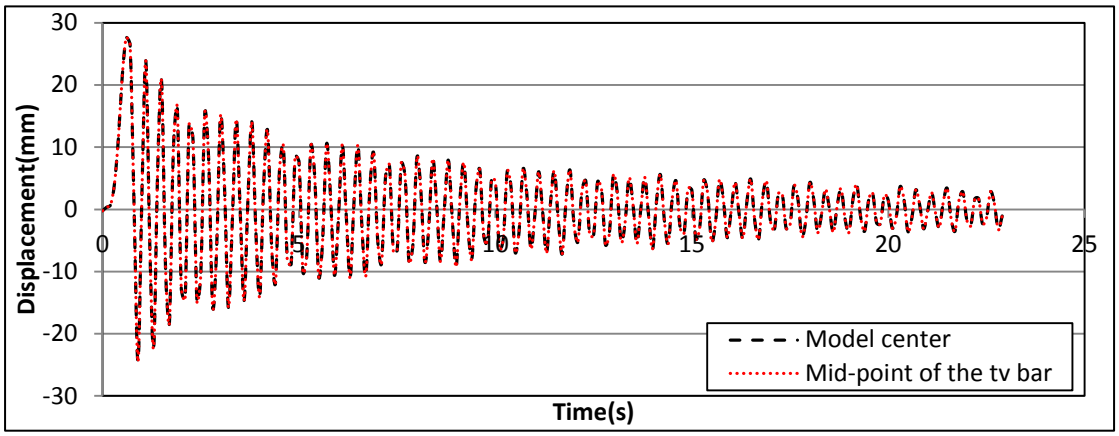

Figure 3.2.3 Free vibration test for the center point of the model and the mid-point of the transversal bar

As the free vibration test result shows above, the displacements of the center of the bridge deck model and the mid-point of the transversal bar have the same values for each individual point in time. Therefore, the vertical displacement of the center of the bridge deck model can be calculated if the displacements of the two measuring points on the transversal bar are obtained. Usually, the wind aerodynamic force will determine asymmetric vibration motion regarding to the $y = 0$ axis. However, the static force part of the aerodynamic force, will shift the average axis and will produce an initial displacement for each case. Hence, the displacements obtained at the center of the model and the corresponding rotational angles, should be calibrated in order to represent the oscillations as symmetric in regard to a "zero average line". The detailed

procedure for calculating the center displacement $D'_M(t)$ and the rotational angle $\alpha'(t)$ is expressed as the flow diagram in Figure 3.2.4.

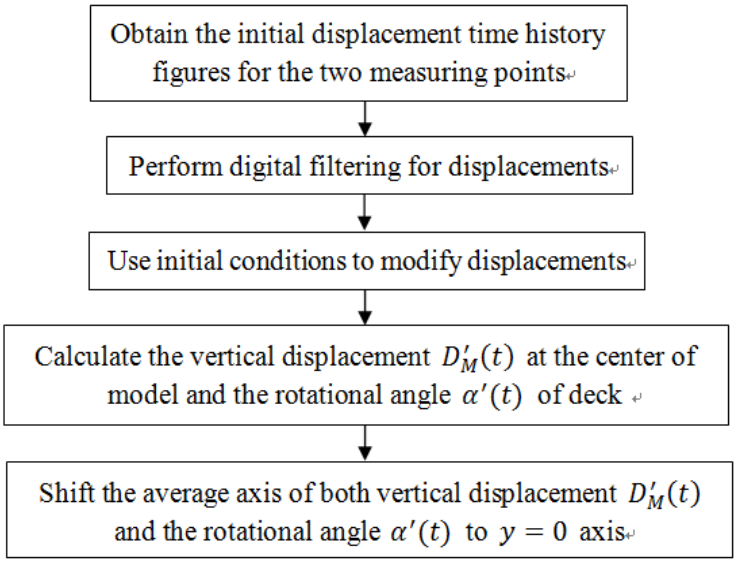

Figure 3.2.4 Flow diagram of the procedure for calculating $D'_M(t)$ and $\alpha'(t)$

The calibration for "zero average line" of the data of displacement time histories recorded by the two displacement sensors, for wind velocity of 4.0 m/s and attack angle of 0° obtained for the bridge deck model with 30 mm high windshield barrier, were chosen as an example of the above procedure as presented in Figures 3.2.5 to 3.2.8 below.

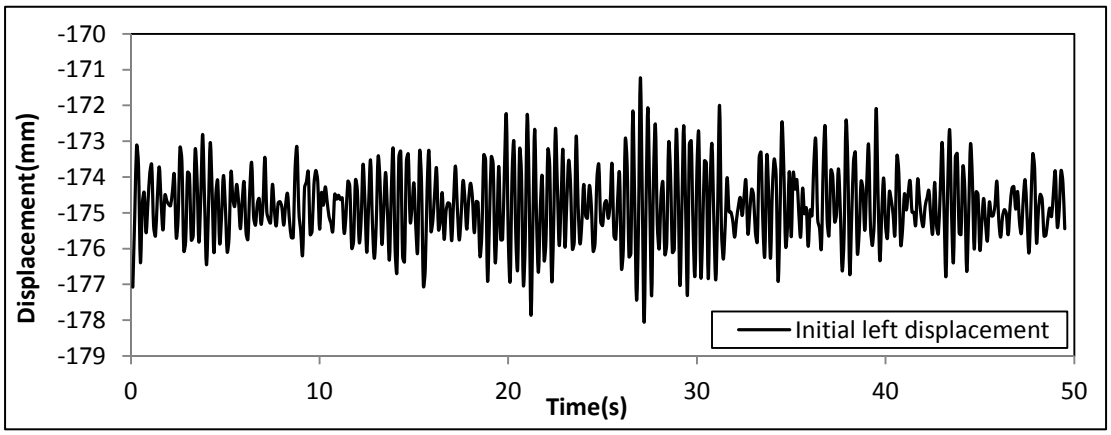

Figure 3.2.5 Initial displacement time history of the experimental model for 4.0 m/s and 0° and 30 mm high windshield barrier (the left displacement sensor)

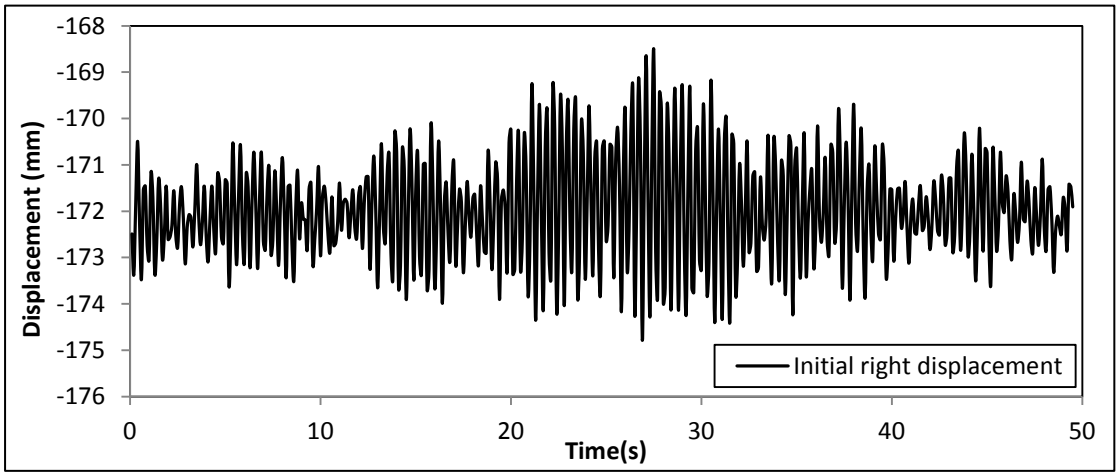

Figure 3.2.6 Initial displacement time history of the experimental model for 4.0 m/s and 0° and 30 mm high windshield barrier (the right displacement sensor)

The initial displacement time histories obtained from displacement sensors situated on the right and left sides of the transversal bar were filtered first and then were calibrated in regard to the initial conditions, to obtain the re-adjusted displacements from the initial positions for the right and left sides respectively. The calibrated results are plotted as displacement time histories in Figures 3.2.7 and 3.2.8.

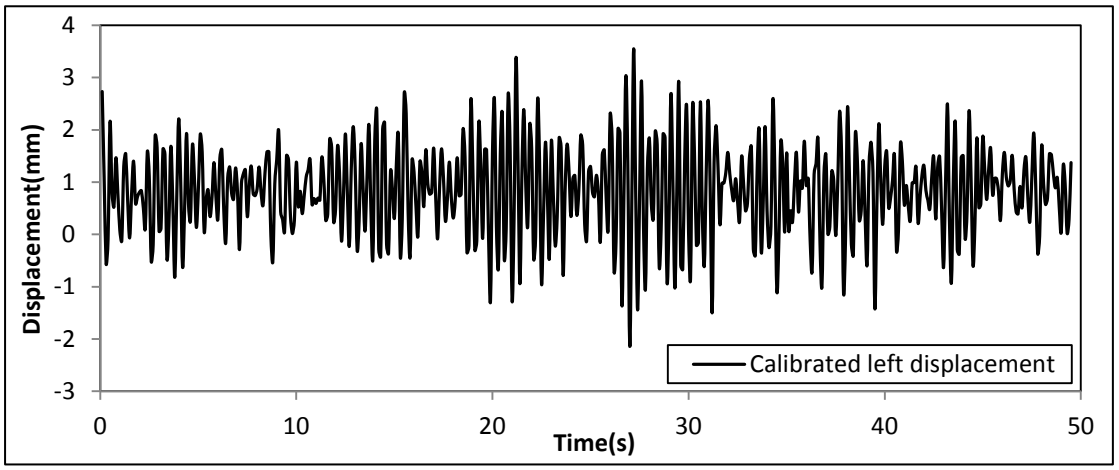

Figure 3.2.7 Calibrated displacement time history of the experimental model for 4.0 m/s and 0° and 30 mm high windshield barrier (the left displacement sensor)

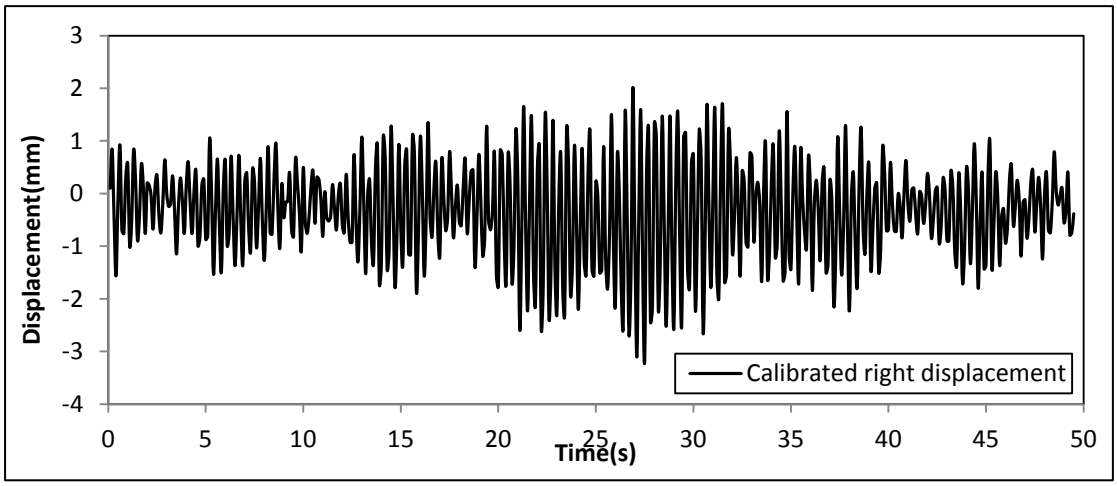

Figure 3.2.8 Calibrated displacement time history of the experimental model for 4.0 m/s and 0° and 30 mm high windshield barrier (the right displacement sensor)

After the processes of filtering and calibrating, the actual displacement of the mid-point and the torsional angle of the transversal bar can be calculated by using the Eq. 3.8 and Eq. 3.9 below:

$$D'_M(t) = \frac{1}{2}(D_L(t) + D_R(t)) \tag{3.8}$$

$$\alpha'(t) = \frac{(D_L(t) - D_R(t))}{d} \tag{3.9}$$

where $D_L(t)$ and $D_R(t)$ represent for the vertical displacement of the left side measuring point and the right side measuring point respectively, as a function of time, $D'_M(t)$ is the vertical displacement at the center of the model, $\alpha'(t)$ is the torsional angle of the model deck, d is the distance between the left side measuring point and the right side measuring point, which was set as 300 mm. Then the results obtained based on Eq. 3.8 and 3.9 were modified in order to get to "zero average line" by using Equations 3.10 and 3.11:

$$D_M(t) = D'_M(t) - \overline{D} \tag{3.10}$$

$$\alpha(t) = \alpha'(t) - \overline{\alpha} \tag{3.11}$$

where, $D_M(t)$ is the modified vertical displacement at the center of the model, $\alpha(t)$ is the modified torsional angle of the model deck, $\overline{D}$ and $\overline{\alpha}$ are the average values for the vertical displacement at the center of the model and the modified torsional angle of the deck model during the testing time, respectively. When the angle of attack is 0°, the results of $D_M(t)$ and $\alpha(t)$ for 4.0 m/s are plotted in Figures 3.2.9 and 3.2.10:

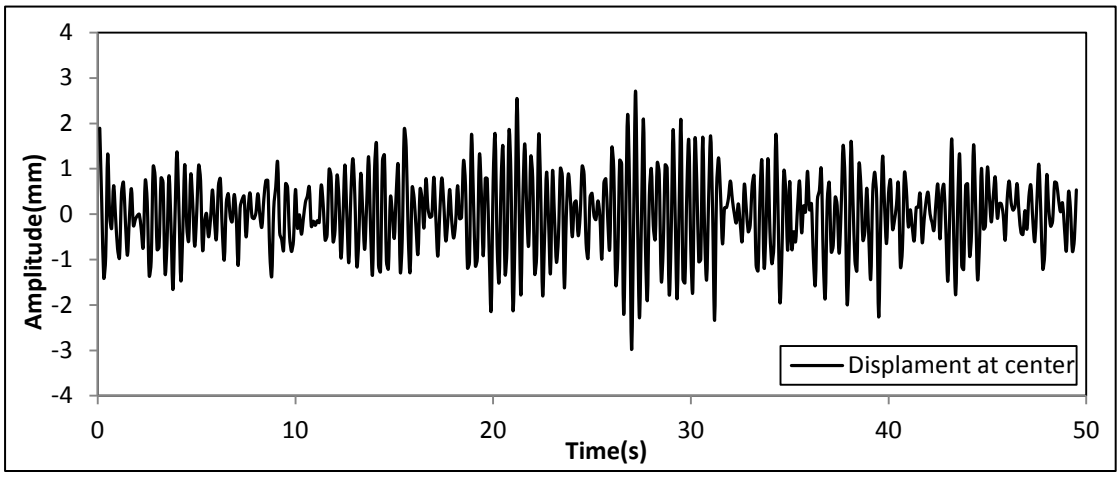

Figure 3.2.9 Displacement time history of the experimental model for 4.0 m/s and 0° and 30 mm high windshield barrier

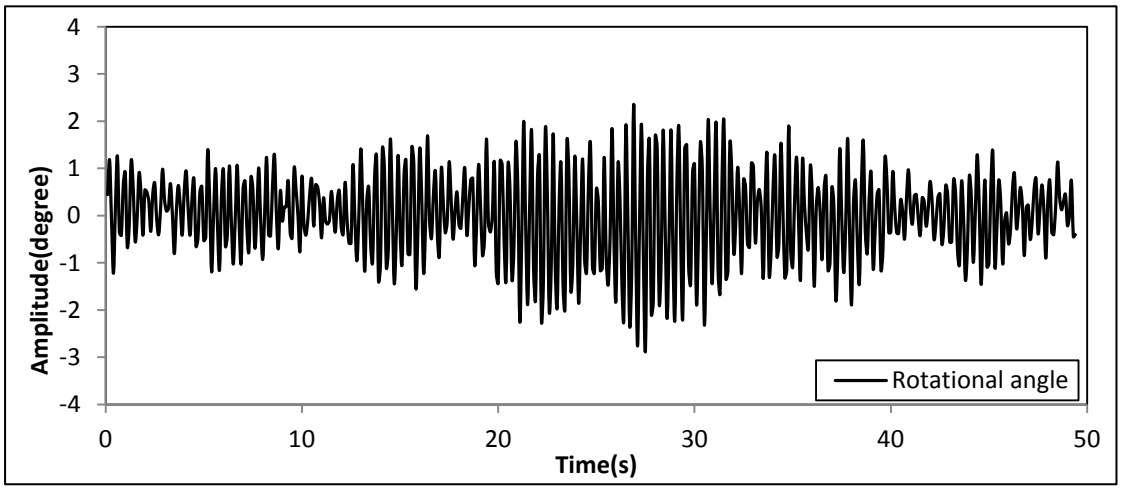

Figure 3.2.10 Rotational angle time history of the experimental model for 4.0 m/s and 0° and 30 mm high windshield barrier

3.3 Important elements in the experimental set-up

3.3.1 Displacement sensors

Suitable displacement sensors with required measuring accuracy and range should be selected to measure the displacement variation. Classic displacement sensors with function of recording data manually cannot perform satisfactory for the time history record with high sampling rate required by the current experiment. Extremely sensitive sensors cannot be used in the wind tunnel due to the small measuring range. Small and light sensors, such as laser sensors or ultrasonic sensors, were chosen as the displacement measuring devices (Fig. 3.3.1). Same accuracy and range should also be a noteworthy part for reducing the measuring errors. By conducting the trial and error experiments for choosing the measuring range, 30 mm was found as a maximum value for the vibration motion of the experimental model, under the effect of the maximum wind speed of 11.0 m/s, provided by the wind tunnel fan. Finally, a laser sensors and a ultrasonic sensor were chosen with 0.01 mm accuracy and 5 mm to 35 mm measuring range. Two groups of displacement data were obtained through the two displacement sensors which were transmitted to the data acquisition system and were outputted as time history figures and excel files directly. Thereafter, the calibrated values for these two groups of data were converted into displacements and rotational angles of midpoint of the transversal bar as detailed in the section 3.2.2. Finally, these displacements and rotational angles were used for extracting the flutter derivatives by applying the ILS (iterative least squares) method.

(a) (b)

Figure 3.3.1 (a) Laser sensor and (b) ultrasonic sensor used in the dynamic test

3.3.2 Spring suspension system

Springs are the most important part of the suspension system because they play a vital role in representing the stiffness of the overall bridge deck system. Eight springs were used in total for the dynamic and the derivatives experiment, four springs for each side of the model, for connecting the transversal bar to the supporting system. Four steel hooks were welded on the top and bottom sides of the transversal bar of each side of the model, for hanging the four springs conveniently. In addition, the eight springs are required to be in tensile state at all times, when the dynamic tests are carried out. Thus, the springs should be selected properly, they should maintain the elastic range under predictable worst case scenario, during the experiment. Therefore, the maximum stretched length of the springs should be considered as the sum of the maximum static deformation and the maximum dynamic deformation resulting from the oscillations under the effect of the maximum wind speed provided in the wind tunnel and also considering some additional deformation as a safety margin; the final deformation should be less than the elastic range of the springs, to ensure they don't reach the plastic range and deform permanently, thus modifying the value of the elastic constant. Hence, the stiffness of the entire spring suspension system will not change for any of the experimental cases performed, which determines obtaining the

results with same precision for all the tests.

Considered that the upper springs will carry the weight of the experimental bridge deck model and the tensile forces from the lower springs, the deformation length of the springs should be designed as different values for the upper and lower parts of the experimental model. The experimental model should be suspended in the required position, approximately in the center, horizontally and vertically, of the testing section of the wind tunnel. For achieving this position, 20% longer springs were used for the upper part of the transversal bar and shorter bars were used for the lower part.

3.3.3 Force balances

Usually, the weight of the small or medium size bridge deck section models is around 3 kg and the corresponding load cells have a maximum measuring limit for 3.5 kg models. The weight of the Megane Bridge deck model was 7.9 kg weight, and standard load cells cannot be used for the force coefficients tests, because these might be damaged. Therefore, higher measuring range equipment was used for this bridge deck section model. Customized force balance made following the principle of a load cell by the Building and Construction laboratory at National Research Council Canada (NRCC); these force balances (Fig. 3.3.2) were usually employed for measuring the force coefficients for the wind-induced uplift tests for the flat roofs and they have a maximum measuring limit of 15 kg. The operating principle of this force balance is to measure the stress variation of the steel member connected to the plate still positioned in the middle of a stable stainless steel frame. The longitudinal bar of the end plate of the bridge deck section model is connected to the measuring steel plate through a special made bolt. Because the force balance can only measure the force for one direction, one force balance is set to measure the force in the vertical direction at one end of the model, and another one is set to measure the force in the

horizontal direction, at the other end of the model, during the static tests. The stress data was transmitted to the data acquisition system for outputting time history figures and excel files. After the relevant calculation, the actual values of the forces in the vertical and horizontal directions can be obtained and can be used for the force coefficients calculation.

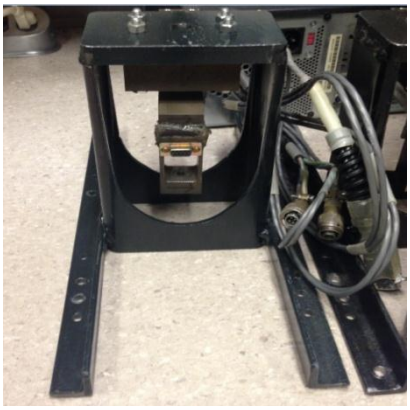

Figure 3.3.2 Force balance

3.3.4 Data acquisition system

In order to obtain more accurate results, a data acquisition system with a suitable sampling rate should be considered as a first choice. A low sampling rate is not suitable for extracting the flutter derivatives with the iterative least squares method. A high sampling rate means sampling large amounts of data which requires much more storing space and involves some unnecessary work for calibrating and filtering, as not all the data will prove essential for the calculation to be performed. The sampling rate should be chosen properly, and in the current experiment this was 1/10 record sampling rate to register the stresses for the force coefficient tests and the displacements for the dynamic tests. The computer software used for connecting the force balances and the displacement sensors is called StrainSmart and the corresponding data acquisition equipment is System 5000 (Inter Technology Model

5100 Scanner). All the stresses and the displacement data has been transmitted to the data acquisition system for processing and outputting the time history figures and excel files.

3.3.5 Wind tunnel experimental facility

A private wind tunnel from Gradient Wind Engineering Inc (Kanata, ON) was used for carrying out all the experimental cases. The suction wind tunnel has an overall length of 27 m and a test section of 2.1 m width and 1.8 m height. The wind velocity for the wind tunnel can be controlled by changing the RPM (revolutions per minute) of the fan, the smallest changing step of the wind velocity is 0.1 m/s and the velocity range is from 0.8 m/s to 11 m/s. A Pitot-static tube is settled above the middle location of the experimental model. The pressure measuring opening situated at the end of the Pitot tube is facing directly to the wind direction with the no inclination angle. A control pad is directly connected to the Pitot tube, which has the function of calculating the current wind velocity through the corresponding wind speed showing it directly on the monitoring screen.

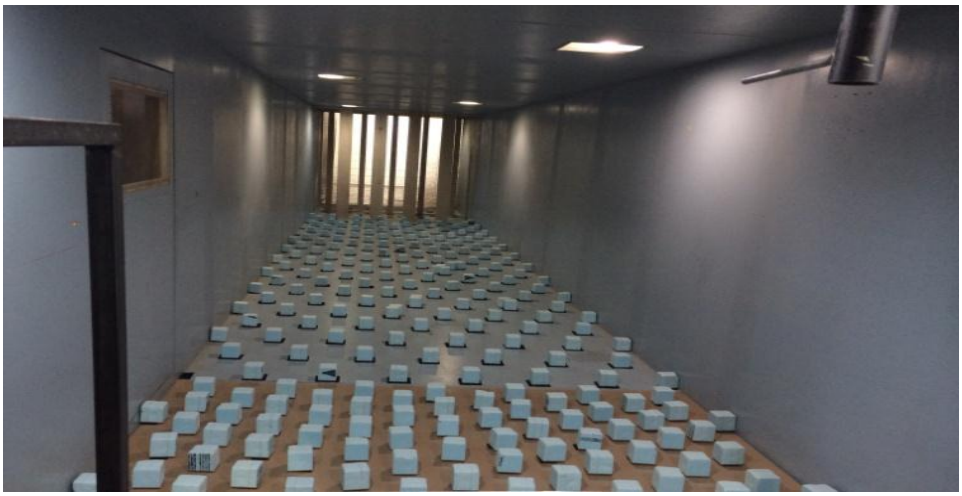

Figure 3.3.3 Wind tunnel in Gradient Wind Engineering Inc.

3.4 Experimental methodology

Proper plan of experiment steps can save time and can help avoiding unnecessary faults. The static test was decided to be the first part of the experiment because the longitudinal bar can simply connect to the force balance and the connecting part is easier to disassemble comparing with the connection between longitudinal bar and transversal bar. In addition, it is easier to adjust the attack angle of the system because the bridge is fixed on the force balance while carrying out the static tests, but for the dynamic tests, the attack angle should be adjusted many times due to the elasticity of the spring system. There are totally 21 cases for the static tests and 266 cases for dynamic tests. As presented by Wang (2014) [15], due to the effect of viscous force for this kind of cross-section shape, the force coefficients at low wind speed experiences more fluctuations until the wind velocity reaches 8.0 m/s and above. Therefore, the static tests were only carried out in the range of wind speed from 8.0 m/s to 10.0 m/s for obtaining the reliable force coefficients.

3.4.1 Steps of the static tests

1. Wooden plates were clamped on the steel frames and the force balances were installed on the wooden plate.
2. The supporting steel frames were mounted inside the wind tunnel.
3. The Megane Bridge deck model was placed in the test section of the wind tunnel and in the proper position.
4. The deck model was connected to the force balances on each side of the test section.
5. The attack angle was set-up as 0°.
6. The window of the wind tunnel was hermetically closed to prepare for starting the tests.

7. The initial data was recorded for 10 seconds under wind-off condition.

8. The wind speed of 8.0 m/s was applied for 60 seconds and data was recorded.

9. The wind speed was increased to 11.0 m/s by 1.0 m/s steps. Same recording procedure was carried out for each case.

10. The fan was turned off and the attack angle of the bridge deck model was adjusted to the next attack angle. The steps 6 to 9 explained above were repeated.

3.4.2 Steps of the dynamic tests

1. The force balance system was replaced by the spring suspension system

2. The transversal bar was installed at the end of the longitudinal bar connected to the end plate of the model.

3. The windshield barriers in the middle were installed on the experimental model.

4. The 30 mm high windshield barriers were installed on the experimental model .

5. The longitudinal bar was connected to the four spring system for each side of the model and the attack angle was set to 0 °.

6. By giving an initial displacement to the model, the free decaying vibration test was carried under wind-off situation. The displacement time history for each displacement sensor was recorded for 60 seconds.

7. The window of the wind tunnel was hermetically closed to prepare for starting tests.

8. The wind velocity was increased from 0.8 m/s to 3.0 m/s in steps of 0.2 m/s and then it was increased from 3.0 m/s to 11.0 m/s by 1.0 m/s at low wind velocity VIV vibration were sought to identify, while for high wind velocity, the galloping and flutter were meant to find. The same recording procedure for the displacement decay histories were carried for 60 seconds.

9. The fan was turned off and the attack angle of the experimental model was adjusted to the next attack angle.

10. Steps 7 to 9 were repeated until all the attack angles (-6 °,-4 °,-2 °,0 °,2 °,4 °,6 °) were tested.

11. The 30 mm high windshield barriers were replaced by the 4.8 m windshield barriers. Steps 6 to 10 detailed above were repeated.

Table 3.1 shows a summary of all the test cases performed for the static and dynamic tests, under all the wind speeds and angles of attack combinations.

Table 3.1 Case summary for the static tests and dynamic tests

Cases	Static tests	Dynamic tests
Angles of attack (degree)	-6 °, -4 °, -2 °, 0 °, 2 °, 4 ° and 6 °	-6 °, -4 °, -2 °, 0 °, 2 °, 4 ° and 6 °
Wind speeds (m/s)	8, 9 ,10	0.8 to 11
Edge windshield barrier (m)	2.4	2.4 and 4.0
Amount	21	280
Total	301	

Chapter 4 Experimental Results

The aerodynamic force coefficients, the vibration amplitudes and the dynamic flutter derivative results obtained from the wind tunnel experiments are presented in this chapter. A comparison of the most relevant parameters with the results reported for other long-span bridges is added for (1) verifying the reliability of the results obtained in the current research; and (2) identifying the differences and similarities of the aerodynamic characteristics, between the Megane Bridge deck and other types of bridge decks.

4.1 Static aerodynamic force coefficients

The formulation used for the principle of calculating the static force coefficients was introduced in Chapter 3. Initially, a suitable load cell device needed to be found for measuring the forces acting on the two perpendicular directions, the lift and the drag force directions. But due to the comparatively large weight of the experimental bridge deck section model, the standard load cell device cannot satisfy the requirement of potential maximum value. Therefore, two force balances calibrated for the range of force values similar to those required in this experiment were available from NRCC (National Research Council Canada) and these were chosen as the force measuring equipment, to obtain the lift and drag forces. The force balances are usually used for up-lift force testing of flat roofs models, and each force balance can only measure the force in one direction; thus each force balance was set on either side of the Megane Bridge deck model to measure the lift and drag forces, respectively.

The Reynolds number for the wind tunnel experiment is an important factor in determining the aerodynamic forces, because the viscous force might affect the results

of the static force coefficients. The Reynolds number is defined as [81]:

$$Re = \frac{UB}{\nu} \tag{4.1}$$

where B is the width of the bridge deck section model, U is the uniform wind velocity and ν is the kinematic viscosity of air, the value at 20℃ is 0.15 cm^2/s. The air temperature in the wind tunnel was measured as approximately 16℃. Here the Sutherland's formula [82] was used for calculating the viscosity of the air at 16℃ which is expressed as:

$$\mu = \mu_0 \left(\frac{T}{T_0} \right)^{\frac{3}{2}} \left(\frac{T_0 + C}{T + C} \right) \tag{4.2}$$

where μ is the dynamic viscosity at the input temperature, μ_0 is the known viscosity at reference temperature T_0, and C is the Sutherland's constant, which is 110.4K for air. By substituting relevant parameters into Eq. 4.2, the dynamic viscosity of air at 16℃ was calculated as 0.148 cm^2/s.

Due to the effect of the viscous force, the Reynolds number used for extracting the static coefficients should satisfy the prerequisite condition of $1\times10^4 < Re < 1\times10^7$, where the boundary layer is considered laminar over the entire length of the bridge deck model, and the influence of the air viscosity can be negligible. As the results represented by Wang [15] revealed, the force coefficients extracted under relatively lower wind velocity (7 m/s) for the multiple-deck aerodynamic shape model experienced much fluctuation, and were not as consistent as the coefficients calculated under higher wind velocities (over 7 m/s). In addition, the lift and the drag coefficients used to quantify the resistance for the wind design are dimensionless quantities, and their values are only affected by the mass density of the air, the attack angle of the induced wind and the shape of the object. In other words, the

aerodynamic force coefficients of the bridge deck model should have a similar trend and values under different wind speeds.

Considering the above conditions, the testing wind speeds in the wind tunnel were chosen as 8 m/s, 9 m/s and 10 m/s. The corresponding Reynolds numbers calculated by Eq. 4.1 varies from 4.85×10^5 to 6.06×10^5. The equations used for expressing the wind load are represented by Simiu and Scanlan [13] as:

$$D(\alpha) = \frac{1}{2}\rho U^2 B C_D(\alpha) \tag{4.3}$$

$$L(\alpha) = \frac{1}{2}\rho U^2 B C_L(\alpha) \tag{4.4}$$

where D and L are the static drag and lift force, respectively; C_D and C_L are the static drag and lift force coefficients, respectively; ρ is the air density with a value of 1.214 $\mathrm{kg/m^3}$ for the current air condition; U is the wind speed;B is the width of the experimental bridge deck model, which is 980 mm for the current model. In order to compare the influence of the windshield barriers on the variation of the force coefficients, the two different windshield barriers of 30 mm and 50 mm were installed on the Megane Bridge deck, and the results were compared with the force coefficients data obtained by Wang for the multiple-deck aerodynamic shape model without any windshield barriers [15]. The results of the force coefficients at 8 m/s, 9 m/s and 10 m/s for the bridge deck model with windshield barriers are shown in Table 4.1, Figure 4.1.1 and Figure 4.1.2:

Table 4.1 Steady-state aerodynamic force coefficients for the Megane Bridge deck with windshield barriers of 30 mm

Attack angle(°)	8 m/s		9 m/s		10 m/s	
	C_D	C_L	C_D	C_L	C_D	C_L
-6	0.151	-0.141	0.152	-0.143	0.153	-0.149
-4	0.131	-0.102	0.129	-0.091	0.128	-0.117
-2	0.079	-0.066	0.094	-0.072	0.084	-0.074
0	0.071	-0.004	0.071	-0.037	0.074	-0.051
2	0.078	0.010	0.083	0.003	0.085	-0.007
4	0.117	0.037	0.110	0.036	0.114	0.037
6	0.137	0.060	0.139	0.061	0.140	0.064

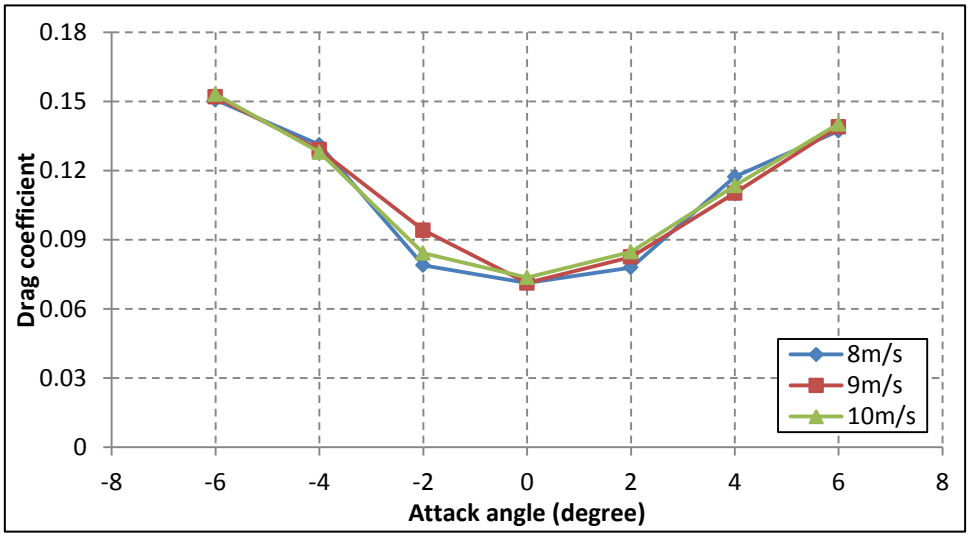

Figure 4.1.1 Drag coefficient C_D for the Megane Bridge deck model (with windshield barriers of 30 mm) at 8 m/s, 9 m/s and 10 m/s

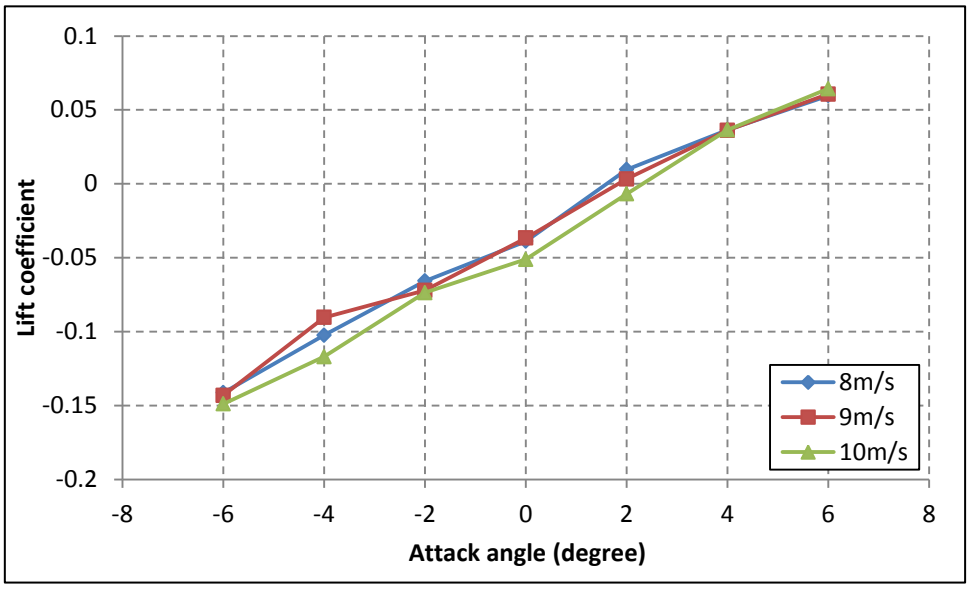

Figure 4.1.2 Lift coefficient C_L for the Megane Bridge deck model (with windshield barriers of 30 mm) at 8 m/s, 9 m/s and 10 m/s

As it can be seen in the Figures 4.1.1 and 4.1.2 above, the drag coefficients had a trend of firstly decreasing from -6° to 0° and then increasing from 0° to 6°, ranging from 0.153 to 0.071. Among all the angles of attack investigated, 0° always reached the lowest point, where for 9 m/s, this registered the minimum value of 0.712, while for the other two cases, 8 m/s and 10 m/s, the drag coefficient had similar values of 0.071 and 0.074, which shows nearly no difference from each other. Under the wind velocity of 10 m/s, the drag coefficients with a maximum value of 0.153 appeared at -6° angle of attack; relatively, a very high value of 0.140 at 6° was registered for 10 m/s. Overall, the drag coefficients C_D presented a high-side among a low situation with the increasing attack angle. The peak values in the left side of 0 axis are higher than that in the right side. The maximum values were always registered at -6° and the minimum values always appeared at 0° in the current experiment. However, based on the general trend and considering the values of the drag coefficients at -6° and 6° angles of attack, the evolution of the drag coefficients beyond this interval cannot be predicted, because the slopes for both sides actually have a decreasing trend as seen in

Table 4.2:

Table 4.2 Drag coefficient slope for the Megane Bridge deck model (with windshield barriers of 30 mm) for wind speeds of 8 m/s, 9 m/s and 10 m/s

Attack angle(°)	C_D'		
	8 m/s	9 m/s	10 m/s
-6	-0.010	-0.012	-0.013
-4	-0.026	-0.018	-0.022
-2	-0.004	-0.012	-0.005
0	0.003	0.006	0.006
2	0.020	0.014	0.014
4	0.010	0.015	0.013
6	0.009	0.011	0.011

From Figure 4.2 it can be noticed that as the attack angle increases from -6° to 6°, the lift coefficients showed an obvious trend of increment. The lift coefficients for wind speeds of 8 m/s, 9 m/s and 10 m/s increased from -0.141, -0.143, -0.149 to 0.060, 0.061 and 0.064, respectively. The maximum values were registered for 6° for all the three cases, which have a similar magnitude of around 0.062. Relatively, the average value of the minimum lift coefficients registered for the three cases was around -0.144 for -6° angle of attack.

Finally it can be concluded that, both the drag and lift coefficients showed good agreement with each other for 8 m/s, 9 m/s and 10 m/s, respectively. In order to identify the effect of the windshield barriers on the drag and lift coefficients, the results are compared with the aerodynamic Megane Bridge deck model without windshield barriers, referenced from Wang [15]. Considering that the trend and the magnitude of the lift and the drag coefficients obtained in the current research for each wind speed are nearly the same, only the results under wind speed of 10 m/s are used for the comparison as shown in Figures 4.1.3 and 4.1.4 below.

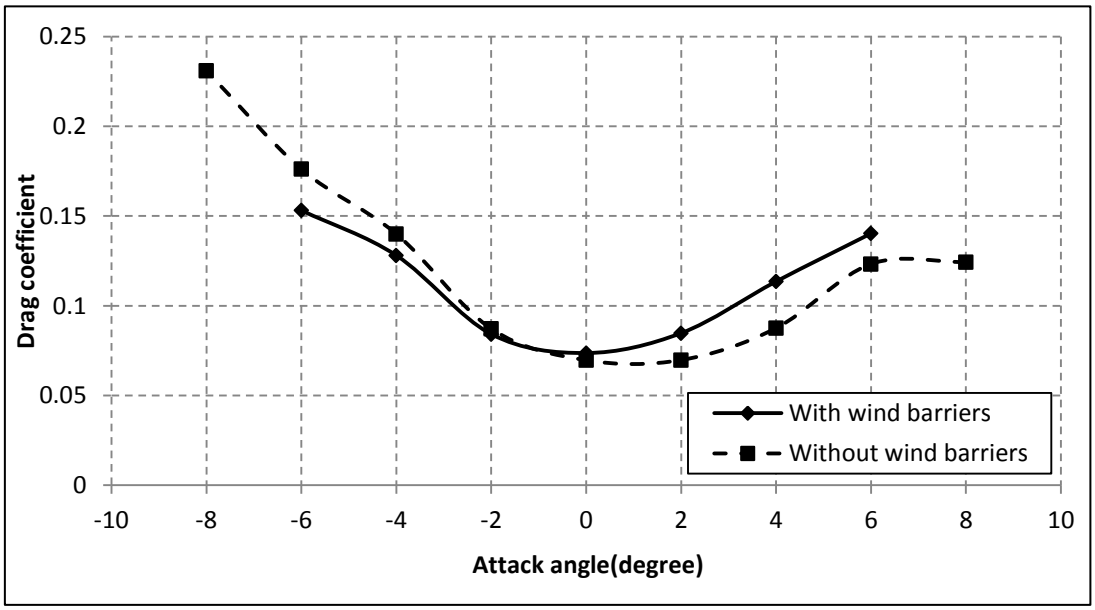

Figure 4.1.3 Drag coefficient C_D for the Megane Bridge deck model with and without windshield barriers [15]

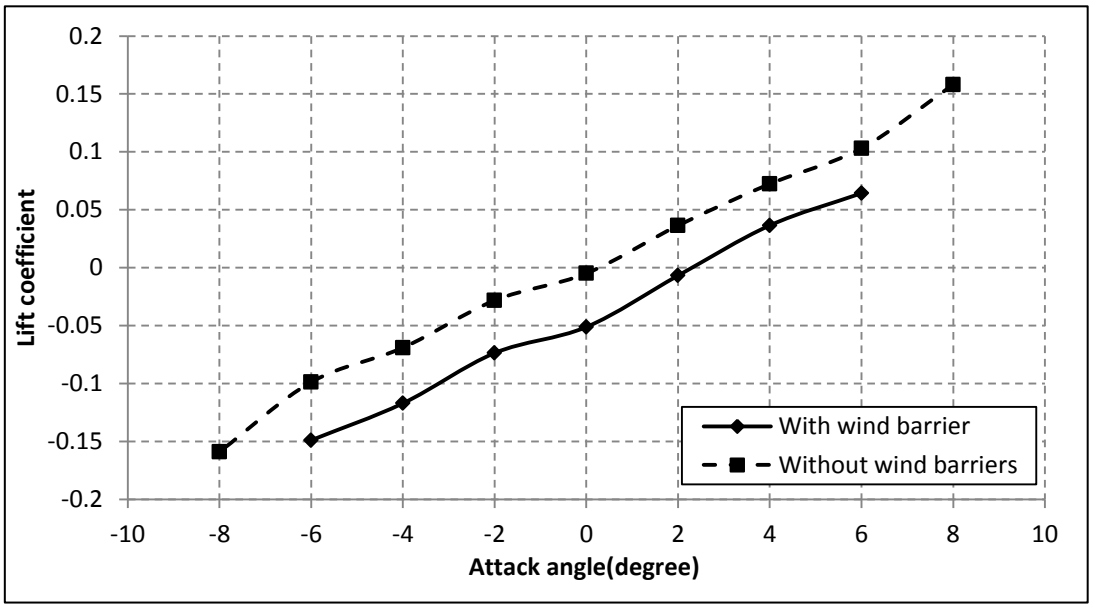

Figure 4.1.4 Lift coefficient C_L for the Megane Bridge deck model with and without windshield barriers [15]

Obviously, the installation of the windshield barriers decreased the value of the lift forces for every angle of attack the lift coefficient becoming smaller than the case of the Megane Bridge deck without windshield barriers, which had good agreement with

the computational results of the single-box girder bridge deck and twin-box girder bridge deck [20]. Also, when compared with the aerodynamic Megane Bridge deck without windshields, it was noticed that despite the different values of the lift and drag coefficients recorded at every angle of attack, overall these had the same trend and were in a similar range. On the other hand, the drag coefficient for the model with windshield barrier increased for the positive angles and reduces for the negative angles. The windshield barriers caused an obvious decrement of the slope of the drag coefficients for the negative range of angles of attack. Meanwhile, the slop of the drag coefficient in the range of the positive angles, has a smoother increment than the drag coefficient slope of the bridge deck model without windshield barriers.

In addition, the results of the force coefficients of the Messina Strait Bridge (triple-box deck bridge) [64], the Stonecutters Bridge (twin-box deck bridge) [55] and the Great Belt Bridge (single-box deck bridge) [83] are added to compare the effect of a different number of box decks on the drag and lift coefficients; all these experimental bridge deck models were built with windshield barriers and were tested in wind tunnels.

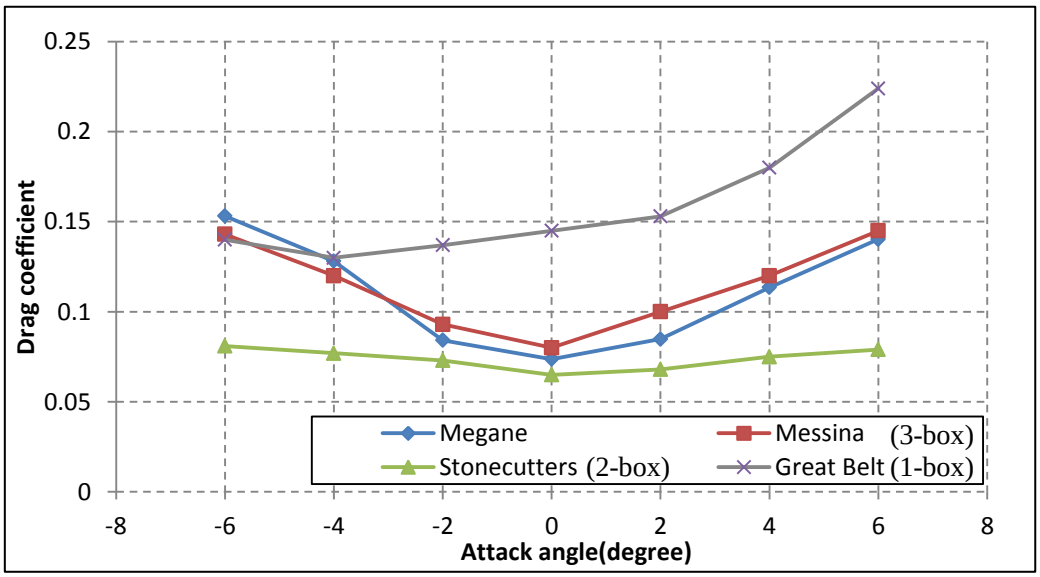

Figure 4.1.5 Drag coefficient C_D comparison for the Megane Bridge, the Messina Bridge [64], the Stonecutter Bridge [55] and the Great Belt Bridge [83] from -6° to 6°

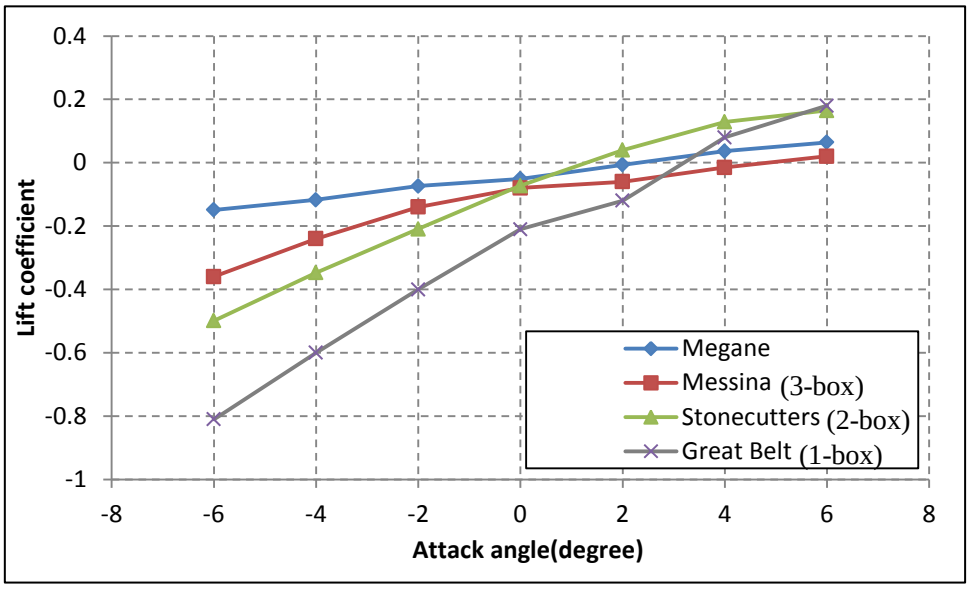

Figure 4.1.6 Lift coefficient C_L comparison for the Megane Bridge, the Messina Bridge [64], the Stonecutter Bridge [55] and the Great Belt Bridge [83] from -6° to 6°

The drag and lift force coefficients (C_D and C_L) summarized for the single-box girder bridge deck (Great Belt Bridge), the twin-box girder bridge deck (Stonecutters Bridge), the triple-box girder bridge deck (Messina Strait Bridge) and the four-box girder bridge deck (Megane Bridge) are plotted in Figures 4.1.5 and 4.1.6. The drag coefficient of the Megane Bridge deck with windshield barriers showed very good agreement with that of the Messina Bridge deck for the range of angles of attack between -6° and 6°. However, the smallest drag coefficient was reported for the twin-box deck of the Stonecutters Bridge, when compared with the other bridge deck geometries. For the lift coefficient, the Megane Bridge had a very similar trend and value for the positive angles of attack, while for lower attack angles, the differences between the lift coefficients for the reported bridge decks increased. It is ascertained that, compared with the single-box girder bridge, the multi-box girder bridge has a more gradual trend and a smaller range of magnitude for the lift coefficient, especially in the range of negative angles of attack. Besides, the triple-box and the four-box girder bridge decks show more stable increment comparatively with the twin-box

girder bridge. On the other hand, the multi-box girder bridges have a much lower value in the range of attack angles between -2° and 6°; the difference shifts to approximately 0.08 units at 0°. The lift coefficients closer to the zero values determined the smallest lift forces and hence are considered as better options; for both, the four-box (Megane) and the triple-box (Messina) decks very low values for the lift coefficients were recorded, thus these decks are considered as having aerodynamic performance.

Section conclusions:

Installation of the windshield barriers on the Megane Bridge deck model can reduce the drag force component of the lateral wind force, for the range of negative attack angles but increase the lift force component of the lateral wind force for positive attack angles. Meanwhile, the windshield barriers have the effect of increasing the slope of the drag force coefficient, for the negative range of angles of attack, which is smoother when compared with the four box bridge deck model without windshield barrier.

Also, it can be concluded that, compared with the single-box girder deck, the four-box girder bridge has a more gradual slope and a smaller range of magnitude for the lift force component, especially in the range of negative angles of attack, which has a stabilizing effect for the galloping instability as it will be discussed in the following section.

4.2 Galloping instability verification

Galloping, also referred to as Den Hartog instability, usually occurs as the low-frequency oscillation of the structure, in the direction transverse to the flow

direction (across-wind direction), especially for the structures with small stiffness and structural damping. Galloping verification formulation is related to the slope of the lift and the drag coefficients [36]. Under specific conditions, the high-speed vortex shedding and the galloping instability take place together, though galloping usually happens for a much lower frequency compared with vortex shedding [38]. Considering the complex cross-section of the Megane Bridge deck and the small structural damping of the current experimental model subjected to a uniform flow, checking galloping should be a necessary part for the aerodynamic stability. The potential of a structure to encounter the galloping condition can be calculated by using the renowned Den Hartog stability criterion formula [36]:

$$H(\alpha) = \left(\frac{dC_L(\alpha_C)}{d\alpha_C} + C_D(\alpha_C) \right)\Bigg|_{\alpha_C=\alpha} < 0 \tag{4.5}$$

If $H(\alpha) < 0$, galloping phenomenon occurs for the Megane Bridge deck model, otherwise, the Megane Bridge deck model does not encounter galloping instability. Calculating the values of C'_L (Table 4.3) and substituting them and the data from Table 4.1 into Eq. 4.5, the $H(\alpha)$ values are determined for 8 m/s, 9 m/s and 10 m/s wind speeds and are presented in Table 4.4.

Table 4.3 Lift coefficient slope for the Megane Bridge deck model (with windshield barriers of 30 mm) for wind speeds of 8 m/s, 9 m/s and 10 m/s

Attack angle(°)	C'_L		
	8 m/s	9 m/s	10 m/s
-6	0.065	0.030	0.066
-4	0.072	0.038	0.086
-2	0.124	0.070	0.046
0	0.028	0.080	0.088
2	0.054	0.066	0.088
4	0.046	0.050	0.054
6	0.042	0.041	0.035

Table 4.4 Galloping ratio $H(\alpha)$ for Megane Bridge deck model with 30 mm high windshield barriers

Attack angle(°)	H(α)		
	8 m/s	9 m/s	10 m/s
-6	0.216	0.182	0.203
-4	0.203	0.167	0.214
-2	0.203	0.164	0.130
0	0.099	0.151	0.162
2	0.132	0.149	0.173
4	0.163	0.160	0.168
6	0.179	0.180	0.175

As it can be noticed from the above chart, all the galloping ratios are positive, thus it can be ascertained that the Megane Bridge has good stability against galloping for 8 m/s, 9 m/s and 10 m/s. The galloping would not take place under any angle of attack; however high-speed vortex shedding vibration happens when the wind tunnel experiments were carried out.

4.3 Vertical displacements and torsional angles

As the calibration method and the calculating procedure for the vibration amplitudes were mentioned in Chapter 3, the exact same procedure was applied for each case of -6°, -4°, -2°, 0°, 2°, 4° and 6°. When performing the experiments, under the same angle of attack condition, the wind speed was changed from 0.8 m/s to 3 m/s by 0.2 m/s increments and from 3 m/s to 11 m/s by 1 m/s increments. The smaller increment steps were used until reaching the test wind speed of 3 m/s to observe the occurrence of the vortex-induced vibration phenomenon, which usually happens for smaller wind speeds, when the frequency of the flow equals the frequency of the structural model. After completing the tests for all the angles of attack and all the wind speed cases, the 30 mm high windshield barriers on the edge of the model, were replaced by the 50 mm high windshield barriers and the same experimental cases were carried out for the

new model. There were a total of 280 cases performed for the dynamic tests, and accordingly a very large amount of results was obtained; only a part of them were presented in this chapter, and the rest will be in Appendix.

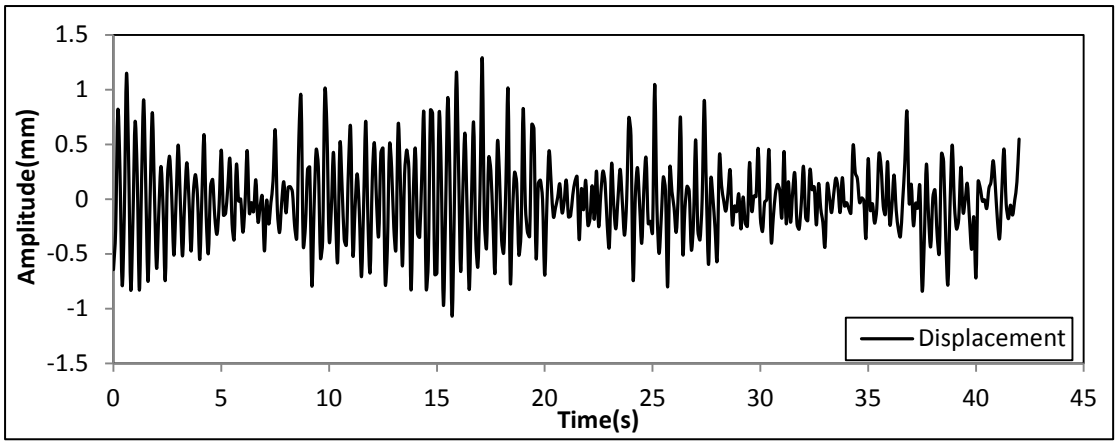

Figure 4.3.1 Vertical displacement time history at centre of the experimental model for 3 m/s and 0° and 30 mm high windshield barrier

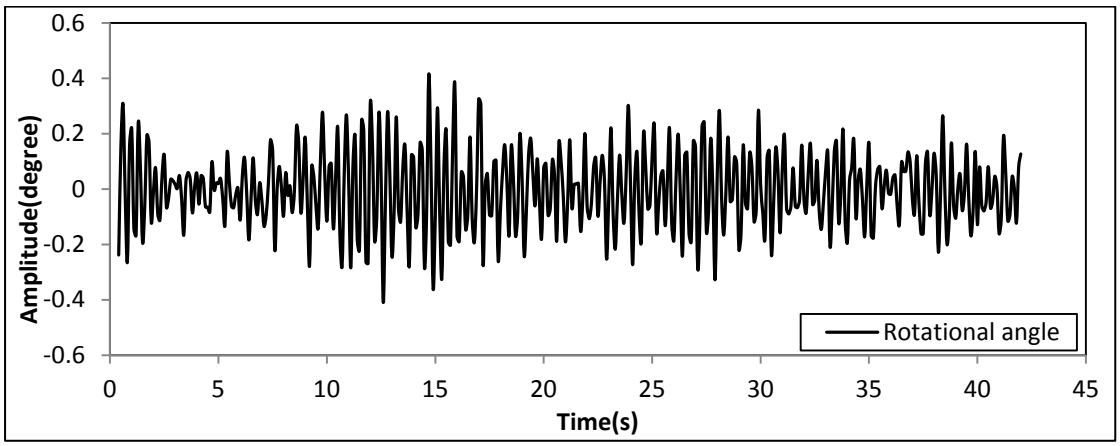

Figure 4.3.2 Rotational angle time history at centre of the experimental model for 3 m/s and 0° and 30 mm high windshield barrier

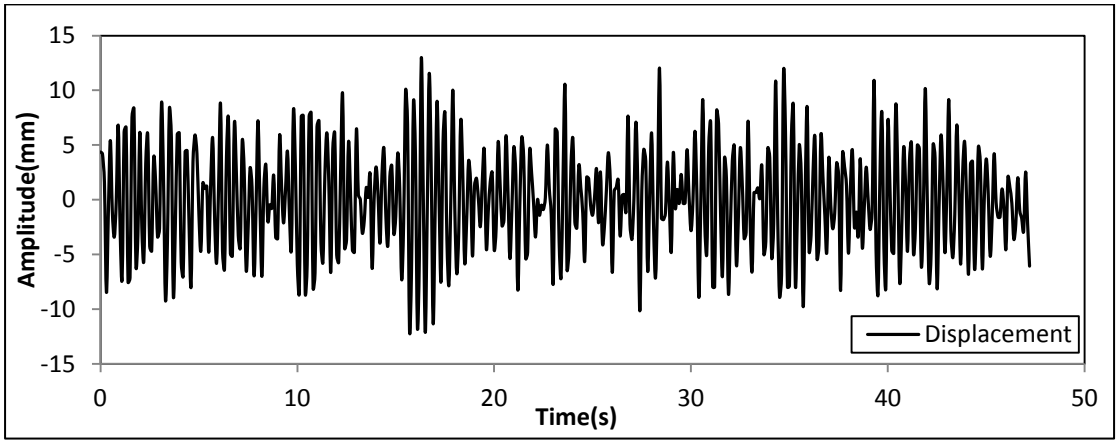

Figure 4.3.3 Displacement time history at centre of the experimental model for 11 m/s and 0° and 30 mm high windshield barrier

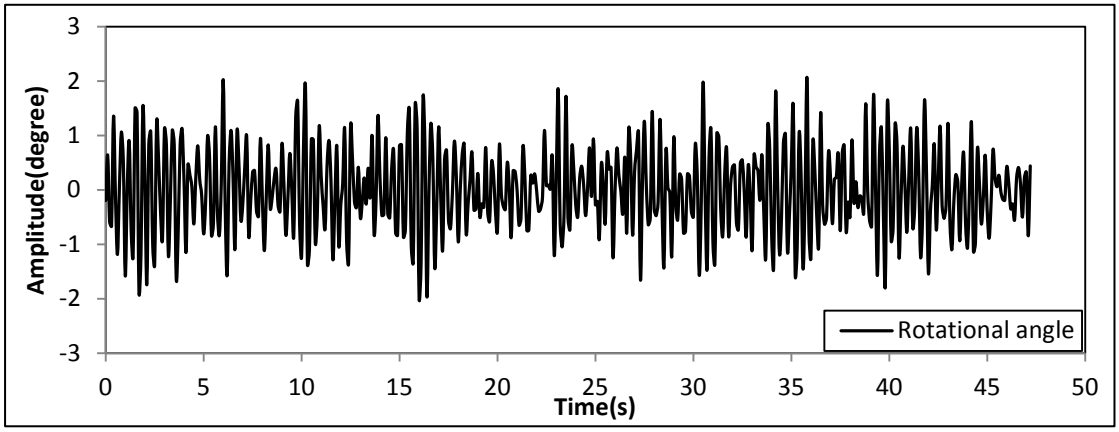

Figure 4.3.4 Rotational angle time history at centre of the experimental model for 11 m/s and 0° and 30 mm high windshield barrier

With the increment of the wind speed, the amplitude for both the vertical displacement $D_M(t)$ and the rotational angle $\alpha(t)$ presented an increasing trend for the Megane Bridge deck model with 30 mm high edge windshield barrier case. For low wind speeds under 3 m/s, the vertical vibration displacements $D_M(t)$ showed relatively low values between -1.5 mm and 1.5 mm (Fig.4.3.1); in the same time, the values of torsional angles $\alpha(t)$ are within the range of -0.3° to 0.3° (Fig.4.3.2). Under the wind velocity of 11 m/s, the absolute values of the peak amplitudes at 0° increased to 6 mm and 1.5° for $D_M(t)$ and $\alpha(t)$, respectively (Fig. 4.3.3, Fig. 4.3.4).

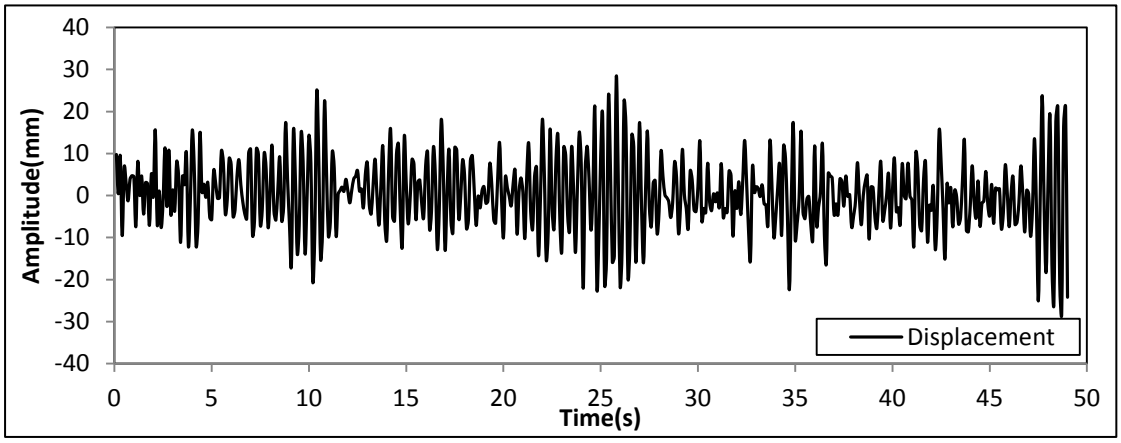

Figure 4.3.5 Displacement time history at centre of the experimental model for 11 m/s and 6° and 30 mm high windshield barrier

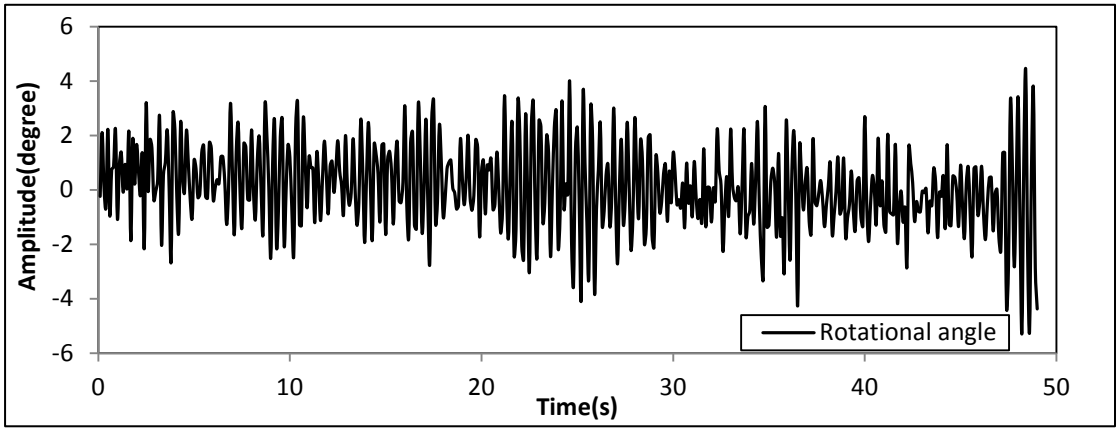

Figure 4.3.6 Rotational angle time history at centre of the experimental model for 11 m/s and 6° and 30 mm high windshield barrier

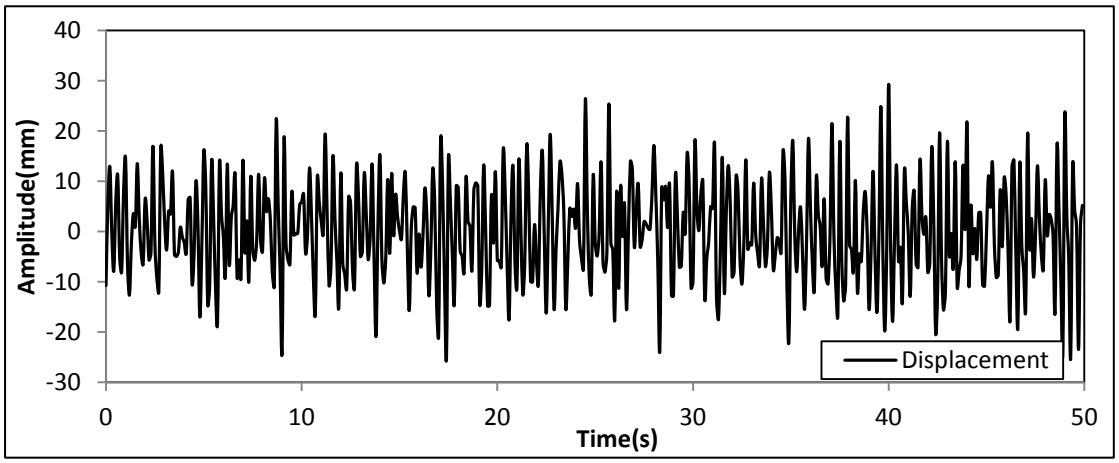

Figure 4.3.7 Displacement time history at centre of the experimental model for 11 m/s

and -6° and 30 mm high windshield barrier

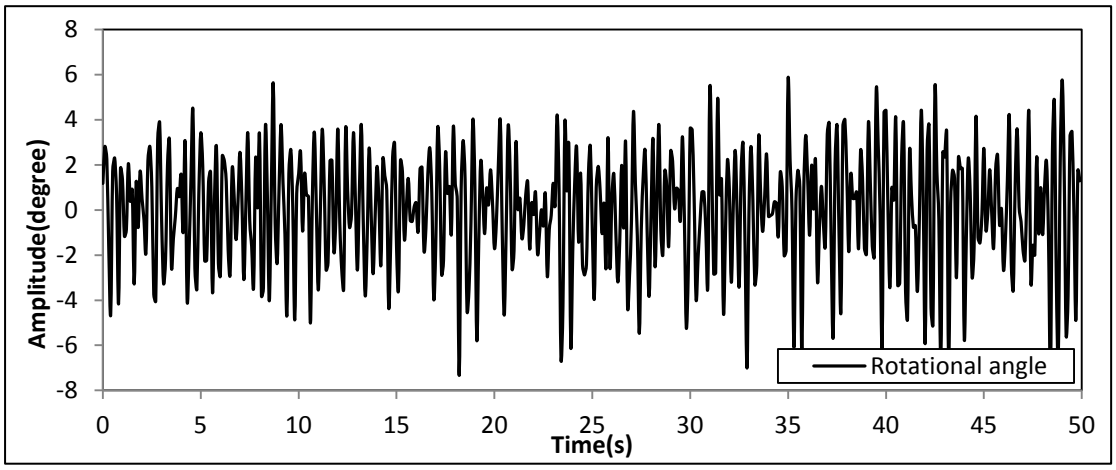

Figure 4.3.8 Rotational angle time history at centre of the experimental model for 11 m/s and -6° and 30 mm high windshield barrier

As the angle of attack increased to 6°, the values of the vertical displacement $D_M(t)$ and the rotational angle $\alpha(t)$ reached 9.98 mm and 1.98° for 30 mm high windshield barrier (Fig. 4.3.5 and Fig. 4.3.6). As the angle of attack decreases to -6°, the values of $D_M(t)$ and $\alpha(t)$ reached higher values of 11.46 mm and 2.1° for the Megane Bridge deck model with 30 mm high windshield barrier case (Fig. 4.3.7 and Fig. 4.3.8). Comparing the peak values recorded for wind velocities changing from 3 m/s to 11 m/s, the cases of -6° and 6° showed much larger increases for $D_M(t)$ and $\alpha(t)$ than the vertical and torsional displacements for 0°. Moreover, the results obtained for -6° case are larger than those obtained for 6°, which can also represent a regular pattern for the other angles-of-attack, namely the negative angles cases have larger vibration amplitudes for $D_M(t)$ and $\alpha(t)$ than the positive angles cases. In addition, the values of $D_M(t)$ and $\alpha(t)$ for the cases of the 30 mm high windshield barrier become larger as the value of the attack angle increased, while the minimum value of the vertical and torsional displacements were recorded for 0° angle of attack.

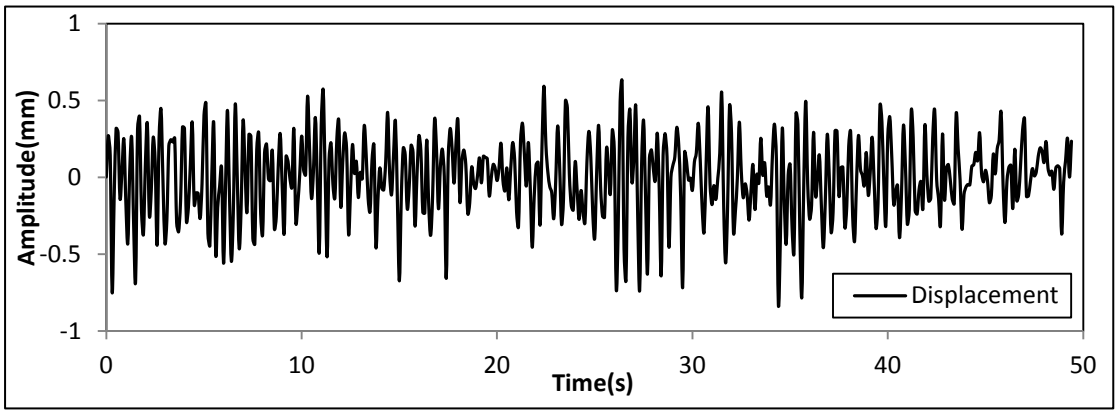

Figure 4.3.9 Displacement time history at centre of the experimental model for 3 m/s and 0° and 50 mm high windshield barrier

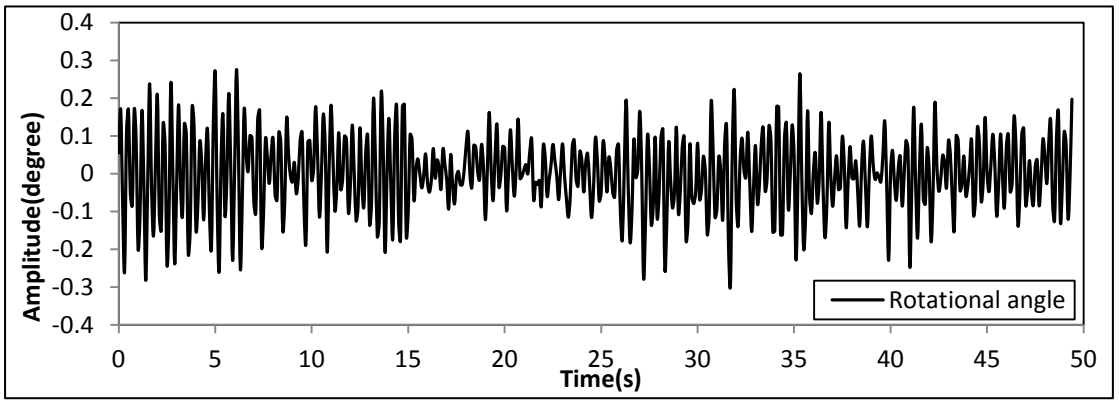

Figure 4.3.10 Rotational angle time history at centre of the experimental model for 3 m/s and 0° and 50 mm high windshield barrier

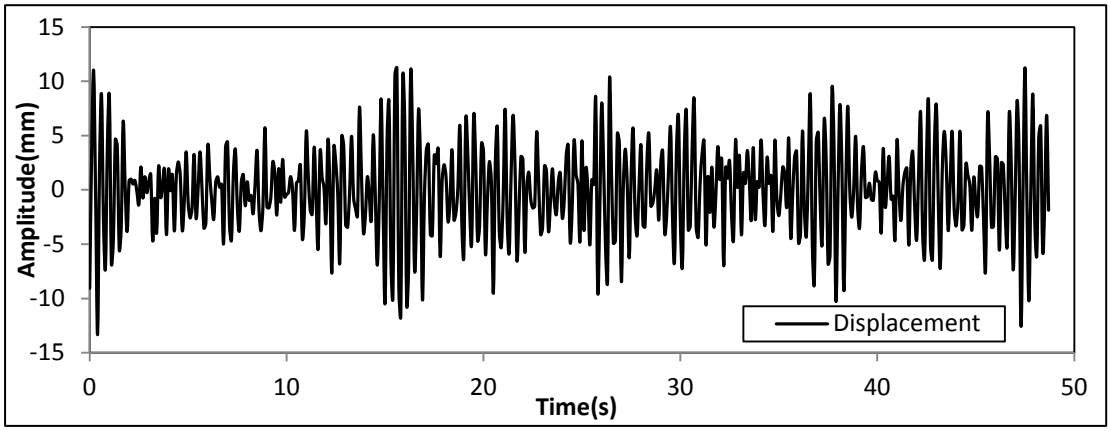

Figure 4.3.11 Displacement time history at centre of the experimental model for 11 m/s and 0° and 50 mm high windshield barrier

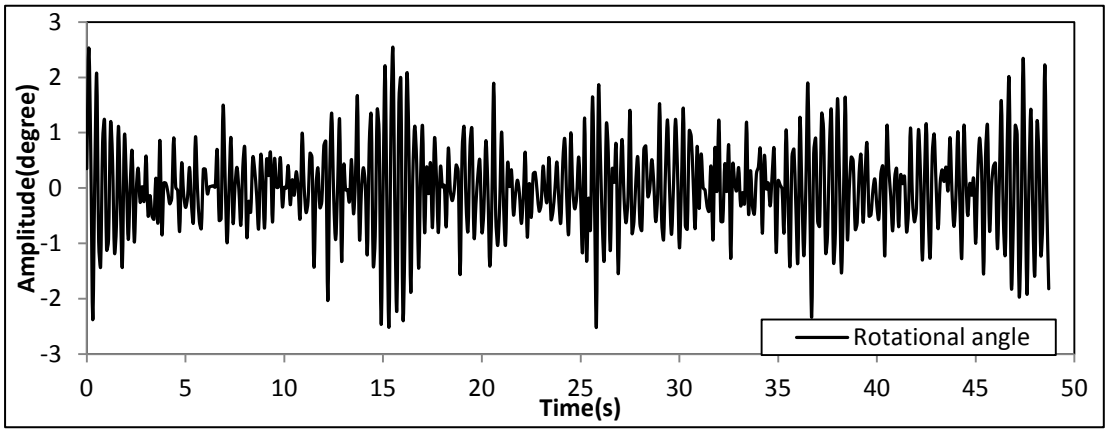

Figure 4.3.12 Rotational angle time history at centre of the experimental model for 11 m/s and 0° and 50 mm high windshield barrier

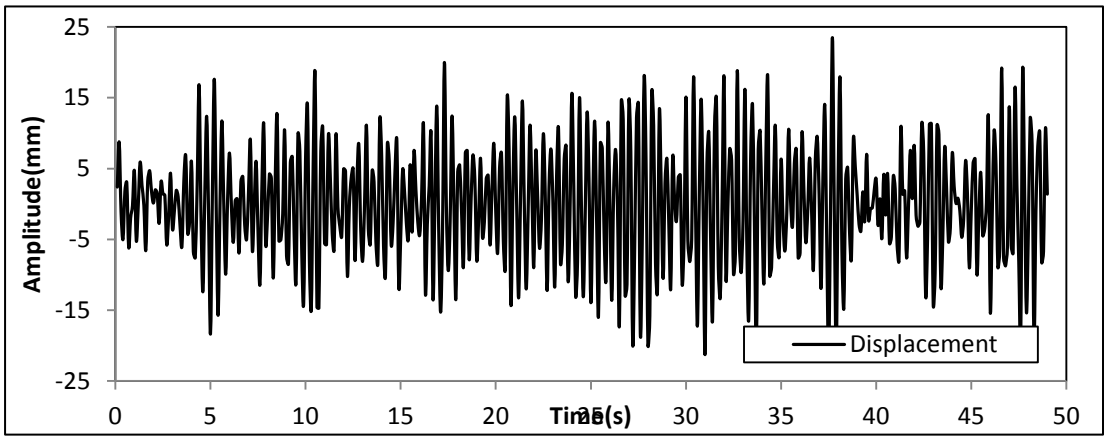

Figure 4.3.13 Displacement time history at centre of the experimental model for 11 m/s and 6° and 50 mm high windshield barrier

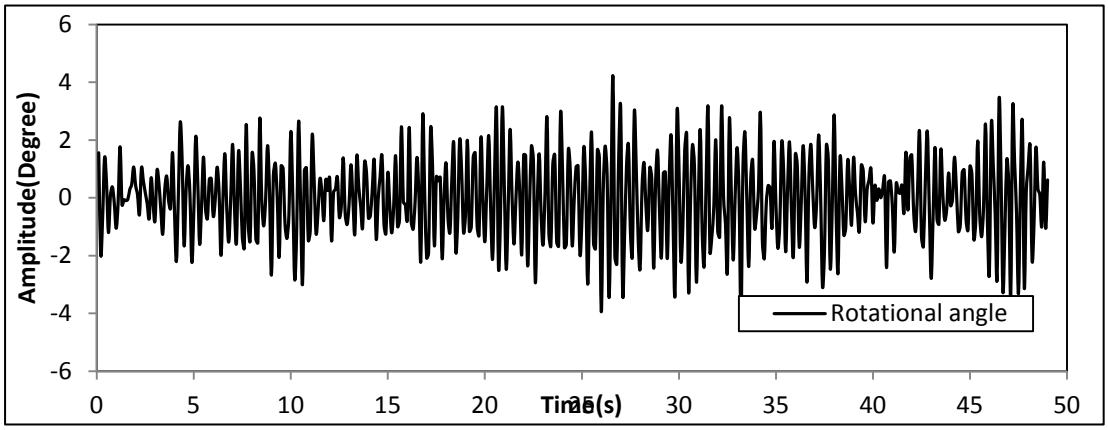

Figure 4.3.14 Rotational angle time history at centre of the experimental model for 11 m/s and 6° and 50 mm high windshield barrier

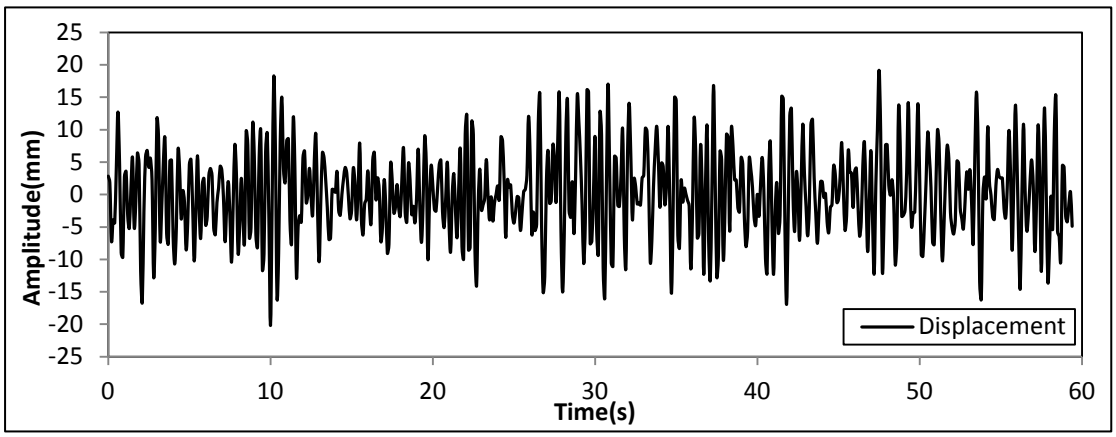

Figure 4.3.15 Displacement time history at centre of the experimental model for 11 m/s and -6° and 50 mm high windshield barrier

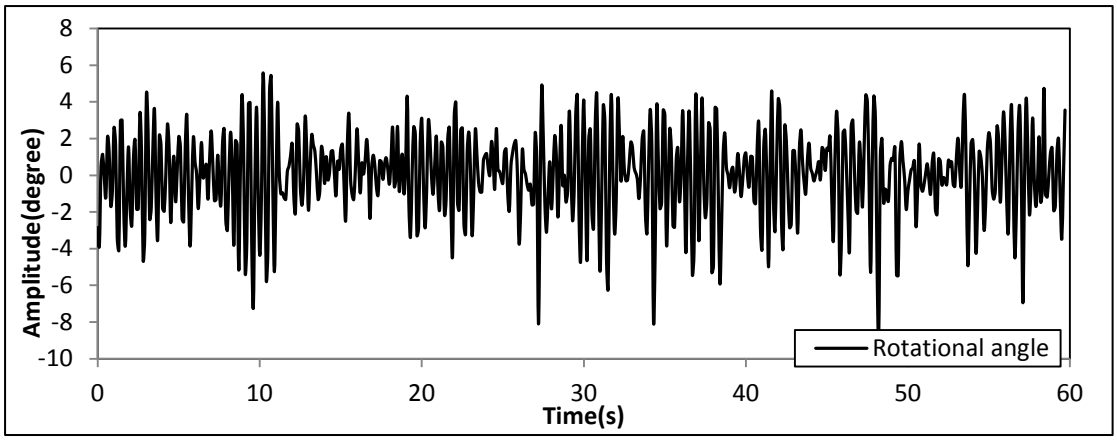

Figure 4.3.16 Rotational angle time history at centre of the experimental model for 11 m/s and -6° and 50 mm high windshield barrier

The vertical and torsional vibration amplitudes $D_M(t)$ and $\alpha(t)$ for the Megane Bridge deck model with 50 mm high windshield barrier cases were 0.37 mm and 0.14° at 0° angle of attack for the wind speed of 3 m/s (Fig. 4.3.9 and Fig. 4.3.10); these values are much smaller compared with the 6° or -6° in the high wind speed range (>8m/s). As it can be seen in Fig. 4.3.9 to Fig 4.3.16, for the Megane deck model with 50 mm high windshield barrier, similar trends for the vibration amplitudes were recorded as for the 30 mm high windshield barrier cases. The values of $D_M(t)$ and $\alpha(t)$, however, became larger for the windshield barriers with 50 mm height, as the values of attack angle increased to positive values, while the negative angles of

attack showed a larger difference than the positive ones; the minimum value for the vertical and torsional displacements were again minimum for 0°. Compared with the displacement time histories of the two windshield barrier cases, the 50 mm high windshield barrier case has peak amplitude values of 0.37 mm and 0.13° for $D_M(t)$ and $\alpha(t)$ (Fig. 4.3.9 and Fig. 4.3.10) at 3 m/s, respectively; these values were lower than the peak values for the deck model with 30 mm high windshield barrier (0.47 mm and 0.18°, respectively). The same comparative relationship, between the different heights of the windshield barrier cases turned up at 11 m/s; the average amplitudes of $D_M(t)$ and $\alpha(t)$ for the Megane Bridge deck model with 50 mm high windshield barrier cases were 4.80 mm and 0.81° (Fig. 4.3.11 and Fig. 4.3.12), respectively, which are smaller than those for the deck model with 30 mm high windshield barrier ones (5.21 mm and 0.89°, respectively). Regardless on the angle of attack, the same condition occurs for all the wind speeds investigated. In order to provide a more comprehensive comparison for the effect of different heights of the windshield barriers on the magnitude of vibrations, the average absolute vibration amplitudes for $D_M(t)$ and $\alpha(t)$ are presented in Figures 4.3.17 to 4.3.23 as function of the wind speed. In addition, using the actual windshield barrier height of 2.4 m and 4.0 m to present the model height of 30 mm and 50 mm, respectively, for easy recognition.

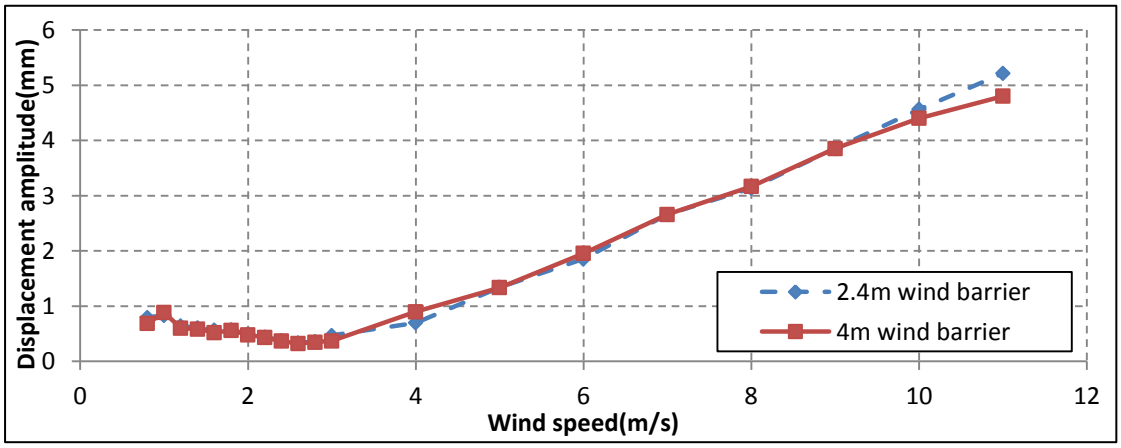

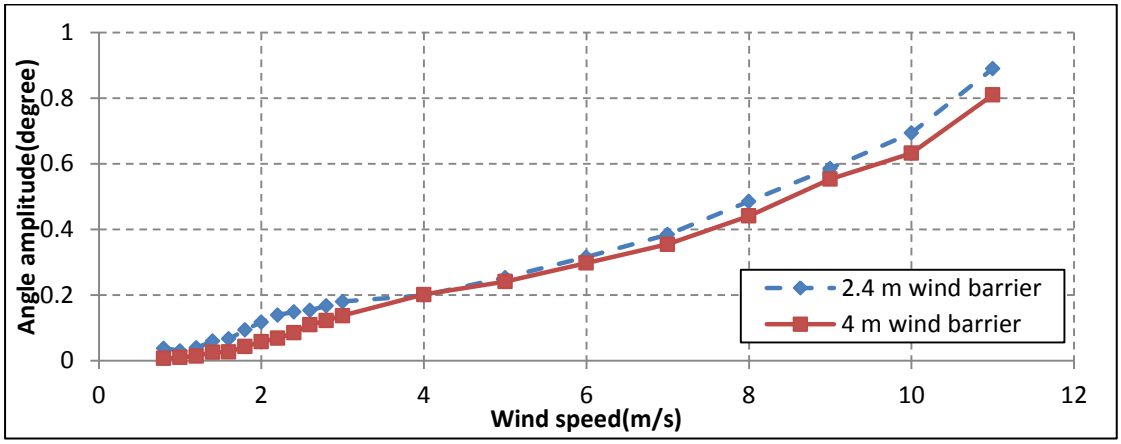

Figure 4.3.17 Average amplitudes of vertical displacements and rotational angles for 30 mm and 50 mm high windshield barrier at attack angle of 0°

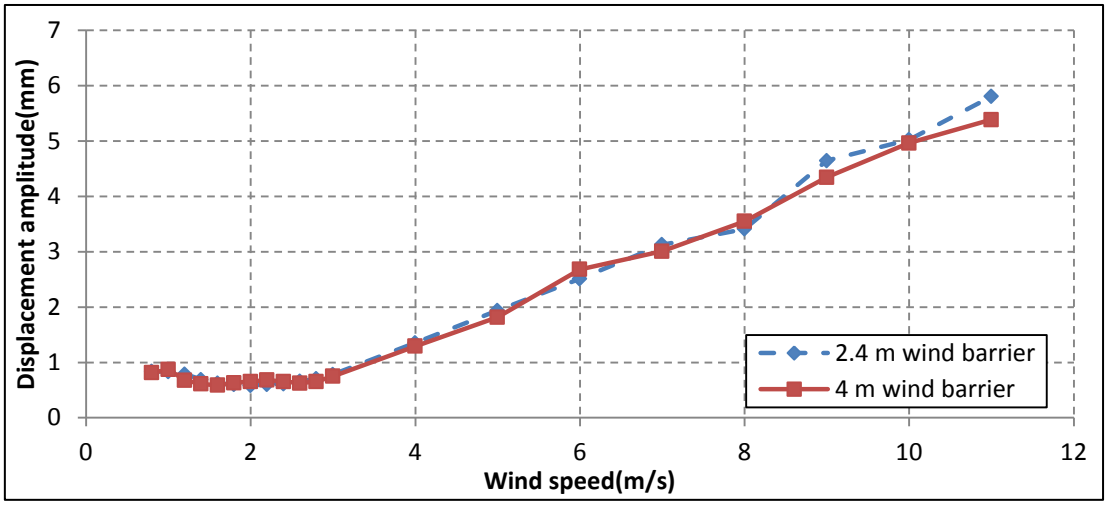

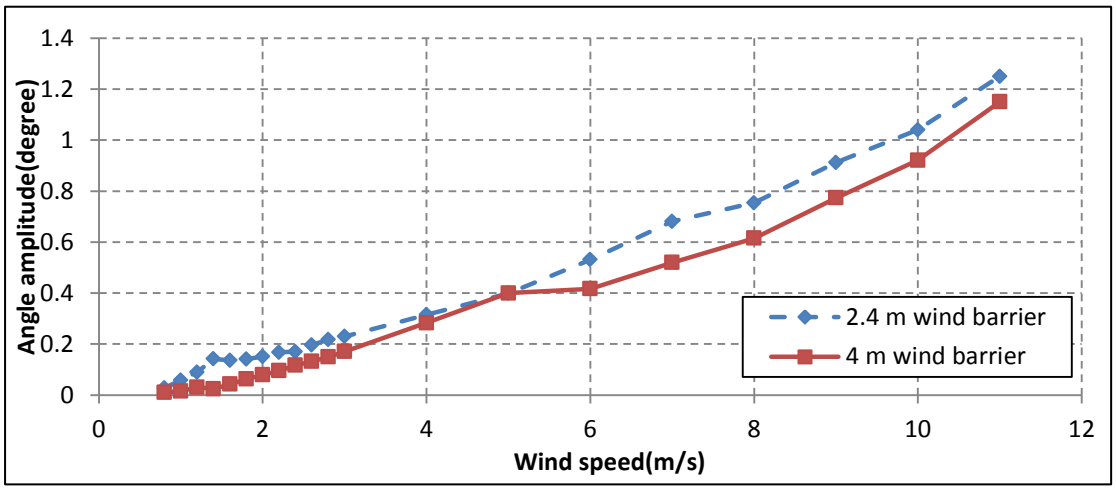

Figure 4.3.18 Average amplitudes of vertical displacements and rotational angles for 30 mm and 50 mm high windshield barrier at attack angle of -2°

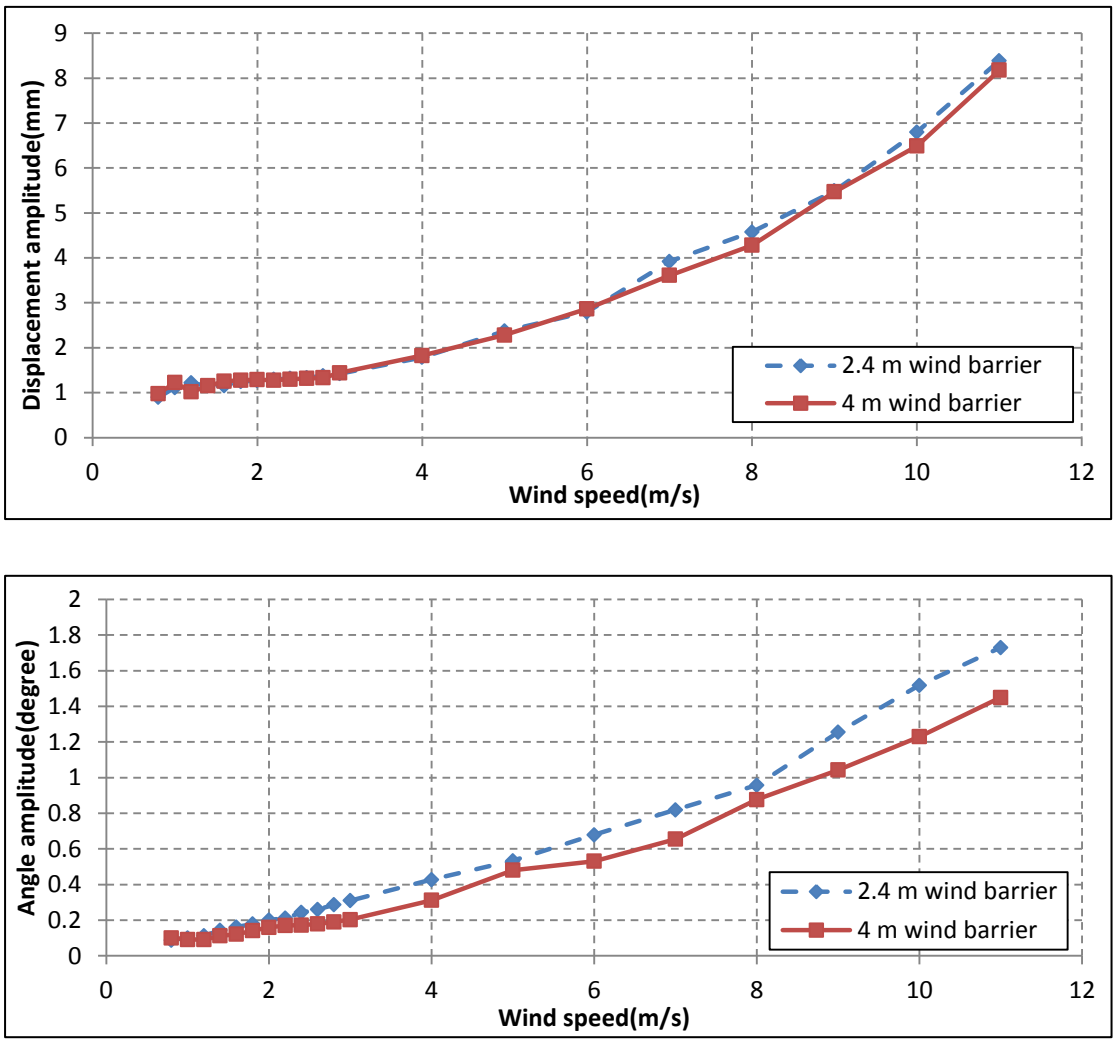

Figure 4.3.19 Average absolute amplitudes of vertical displacements and rotational angles for 30 mm and 50 mm high windshield barrier at attack angle of -4°

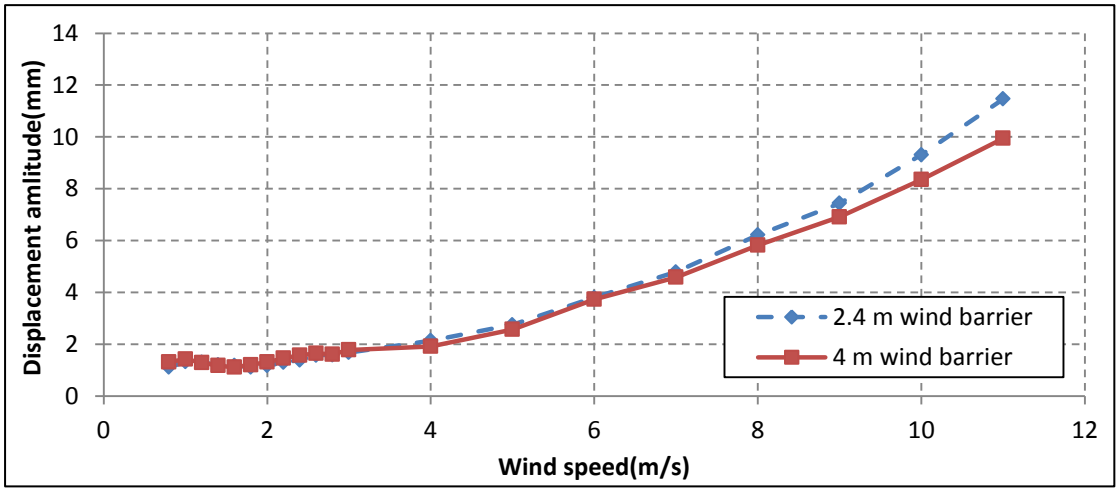

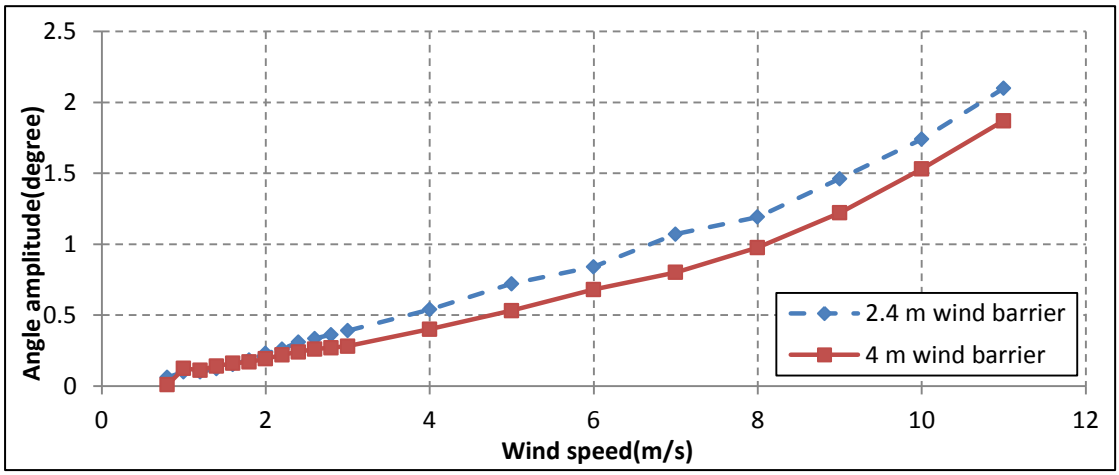

Figure 4.3.20 Average amplitudes of vertical displacements and rotational angles for 30 mm and 50 mm high windshield barrier at attack angle of -6°

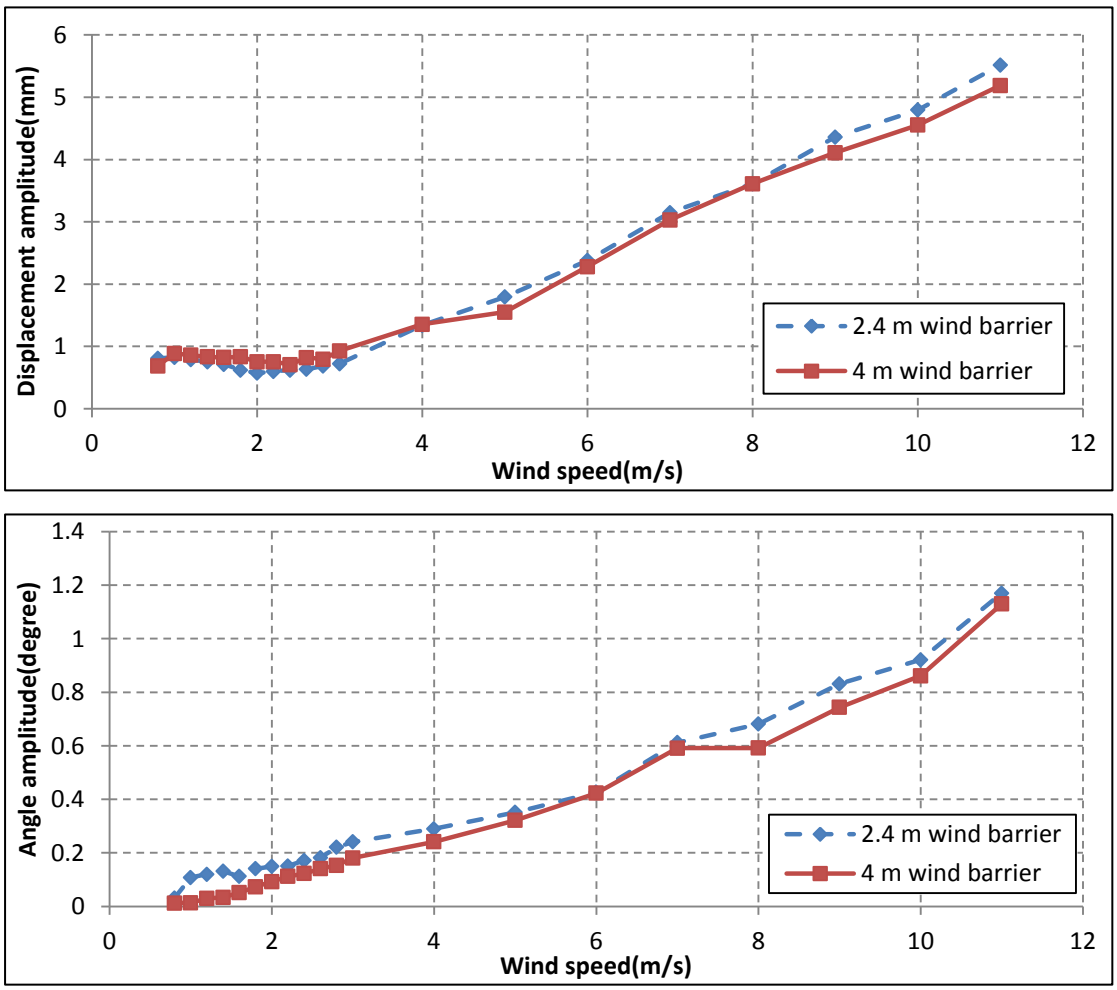

Figure 4.3.21 Average amplitudes of vertical displacements and rotational angles for 30 mm and 50 mm high windshield barrier at attack angle of 2°

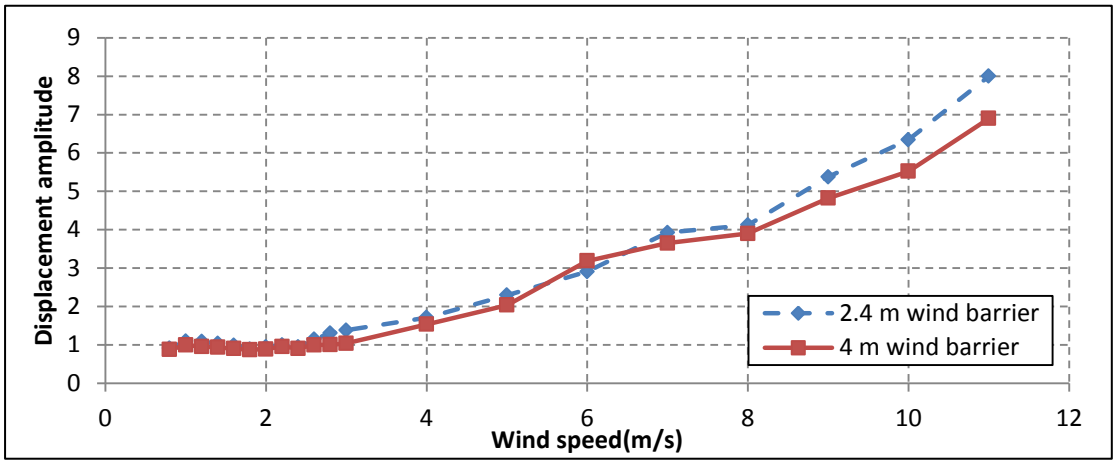

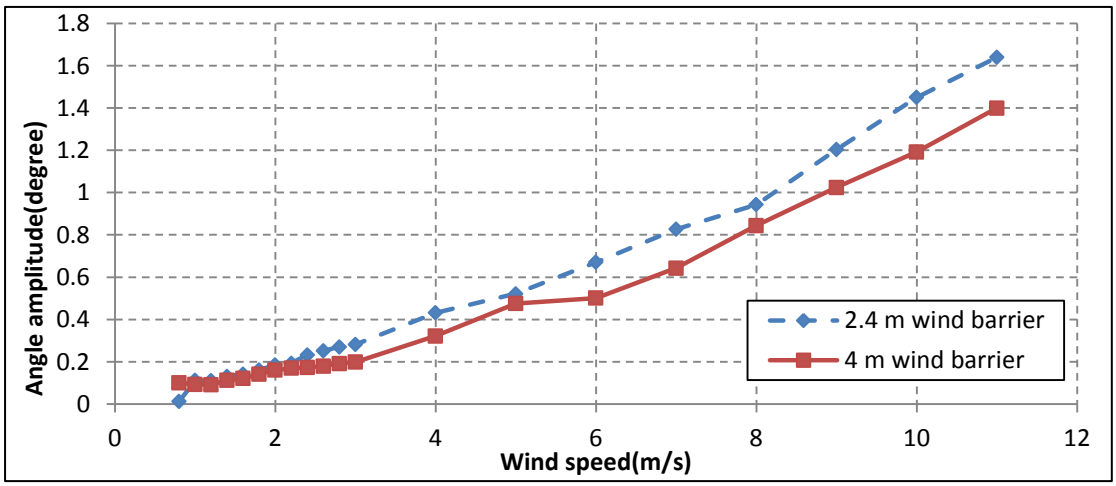

Figure 4.3.22 Average amplitudes of vertical displacements and rotational angles for 30 mm and 50 mm high windshield barrier at attack angle of 4°

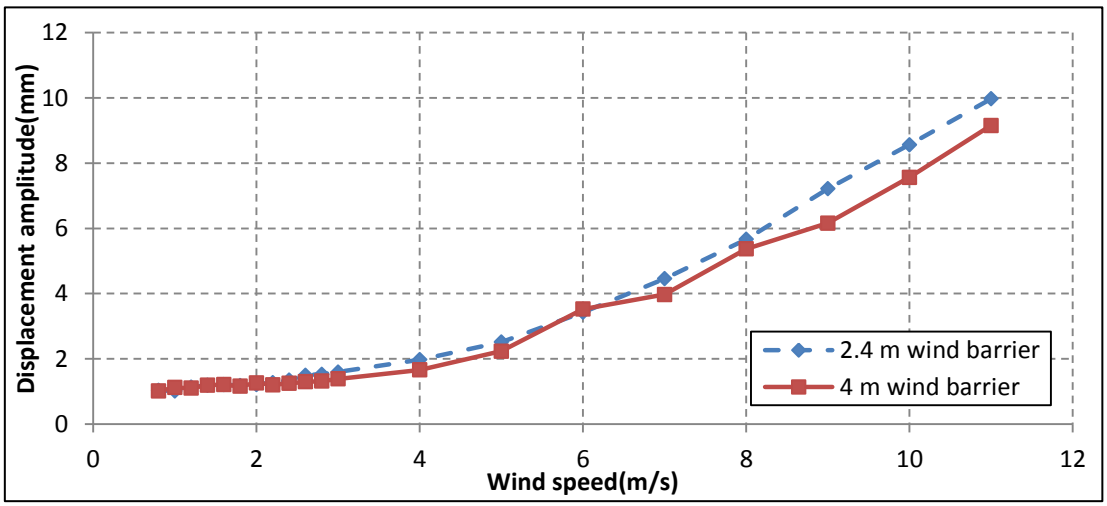

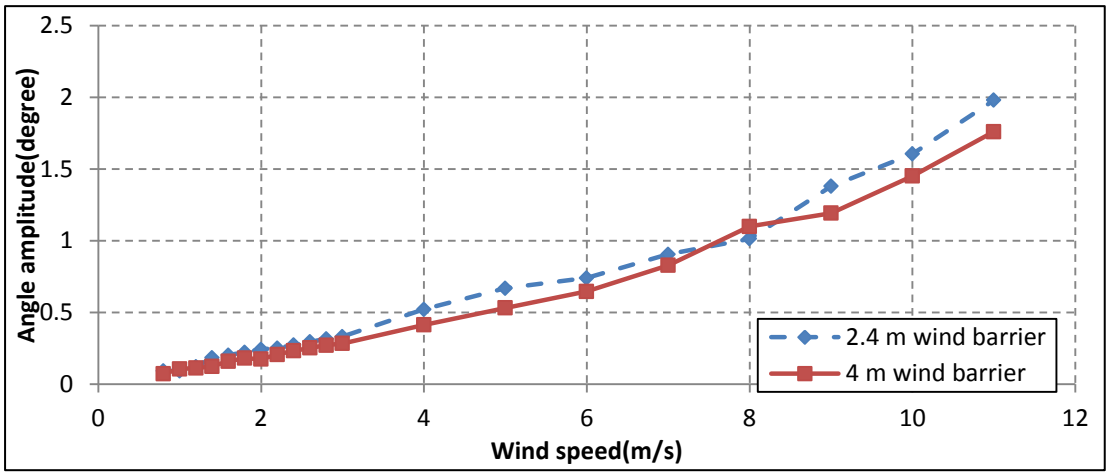

Figure 4.3.23 Average amplitudes of vertical displacements and rotational angles for 30 mm and 50 mm high windshield barrier at attack angle of 6°

Figures 4.3.17 to 4.3.23 shown above are aimed to identify how the different heights of windshield barriers influence the bridge vibrations in the vertical and torsional directions when the bridge deck model was under laminar wind flow varying from 0.8 m/s to 11.0 m/s. In general, it was noticed that:

(1) for both 30 mm and 50 mm high windshield barrier cases, the amplitudes of vertical displacements $D_M(t)$ and torsional angles $\alpha(t)$ had an obvious increasing trend with the wind speed increased; the maximum amplitudes of $D_M(t)$ and $\alpha(t)$ for both windshield barrier cases took place at -6°, which are 11.46 mm and 2.1° for 30 mm high windshield barrier case and 9.95 mm and 1.87° for 50 mm high windshield barrier case.

(2) Normally for each angle of attack and each wind speed, the 30 mm high windshield barrier case shows higher values of $D_M(t)$ and $\alpha(t)$ when compared with the 50 mm high windshield barrier case, but a few number of points have opposite relations between the 30 mm and 50 mm high windshield barrier cases, such as the vertical displacement time histories at 6.0 m/s and torsional angle time histories at 8.0 m/s.

(3) When wind speed is below 4.0 m/s, the values and trends for both $D_M(t)$ and $\alpha(t)$ did not have significant difference between the two windshield barrier cases; the apparent distinctiveness usually happens for wind speeds higher than 7 m/s.

The amplitudes were not only affected by different heights of the windshield barriers, but also the different angles of attack influenced the bridge deck vibrations in the vertical and torsional directions. The vibration amplitude variation with the attack angles are shown in Figures 4.3.24 and 4.3.25.

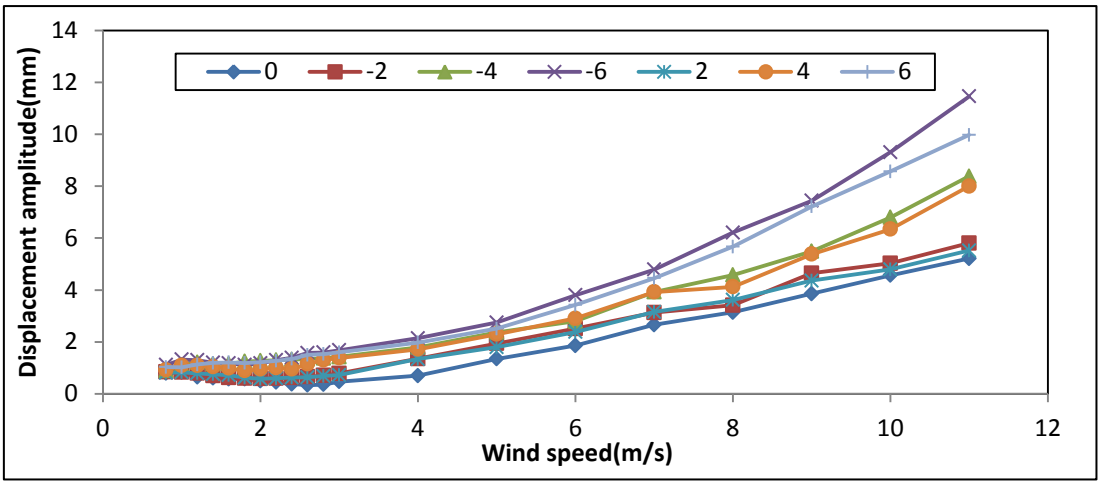

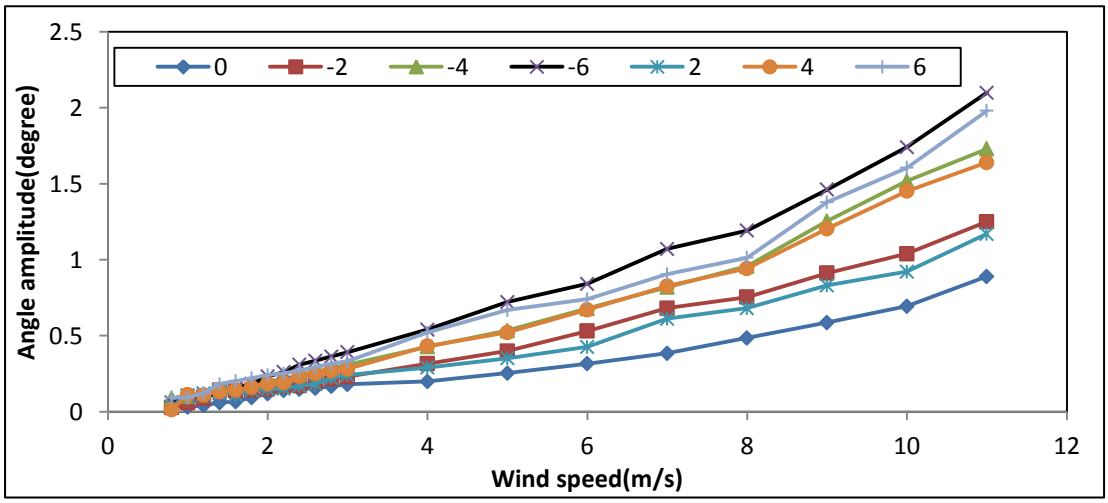

Figure 4.3.24 Average amplitudes of vertical displacement and rotational angles for 30 mm high windshield barrier

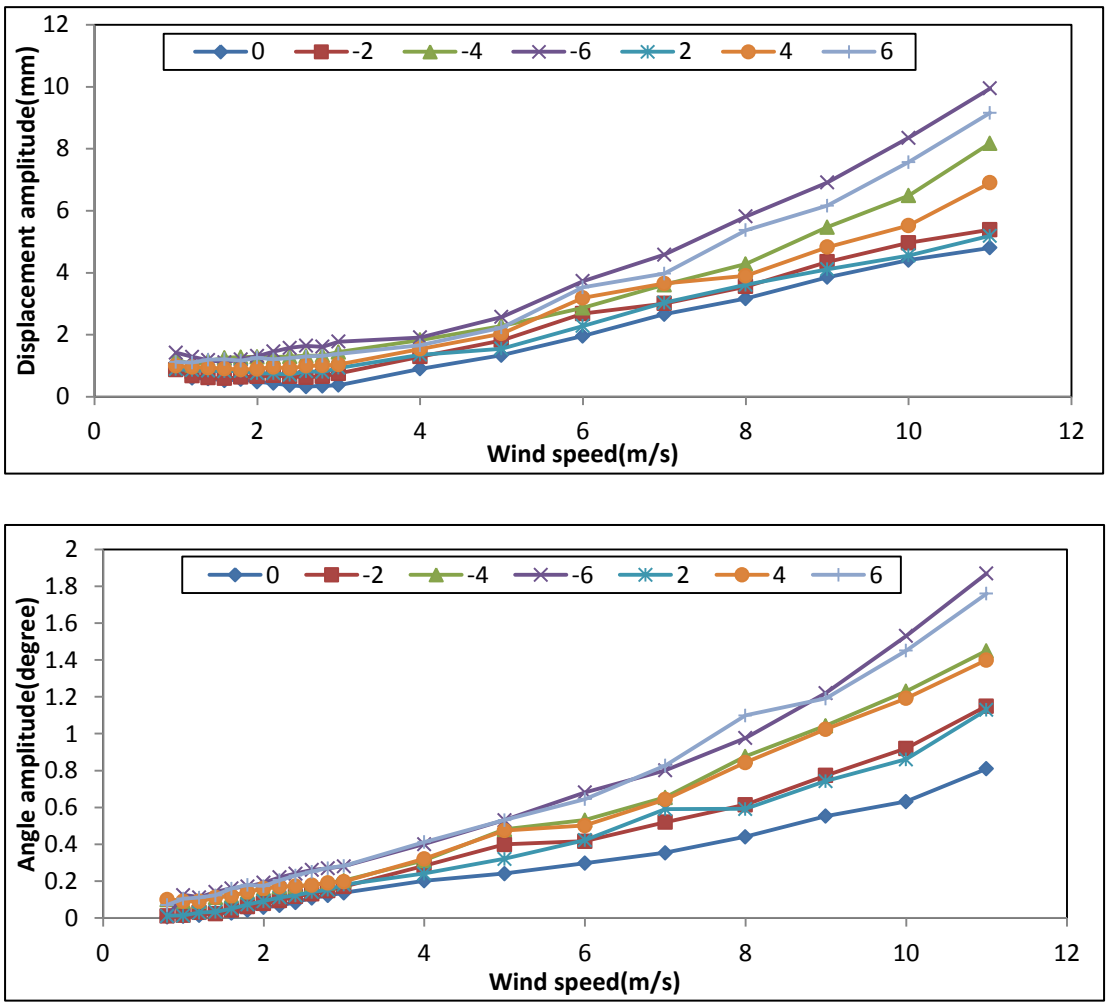

Figure 4.3.25 Average amplitudes of vertical displacements and rotational angles for 50 mm high windshield barrier

It is ascertained that, for negative angles of attack much larger amplitudes of both vertical and torsional vibrations were registered, compared with the vibration magnitudes for positive angle cases. The general amplitude increased gradually by groups of angles, following the relationship A(-6°)>A(6°)> A(-4°)> A(4°)> A(-2°)> A(2°)> A(0°) for most of the cases, especially in the range of wind speeds higher than 7 m/s. The amplitude curves for the low wind speed (<3m/s) cases were close to each other, but the curves of -6° and 6° cases were still obviously higher than the rest of the cases.

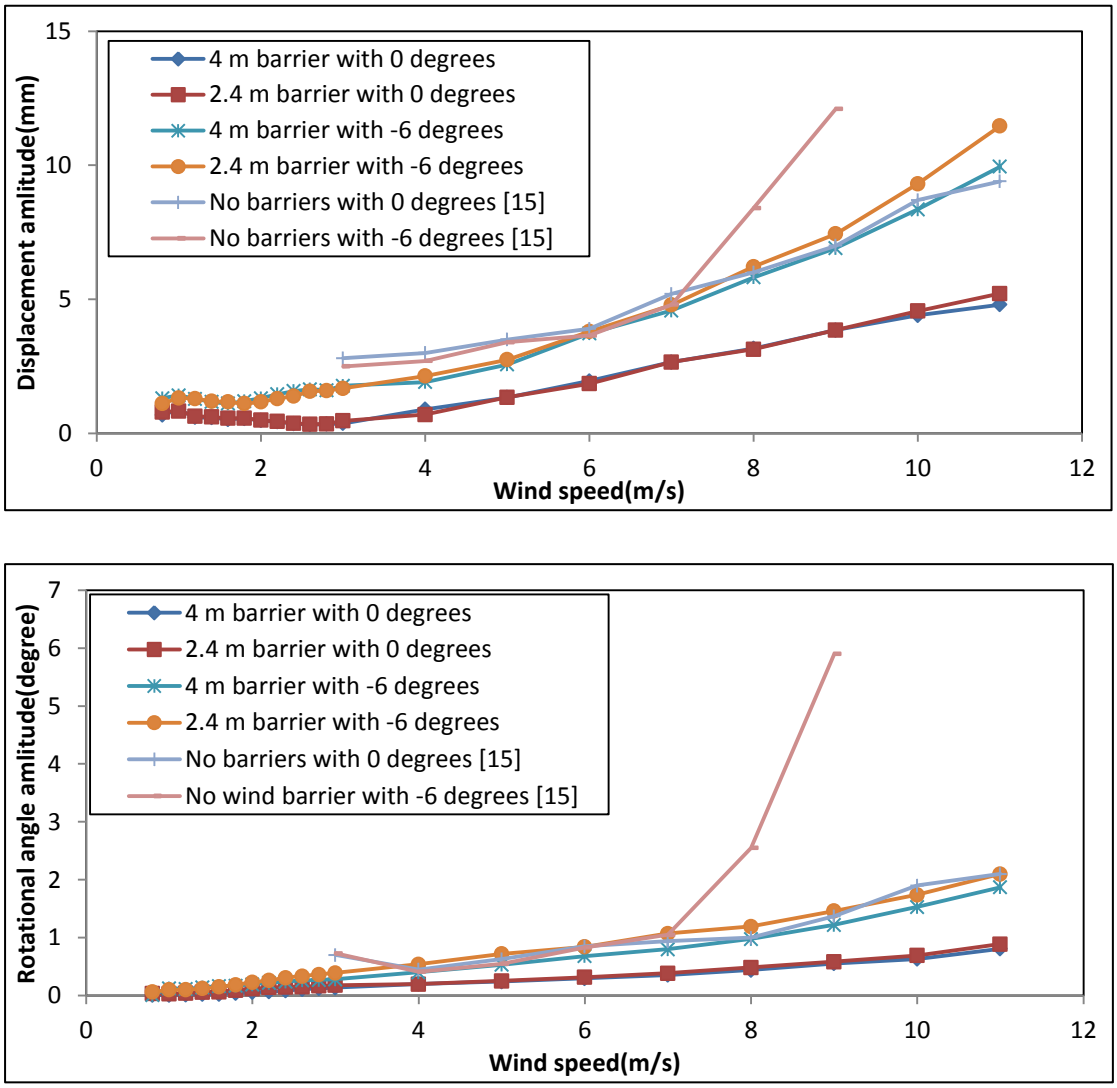

Figure 4.3.26 Average amplitudes for vertical displacements and rotational angles for 30 mm high windshield barrier case, 50 mm high edge windshield barrier case and without windshield barrier [15] under attack angles of 0° and -6°

The results for the -6° angle of attack for which the highest vibrations were noticed and the initial case at 0° were compared for the Megane Bridge deck with 30 mm high windshield barrier, with the 50 mm high windshield barrier and without windshield barriers [15] have been collected and plotted in Fig. 4.3.26. For 0° angle of attack, the bridge deck model without windshield barrier case has a much higher displacement amplitude than the 30 mm high windshield barrier and the 50 mm high windshield barrier case, and the curve of the bridge deck model displacements

without windshield barrier case is close to the curve of the 50 mm high windshield barrier case but at -6° angle of attack. The rotational angle amplitudes of the deck without windshield barrier were close to those of the 30 mm high windshield barrier case for -6°. Also, for -6° angle of attack, the slopes of the displacement and rotational angle amplitudes for the deck without windshield barrier case met a sudden increase after 7 m/s, but the 30 mm high windshield barrier and the 50 mm high edge windshield barrier cases still kept a comparatively slow increasing slope. In general, the installation of the windshield barriers can reduce the vibration amplitudes for both vertical displacements and rotational angles, and it can also make the amplitude slopes increase smoothly.

Section conclusions:

In general, both 30 mm and 50 mm high windshield barriers models had the effect of decreasing the vertical and torsional vibrations, when compared with the model without windshield barriers, which obviously encountered aerodynamic instability for high wind speeds. The model with 50 mm high windshield barriers performed better than the model with 30 mm high windshield barriers, in mitigating the increase of both vertical and torsional vibrations. Always for negative angles of attack, the wind-induced vibrations were higher than for the positive angles, which is expected for any shape of bridge deck.

4.4 Flutter derivatives

The calculation procedure and the extraction method (ILS) for the flutter derivatives have been introduced in detail in Chapter 2. For a two-DOF system, the eight flutter derivatives, A_i^* and H_i^* (i=1,2,3,4), are the most important parameters to evaluate the aerodynamic properties for every kind of bridge deck. In the current research, the

results obtained for the eight flutter derivatives of the Megane Bridge deck, extracted from the wind tunnel experiments were used for comparing the aerodynamic efficiency of different windshield barrier heights, at different angles of degree. Scanlan and Tomoko [48] introduced the reduced wind speed parameter, which is usually the tool for normalizing the flutter derivatives, and has been adopted by most of the bridge aerodynamic researches. While the flutter derivative is a wind speed dependent variable, the reduced wind speed acts as the independent coefficient and it can be written as [48]:

$$U_{red} = \frac{\overline{U}}{B \cdot f} \tag{4.6}$$

where $\overline{U}$ is represented as the mean wind speed produced in the wind tunnel, B is the width of the bridge deck model and f is the structural system's vibration frequency.

4.4.1 Comparison for different angles of attack

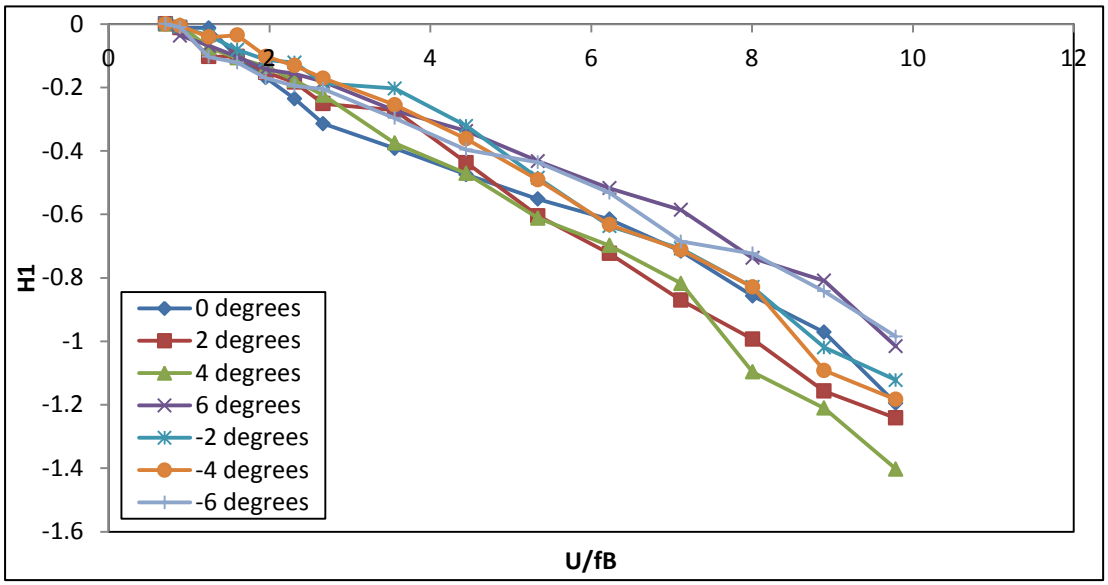

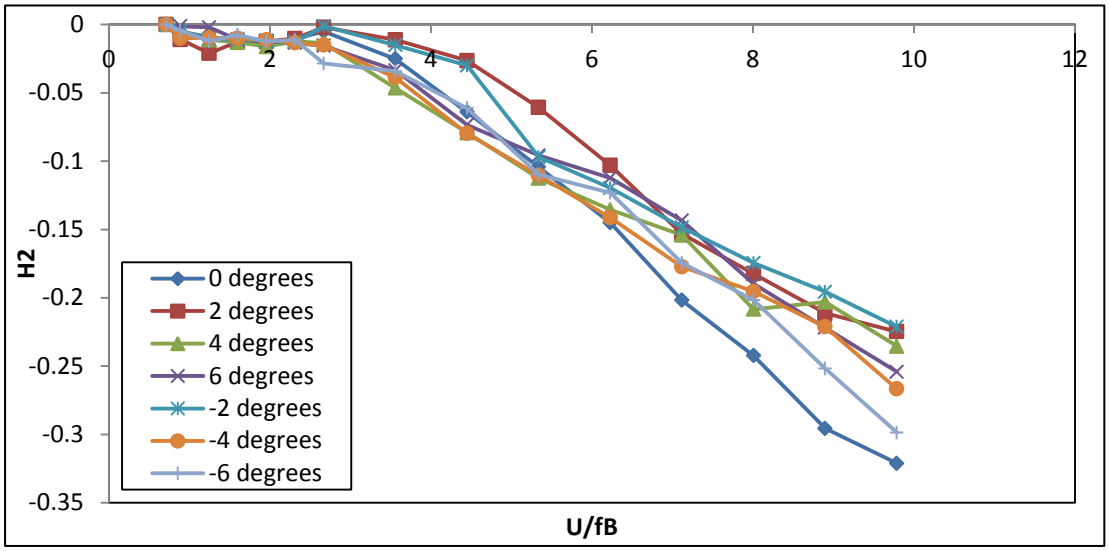
0
-0.05
-0.1
-0.15
-0.2
-0.25
-0.3
-0.35
H2
0
2
4
6
8
10
12
U/fB
0 degrees
2 degrees
4 degrees
6 degrees
-2 degrees
-4 degrees
-6 degrees

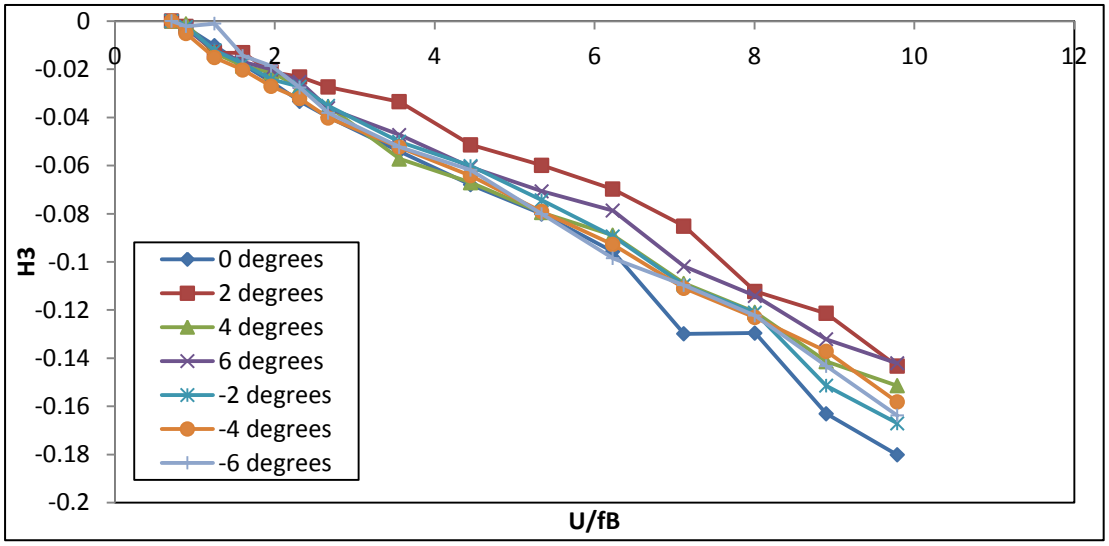
0
-0.02
-0.04
-0.06
-0.08
-0.1
-0.12
-0.14
-0.16
-0.18
-0.2
H3
0
2
4
6
8
10
12
U/fB
0 degrees
2 degrees
4 degrees
6 degrees
-2 degrees
-4 degrees
-6 degrees

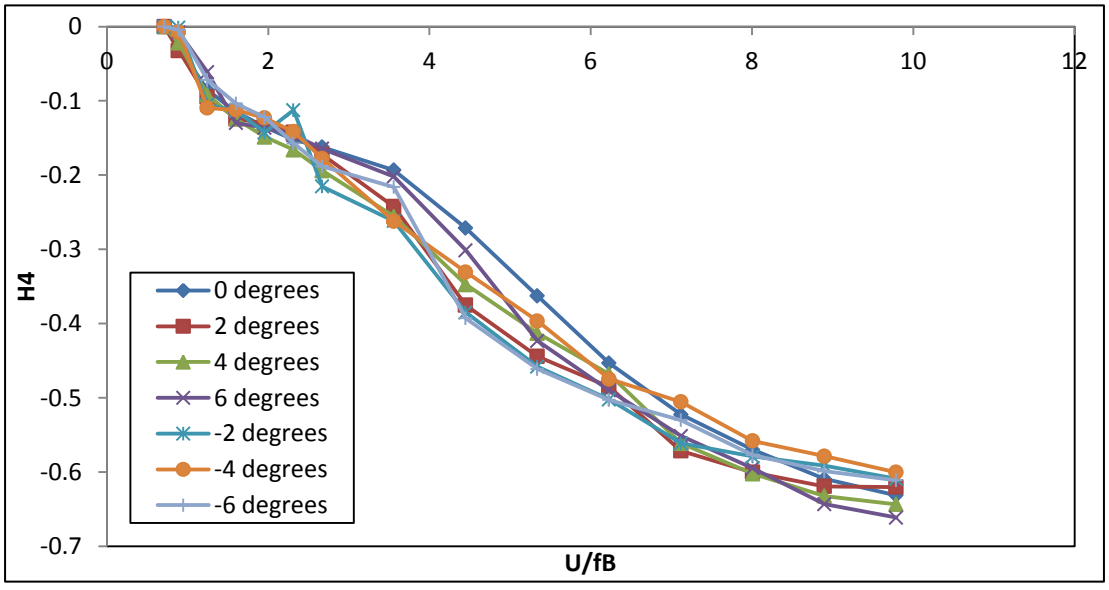
0
-0.1
-0.2
-0.3
-0.4
-0.5
-0.6
-0.7
H4
0
2
4
6
8
10
12
U/fB
0 degrees
2 degrees
4 degrees
6 degrees
-2 degrees
-4 degrees
-6 degrees

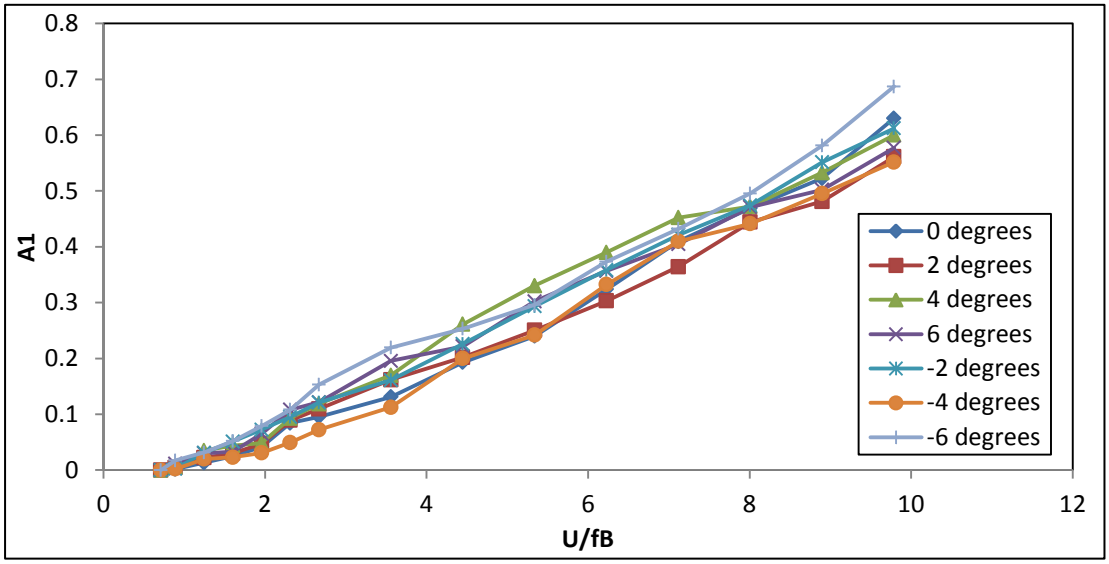
A1
U/fB
0 degrees
2 degrees
4 degrees
6 degrees
-2 degrees
-4 degrees
-6 degrees

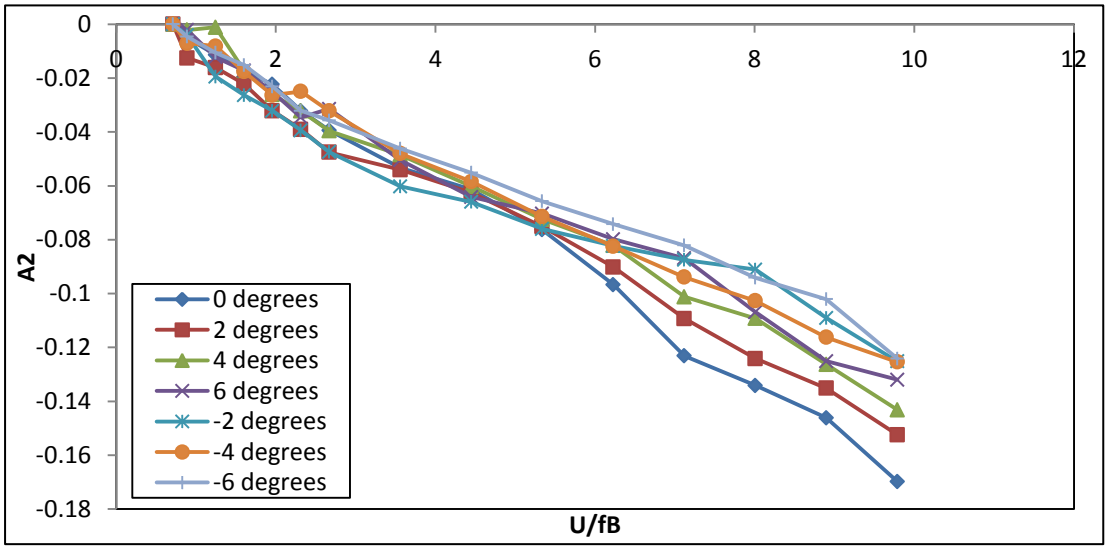
A2
U/fB
0 degrees
2 degrees
4 degrees
6 degrees
-2 degrees
-4 degrees
-6 degrees

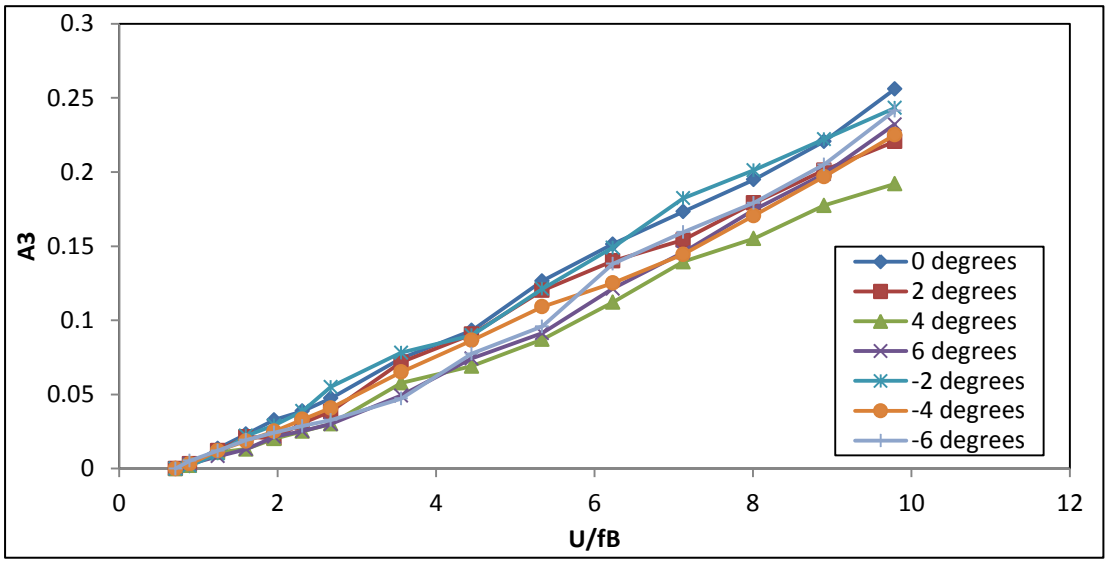
A3
U/fB
0 degrees
2 degrees
4 degrees
6 degrees
-2 degrees
-4 degrees
-6 degrees

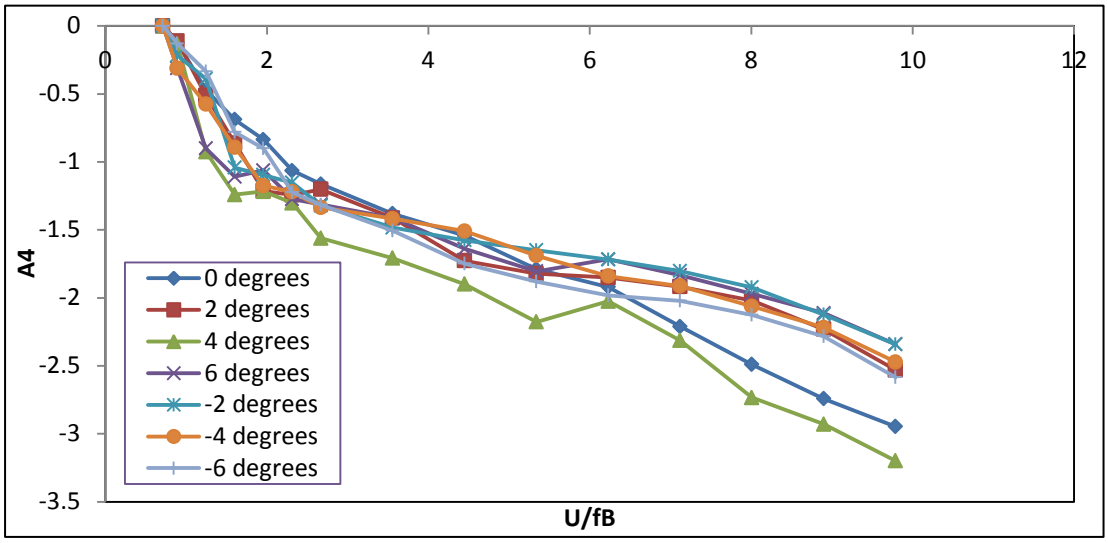

Figure 4.4.1 Flutter derivatives of 30 mm high windshield barrier case in the range of attack angles of -6° to 6°

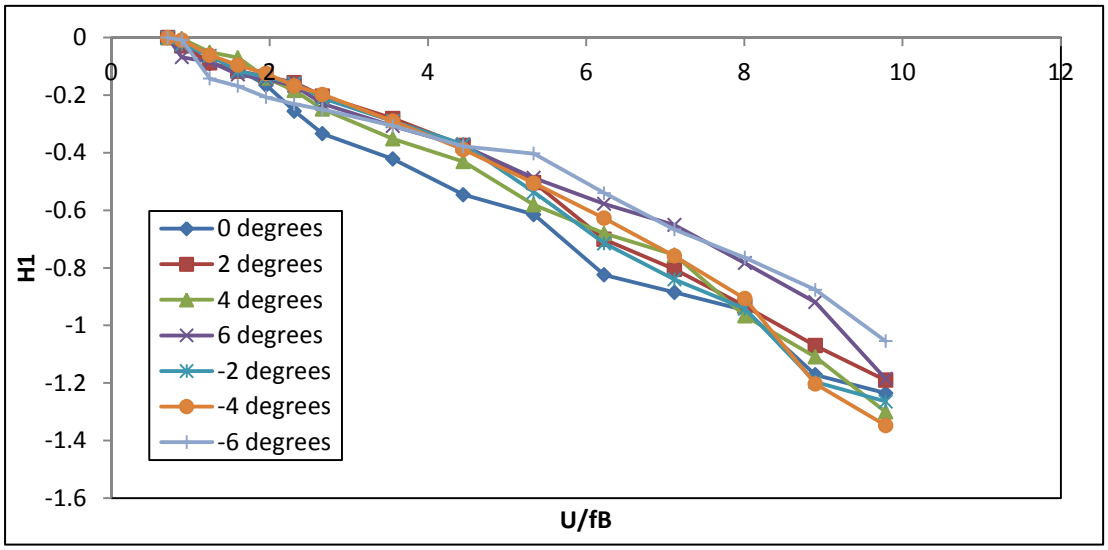

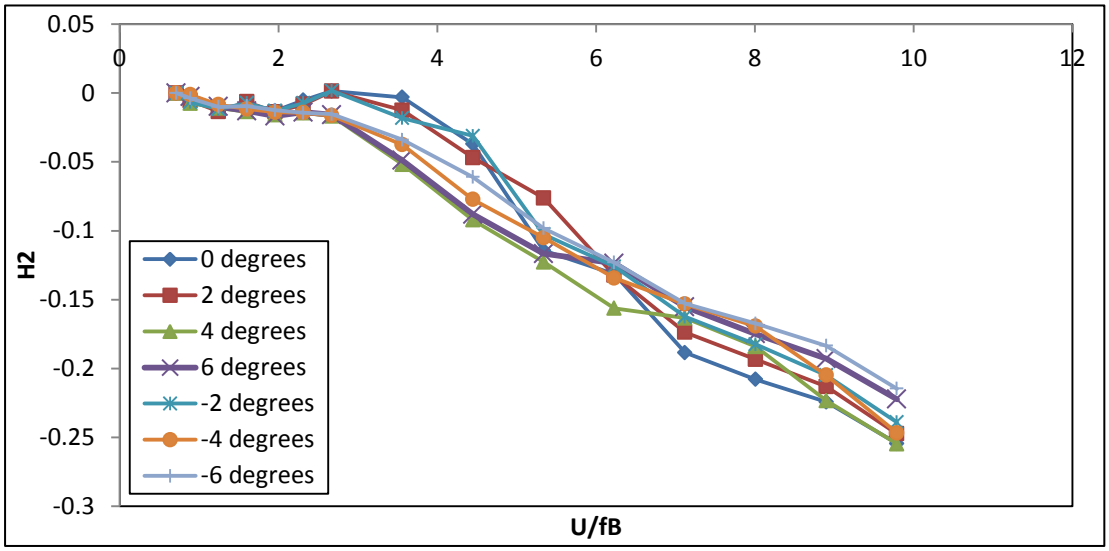
0.05
0
-0.05
-0.1
-0.15
-0.2
-0.25
-0.3
0
2
4
6
8
10
12
H2
U/fB
0 degrees
2 degrees
4 degrees
6 degrees
-2 degrees
-4 degrees
-6 degrees

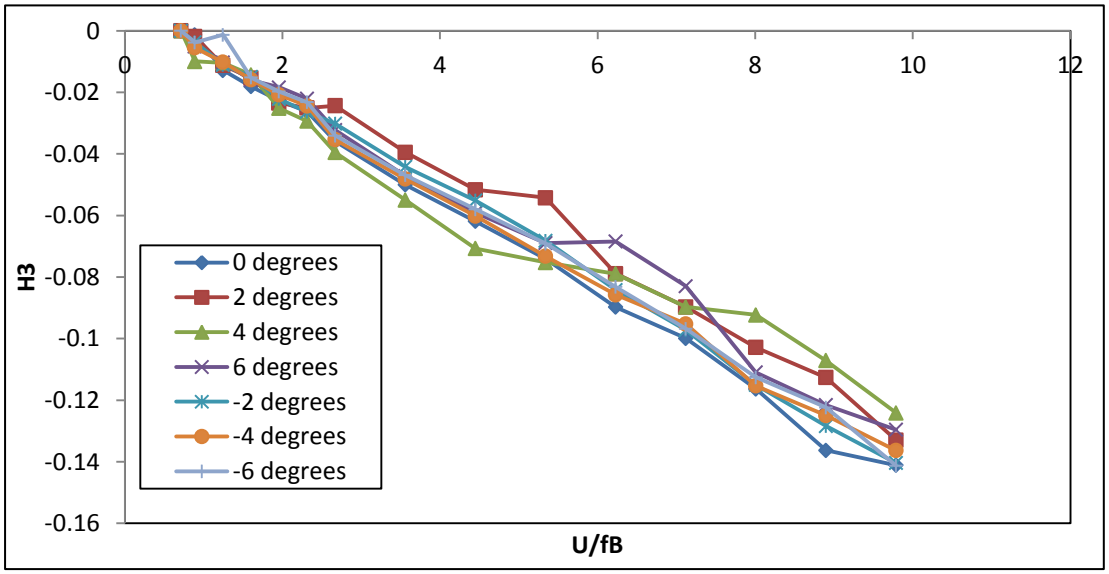
0
-0.02
-0.04
-0.06
-0.08
-0.1
-0.12
-0.14
-0.16
0
2
4
6
8
10
12
H3
U/fB
0 degrees
2 degrees
4 degrees
6 degrees
-2 degrees
-4 degrees
-6 degrees

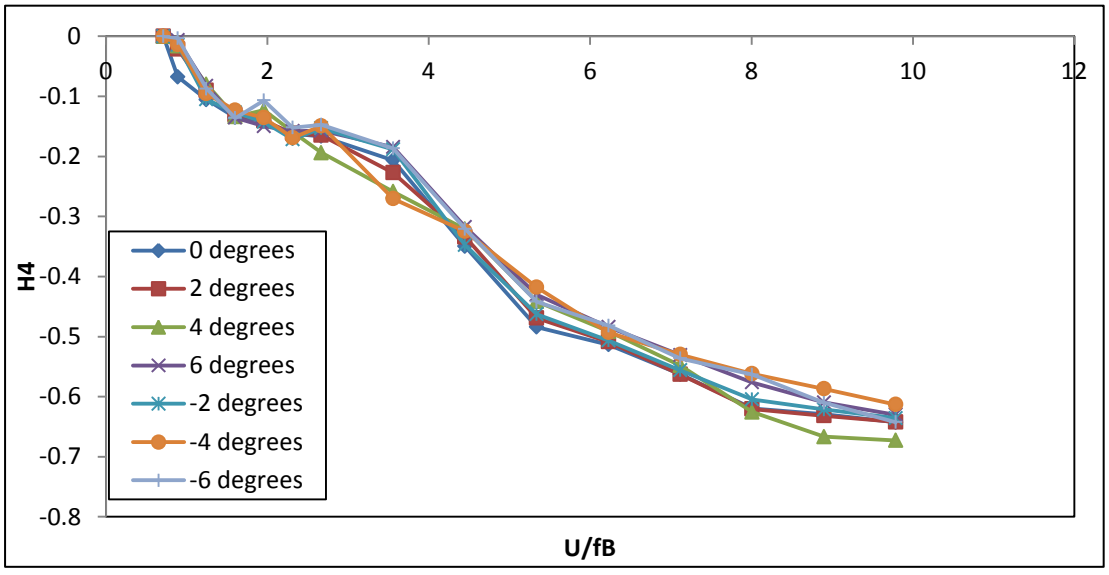
0
-0.1
-0.2
-0.3
-0.4
-0.5
-0.6
-0.7
-0.8
0
2
4
6
8
10
12
H4
U/fB
0 degrees
2 degrees
4 degrees
6 degrees
-2 degrees
-4 degrees
-6 degrees

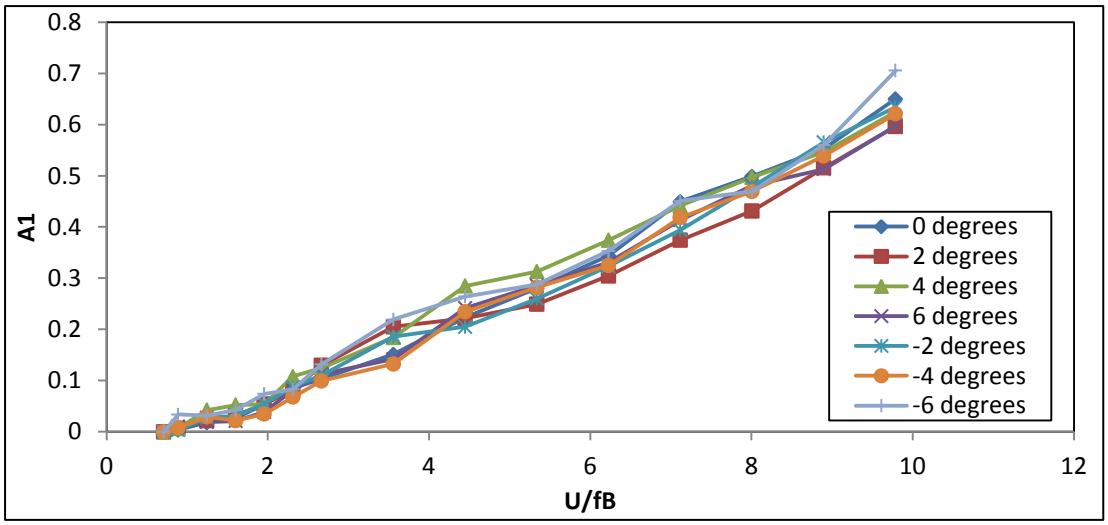
A1
U/fB
0 degrees
2 degrees
4 degrees
6 degrees
-2 degrees
-4 degrees
-6 degrees

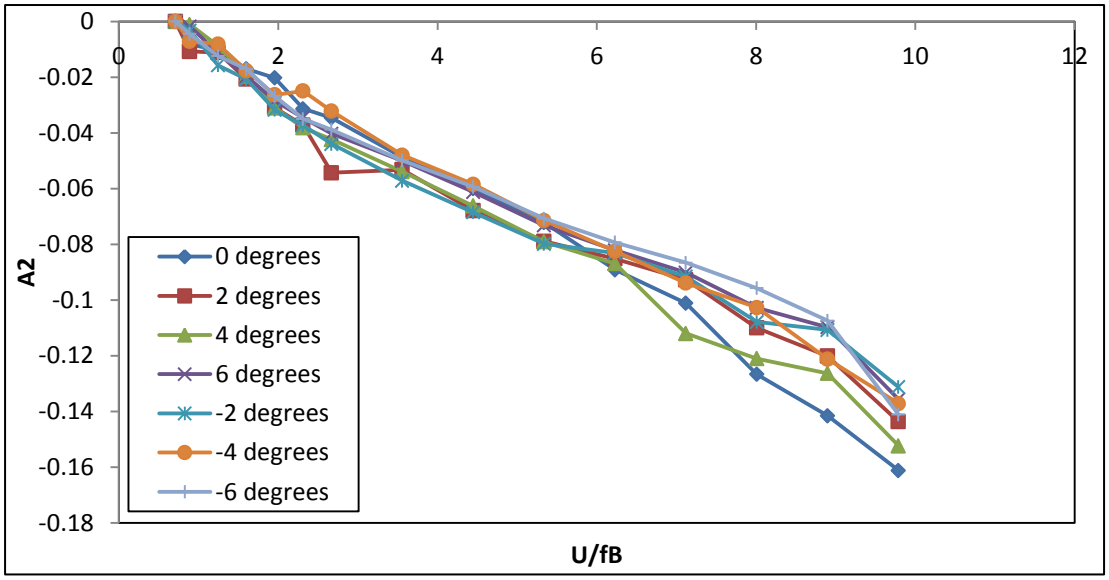
A2
U/fB
0 degrees
2 degrees
4 degrees
6 degrees
-2 degrees
-4 degrees
-6 degrees

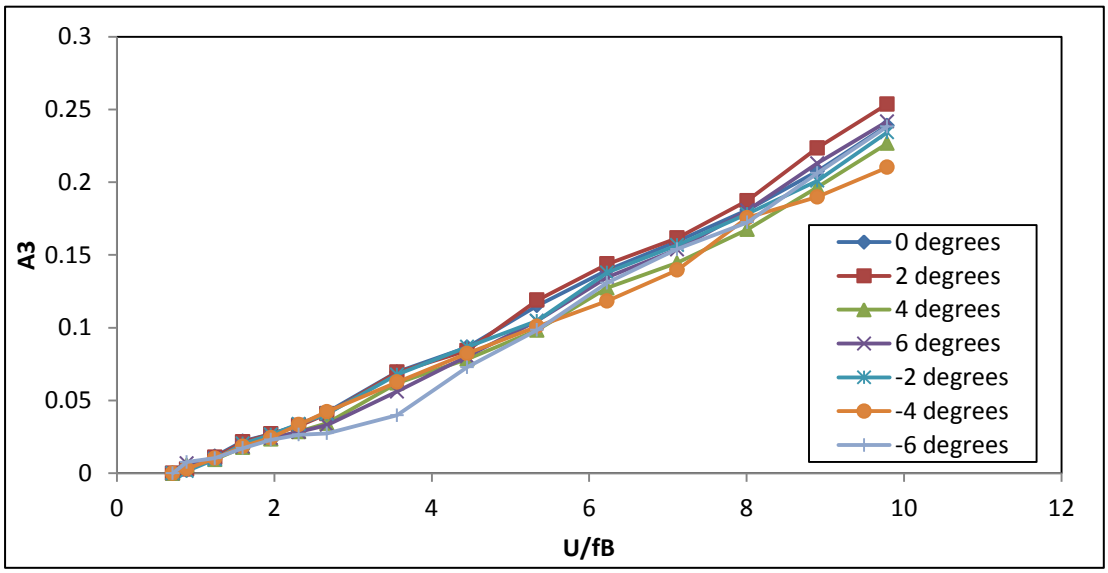
A3
U/fB
0 degrees
2 degrees
4 degrees
6 degrees
-2 degrees
-4 degrees
-6 degrees

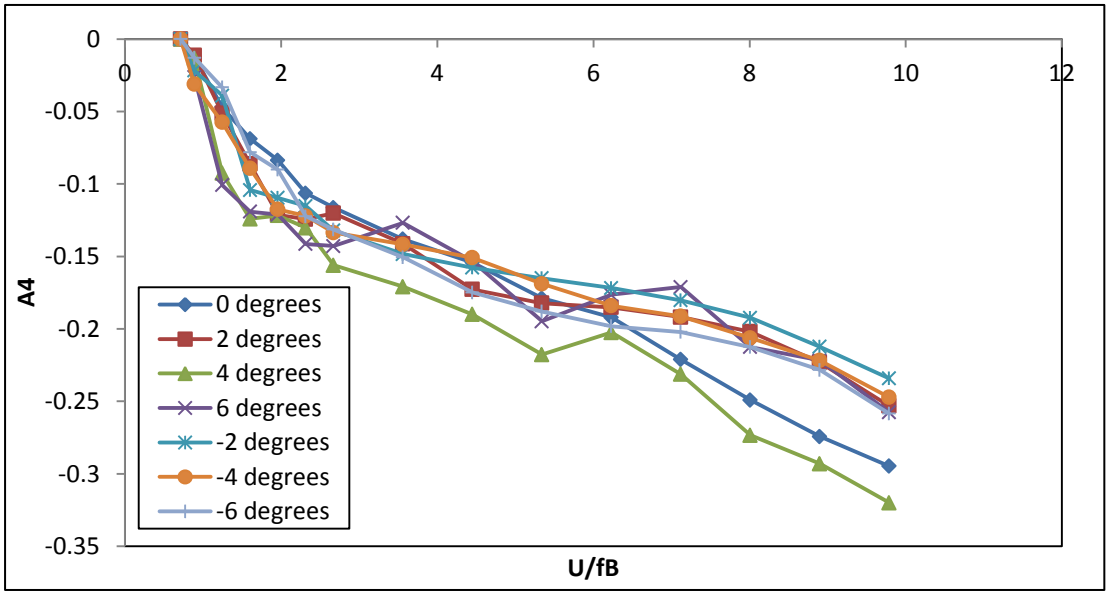

Figure 4.4.2 Flutter derivatives of 50 mm high windshield barrier case in the range of attack angles of -6° to 6°

Figures 4.4.1 and 4.4.2 present the flutter derivatives of the 30 mm and 50 mm high windshield barrier cases, in the range of attack angles of -6° to 6°, respectively. For the Megane Bridge deck model, the absolute values of all eight flutter derivatives have a general increasing trend, as the reduced wind speed increases. Among the eight flutter derivatives, H_2^*, H_4^* and A_4^* showed more variation along the general increment or decrement trends. For both heights of windshield barrier cases, H_2^* decreased and then increased in the range of reduced wind speed between 0 and 2.8; after that, the values of H_2^* decreased until the max reduced wind speed of 9.8. H_4^* of both windshield barrier cases had a similar trend with H_2^*, but the increasing part, in the range of 2 to 3 reduced wind speed, was not apparent. Moreover, for the reduced wind speed from 0.6 to 9.8, A_4^* had the largest variation range of values (3 units) while H_3^* has the smallest variation range (0.14 units). It was also found that, for the reduced wind speed over 2, the curves of A_4^* were uneven, compared with the other flutter derivatives, but overall the values were still increased as the reduced wind speed increases. Particularly it was worth mentioning that A_1^* of 30 mm and 50

mm high windshield barrier cases showed relatively compact curves, which suggested that the difference for different attack angles was very small; in other words, the angle of attack did not affect much the values of A_1^* compared with the other flutter derivatives. In general, it could be concluded that (1) there was no obvious trend of increment or decrement for the values of the flutter derivatives when the angle of attack changed; and (2) the angle of attack affects the variation range of flutter derivatives, especially for A_4^*, while — the influence on A_1^* was the smallest.

4.4.2 Comparison for different heights of the windshield barrier

It was concluded from above section 4.4.1 that angle of attack has a small effect on the flutter derivatives. To determine the most efficient windshield dimensions for mitigation of aerodynamic effects, the comparison of the results for different windshield barrier height cases were used and the effect on the flutter derivatives was discussed.

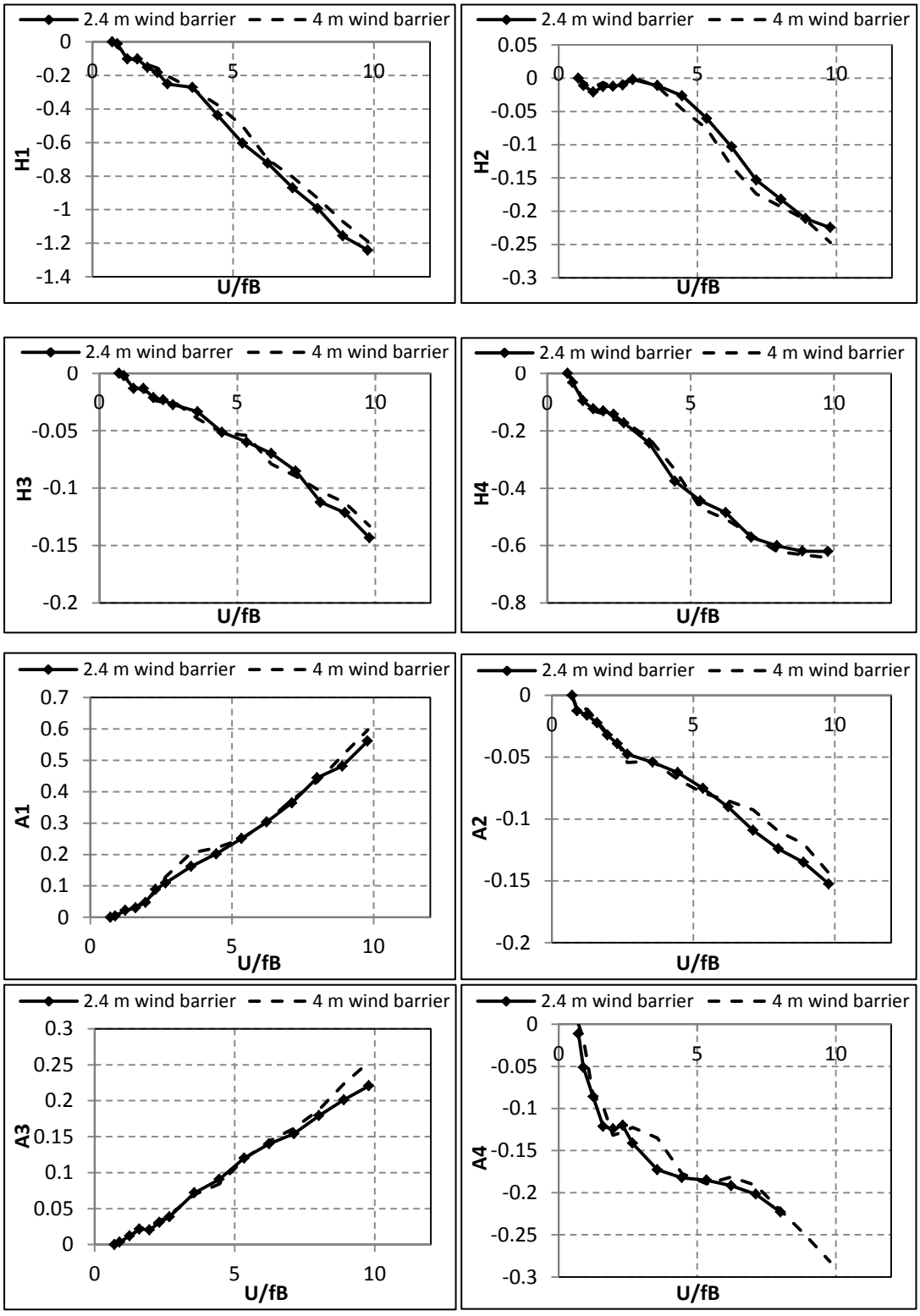

Figure 4.4.3 Flutter derivatives of the 30 mm and 50 mm high windshield barrier cases at attack angle of 2°

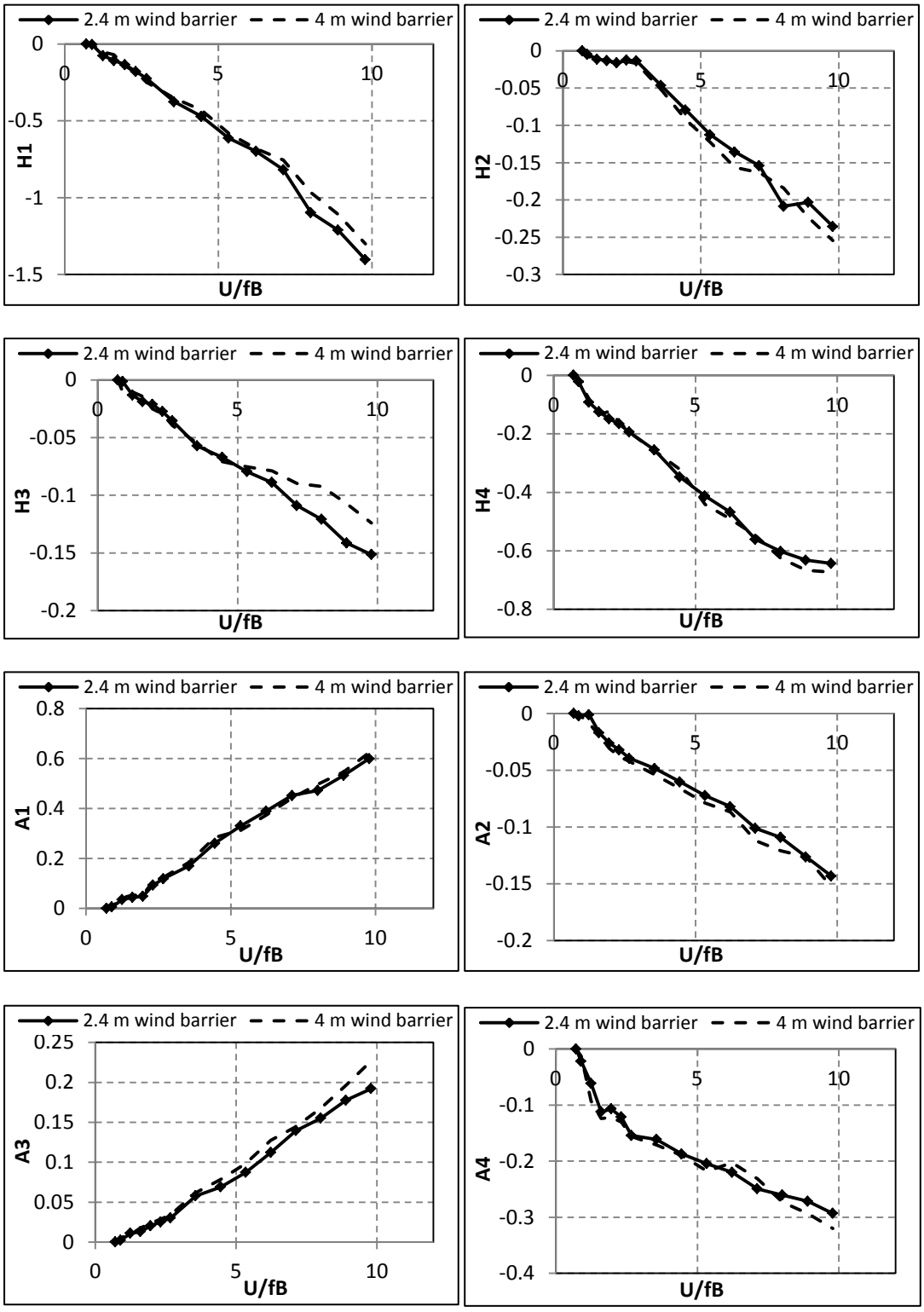

Figure 4.4.4 Flutter derivatives of the 30 mm and 50 mm high windshield barrier cases at attack angle of 4°

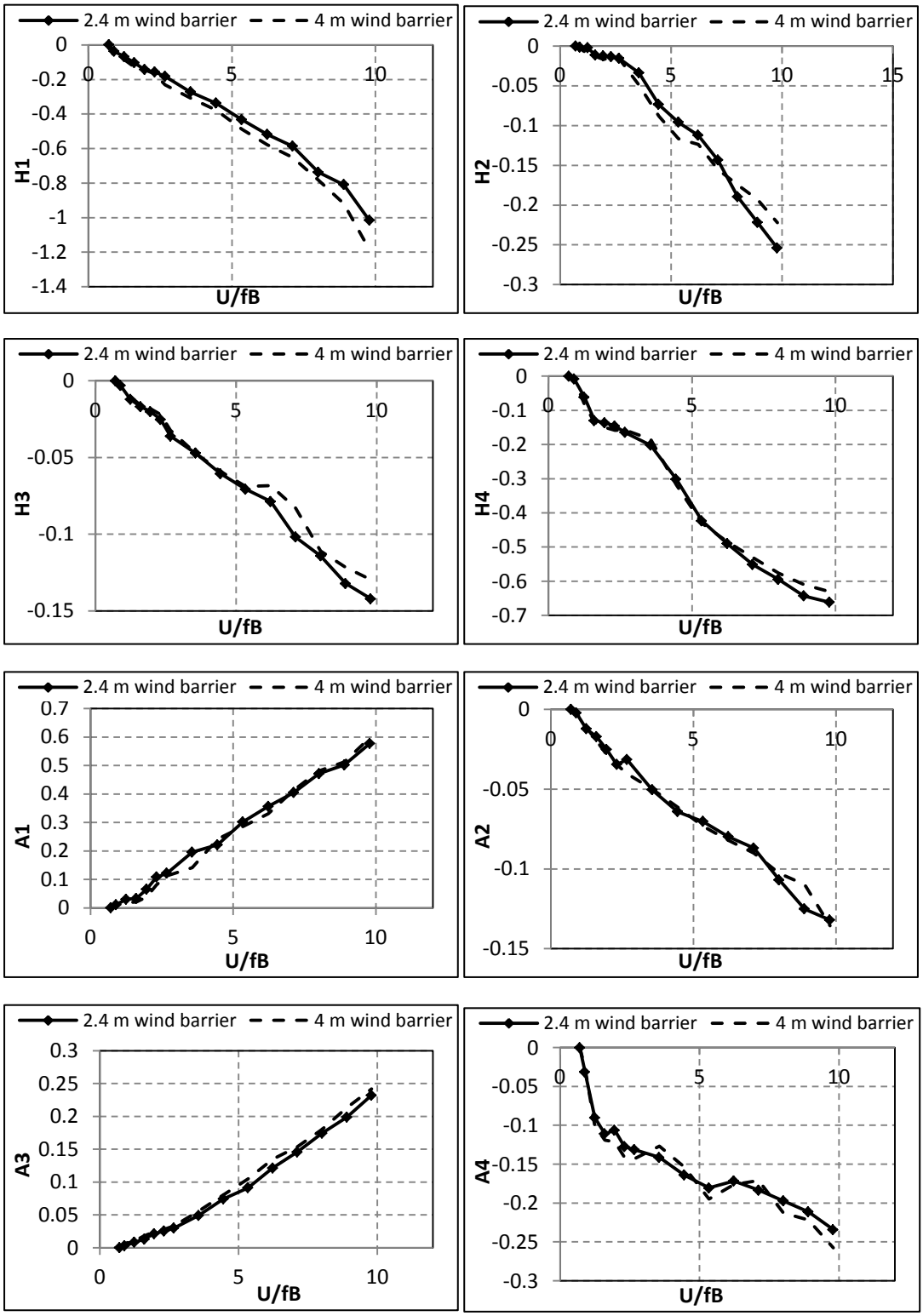

Figure 4.4.5 Flutter derivatives of the 30 mm and 50 mm high windshield barrier cases at attack angle of 6°

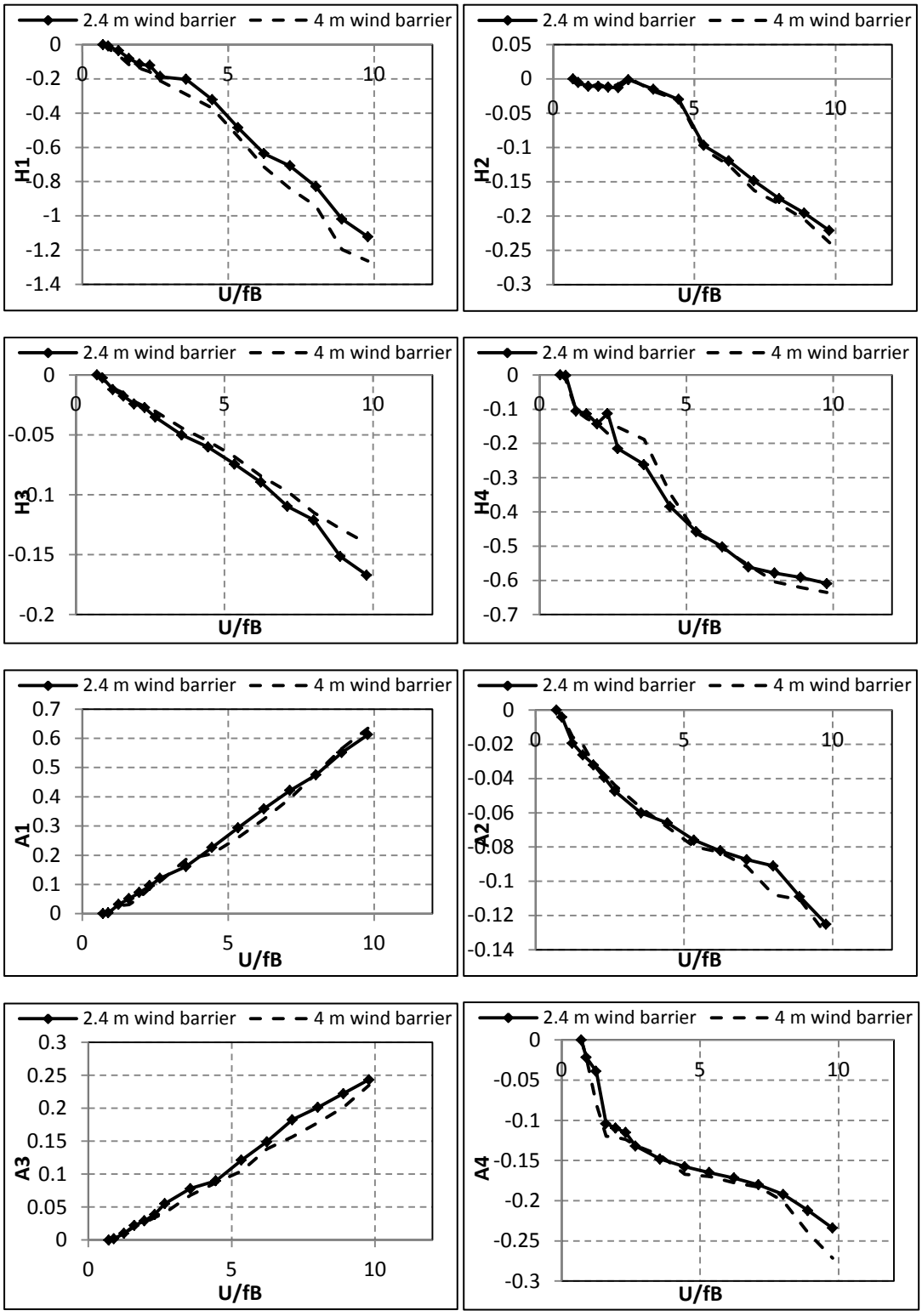

Figure 4.4.6 Flutter derivatives of the 30 mm and 50 mm high windshield barrier cases at attack angle of -2°

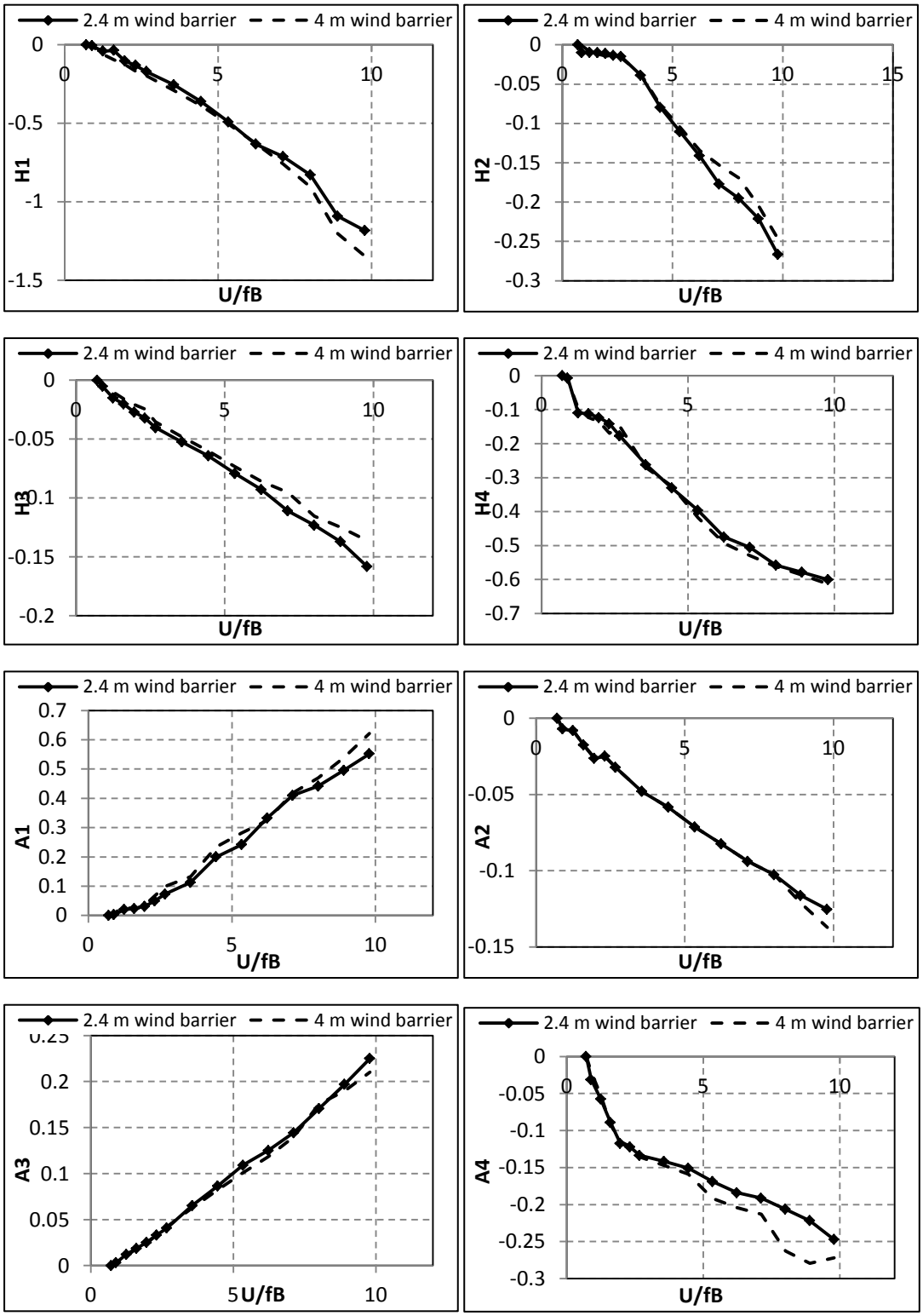

Figure 4.4.7 Flutter derivatives of the 30 mm and 50 mm high windshield barrier cases at attack angle of -4°

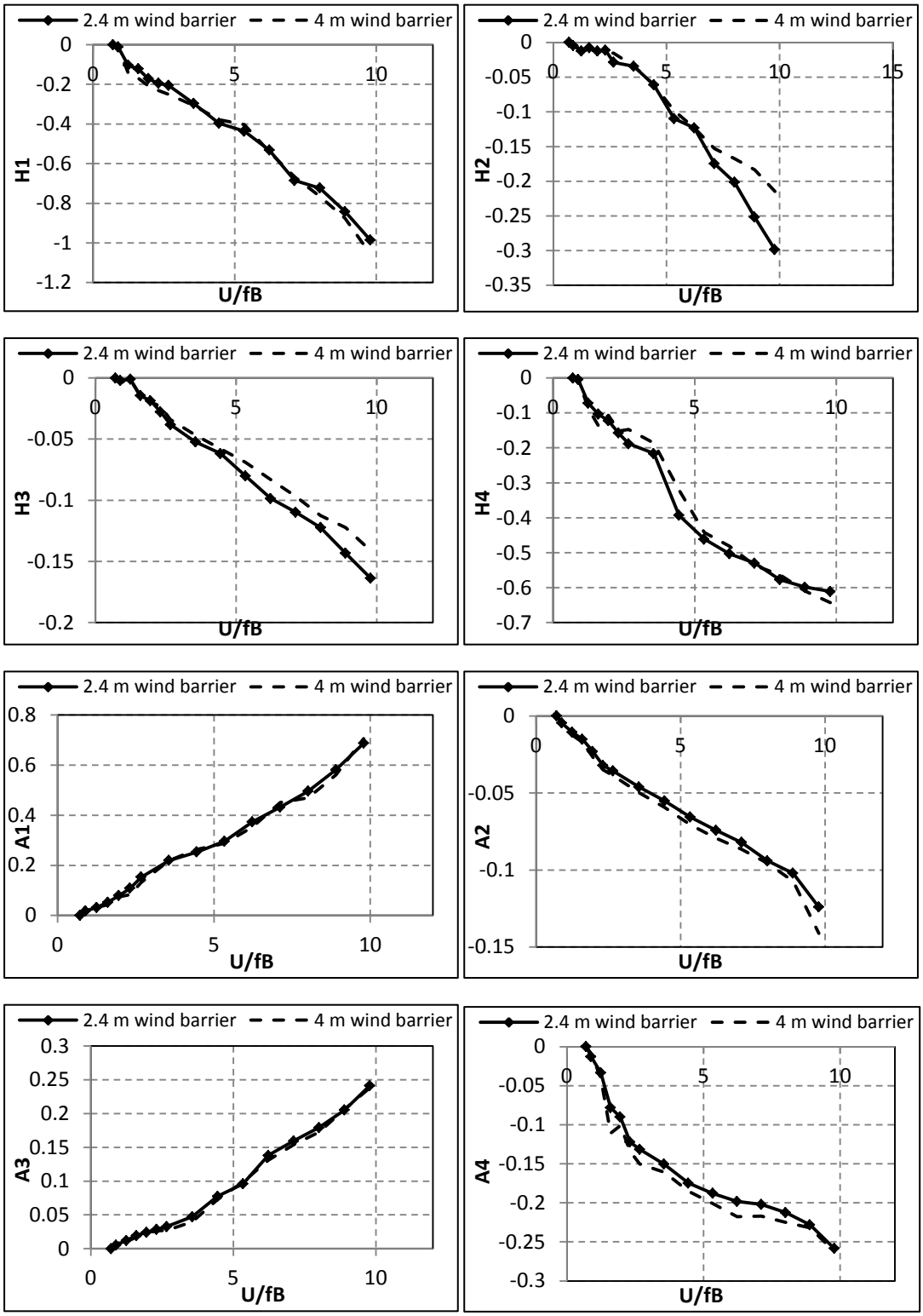

Figure 4.4.8 Flutter derivatives of the 30 mm and 50 mm high windshield barrier cases at attack angle of -6°

Figures 4.4.3 to 4.4.8 presented the variation of all eight flutter derivatives for 30 mm

and 50 mm high windshield barriers as the reduced wind speeds changed in the range of attack angles of -6°, -4°, -2°, 2°, 4° and 6°; the flutter derivatives variation for 0° were plotted in Figures 4.4.1. In order to make the description for the variation of all eight flutter derivatives clear, the direct flutter derivatives (H_1^*, H_4^*, A_2^* and A_3^*) and the cross-flutter derivatives (H_2^*, H_3^*, A_1^* and A_4^*) were discussed one by one below:

H_1^*: The curve representing for flutter derivative H_1^* of the 30 mm high windshield barrier case was higher than that of 50 mm high windshield barrier case for the attack angles of 0°, 2° and 4°, but was below the curve of 50 mm high windshield barrier case for the attack angles of 6°, -2° and -4°. The two curves matched well with each other at the attack angle of -6°. Considering that the value of H_1^* was related to the aerodynamic damping in the vertical direction, and the non-uniform condition indicated that the shape of the Megane Bridge deck model and the height of the windshield barrier should have a simultaneous effect on the incoming wind flow, which leads to uncertainty of aerodynamic damping changing.

H_4^*: In comparison to H_1^*, H_4^* presented a regular relationship between the two windshield barrier cases; curves of both windshield barriers were close to each other except for the case of attack angle of -6°. The absolute values of the 30 mm high windshield barrier curve were slightly higher in the range of reduced wind speed between 2.9 and 6.2. Therefore, changing the height of the edge windshield barrier did not affect significantly the values of H_4^*.

A_2^*: The negative values of A_2^* demonstrated that the aerodynamic damping in the torsion direction had to be positive. Among all eight flutter derivatives, an obvious result showed that different heights of the windshield barrier on the edge did not have a direct influence on parameter A_2^*. The two curves registered for each attack angle condition were extremely close to each other, especially for 0° and -4° for which — they almost coincide.

A_3^*: A_3^* presented the influence of the uncoupled aerodynamic stiffness on the frequency and damping parameters. The two trends of 30 mm and 50 mm high windshield barrier cases were basically the same for 0°, -4° and -6°. The A_3^* values for the low windshield barrier line were lower than that of the high windshield barrier line for the attack angles of 4° and 6°; similarly, this showed an opposite trend when the attack angle was -2°.

H_2^*: H_2^* indicated that the torsional damping in the coupled motion vibration showed an uneven decreasing trend as the wind speed increases. The values decreased at first, and then increased in the range of low reduced wind speed between 0 and 3.2 for all attack angles, where 0° and -2° had the most obvious increment particularly that the value of H_2^* even reached positive value (0.0014 and 0.0013, respectively). Unlike the other flutter derivatives, where the difference was within 0.03 between two points at the same reduced wind speed, the case for the attack angle of -6° showed a different evolution. For the reduced wind speeds from 6 to 9.8, the difference between two curves increased from 0.001 at reduced wind speed of 5.3 to 0.08 at reduced wind speed of 9.8.

H_3^*: H_3^* is the flutter derivative parameter corresponding to the lift force resulted from the torsional motion. According to the figures shown above, H_3^* presented the smallest variation range and values among the eight flutter derivatives. The H_3^* curve presented for the 30 mm high windshield barrier case always stayed below the curve of the 50 mm high windshield barrier case, except for the attack angles of 0° and 2°, where the two curves interweaved with each other.

A_1^*: The third cross-flutter derivative A_1^* was related to the vertical motion in the coupled vibration. The two evolution curves for A_1^* of both windshields investigated cases had good agreement with each other, the largest difference between the two windshield barrier cases was 0.027, which was much smaller compared with the

variation range (average 0.6) of this flutter derivative in the range of the reduced wind speeds of 0.6 to 9.8.

A_4^*: A_4^* expressed some relationship with the pitching moment component of the vertical motion in the coupled vibration, which also means there's relevance between A_4^* and A_1^*. The trend curves for 30 mm high windshield barrier and 50 mm high windshield barrier cases interweaved each other below a reduced wind speed of 0.52, and then the difference of the two curves increased as the reduced wind speed increased. Except for the attack angle of -6°, the two curves interweaved together until the maximum reduced wind speed of 9.8, but do not separately decreased as for the other cases.

4.4.3 Comparison with the Theodorsen's thin plate theoretical results and with multiple-box deck without windshield barrier results

In order to clarify the appropriateness of the currently obtained results, the Theodorsen's thin plate theory [22] presented by Simiu and Scanlan was used as an examining approach for the approximate prediction. The theoretical values of the flutter derivatives calculated by using Theodorsen's thin plate theory might have some differences from the experimental results obtained for the Megane Bridge deck, because Theodorsen's thin plate theory was designed for thin plate or streamlined structures, such as airfoil or thin rectangular decks, however the Megane Bridge deck is a combination of four airfoils connected. Moreover, the numerous bridges constructed lately, have different and complex geometrical shapes of the bridge deck cross-sections, thus Theodorsen's thin plate theory can only be used for potential predictions of some of the flutter derivatives. For the current experimental object, the same procedure has been carried out to identify the similarity and the difference between the results extracted from Theodorsen's thin plate theory and ILS method.

The theoretical flutter derivatives of Theodorsen's thin plate theory can be expressed as [22]:

$$H_1^*(K) = -\frac{2\pi}{K} \cdot F(K)$$

$$H_2^*(K) = -\frac{\pi}{2K} \cdot \left[1 + \frac{4 \cdot G(K)}{K} + F(K)\right]$$

$$H_3^*(K) = -\frac{\pi}{K^2} \cdot \left[2 \cdot F(K) - \frac{G(K) \cdot K}{2}\right]$$

$$H_4^*(K) = -\frac{\pi}{2} \cdot \left[1 + \frac{4 \cdot G(K)}{K}\right]$$

$$A_1^*(K) = \frac{\pi}{K} \cdot F(K)$$

$$A_2^*(K) = -\frac{\pi}{2K^2} \cdot \left[\frac{K}{4} - G(K) - \frac{K \cdot F(K)}{4}\right]$$

$$A_3^*(K) = -\frac{\pi}{2K^2} \cdot \left[\frac{K^2}{32} + F(K) - \frac{K \cdot G(K)}{4}\right]$$

$$A_4^*(K) = -\frac{\pi}{2K} \cdot G(K) \tag{4.7}$$

where $F(K)$ is the real part of the Theodorsen function $C(K)$, $G(K)$ is the imaginary part of $C(K)$, and K is the reduced frequency, which has been mentioned in Chapter 3.

$$C(K) = F(K) + i \cdot G(K) \tag{4.8}$$

where the real and imaginary parts of $C(K)$ can be presented as [46]:

$$F(K) = \frac{0.500502 \cdot K^3 + 0.512607 \cdot K^2 + 0.210400 \cdot K + 0.021573}{K^3 + 1.035378 \cdot K^2 + 0.251239 \cdot K + 0.021508} \quad (4.9)$$

$$G(K) = -\frac{0.000146 \cdot K^3 + 0.122397 \cdot K^2 + 0.327214 \cdot K + 0.001995}{K^3 + 2.481481 \cdot K^2 + 0.934530 \cdot K + 0.089318} \quad (4.10)$$

In order to observe the impact of the aerodynamic properties produced by the height of the windshield barriers, the flutter derivatives calculated based on the above comprising formulations and based on the ILS identification performed for the current experiment are added to the relevant results obtained by Wang [15] who performed the aerodynamic experimental and CFD research on the aerodynamic shape of the Megane Bridge deck without windshield barriers. Firstly, the results of the eight flutter derivatives of the 30 mm high windshield barrier and of the 50 mm high windshield barrier cases extracted from the experimental results recorded for the Megane Bridge deck at attack angle of 0° are used to compare with the results calculated by using the Theodorsen's thin plate theory and with the referenced experimental case of the deck without windshield barrier [15].

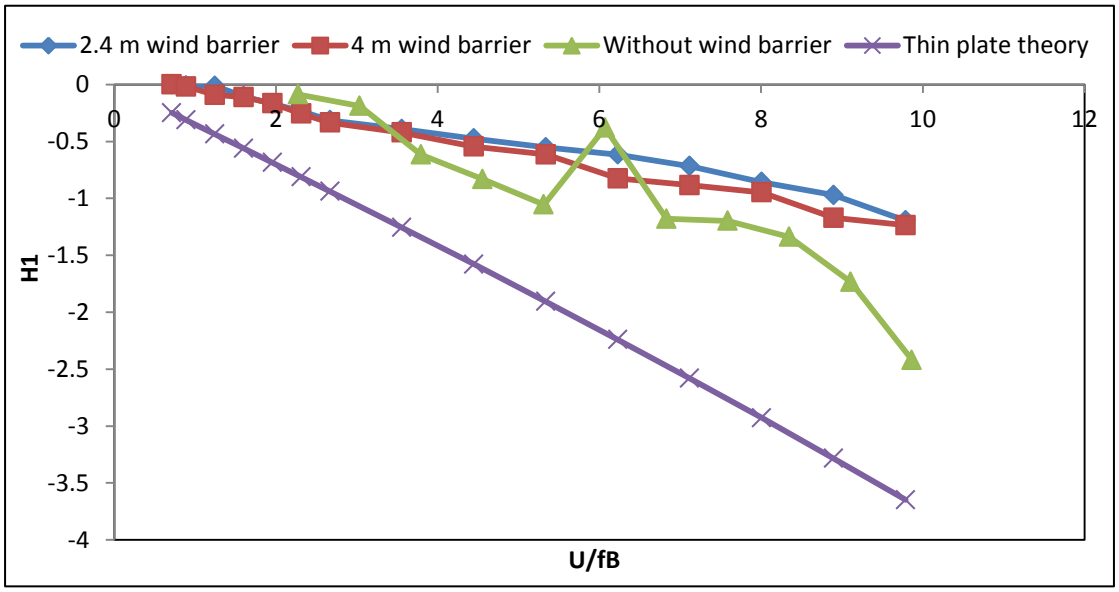

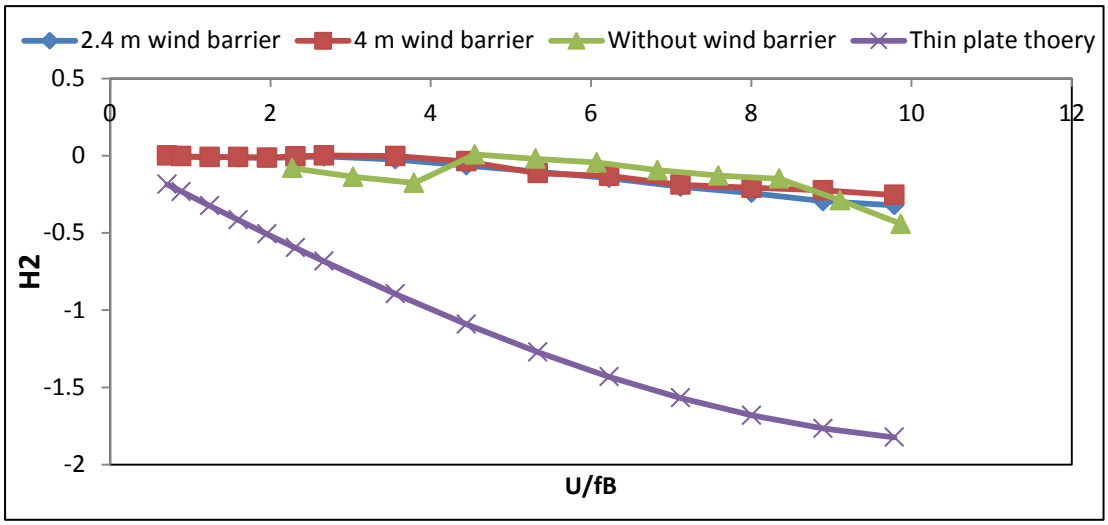
2.4 m wind barrier
4 m wind barrier
Without wind barrier
Thin plate thoery
0.5
0
-0.5
-1
-1.5
-2
0
2
4
6
8
10
12
H2
U/fB

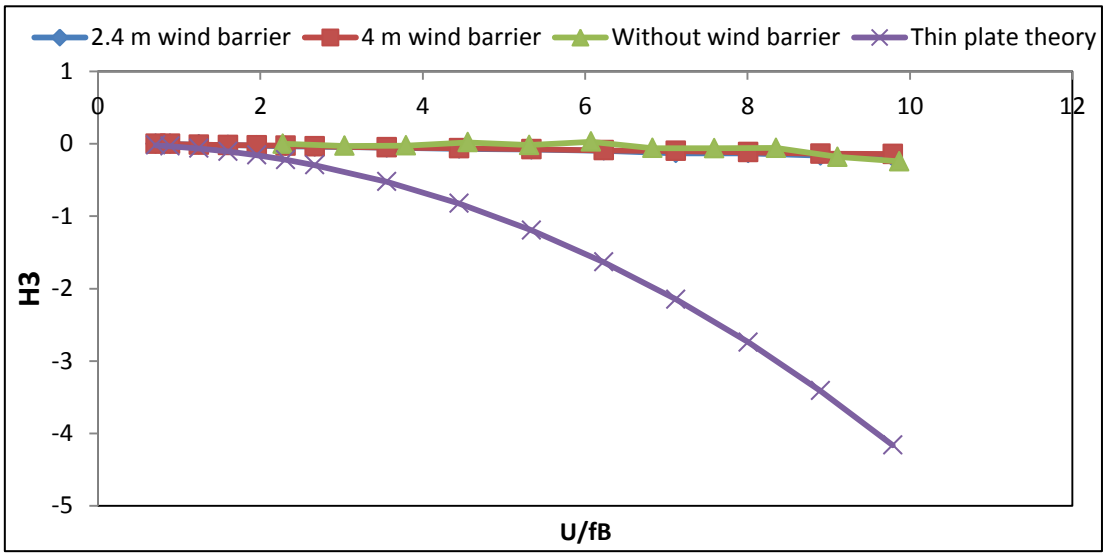
2.4 m wind barrier
4 m wind barrier
Without wind barrier
Thin plate theory
1
0
-1
-2
-3
-4
-5
0
2
4
6
8
10
12
H3
U/fB

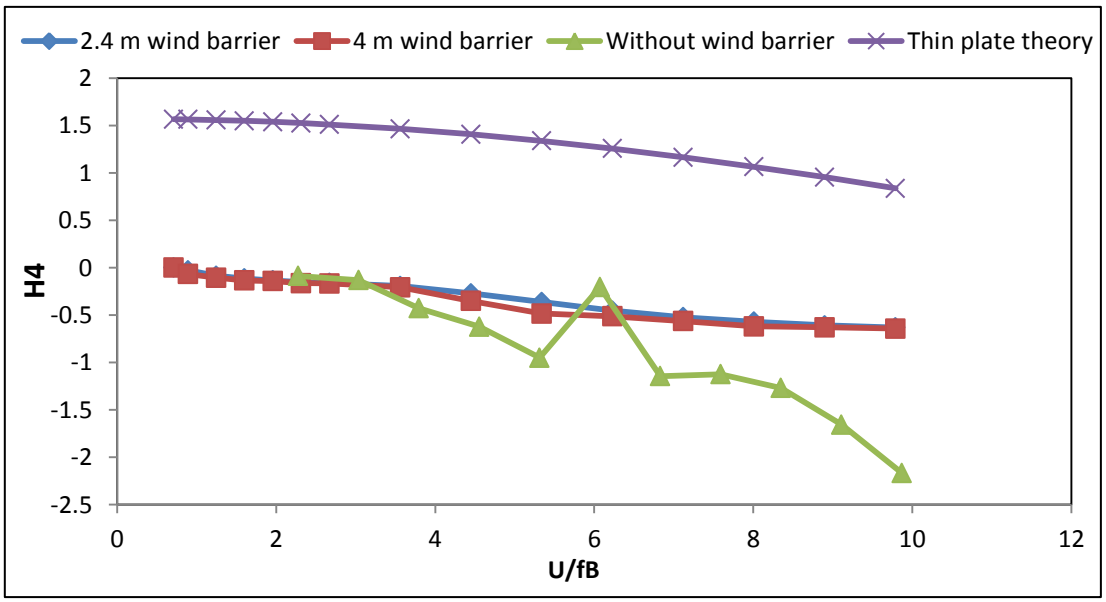
2.4 m wind barrier
4 m wind barrier
Without wind barrier
Thin plate theory
2
1.5
1
0.5
0
-0.5
-1
-1.5
-2
-2.5
0
2
4
6
8
10
12
H4
U/fB

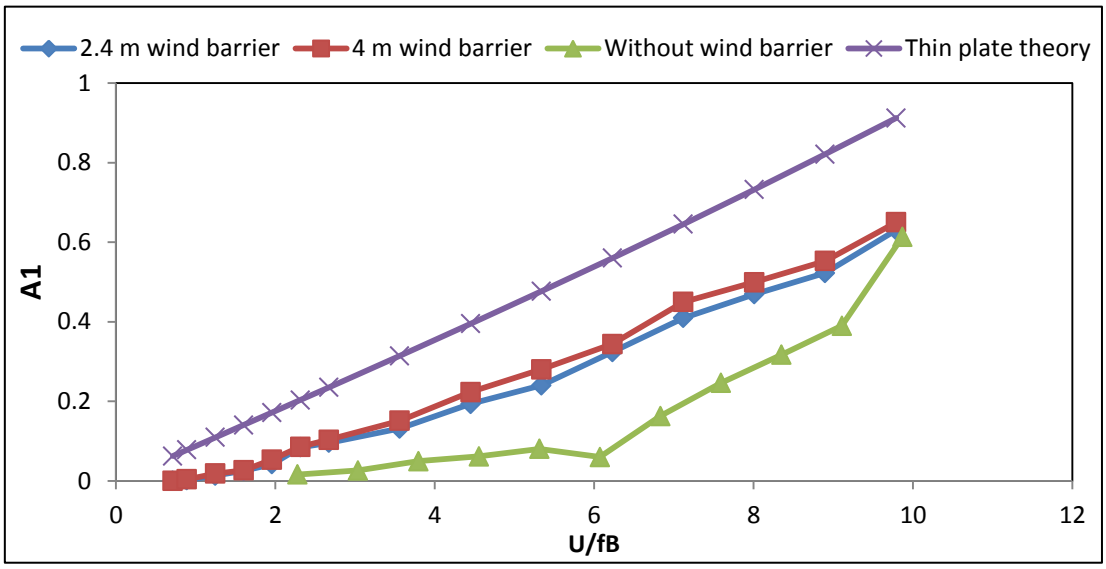
2.4 m wind barrier
4 m wind barrier
Without wind barrier
Thin plate theory
A1
U/fB
0
0.2
0.4
0.6
0.8
1
0
2
4
6
8
10
12

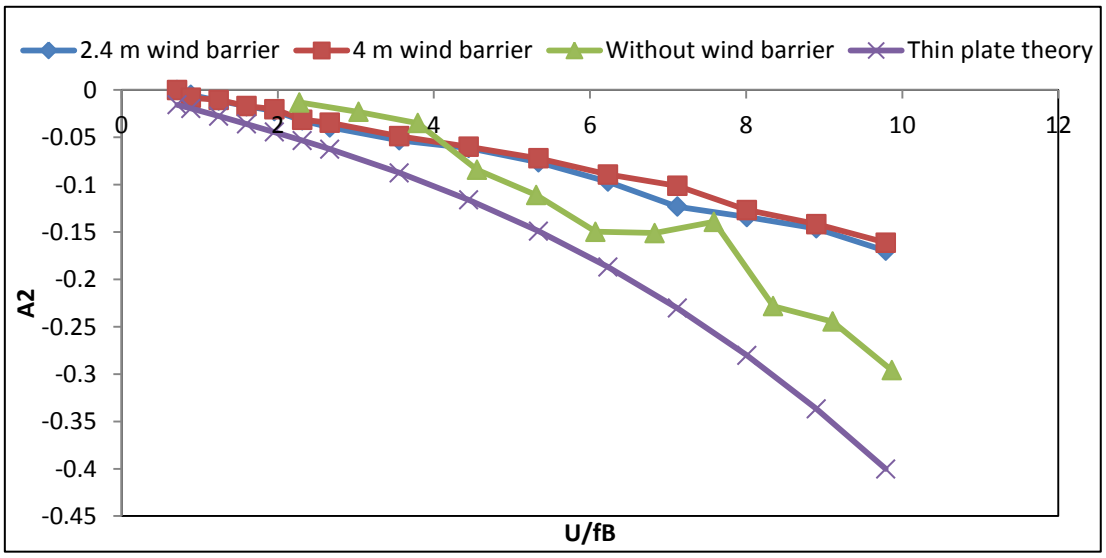
2.4 m wind barrier
4 m wind barrier
Without wind barrier
Thin plate theory
A2
U/fB
0
-0.05
-0.1
-0.15
-0.2
-0.25
-0.3
-0.35
-0.4
-0.45
0
2
4
6
8
10
12

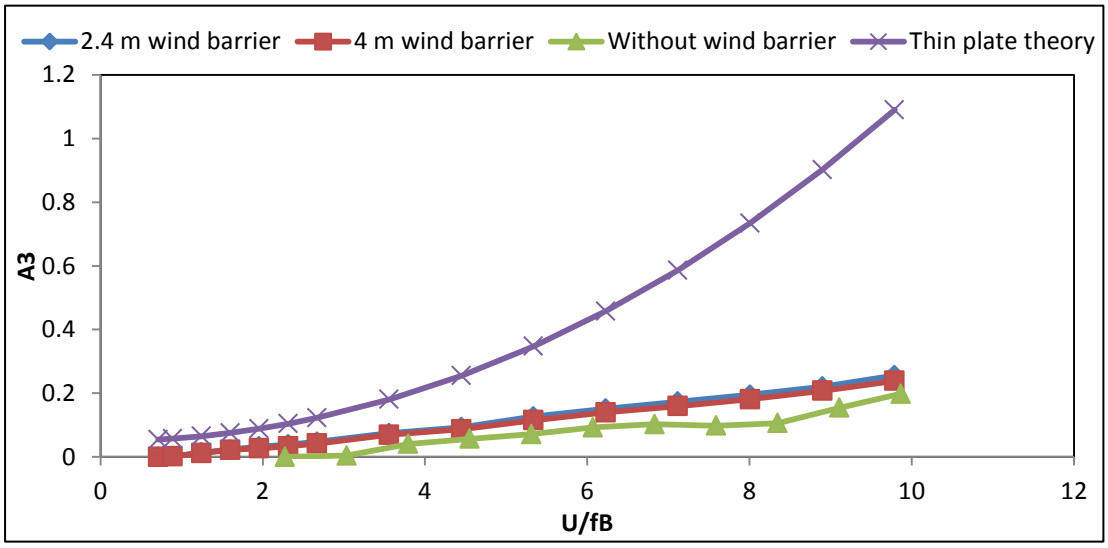
2.4 m wind barrier
4 m wind barrier
Without wind barrier
Thin plate theory
A3
U/fB
0
0.2
0.4
0.6
0.8
1
1.2
0
2
4
6
8
10
12

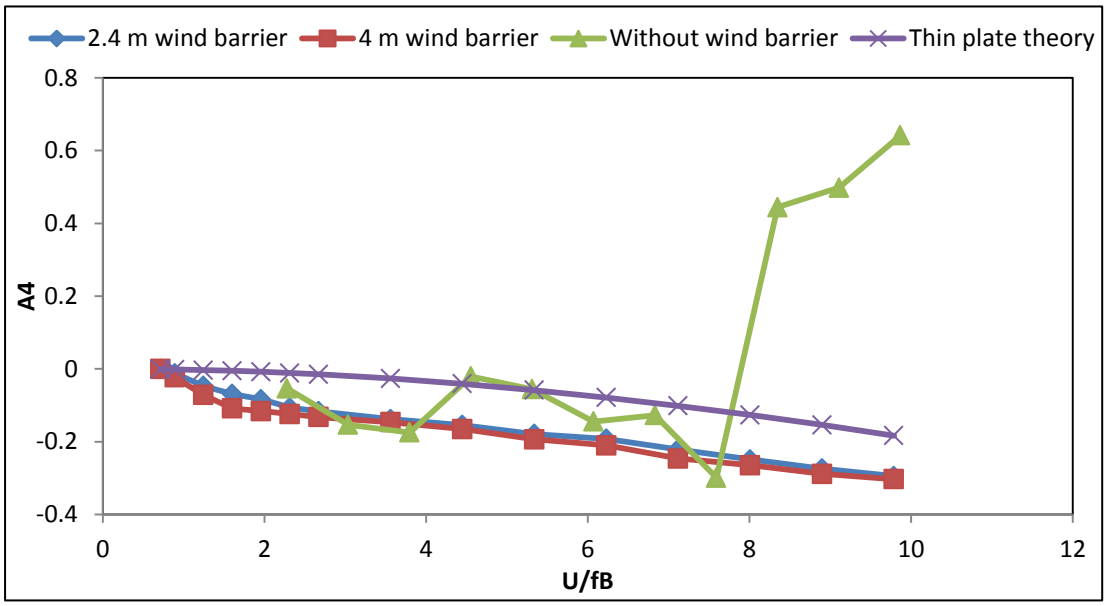

Figure 4.4.9 Flutter derivatives of 30 mm high windshield barrier case, 50 mm high windshield barrier case, without windshield barrier case [15] and Theodorsen's thin plate theory.

As it can be seen in Figure 4.4.9, the eight flutter derivatives extracted from the experimental results of the Megane Bridge multiple-box deck with 30 mm and 50 mm high windshield barriers, showed similar trends with the theoretical results calculated by Theodorsen's thin plate theory. However, the values of the flutter derivatives H_1^*, H_2^*, H_3^* and A_3^* obtained from the Theodorsen's thin plate theory, were higher than the experimental results of different windshield barrier cases, for all the each reduced wind speeds investigated. For H_1^*, the value around 6 for the without windshield barrier case presents a sudden increase, and then meet a sudden decrease again, which shows weird when considering the continuous trend, this might because of some technical reason in the experiment. The values of H_4^*, A_1^*, A_2^* and A_4^* resulting from the Theodorsen's thin plate theory were always below the experimental results. Besides, with the increment of the reduced wind speed, the discrepancy between the experimental results and the Theodorsen's theoretical results increased obviously for H_1^*, H_3^*, A_2^*, A_3^* and A_4^*. The evolution with reduced wind speed of the eight flutter derivatives for the two cases, the 30 mm high windshield barrier and the 50 mm high

windshield barrier cases, were very close to each other, especially for the angle of attack of 0°; specifically, the results of H_2^*, H_3^*, H_4^* and A_3^* of the two windshield barrier cases, almost coincided in the range of the tested wind speed. The values of H_1^*, A_1^* and A_4^* had comparative trends, in the sense that the curve of the 30 mm high windshield barrier case was higher than 50 mm high windshield barrier for H_1^* and A_4^*, but lower than 50 mm high windshield barrier case for A_1^*. Comparing the experimental results with the data referenced from the experimental results obtained by Wang [15] for the aerodynamic deck of the Megane Bridge, without windshield barrier case, it was noticed that the H_2^*, H_3^* and A_3^* results matched well for all three cases. However, the experimental results of the flutter derivative A_4^* presented a big discrepancy when compared with the results obtained from the multiple-box deck without windshield barrier case, and the same discrepant condition happens for the results of H_4^*, but the difference was not as large as for A_4^*.

4.4.4 Comparison with other bridge decks

In order to identify the discrepancy and similarity of the aerodynamic properties of the four-box deck of the Megane Bridge, it was necessary to compare the flutter derivatives with those reported for other kinds of box girder bridge decks. In addition, the influence induced by different numbers of boxes composing the bridge decks might affect the overall aerodynamic properties of the suspension bridge. Therefore, the experimental results of the flutter derivatives of the Messina Bridge (triple-box deck) [78][84], the Stonecutters Bridge (twin-box deck) [55] and the Great Belt Bridge (single-box deck) [54] for the attack angle of 0° were collected and shown in Figure 4.4.10 as follows:

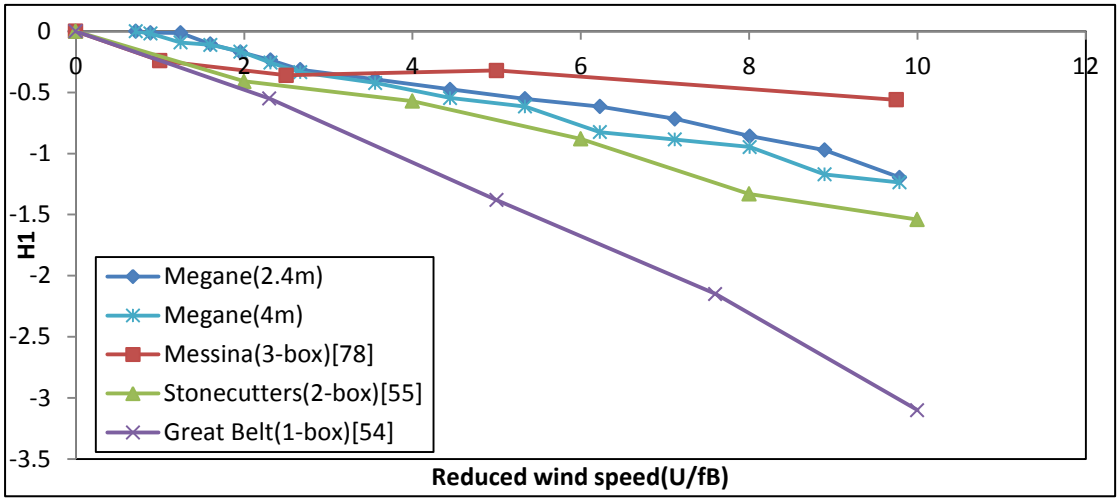
H1
Reduced wind speed(U/fB)
Megane(2.4m)
Megane(4m)
Messina(3-box)[78]
Stonecutters(2-box)[55]
Great Belt(1-box)[54]

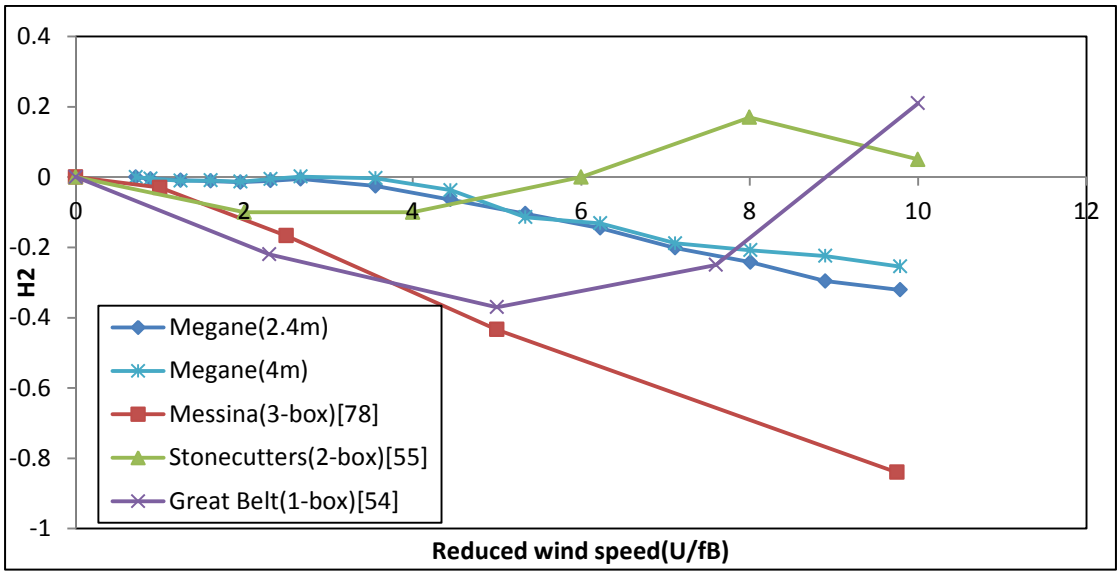
H2
Reduced wind speed(U/fB)
Megane(2.4m)
Megane(4m)
Messina(3-box)[78]
Stonecutters(2-box)[55]
Great Belt(1-box)[54]

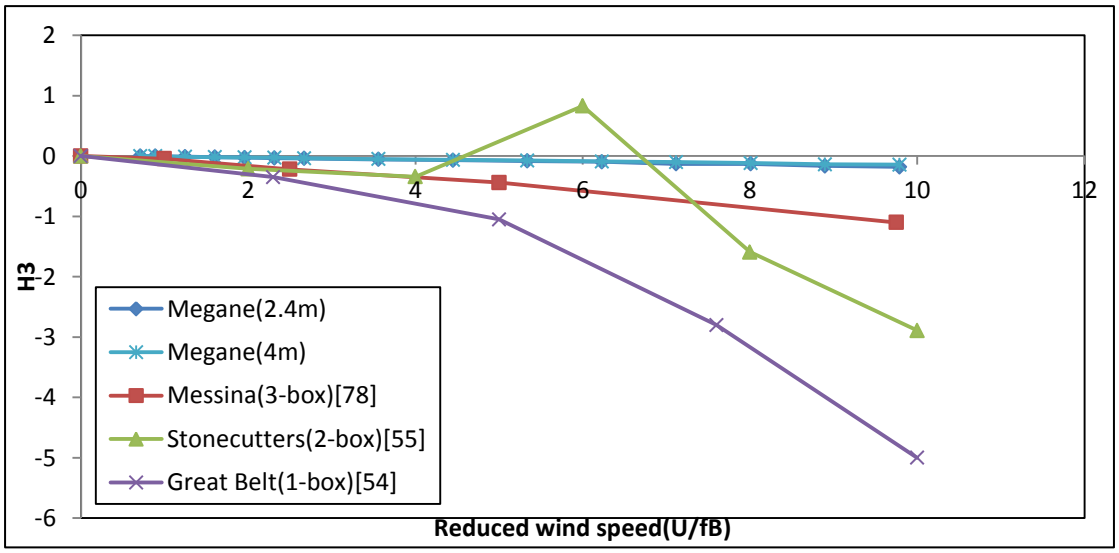
H3
Reduced wind speed(U/fB)
Megane(2.4m)
Megane(4m)
Messina(3-box)[78]
Stonecutters(2-box)[55]
Great Belt(1-box)[54]

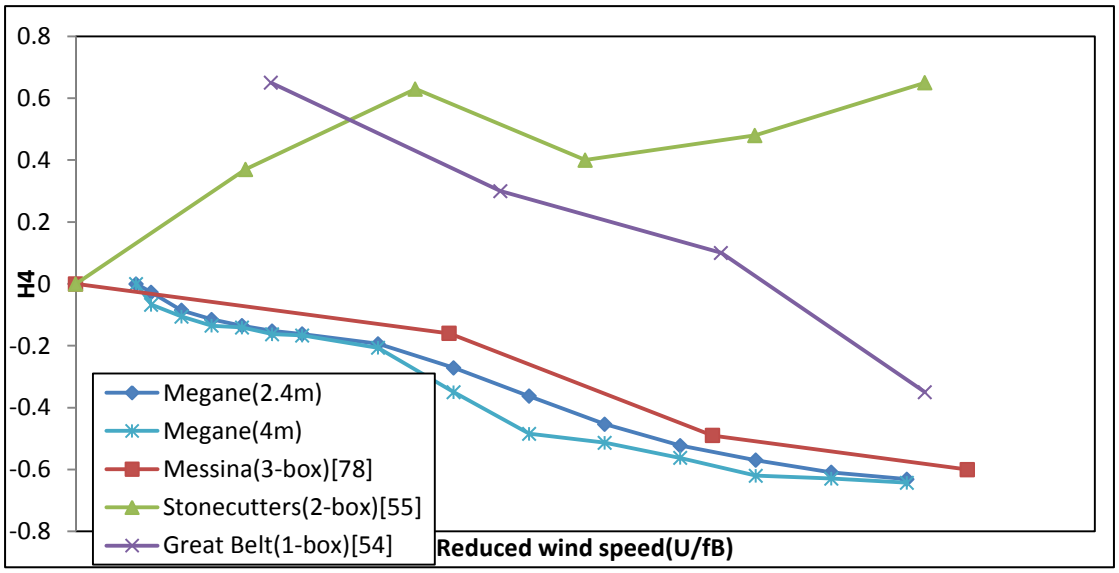
0.8
0.6
0.4
0.2
0
-0.2
-0.4
-0.6
-0.8
H4
Megane(2.4m)
Megane(4m)
Messina(3-box)[78]
Stonecutters(2-box)[55]
Great Belt(1-box)[54]
Reduced wind speed(U/fB)

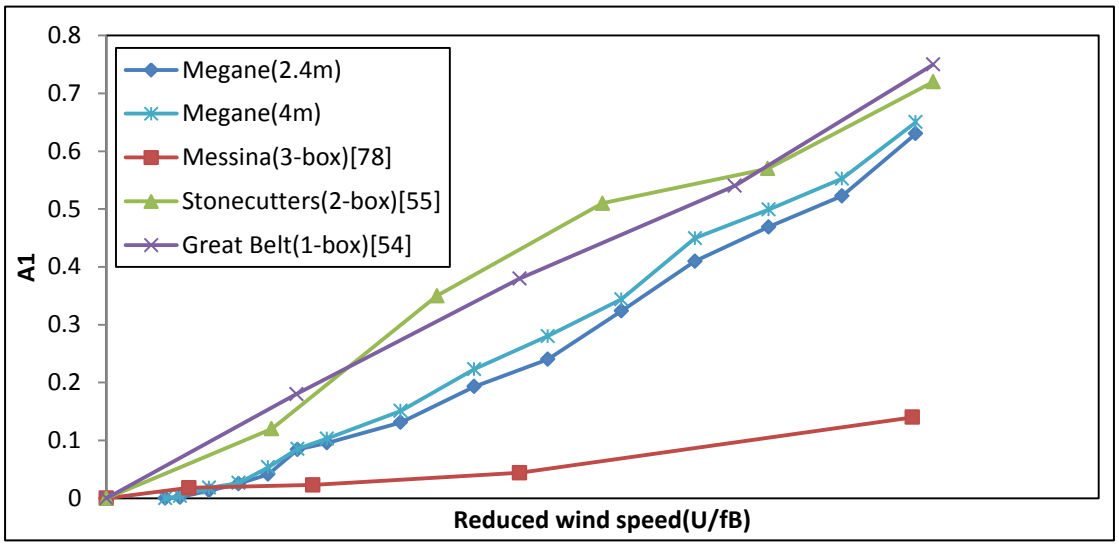
0.8
0.7
0.6
0.5
0.4
0.3
0.2
0.1
0
A1
Megane(2.4m)
Megane(4m)
Messina(3-box)[78]
Stonecutters(2-box)[55]
Great Belt(1-box)[54]
Reduced wind speed(U/fB)

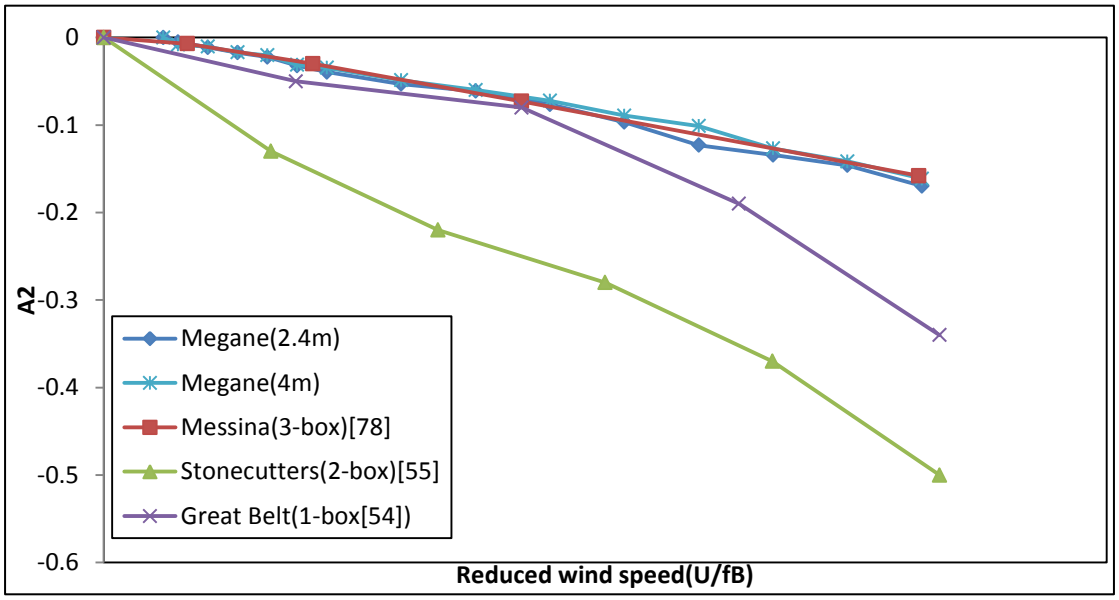
0
-0.1
-0.2
-0.3
-0.4
-0.5
-0.6
A2
Megane(2.4m)
Megane(4m)
Messina(3-box)[78]
Stonecutters(2-box)[55]
Great Belt(1-box[54])
Reduced wind speed(U/fB)

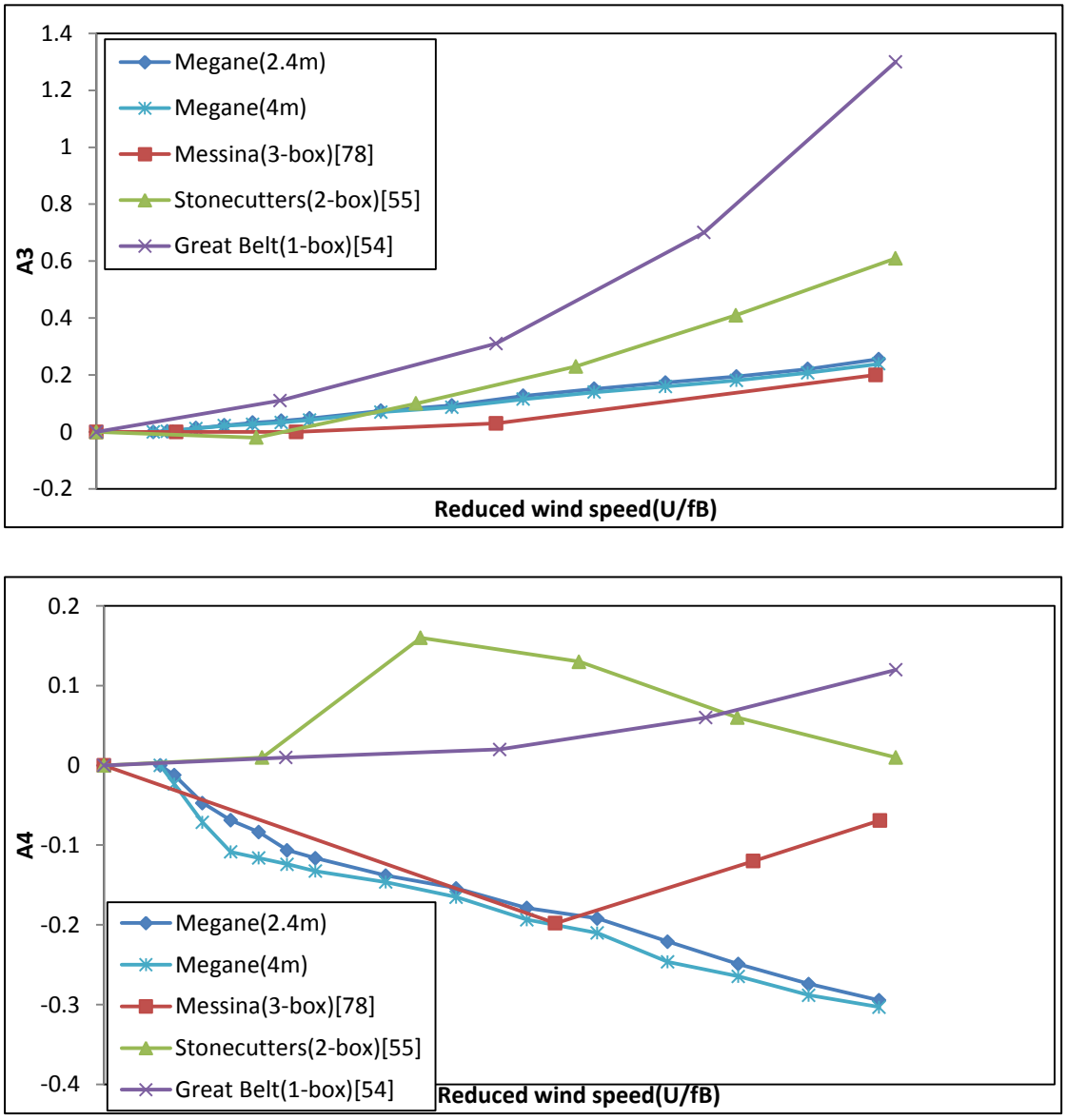

Figure 4.4.10 Flutter derivatives of the Megane Bridge deck with 30 mm and 50 mm windshield barriers, the Messina Strait Bridge deck [78][84], the Stonecutters Bridge deck [55] and the Great Belt Bridge deck [56]

As seen from Figure 4.4.10, it was evident that the numbers of boxes composing the girder decks of the above mentioned bridges, had an influence on the aerodynamic properties of the respective suspension bridges. For the direct-flutter derivatives, H_1^*, H_4^*, A_2^* and A_3^*, there was noticed that all the direct-flutter derivatives of the Megane Bridge deck showed good agreement with that of the Messina Strait Bridge deck; also it should be noted that the geometry of these two bridge decks were somehow similar

(have similar principle of multiple gaps). Besides, only the H_1^* values of the Stonecutters Bridge deck and the A_2^* values of the Great Belt Bridge deck had some similarity with that of the Megane Bridge deck or the Messina Strait Bridge deck; the other flutter derivatives indicated large discrepancies from the three-deck and four-deck bridges. In other words, for the one-degree-of-freedom vibration motions, only the four-box girder bridge deck of the Megane Bridge, matched well with the three-box deck girder bridge of the Messina Strait Bridge, thus grouping them in a distinct category of multiple-box bridge decks.

Due to the fact that the cross-flutter derivatives, H_2^*, H_3^*, A_1^* and A_4^* can be obtained only through coupled motion vibration, these parameter's evolution for the Megane Bridge and for the Messina Strait Bridge were unlike the evolution of the direct-flutter derivatives, which present more or less discrepancies between them. Take one of the most obvious discrepancies for A_2^*, for example: the difference between the value of H_2^* corresponding to the same reduced wind speed increased from 0 to approximately 0.5, which was much larger than the relevant values for any of the direct-flutter derivatives. For H_2^*, it showed big differences between the four kinds of bridges that values of the Great Belt Bridge deck and the Stonecutters Bridge deck encountered a decreasing trend first and then an increasing to positive values, but the H_2^* values of the Messina Strait Bridge deck and the Megane Bridge deck decreased at all times. In addition, the A_4^* trendlines of the four kinds of bridges were totally different from each other, as the reduced wind speed increased from 0 to 9.8, while the A_4^* values of the Megane Bridge deck decreased from 0 to -0.27. However, the A_4^* values of the Messina Bridge decreased from 0 to -0.2 between 0 and 5.8, and then increased to -0.08 at the reduced wind speed of 9.8. Aside from the Stonecutters Bridge deck and the Great Belt Bridge deck, the two curves presented for A_4^* were even above 0 at all times. In summary, the cross-flutter derivatives of Megane Bridge deck had some similarities on the decreasing or increasing trends with the Messina

Bridge deck except for A_4^*, but showed almost different conditions for the Great Belt Bridge and the Stonecutters Bridge decks.

Section conclusions:

There is no obvious trend of increment or decrement for the values of the flutter derivatives when the angle of attack changes, especially for A_4^*, while — the influence on A_1^* was the smallest. The results of the direct flutter derivatives (H_1^*, H_4^*, A_2^* and A_3^*) prove that the non-uniform geometry of the Megane Bridge deck shape in combination with the height of the windshield barrier have the effect of changing the aerodynamic damping changing. The height of the edge windshield barrier doesn't affect much the aerodynamic damping for the torsional direction and the uncoupled aerodynamic stiffness for the frequency and damping parameters, but it has some influence on the torsional damping and the vertical motion in the coupled motion vibration; the lift force resulted from the torsional motion and the pitching moment component of the vertical motion from the coupled vibration.

By comparing the flutter derivatives in the dynamic tests, it can be concluded that the aerodynamic performance of the triple-box and the four-box bridge decks, when compared with the twin-box and the single-box bridge decks. The direct-flutter derivatives of the triple-box and the four-box bridge decks are very similar, but as the results obtained by comparing the cross-flutter derivatives present, the triple-box girder bridge deck has a slightly better aerodynamic efficiency than the four-box bridge deck. In addition, the height of windshield barrier on the edge does not affect much the aerodynamic flutter instability of the four-box bridge deck as well for different angles of attack.

Chapter 5 Conclusions and Recommendations

5.1 Conclusions

As modern science and technology develops, the new emergent generation of super-long span suspension bridges constructed to meet the needs of the current society, reach more challenging geometrical shapes, but also have smaller damping ratios, which makes the respective bridge structures extremely susceptible to wind-induced effect [85]. The wind resistance becomes a governing factor for evaluating the stability of the long-span suspension bridges, for which the box-girder decks were considered to have better aerodynamic performance when compared with the normal plate girder decks [86]. The new generation of multi-box deck bridges, such as the Stonecutters Bridge (twin-box girder deck) and the Strait of Messina Bridge (three box girder deck), has been introduced in order to satisfy the current requirement of aerodynamic stability for even longer suspension bridges. In the view of the success of the twin-box and three box girder bridges, which reached the remarkable design of 3,000 m length of the main span, the research on a four box girder deck presented in the current research, the Megane Bridge deck, can be regarded as the following step in the development of such long span bridge structures. Wind tunnel experiments have been carried out for verifying the aerodynamic stability of the four box deck and for predicting the aerodynamic flutter derivatives..

The verification of the aerodynamic stability of the bridge deck model is based on two parts: the static aerodynamic force coefficients, which can be calculated by using the results obtained from the static wind tunnel tests and the flutter derivatives which can be extracted from the results of the dynamic wind tunnel tests. Both the static wind tunnel tests and dynamic wind tunnel tests were carried out in the wind tunnel facility

of the Gradient Wind Engineering Inc. which has a test section of 2.1 m width and 1.8 m height. After pre-dimensioning preparation and modification of the bridge deck section model, relevant experimental instrumentation and setup, such as supporting frames, springs, sensors, etc. were bought or borrowed and the experiment steps were designed in order to carry out effectively the wind tunnel tests.

For a two degrees of freedom vibration system, the drag coefficient C_D and the lift coefficient C_L of the section bridge deck model were determined based on the formulas of the quasi-steady aerodynamic forces presented by Simiu and Scanlan (1996) [22] and on the force data measurements obtained from the static wind tunnel test. As mentioned in section 4.1, only the high wind speed corresponding to relatively high Reynolds numbers can be used for obtaining stable results of the two static force coefficients. The aerodynamic drag and lift coefficients, C_D and C_L, obtained experimentally for the aerodynamic shape of the four-box bridge deck, without windshield barriers, for the Messina Strait Bridge (triple-box bridge deck), the Stonecutters Bridge (twin-box bridge deck) and the Great Belt Bridge (single-box bridge deck) were added for comparison. The results showed that the installation of the windshield barriers reduces the values of the lift coefficient C_L for the attack angles in the range of -6° to 6°, which indicates that the windshield barriers can determine a better performance of the overall four-box Megane Bridge deck. On the other hand, the drag coefficient C_D determined for the Megane Bridge deck model with windshield barriers increased in the positive attack angle range and decreased in the negative attack angle range, which means that the windshield barriers can have a good aerodynamic effect mainly for the negative angles of attack. By comparing with other box girder bridge decks, both drag and lift coefficients of the Megane Bridge deck with windshield barriers showed good agreement especially with the three-box deck of the Messina Strait Bridge. In addition, the four-girder bridge deck (Megane Bridge deck) and the triple-girder bridge deck (Messina Strait Bridge deck) showed a

better wind resistant stability than the twin-girder bridge deck (Stonecutters Bridge deck) and the single-girder bridge deck (Great Belt Bridge deck). In general, the installation of the windshield barriers is necessary for increasing the static stability in the direction of lift force. Moreover, the four-box girder bridge deck had similar static properties with the triple-box girder bridge deck. Besides, the Den Hartog stability criterion has been used for checking, based on the static test cases, the possibility of encountering the galloping instability, which proved that the Megane Bridge deck has a good stability against galloping.

As mentioned in Chapter 3, for a 2-DOF vibration system, all eight flutter derivatives were identified, for predicting the aerodynamic stability of the Megane Bridge deck model. Before extracting the flutter derivatives, results obtained from the wind tunnel tests were calibrated in order to calculate the vertical displacements and torsional angles for each vibration case. It was found that, (1) for both 30 mm and 50 mm high windshield barriers, the amplitudes of vertical displacements $D_M(t)$ and rotational angles $\alpha(t)$ have an obvious increasing trend as the wind speed increases; (2) usually for each angle of attack and every wind speed test, the model with 30 mm high windshield barrier showed higher values of $D_M(t)$ and $\alpha(t)$ when compared with the 50 mm high windshield barrier model; (3) when the wind speeds were lower than 4.0 m/s, the values and trends for both $D_M(t)$ and $\alpha(t)$ did not show an obvious difference, for the two windshield barrier models, but the apparent distinctiveness happened usually after 7.0 m/s. (4) the general amplitude followed the quantitative relationship of A(-6°)>A(6°)> A(-4°)>A(4°)> A(-2°)> A(2°)> A(0°), for most of the cases, especially in the high wind speeds range. In summary, 50 mm high windshield barrier model presented a better effect on the wind-induced vibration stability of the Megane Bridge deck then the 30 mm high windshield barrier model.

Among the system identification methods available in the literature, the Iterative

Least Squares (ILS) was selected because (1) extracting the flutter derivatives for combination of different degrees of freedom cases can be calculated by a single computer Matlab code; (2) instead of calculating the eigenvalues and eigenvectors, the system stiffness and damping matrices are calculated from the free-vibration displacement time histories directly; and (3) the parameters identified have a good accuracy, which has been proved numerically and experimentally. By comparing the results of the three four-box decks models, namely the 30 mm high windshield barrier model, 50 mm high windshield barrier model and the model without windshield barriers, with the Theodorsen's thin plate theory, it was found the eight flutter derivatives extracted from 30 mm and 50 mm high windshield barrier cases showed similar trends with the results calculated by Theodorsen's thin plate theory, but had different values. The H_2^*, H_3^* and A_3^* results of the 30 mm and 50 mm high windshield barrier models matched well with the same flutter derivatives of the without windshield barrier model, however the results for A_4^* and H_4^* presented a big discrepancy. The results also showed that the height of the edge windshield barrier doesn't affect much the aerodynamic damping for the torsional direction and the uncoupled aerodynamic stiffness for the frequency and damping parameters, but it had some influence on the torsional damping and the vertical vibration in the coupled motion vibration, the lift force resulting from the torsional motion and the pitching moment component of the vertical motion for the coupled vibration.

In order to identify the discrepancies and similarities of the aerodynamic properties of the four-box girder bridge deck (Megane Bridge deck), the aerodynamic flutter derivatives were compared with other kinds of box girder bridges. The results of the flutter derivatives of the Messina Strait Bridge deck (triple-girder bridge deck), the Stonecutters Bridge deck (twin-girder bridge deck) and the Great Belt Bridge deck (single-girder bridge deck) have been collected for comparison with the experimental results of the Megane Bridge deck. All the direct-flutter derivatives of the Megane

Bridge agreed well with those of the Strait of Messina Bridge, which indicated that the triple-box girder deck and the four-box girder deck are very similar for 1-DOF vibration. On the other hand, the cross-flutter derivatives obtained through coupled motion vibration presented more discrepancies between the triple-box girder bridge and the four-box girder bridge. In addition, the triple-box girder bridge deck and the four-box girder bridge deck have a smoother decreasing or increasing trends for all eight flutter derivatives than the single-box girder bridge deck and the twin-box girder bridge deck.

Finally, it is proved that ILS method can be successfully used for identifying the flutter derivatives of the multi-deck model and the obtained flutter derivatives can be used for the prediction of the aerodynamic stability of the Megane Bridge deck. Also it can be also concluded that the windshield barriers have a good effect on the aerodynamic stability of the deck model investigated and the 50 mm high windshield barrier reduces the wind-vibration amplitudes for the Megane Bridge.

5.2 Recommendations and further studies

For further studies similar or related to the current research, it is recommended that:

1. For the Megane Bridge deck, the 50 mm high windshield barrier is better than the 30 mm high windshield barrier, but more cases of different heights of the windshield barrier can be added, such as height between 30 mm and 50 mm.

2. The windshield barriers in the middle are fixed on the surface of the model, in the current experiment. Some future other research about replacing the middle windshield barriers or changing their height, represent a possible research direction to be studied, in order to find the optimum aerodynamic properties.

Reference

[1] Robert G. Fuller, Charles R. Lang, Roberta H. Lang. Twin views of the Tacoma Narrows Bridge collapse. American Association of Physics Teachers. ISBN 0-917853-95-4. 2000.

[2] K. Yusuf Bilah and Robert H. Scanlan. Resonance, Tacoma Narrows bridge failure, and undergraduate physics textbooks. American Journal of Physics 59 (2),118-124，1991.

[3] Richard Scott. In the Wake of Tacoma: Suspension Bridges and the Quest for Aerodynamic Stability. American Society of Civil Engineers. ISBN 0-7844-0542-5. Jun 2001.

[4] Susan M. Lashomb, Jine-Wen Kou, Edward V.Gant, John T. Dewolf. Study of bridge vibrations for Connecticut. Thesis (M. Sc.)-Joint Highway Research Advisory Council of the University of Connecticut.JHR 85-165, Oct 1985.

[5] Cuixin Liu and Xin Cui, Wind resistant Design of 2800 m long-span suspension Bridge in Japan, Journal of World Bridge, 2009 (3), 12-17.

[6] R. Keith Mobley. Root Cause Failure Analysis. Technology & Engineering, p291.

[7] Ming Gu, Ruoxue Zhang, Haifan Xiang. Identification of flutter derivatives of bridge decks. Journal of Wind Engineering and Industrial Aerodynamics 84 (2000) 151-162.

[8] Zakia Begum. Analysis and behavior investigations of box girder bridges. Thesis--University of Maryland, 2010.

[9] Y.J. Ge, H.F. Xiang. Aerodynamic Challenges of Major Chinese Bridges. IABSE Symposium Report, IABSE Workshop, Shanghai 2009, pp. 142-164(23).

[10] Soon-Deck Kwon, Dong Hyawan Kim, Seung Ho Lee, Ho Sung Song. Design criteria of wind barriers for traffic (Part 1: wind barrier performance). Wind and Structures, Vol. 14, No. 1 55-70, 2011.

[11] Min-Jae Lee. Si-chul Kim, Young-hwa Seo. The Yi Sun-sin Bridge: Innovative Solutions for Suspension Bridges. Structural Engineering International, Volume 22, Number 1, pp. 32-35(4), February 2012.

[12] Leung, Yuen-yee. The Tsing Ma Bridge and urban development in Hong Kong : a post-modern approach. Thesis (M. Sc.)--University of Hong Kong, 2000.

[13] G. Morgenthal, R. Sham, B. West. Engineering the tower and main span construction of Stonecutters Bridge. Journal of Bridge Engineering, Volume 15, Issue 2, March 2010.

[14] Giorgio Diana, Giuseppe Fiammenghi. Wind tunnel tests and numerical approach for long span bridges: the Messina bridge. The Seventh International Colloquium on Bluff Body Aerodynamics and its Applications (BBAA7), Shanghai, China, September 2-6, 2012.

[15] Zhida Wang. Experimental and CFD investigations of the Megane multi-box bridge deck aerodynamic characteristics. Thesis (M.A. Sc.)--Department of Civil

Engineering University of Ottawa, 2015.

[16] Changlin Chen, Peiliang Li, Maochong Shi, Juncheng Zuo, Mengxiang Chen, Haiping Sun. Numerical study of the tides and residual currents in the Qiongzhou Strait. Chinese Journal of Oceanology and Limnology 27:4, pp. 931-942, Nov 2009.

[17] H.F. Xiang, Y.J. Ge. On Aerodynamic Limit to Suspension Bridges. Proc. 11th International Conference on Wind Engineering, Texas, June 2-5, 2003.

[18] Lin, T. Y.; Chow, Philip. Gibraltar Strait Crossing- A Challenge to Bridge and Structural Engineers. Structural Engineering International, Volume 1, Number 2, pp. 53-58(6), May 1991.

[19] Yaojun Ge, Yahui Shao. Aerodynamic flutter prediction for super long span suspension bridges. The 12th Americas Conference on Wind Engineering (12ACWE), Seattle, Washington, USA, June 16-20, 2013.

[20] Felix Nieto , Santiago Hernández , Ibuki Kusano , José Á. Jurado. CFD aerodynamic assessment of deck alternatives for a cable-stayed bridge. The Seventh International Colloquium on Bluff Body Aerodynamics and Applications (BBAA7), Shanghai, China; September 2-6, 2012.

[21] Xiaohua Meng. Study on the windbreak performance of wind barrier on the long-span bridge. Thesis (M. Sc.)--Beijing Jiaotong universtity,2013.

[22] E. Simiu, R.H. Scanlan. Wind Effects on Structures: Fundamentals and Applications to Design. 3rd Edition. John Wiley & Sons, Inc. Canada, 1996.

[23] Yihua Cui, Guoping Chen. Identification of flutter derivatvies under forced coupling effect", Journal of Vibration Engineering, Vol.20 No.1 Feb. 2007

[24] D.H. Hodges and A. Pierce. Introduction to Structural Dynamics and Aeroelasticity. Cambridge, 2002.

[25] Yozo Fujino. Control, simulation and monitoring of bridge vibration – Japan's recent development and practice. IABSE-JSCE Joint Conference on Advances in Bridge Engineering-II, August 8-10, Dhaka, Bangladesh,2010.

[26] You-lin Xu. Wind Effects on Cable-Supported Bridges. John Wiley & Sons, 2013.

[27] Van Dyke. An Album of Fluid Motion. The Parabolic Press, Stanford,2002.

[28] C.M Leong T Wei. Two-degree-of-freedom Vortex-induced Vibration of A Pivoted Cylinder Below Critical Mass Ratio. The Royal Society, Nov. 2008.

[29] Nakamura Y, Mizota T . Unsteady lifts and wakes of oscillating rectangular prism. Journal of the Engineering Mechanics Division, 101: 855-871, 1975.

[30] Bishop R E D, Hassan A Y. The lift and drag forces on a circular cylinder oscillating in a flowing fluid. Proceeding of the Royal Society of London. Series A: Mathematical and Physical Sciences, 277(1368): 51-75,1964.

[31] Sarpkaya T. Vortex-induced oscillations. Journal of Applied Mechanics, 46(2): 241–258,1979.

[32] Bearman P W. Vortex shedding from oscillating bluff bodies. Annual Review of Fluid Mechanics, 16(1): 195–222, 1984.

[33] Williamson C H K. Vortex dynamics in the cylinder wake. Annual Review of Fluid Mechanics, , 28(1): 477–539,1996.

[34] E. Simiu, and R.H. Scanlan, Wind Effects on Structures. Second Edition, Wiley-Interscience, New York, 1986.

[35] Glauert, H., 1919. The Rotation of an Airfoil About a Fixed Axis. Reports and Memoranda 595, Aeronautical Research Committee, UK.

[36] J.P. Den Hartog. Mechanical Vibrations. 4th ed, McGraw-Hill, New York, 1956.

[37] G. Alonso, J. Meseguer, I. Pérez-Grande. Galloping oscillations of twodimensional triangular cross-sectional bodies. Exp. Fluids 38, 789-795. IDR/UPM, E.T.S.I. Aeronáuticos, Universidad Politécnica de Madrid, 2005.

[38] R.D. Blevins. Flow-Induced Vibrations. 2nd ed Krieger, Malabar, 2001.

[39] G. Alonso, J. Meseguer, I. Pérez-Grande. Galloping stability of triangular cross-sectional bodies: a systematic approach. J. Wind Eng. Ind. Aerodyn. 95, 928-940, 2007.

[40] G. Alonso, J. Meseguer, I. Pérez-Grande. An analysis on the dependence on cross section geometry of galloping stability of two-dimensional bodies having either biconvex or rhomboidal cross sections. Eur. J. Mech. B Fluids 28, 328-334, 2009.

[41] H. Gjelstrup, C.T. Georgakis. A quasi-steady 3 degree-of-freedom model for the determination of the onset of bluff body galloping instability, Journal of Fluids and Structures, 27, 1021–1034, 2011.

[42] J.H.G. Macdonald, G.L. Larose. Two-degree-of-freedom inclined cable galloping—Part 1: general formulation and solution for perfectly tuned system. Journal of Wind Engineering and Industrial Aerodynamics 96 (3), 291–326, 2008.

[43] X. Chen, A. Kareem. Efficacy of tuned mass damper for bridge flutter control. J. Struct. Eng. 129 (10),1291–1300, 2003.

[44] D.M. Tang and E.H. Dowell. Effects of geometric structural nonlinearity on flutter and limit cycle oscillations of high-aspect-ratio wings. Journal of Fluids and Structures, Volume 19, Issue 3,pp. 291-306, April 2004.

[45] T. Theodorsen. General Theory of Aerodynamic Instability and the Mechanism of Flutter. NACA TR No. 496, May 1934.

[46] U. Starossek. Brückendynamik. Winderregte Schwingungen von Seilbrücken. Friedr. Vieweg & Sohn Verlagsgesellschaft mbH, Braunschweig/Wiesbaden, 1992

[47] F. Bleich. Dynamic Instability of Truss-Stiffened Suspension Bridges Under Wind Action," Proceedings ASCE, Vol 75, No 8. 1948.

[48] R.H. Scanlan, J.J. Tomoko, "Airfoil and bridge deck flutter derivatives," Journal of the Engineering Mechanics, ASCE 97, 1717-1737, 1971.

[49] Yaojun Ge, Hiro Shi. Aerodynamic stability of long-span suspension bridge

sundererection. Journal of Structural Engineering, Tanaka, ASCE, 126(12), 1404-1412, 2000.

[50] H. Wagner. Über die Entstehung des dynamischen Auftriebes von Tragflügeln. Zeitschrift für Angewandte Mathematic und Mechanik 5 (1), 17–35, 1925.

[51] H.G. Küssner. Zusammenfassender Bericht über den instationären Auftrieb von Flügeln (Summary report on the instationary lift of wings). Luftfahrtforschung (in German) 13 (12): 410–424, December, 1936.

[52] W. R. Sears. Some aspects of non-stationary airfoil theory and its practical application. J. Aeron. Sc. 8(3), 104–108, 1941.

[53] A. G. Davenport. Buffeting of a suspension bridge by stormy winds. J. Struct. Div., ASCE, 88(3), 233–268, 1962.

[54] Liu Ketong, Tang Aiping. Numerical investigation for aerodynamic derivatives of bridge deck using DES. The Open Civil Engineering Journal, 8, 326-334, 2014.

[55] Michael C.H. Hui. Full-bridge aero-elastic model wind tunnel tests for the Stonecutters Bridge. HKIE Transactions, 20:2, 109-123, 2013.

[56] Yuh-Yi Lin, Chii-Ming Cheng, Jong-Cheng Wu, Tsang-Lien Lan, Kuo-Ting Wu. Effects of deck shape and oncoming turbulence on bridge aerodynamics. Tamkang Journal of Science and Engineering, Vol. 8, No 1, pp. 4356, 2005.

[57] Allan Larsen. Aerodynamic aspects of the final design of the 1624 m suspension bridge across the Great Belt. Journal of Wind Engineering and Industrial

Aerodynamics, Volume 48, Issues 2 – 3, Pages 261 – 285, October 1993.

[58] J. H. Walther, A. Larsen. Discrete vortex simulation of flow around five generic bridge deck sections. J. Wind Eng. Indust. Aerodyn., vol. 77-78, pp. 591-602, 1998.

[59] R. P. Silva, M. J. Tarini, A. Larsen. Computer modeling of flow around bridges using LES and FEM. J. Wind Eng. Indust. Aerodyn., vol. 77-78, pp. 643-651, 1998.

[60] Qi Wang, Hai-li Liao, Ming-shui Li, Rong Xian,"Wind Tunnel Study on Aerodyanmic Optimization of Suspension Bridge Deck Basd on Flutter Stability", The Seventh Asia-Pacific Conference on Wind Engineering, November 8-12, 2009,Taipei, Taiwan.

[61] Lin Zhixing, Ge Yaojun, Cao Feng chan. Wind resistant study and prevention research of steel box girders. Journal of Tonji University (Natural Science), 2002, 30(5): 614-617.

[62] Wen-Li Chen, Hui Li, Hui Hu,. An experimental study on the unsteady vortices and turbulent flow structures around twin-box-girder bridge deck models with different gap ratios. Jounral of Wind Engineering and Industrial Aerodynamics, 132 27–36, 2014.

[63] Fabio Brancaleoni and Giorgio Diana. The aerodynamic design of the Messina Straits Bridge. Journal of Wind Engineering and Industrial Aerodynamics, 48, pp.395-409, 1993.

[64] G. Diana , M. Falco , S. Bruni a, A. Cigada , G.L. Larose , A. Damsgaard , A. Collina. Comparisons between wind tunnel tests on a full aeroelastic model of the

proposed bridge over Stretto di Messina and numerical results. Journal of Wind Engineering and Industrial Aerodynamics 54/55 101-113, 1995.

[65] J. Ramsden. A critical analysis of the proposed bridge over the strait of messina. Proceedings of Bridge Engineering 2 Conference 2009.

[66] Fujun Wang. Computational fluid dynamics analysis--CFD theories and applications. Tsinghua University Press, 2003.

[67] Stephane Sanquer, Chri stian Barre, Marc Dufresne de Virel. Effect of cross winds on high—speed trains: development of a new experimental methodology. Journal of Wind Engineering and Industrial Aerodynamics, 92(7—8): 535-545, 2004.

[68] Qi Zhou, Zhenshan Guo, Ledong Zhu. The numerical simulation of wind sheltering effect of curved wind barrier on the bridge. The 14th structure wind engineering academic conference, Shanghai, Feb 2000.

[69] Zhenshan Guo, Ledong Zhu, Zhiyong Zhou. Optimization of wind barrier and the corresponding effect on bridge aerodynamic characteristics. The 14th structure wind engineering academic conference, Beijing, Aug 2009.

[70] DONG Xiangting, DANG Xiangpeng. Study on influence of wind barriers on traffic safety of trains under crosswind by numerical simulation[J]. Journal of the China railway Society, 30(5):36-40, 2008.

[71] Guo WeiWei, Wang Yujing, Xia He, Lu Shan. Wind tunnel test on aerodynamic effect of wind barriers on train-bridge system. Science China, Technological Sciences, Vol.58 No.2: 219–225, February 2015.

[72] Jan R. Wright and Jonathan E. Cooper. Introduction to Aircraft Aeroelasticity and Loads (2nd ed.). John Wiley & Sons, Ltd, 2015.

[73] M. Iwamoto, Y. Fujino. Identification of flutter derivatives of bridge deck from free vibration data. Journal of Wind Engineering and Industrial Aerodynamic, 54/55, pp. 55-63, 1995.

[74] Sarkar, P. P..New identification methods applied to the response of flexible bridges to wind. PhD thesis, The John Hopkins University, Baltimore, Md, 1992.

[75] A. Namini, P. Brech, H. Bosch. Finite Ele-ment-based Flutter Analysis of Cable-suspended Bridges. Journal of Structural Engineering, 118(6):1 509-1 526, 1992.

[76] Z. Yang, L. Zhang, H. Liu, J. Zhang. Optimization of Extracting Fremitus Derivative Based on MITD Method. Journal of Civil, Architectural& Environmental Engineering, Vol.32, No.2, p.78-81, Apr. 2010.

[77] G.F. Sirca Jr., H. Adeli. System Identification In Structural Engineering. Scientia Iranica A , 19 (6), 1355–1364, 2012.

[78] A. Baldomir , I. Kusano, S. Hernandez, J.A. Jurado. A reliability study for the Messina Bridge with respect to flutter phenomena considering uncertainties in experimental and numerical data, Computers and Structures 128, 91–100, 12 July 2013.

[79] Zhuanyun Yang, Liangliang Zhang, Hui Liu, Jinmei Zhang. Optimization of extracting flutter derivative based on Modified Ibrahim Time-Domain method.

Journal of Civil, Architectural & Environmental Engineering, Vol. 32 No. 2 Apr. 2010.

[80] Arindam Gan Chowdhury, Partha P. Sarkar. A new technique for identification of eighteen flutter derivatives using a three-degree-of-freedom section model. Engineering Structures, Volume 2, Issue 14, Pages 1763–1772. December 2003.

[81] Elsa de Sa Caetano. Cable vibrations in cable-stayed bridges. International Association for Bridge and Structural Engineering, 2007.

[82] Smits, Alexander J. and Du ssauge, Jean-Paul. Turbulent shear layers in supersonic flow, Birkh äuser, ISBN 0-387-26140-0 p. 46, 2006

[83] T.A. Reinhold, M. Brinch and A. Damsgaard. Wind tunnel tests for the Great Belt Link. Proc. Aerodynamics of Large Bridges, Copenhagen, Denmark, 1992.

[84] Xu XU. Parametric studies on relationships between flutter derivatives of slender bridge. Appl. Math. Mech. -Engl. Ed. 30(2), 237–245, DOI: 10.1007/s 10483-009-0211-2, 2009.

[85] Youxiang Li. The research on flutter derivatives of long-span bridges based on time-domain identification. B.E. Chongqing University,2006.

[86] Hao Zhan, Tao Fang. Flutter stability studies of Great Belt East Bridge and Tacoma Narrows Bridge by CFD numerical simulation. The seventh International Colloquium on Bluff Body Aerodyanmics and Applications (BBAA7), Shanghai, China, Sep 2-6, 2012.

Appendix A

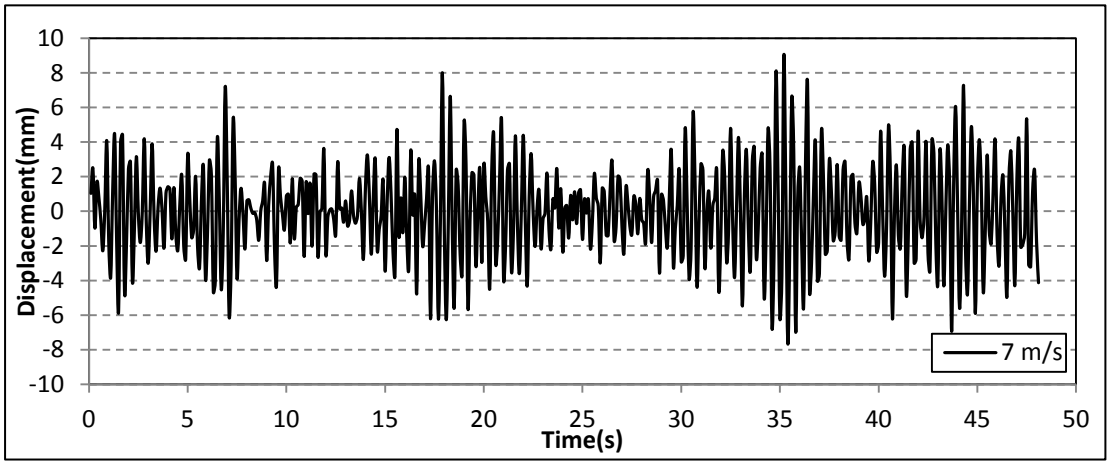
Displacement(mm)
Time(s)
7 m/s

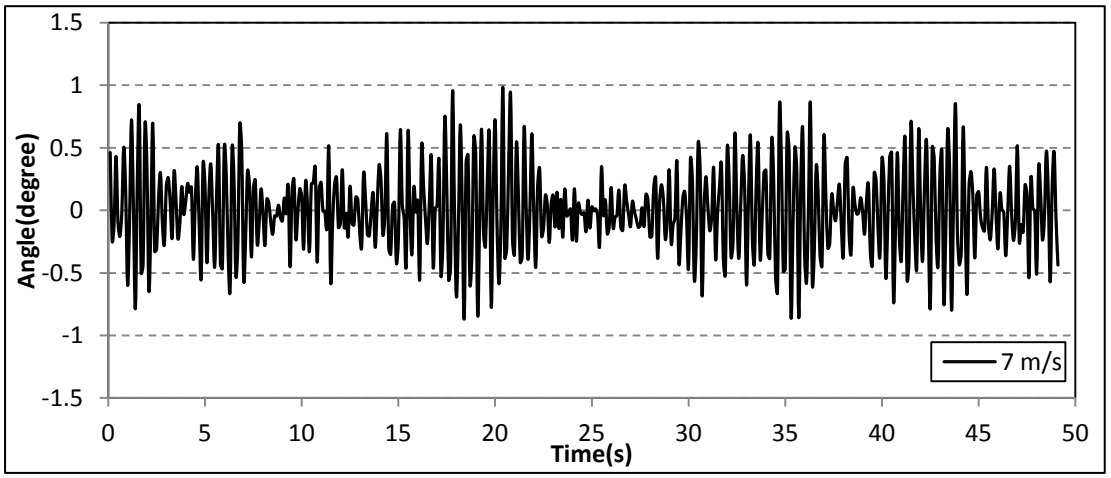
Angle(degree)
Time(s)
7 m/s

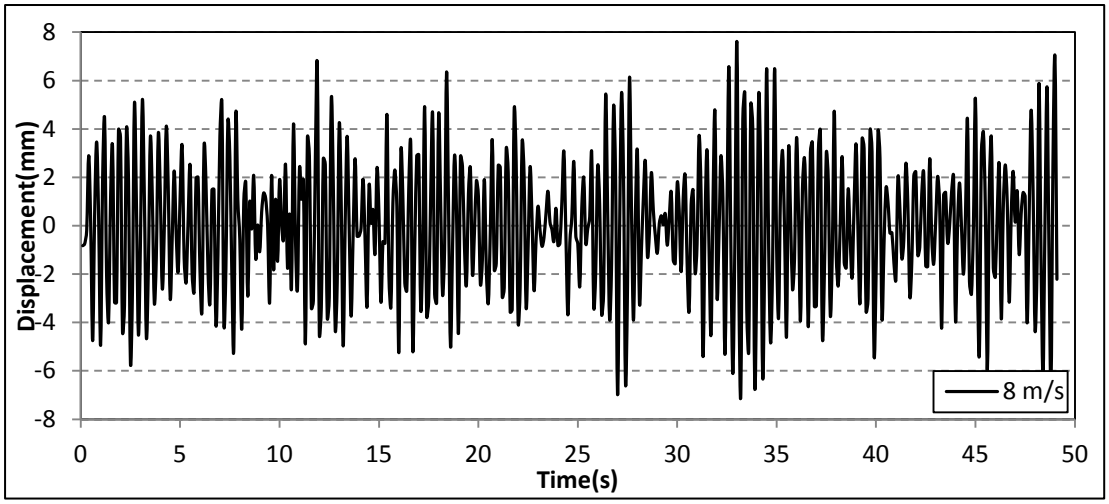
Displacement(mm)
Time(s)
8 m/s

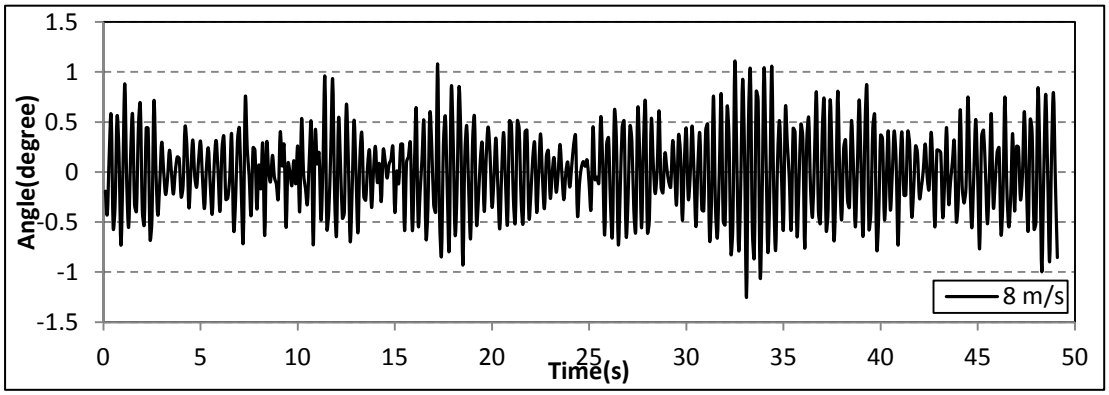
Angle(degree)
Time(s)
8 m/s

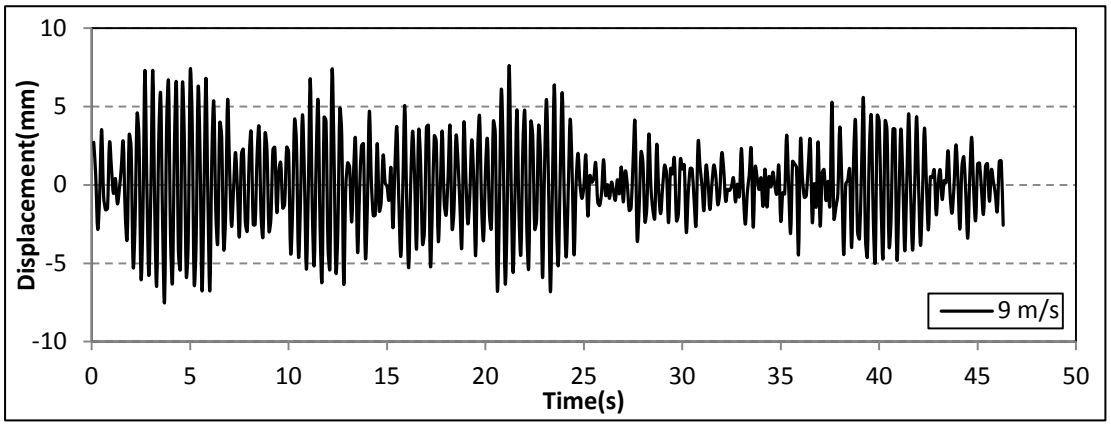
Displacement(mm)
Time(s)
9 m/s

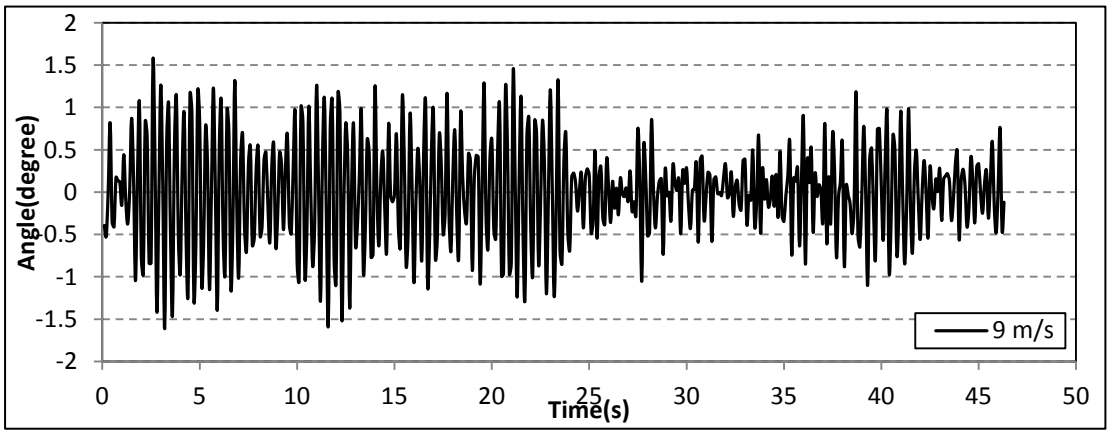
Angle(degree)
Time(s)
9 m/s

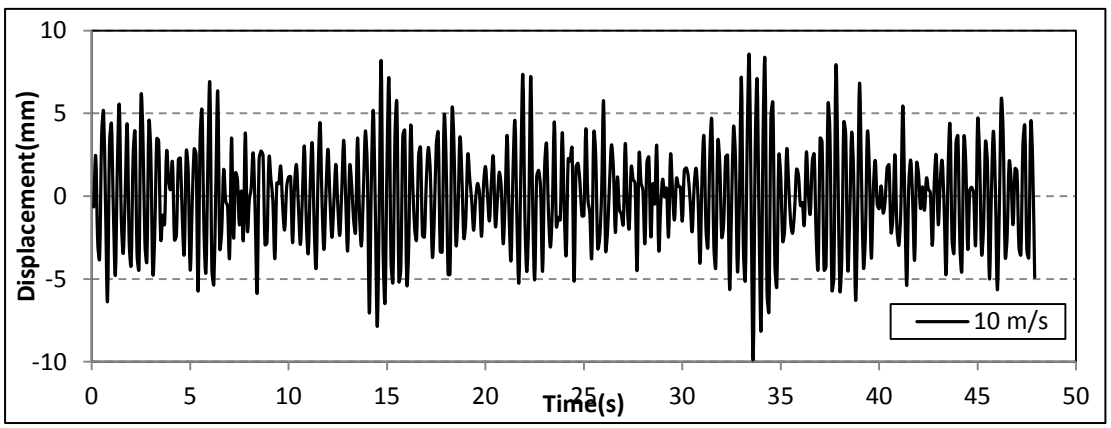
Displacement(mm)
Time(s)
10 m/s

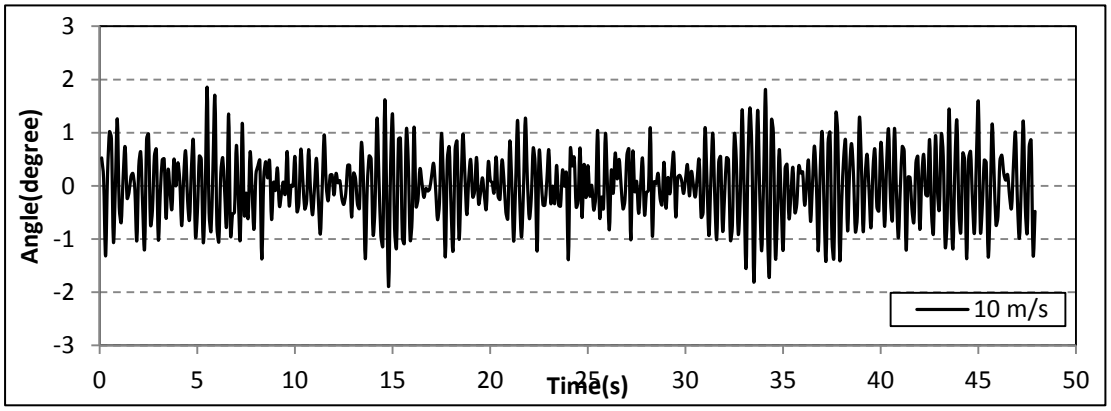

Vertical displacement and torsional angle time histories from 7 m/s to 10 m/s wind speed under 0 °attack angle (30 mm high wind barrier)

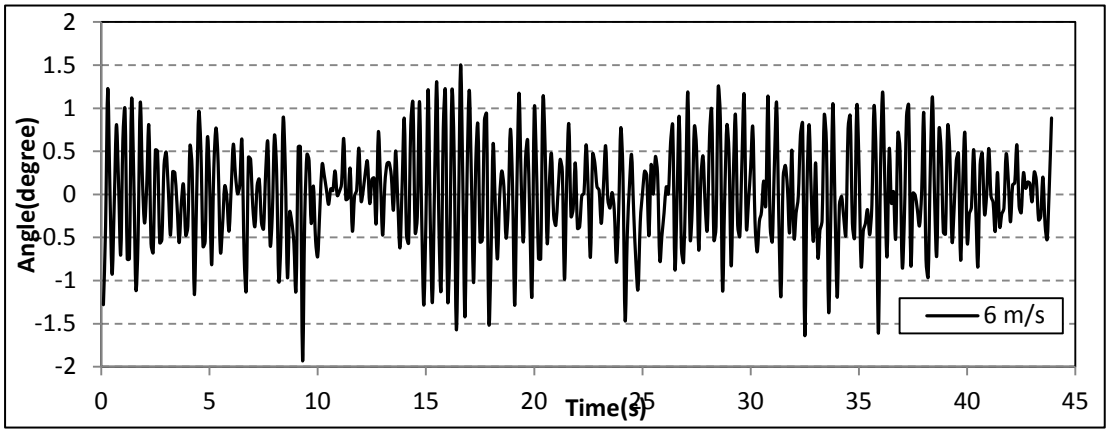

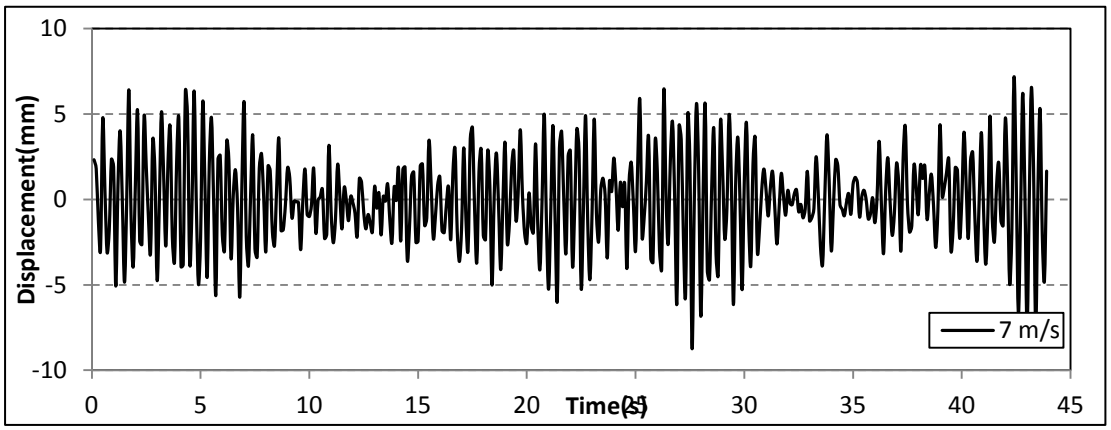

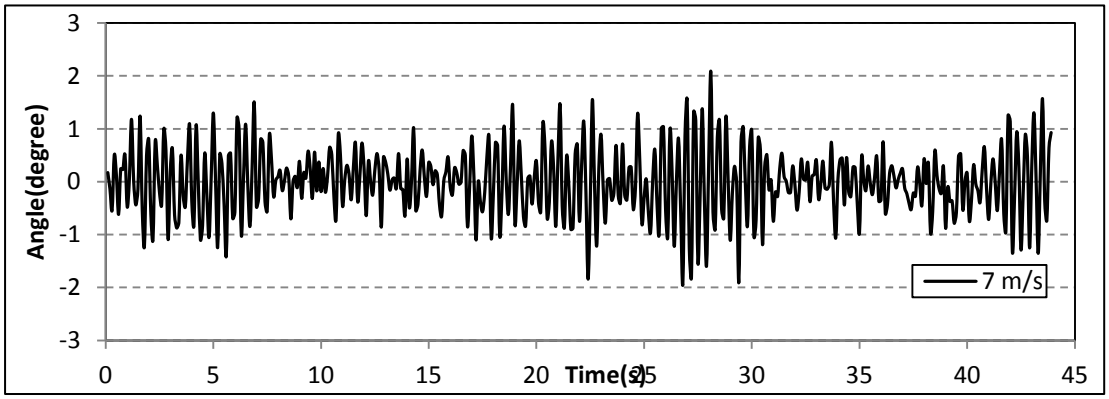
Angle(degree)
Time(s)
7 m/s

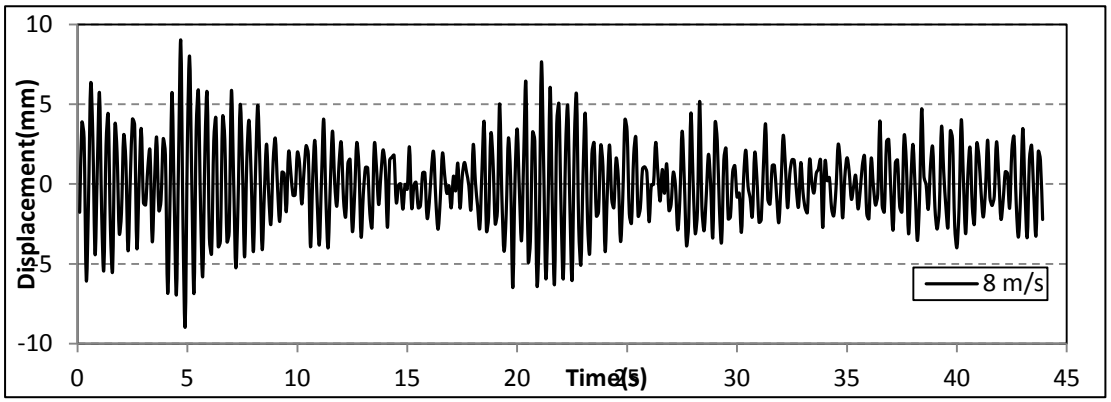
Displacement(mm)
Time(s)
8 m/s

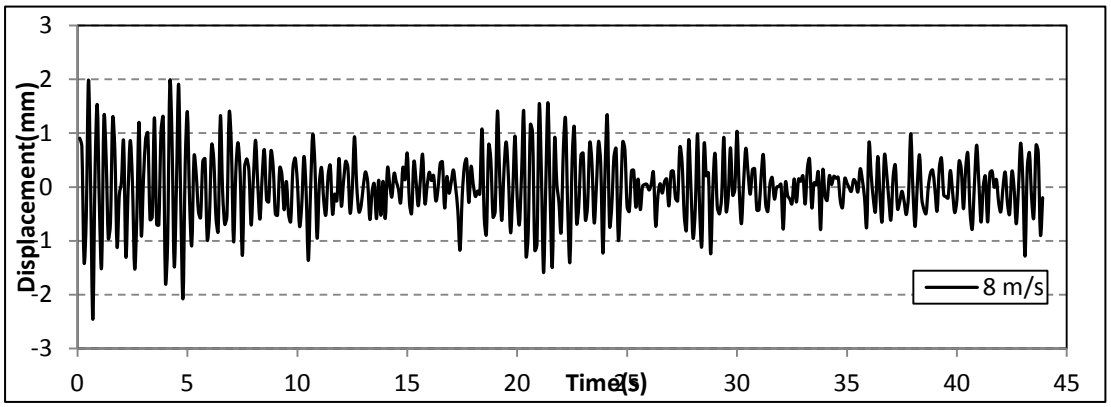
Displacement(mm)
Time(s)
8 m/s

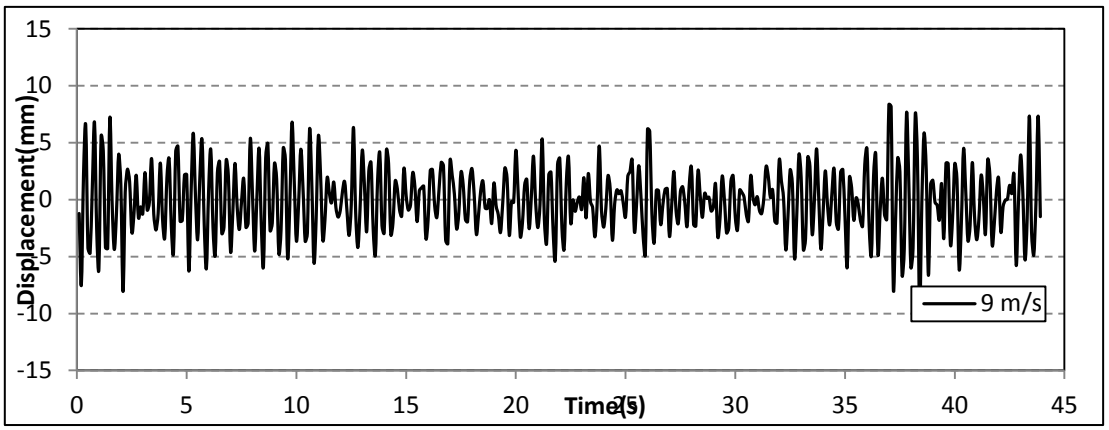
Displacement(mm)
Time(s)
9 m/s

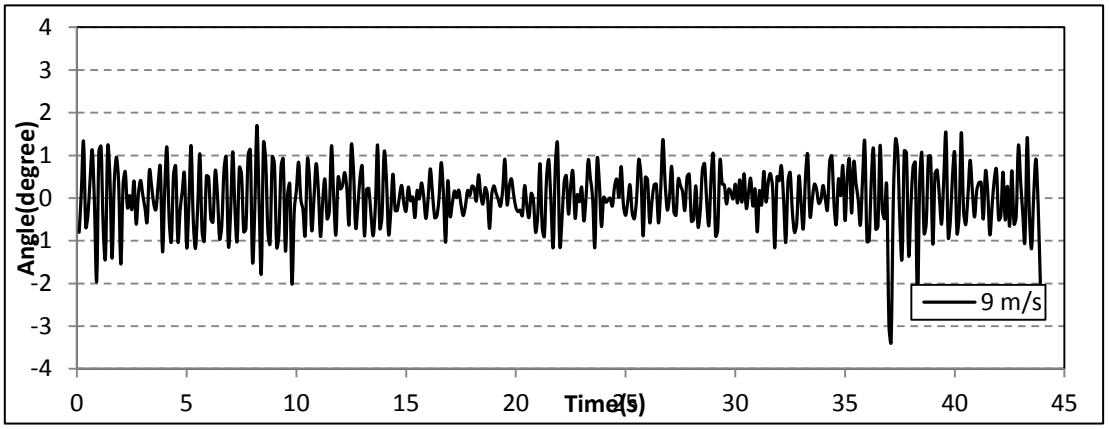
Angle(degree)
Time(s)
9 m/s

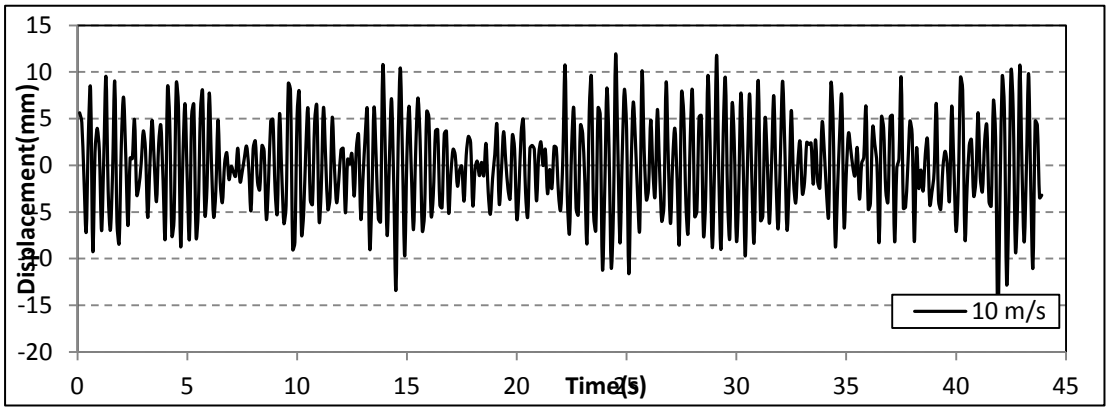
Displacement(mm)
Time(s)
10 m/s

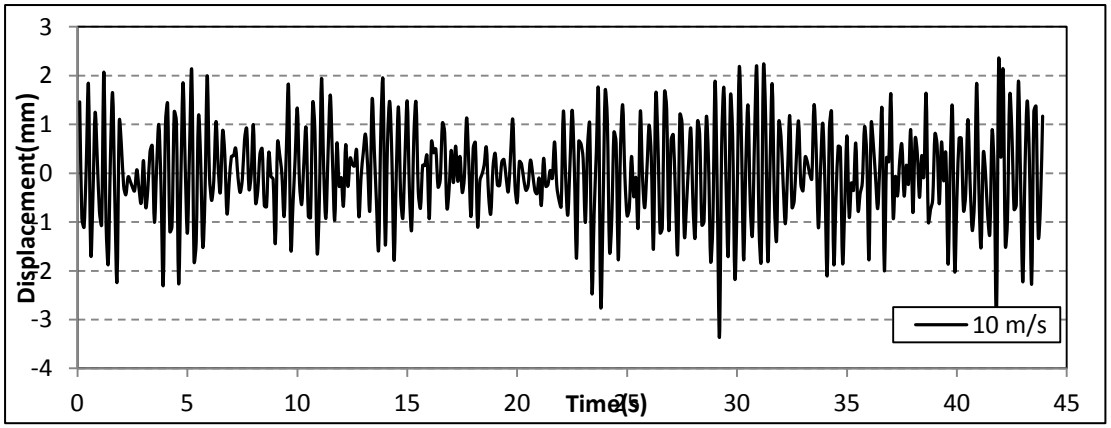
Displacement(mm)
Time(s)
10 m/s

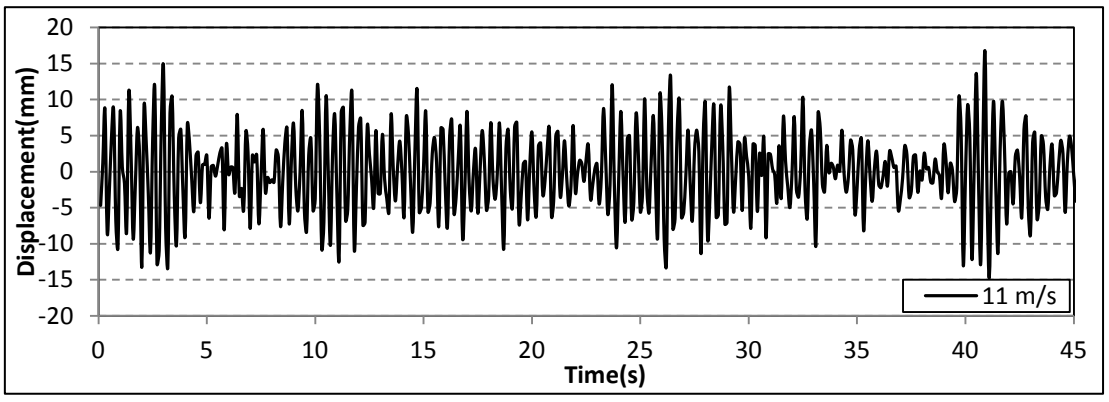
Displacement(mm)
Time(s)
11 m/s

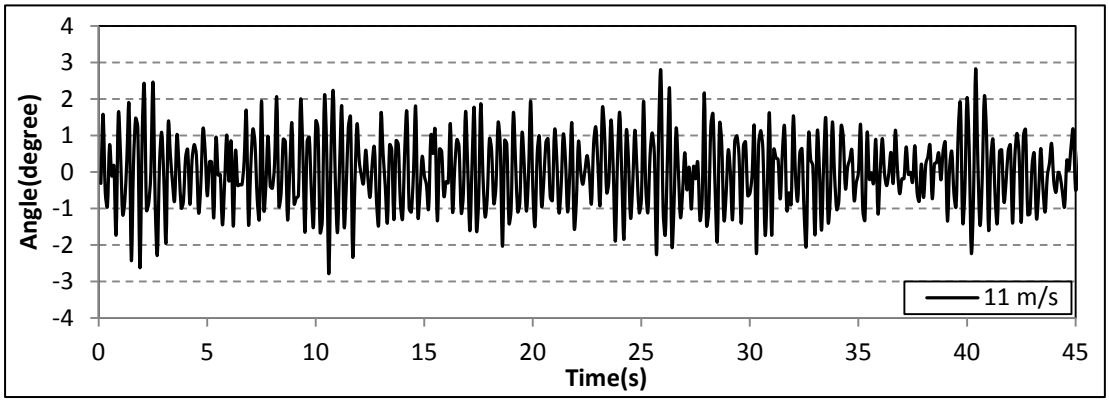

Vertical displacement and torsional angle time histories from 7 m/s to 11 m/s wind speed under -2 °attack angle (30 mm high edge wind barrier)

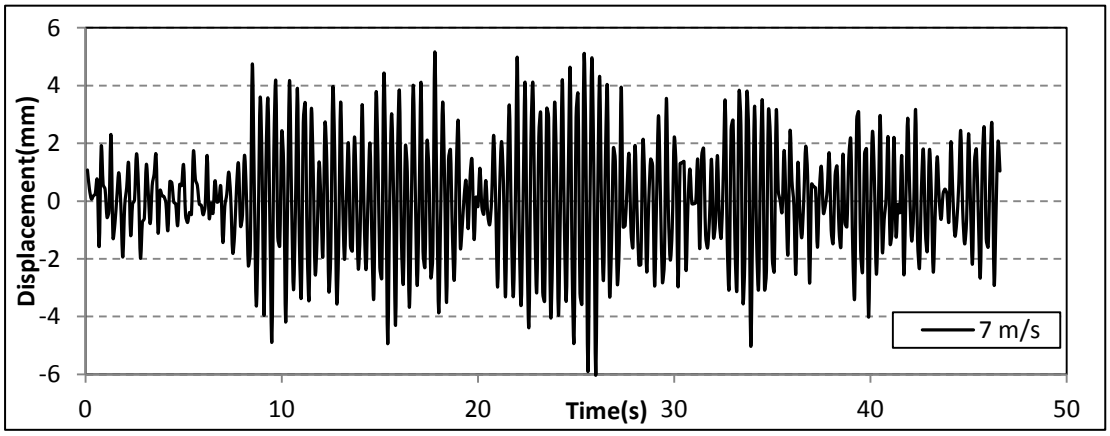

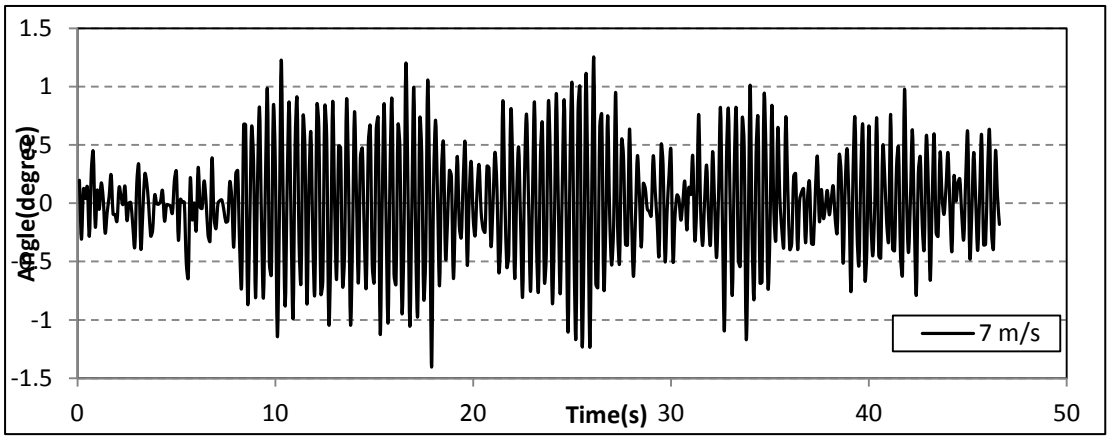

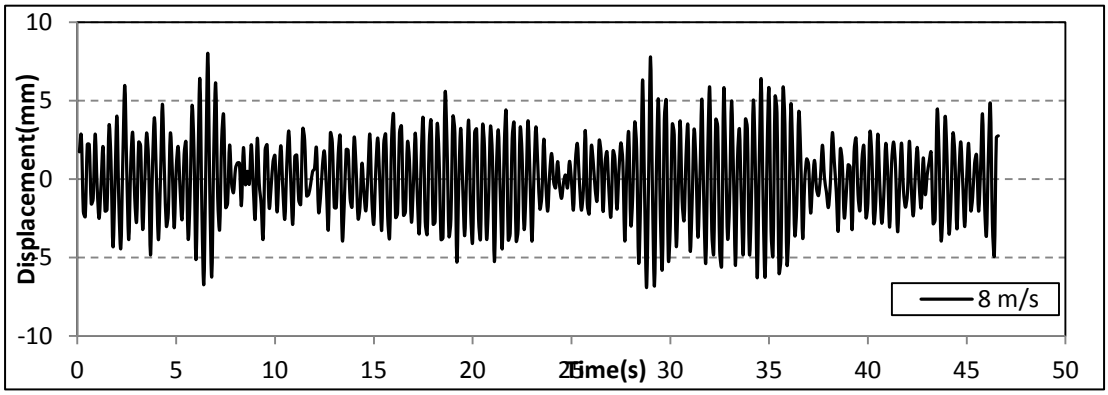
Displacement(mm)
Time(s)
8 m/s

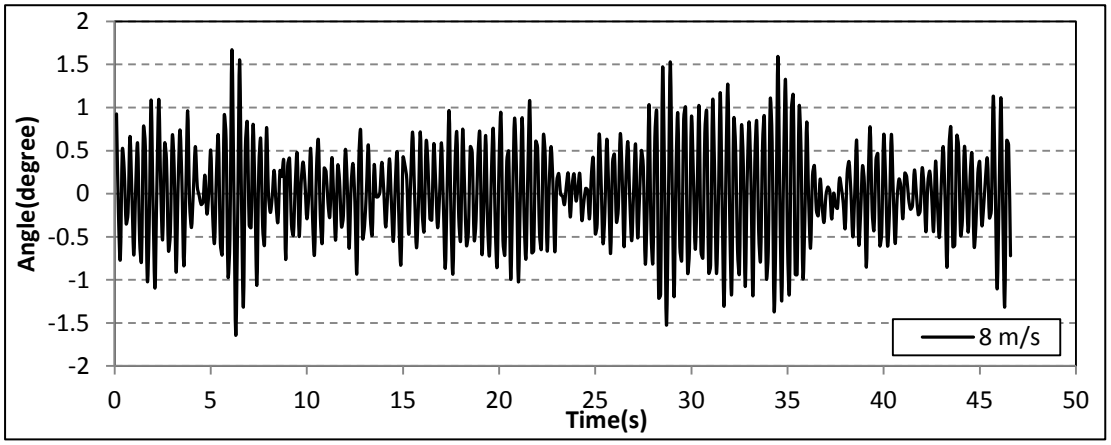
Angle(degree)
Time(s)
8 m/s

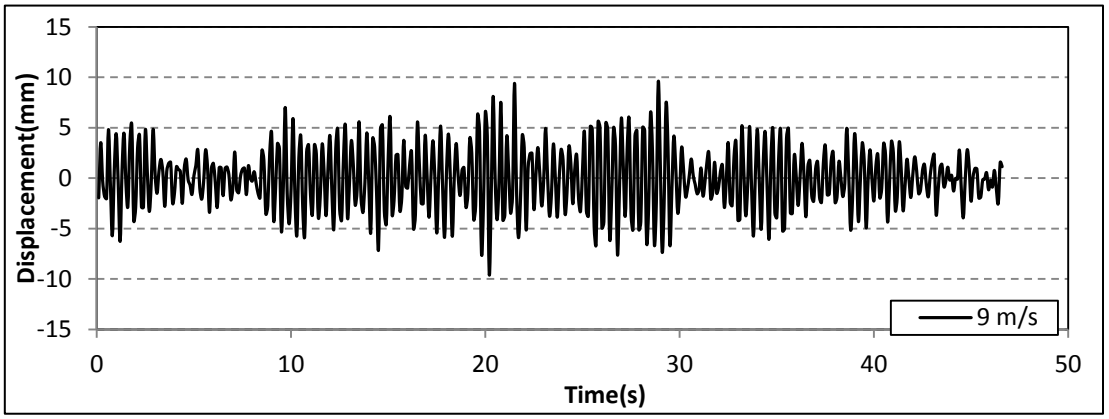
Displacement(mm)
Time(s)
9 m/s

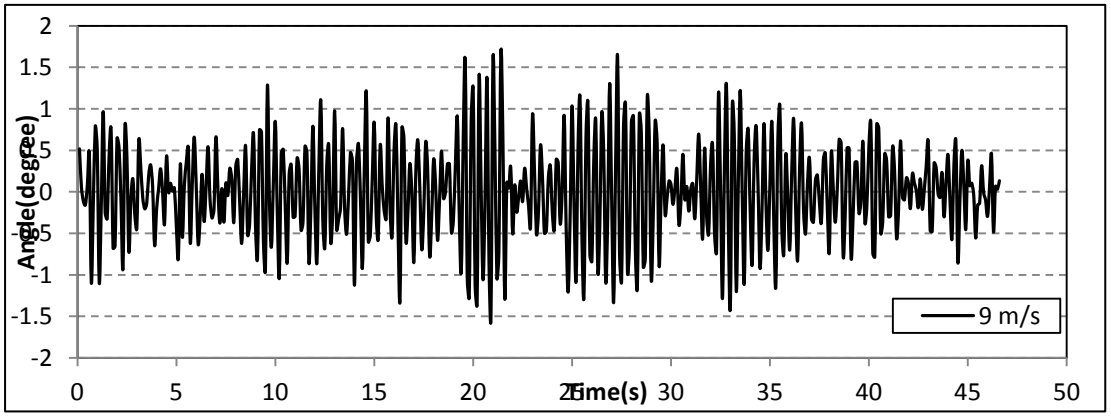
Angle(degree)
Time(s)
9 m/s

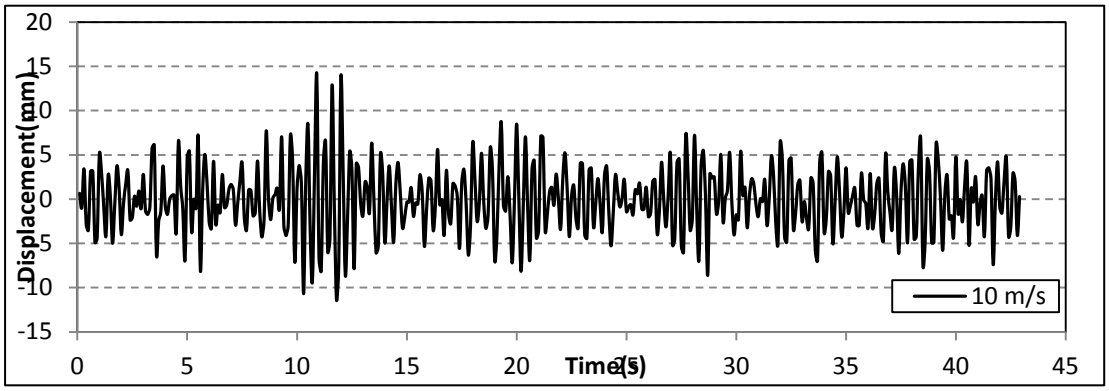
Displacement(mm)
Time(s)
10 m/s

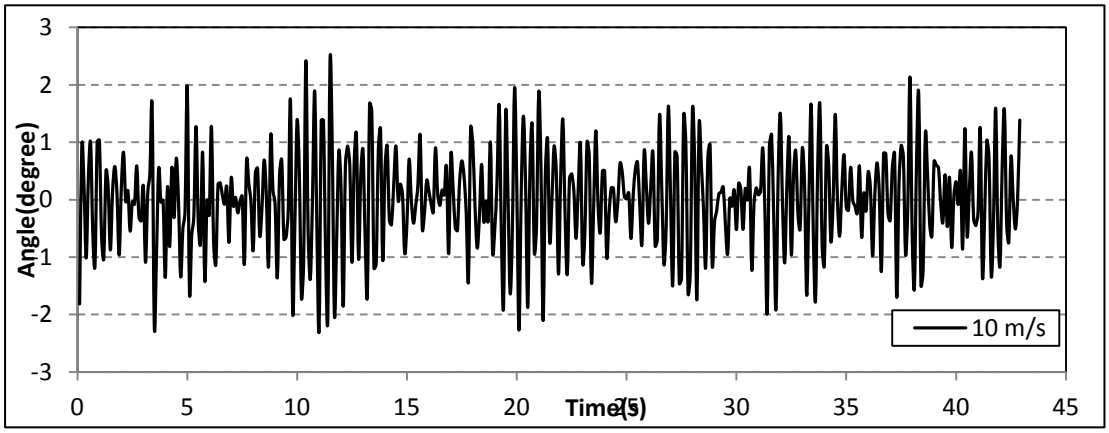
Angle(degree)
Time(s)
10 m/s

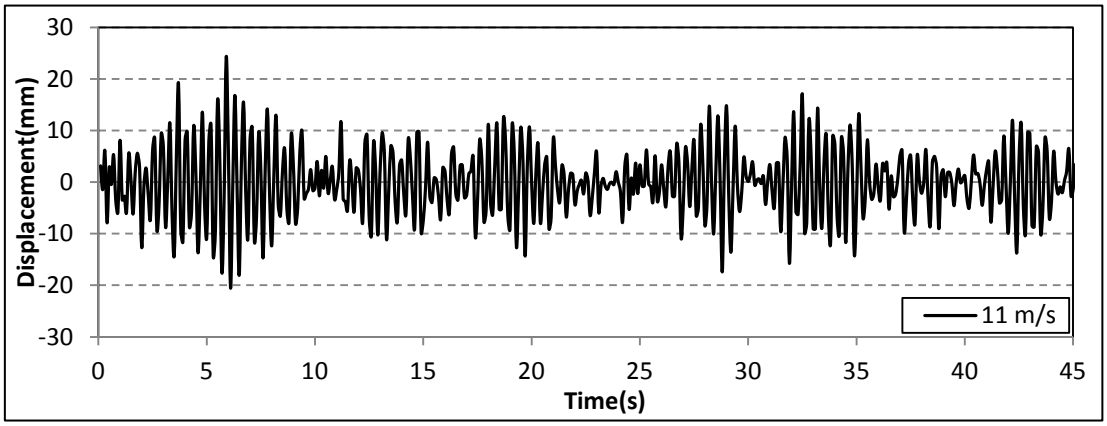
Displacement(mm)
Time(s)
11 m/s

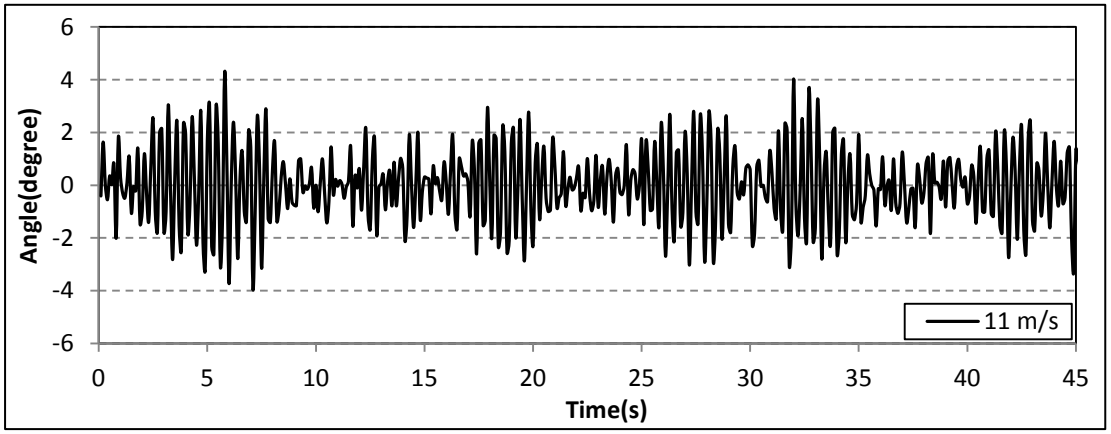
Angle(degree)
Time(s)
11 m/s

Vertical displacement and torsional angle time histories from 7 m/s to 11 m/s wind speed under -4 °attack angle (30 mm high edge wind barrier)

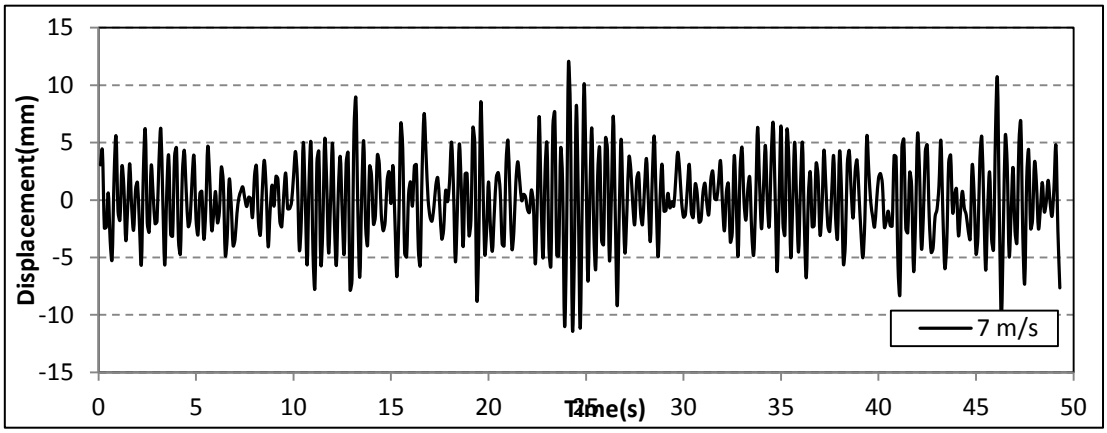

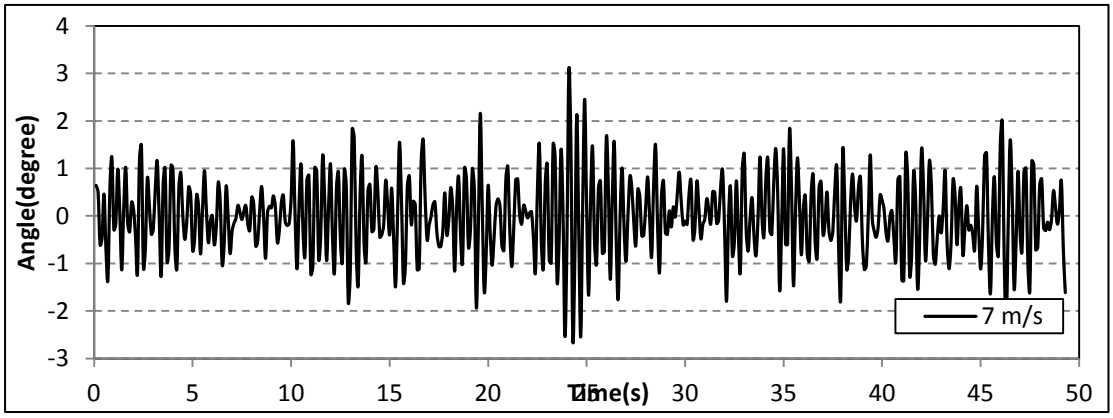

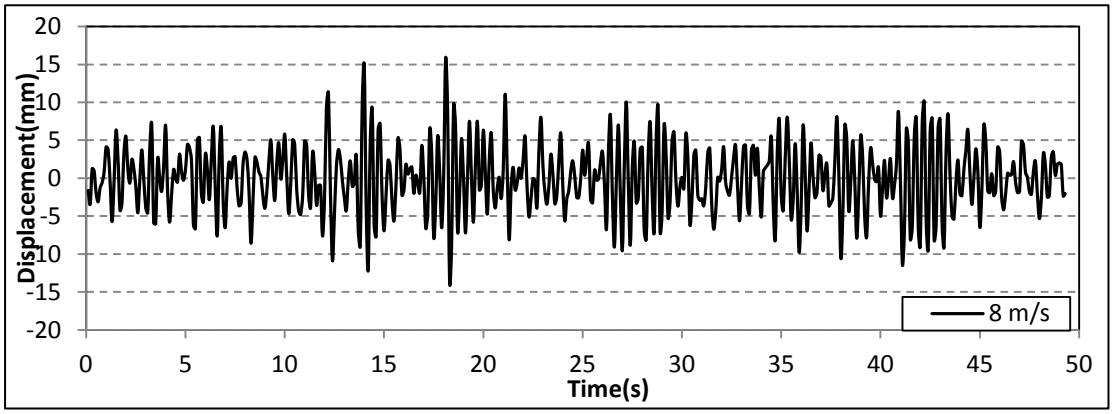

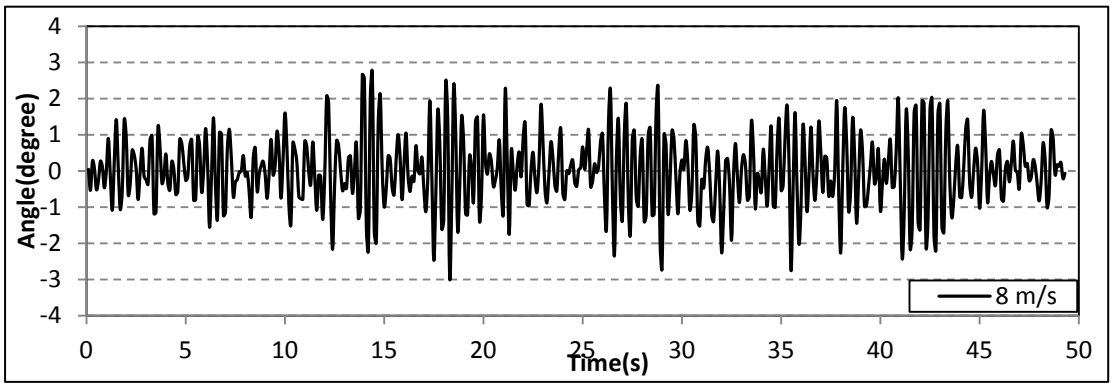
Angle(degree)
Time(s)
8 m/s

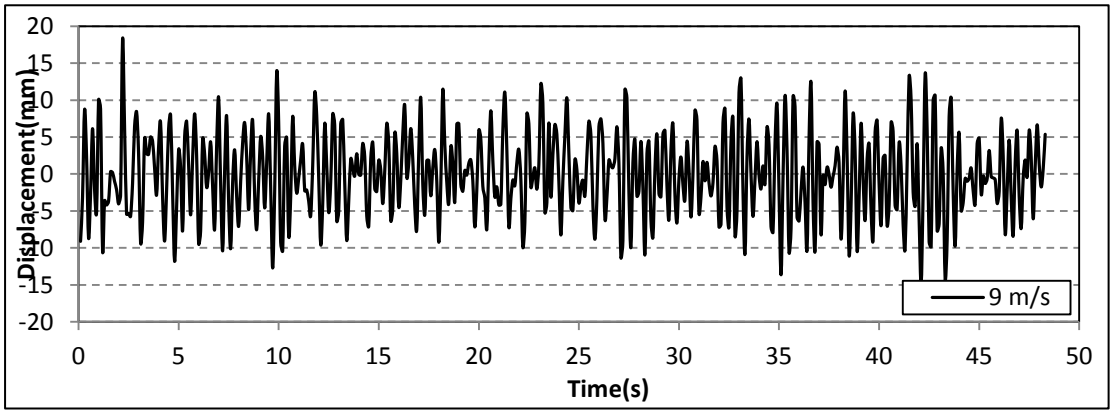
Displacement(mm)
Time(s)
9 m/s

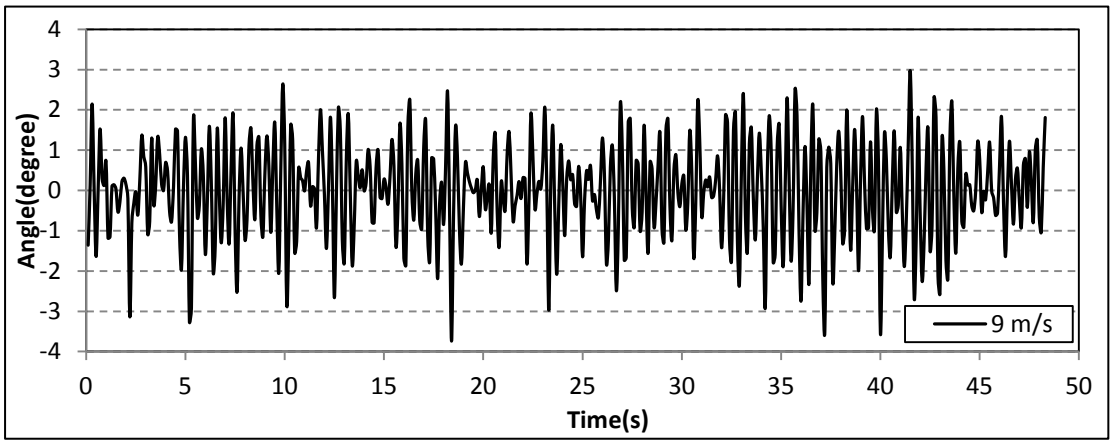
Angle(degree)
Time(s)
9 m/s

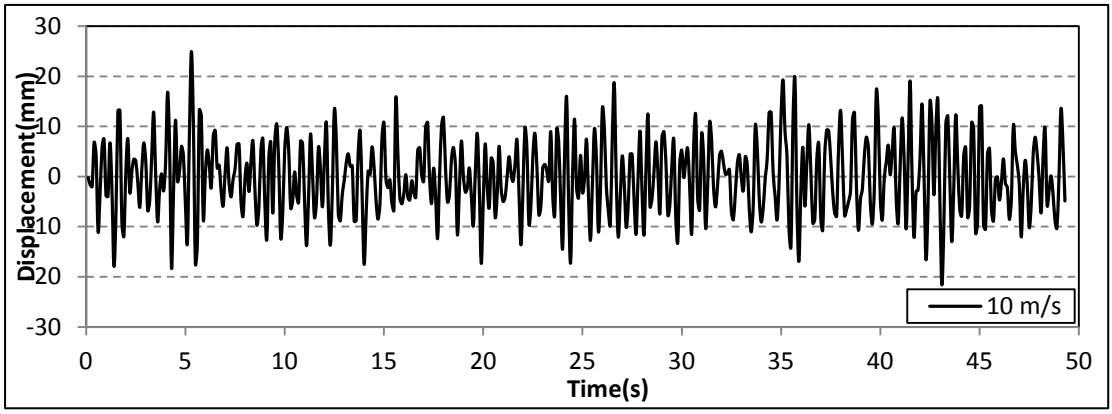
Displacement(mm)
Time(s)
10 m/s

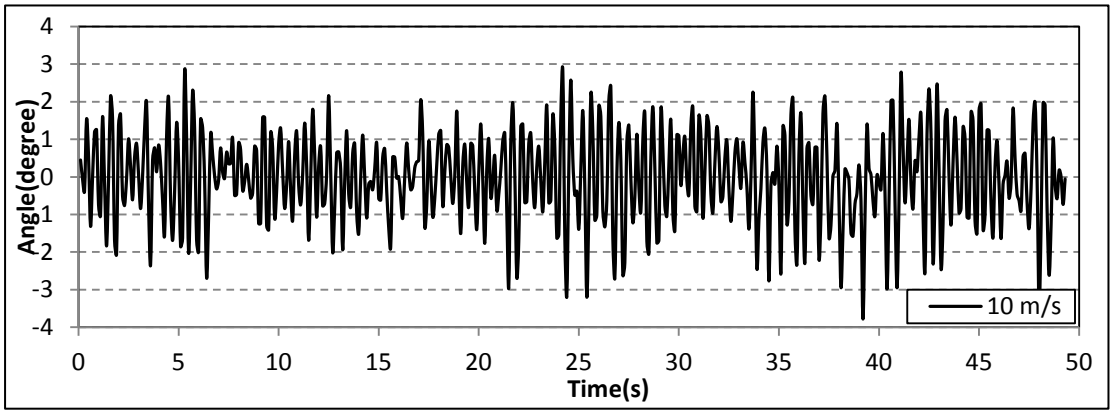

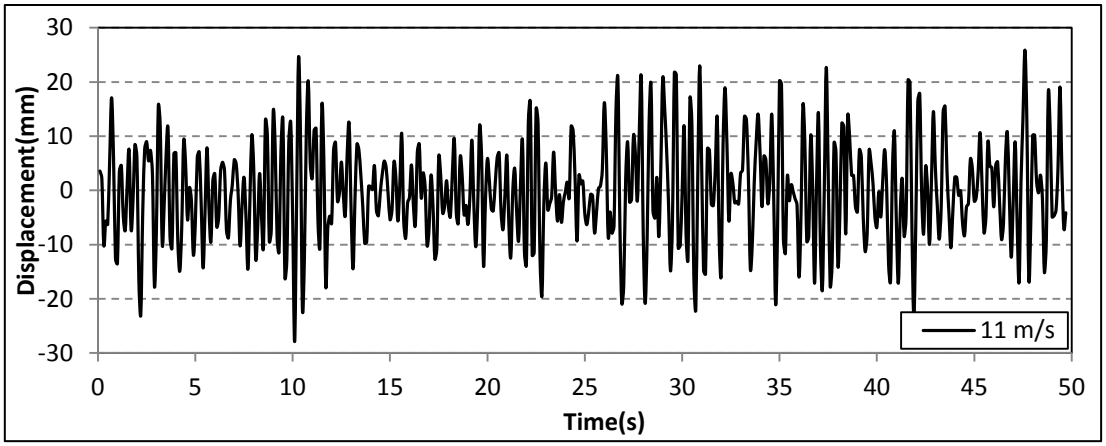

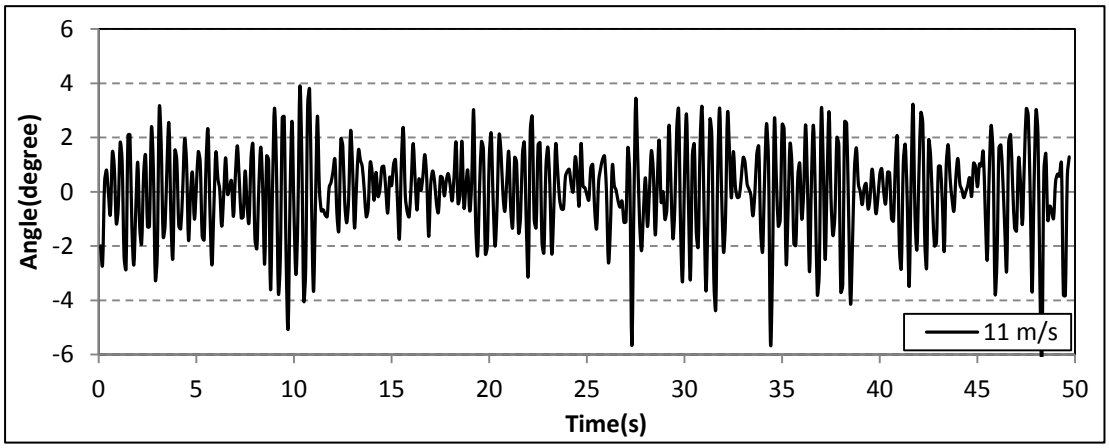

Vertical displacement and torsional angle time histories from 7 m/s to 11 m/s wind speed under -6 °attack angle (30 mm high edge wind barrier)

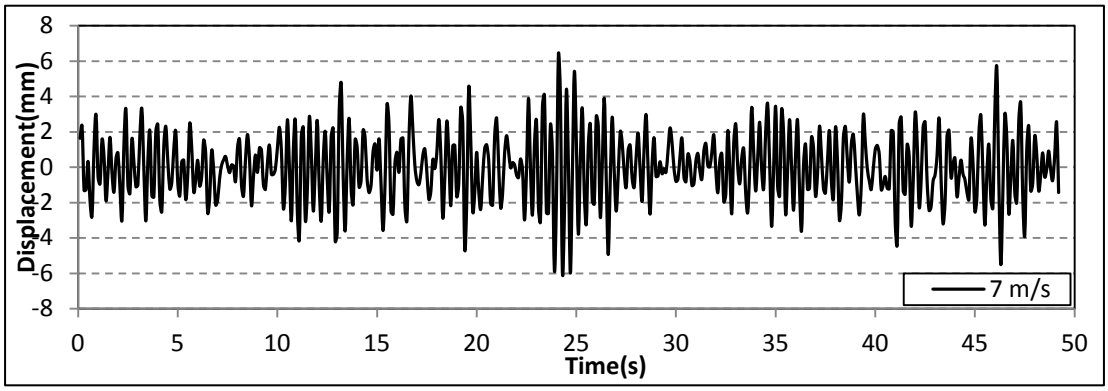
Displacement(mm)
8
6
4
2
0
-2
-4
-6
-8
0
5
10
15
20
25
30
35
40
45
50
Time(s)
7 m/s

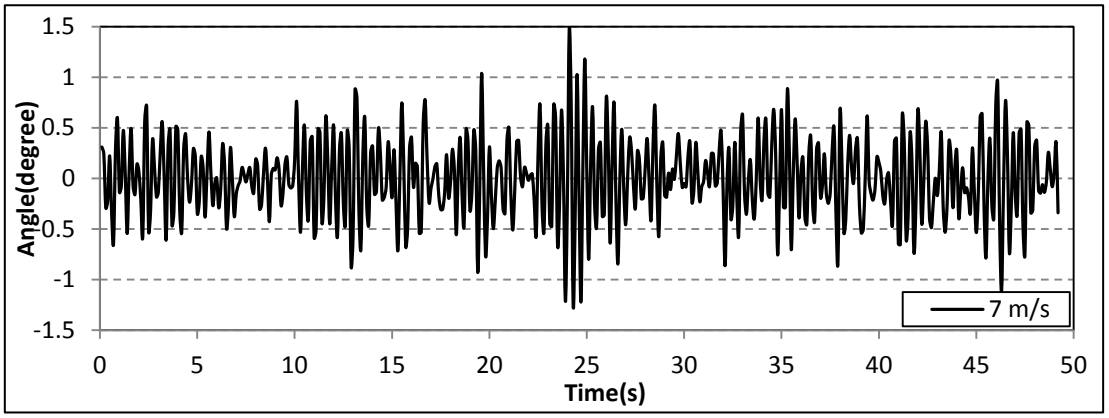
Angle(degree)
1.5
1
0.5
0
-0.5
-1
-1.5
0
5
10
15
20
25
30
35
40
45
50
Time(s)
7 m/s

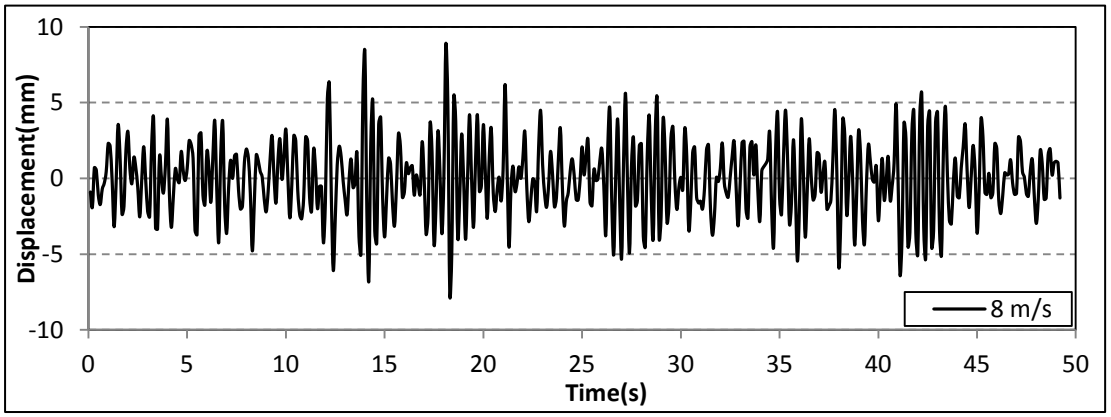
Displacement(mm)
10
5
0
-5
-10
0
5
10
15
20
25
30
35
40
45
50
Time(s)
8 m/s

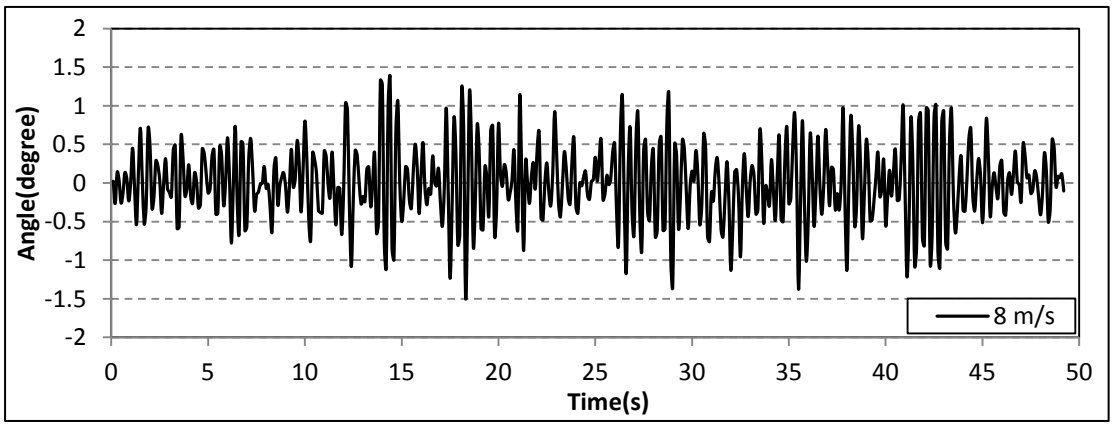
Angle(degree)
2
1.5
1
0.5
0
-0.5
-1
-1.5
-2
0
5
10
15
20
25
30
35
40
45
50
Time(s)
8 m/s

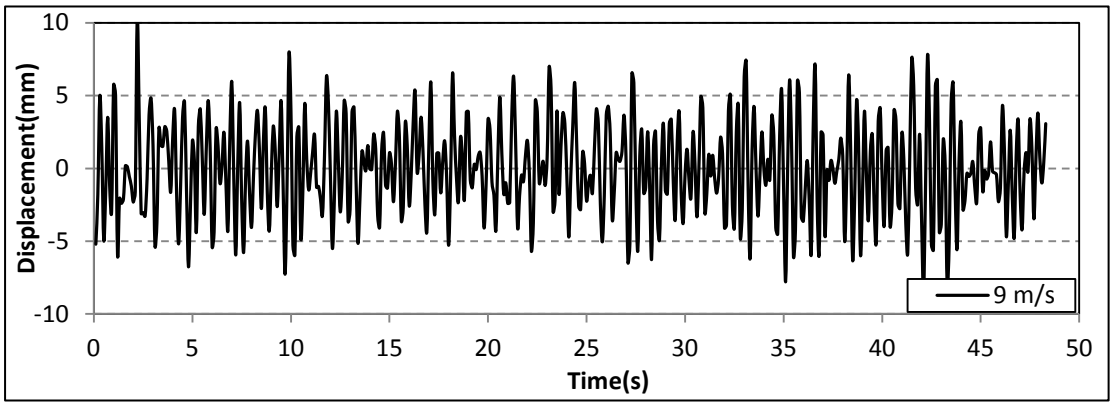
Displacement(mm)
10
5
0
-5
-10
0
5
10
15
20
25
30
35
40
45
50
Time(s)
9 m/s

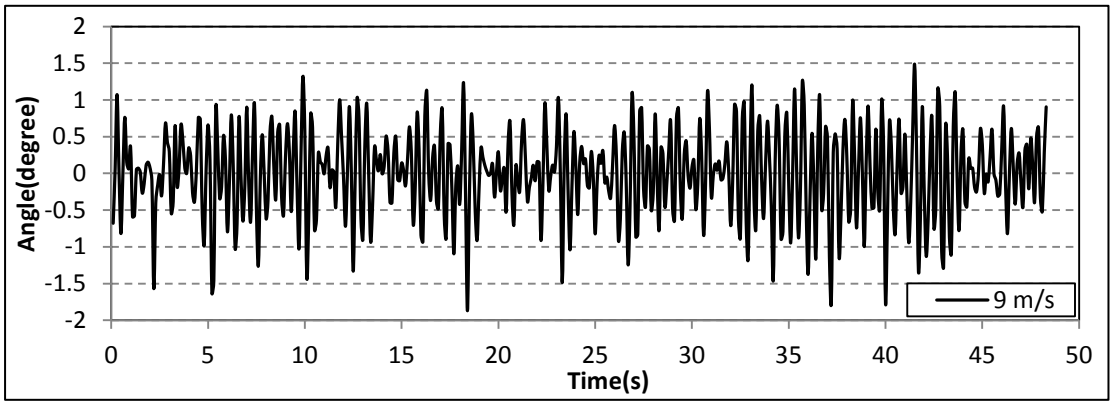
Angle(degree)
2
1.5
1
0.5
0
-0.5
-1
-1.5
-2
0
5
10
15
20
25
30
35
40
45
50
Time(s)
9 m/s

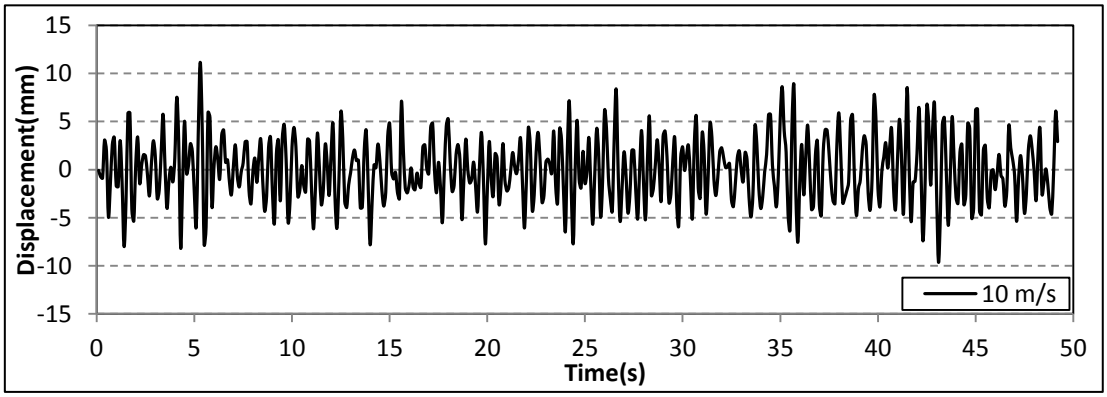
Displacement(mm)
15
10
5
0
-5
-10
-15
0
5
10
15
20
25
30
35
40
45
50
Time(s)
10 m/s

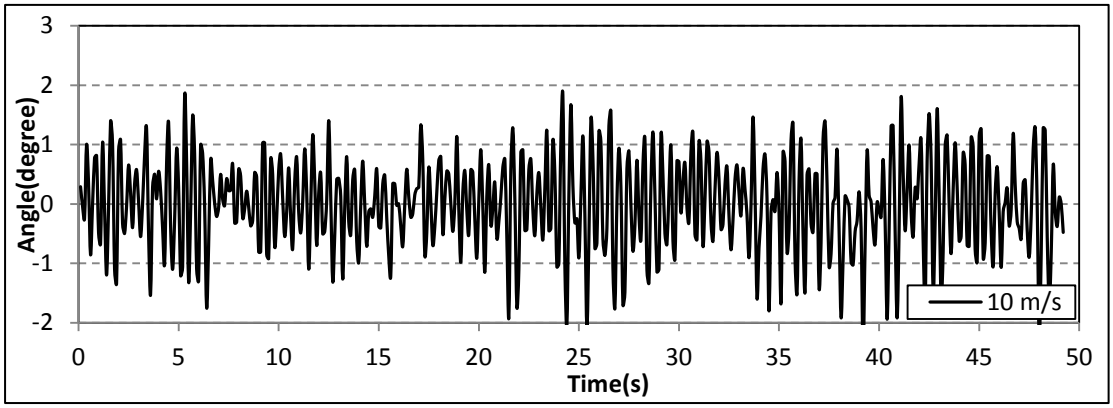
Angle(degree)
3
2
1
0
-1
-2
0
5
10
15
20
25
30
35
40
45
50
Time(s)
10 m/s

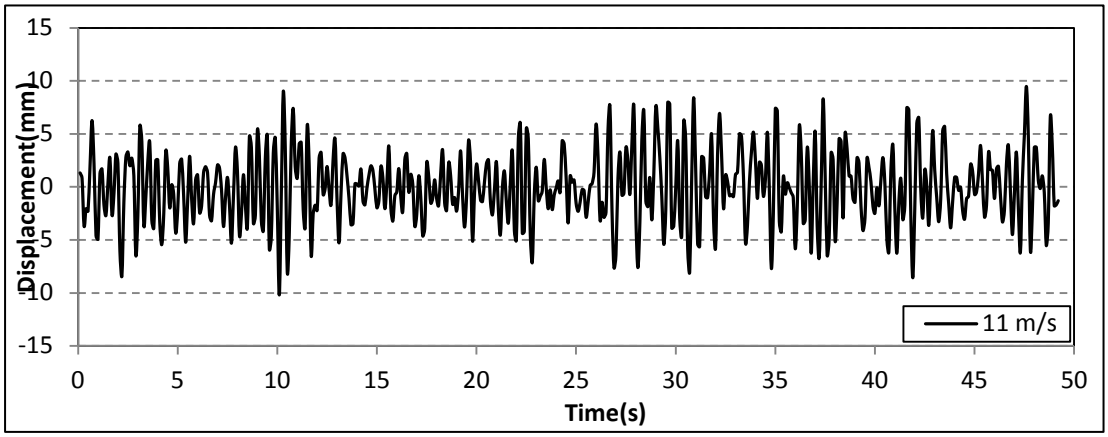

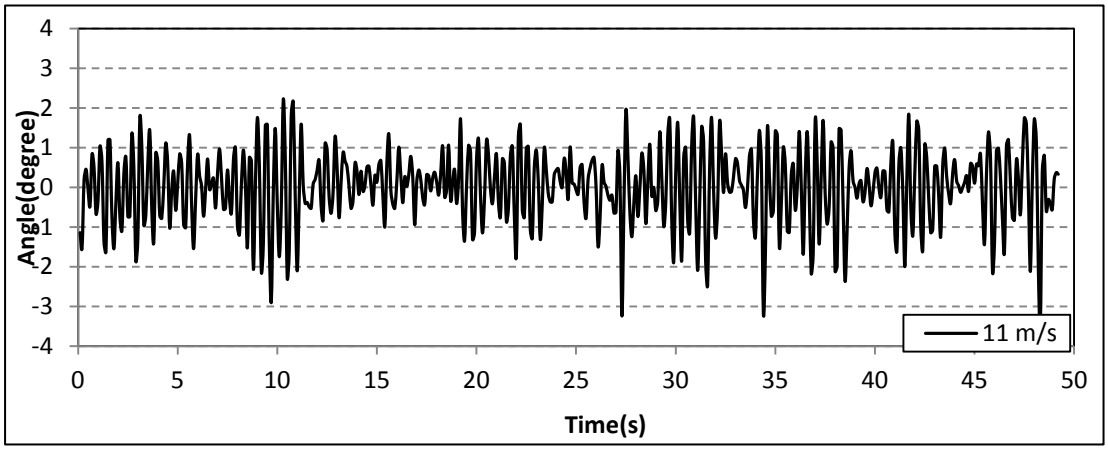

Vertical displacement and torsional angle time histories for 7 m/s to 11 m/s wind speed under 2 °attack angle (30 mm high edge wind barrier)

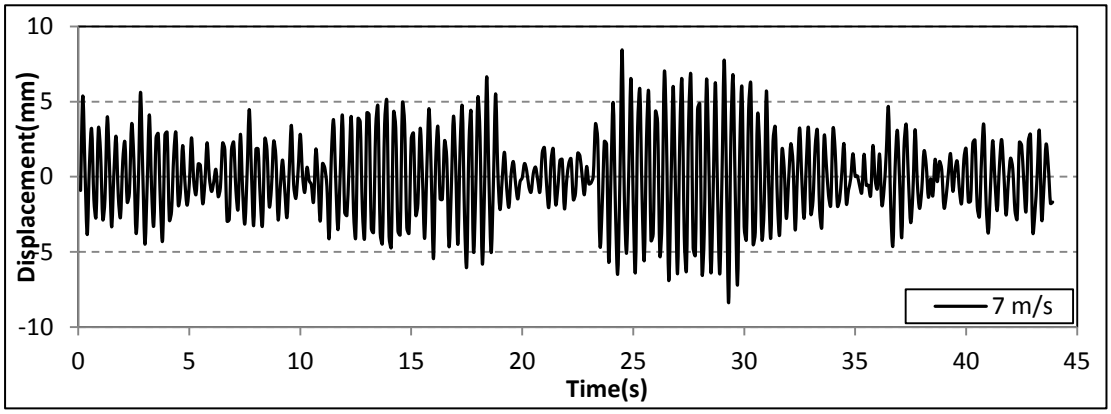

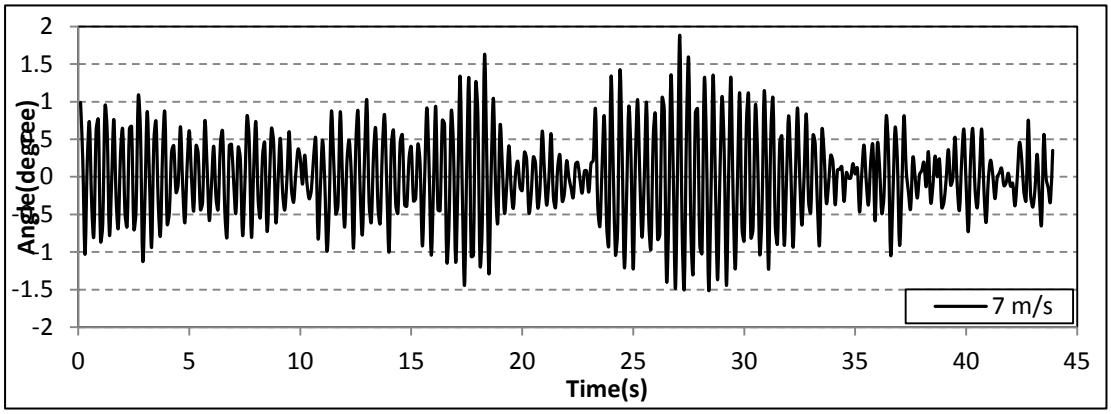
Angle(degree)
Time(s)
7 m/s

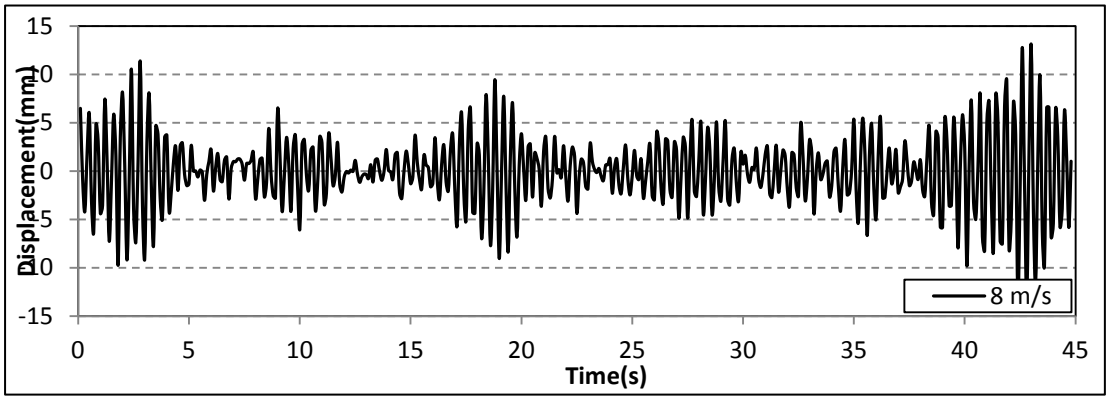
Displacement(mm)
Time(s)
8 m/s

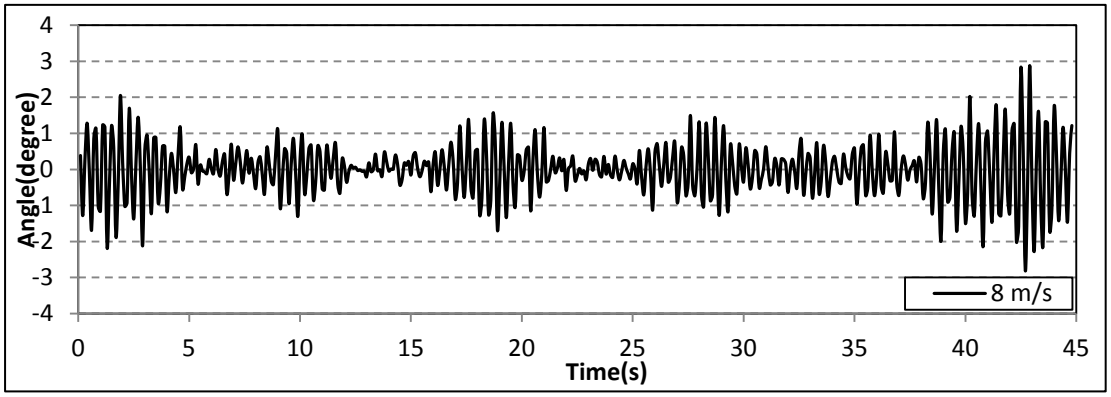
Angle(degree)
Time(s)
8 m/s

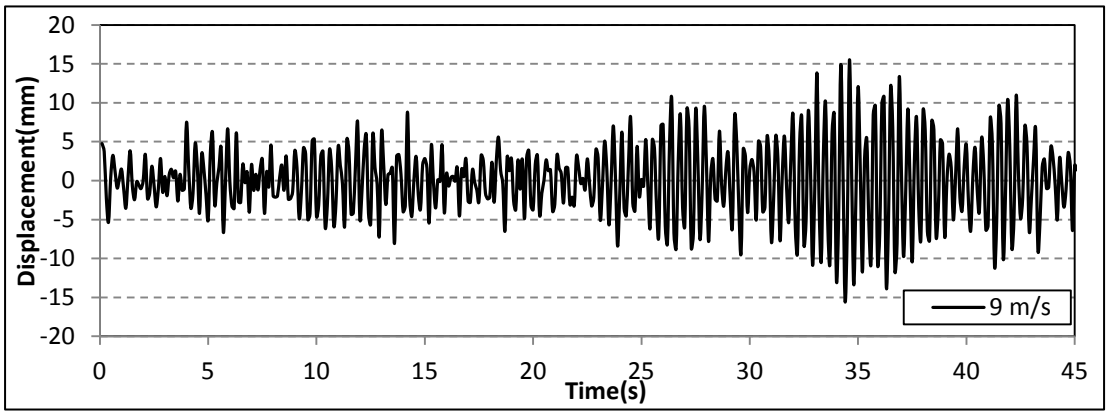
Displacement(mm)
Time(s)
9 m/s

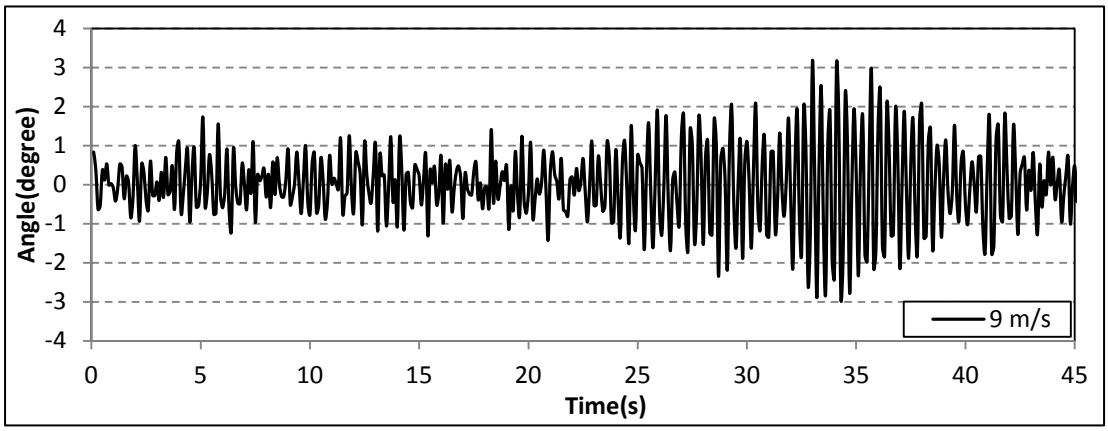
Angle(degree)
Time(s)
9 m/s

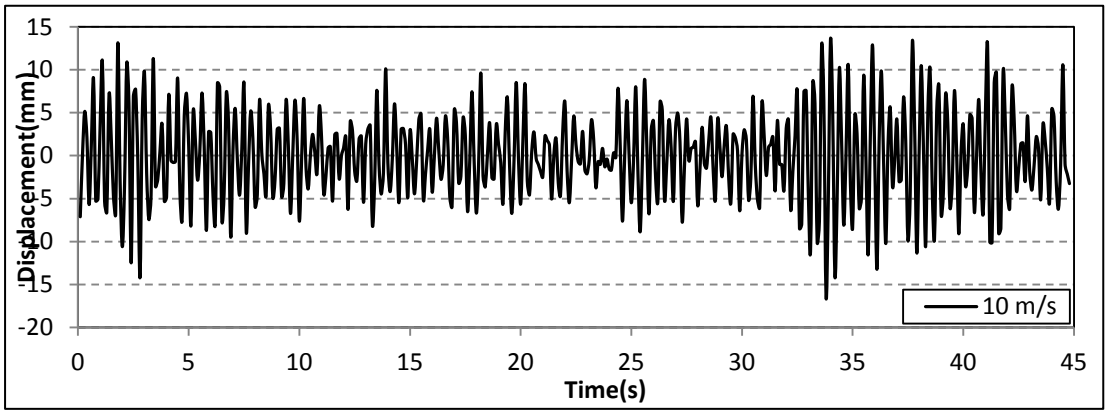
Displacement(mm)
Time(s)
10 m/s

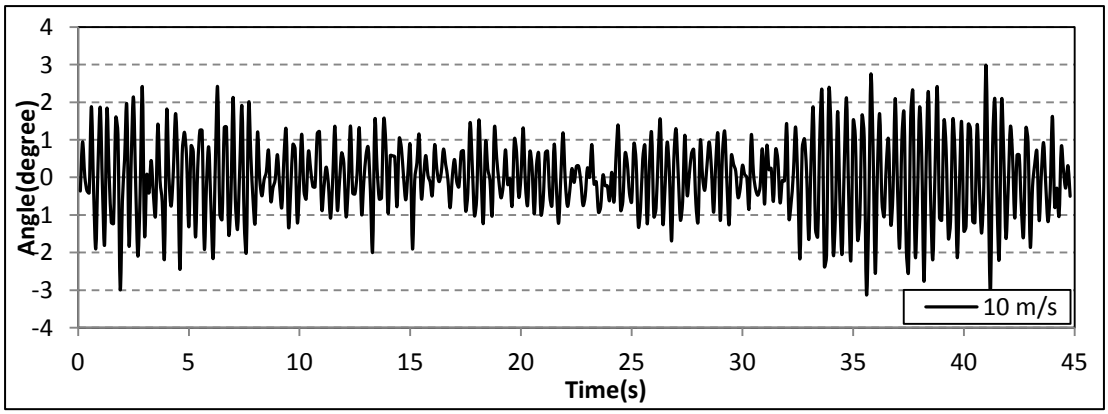
Angle(degree)
Time(s)
10 m/s

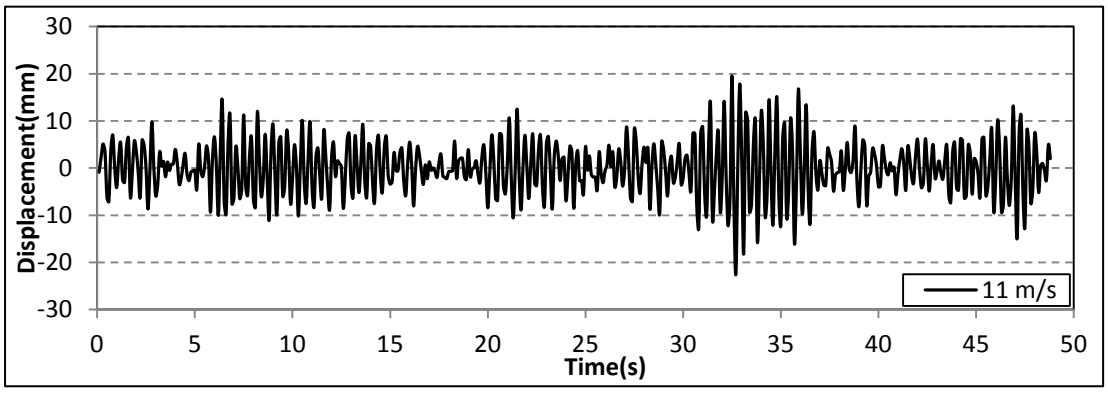
Displacement(mm)
Time(s)
11 m/s

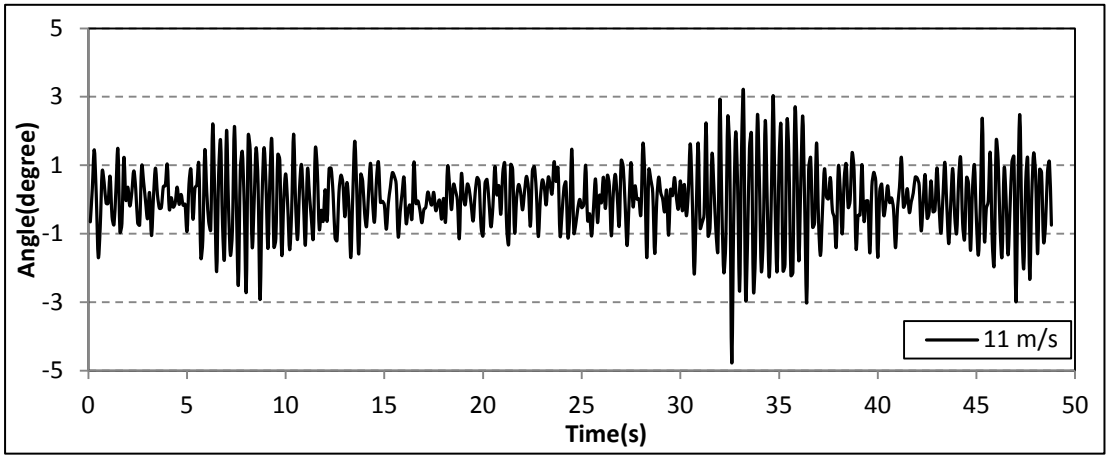

Vertical displacement and torsional angle time histories for 7 m/s to 11 m/s wind speed under 4 °attack angle (30 mm high edge wind barrier)

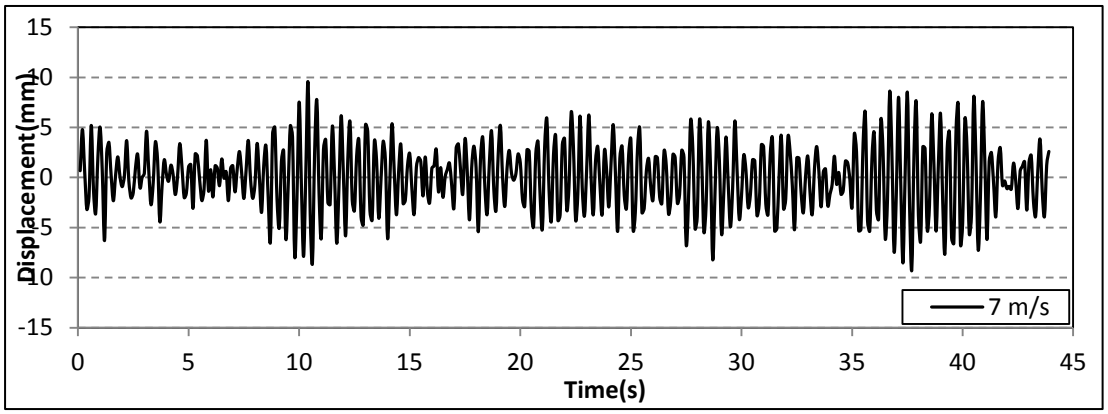

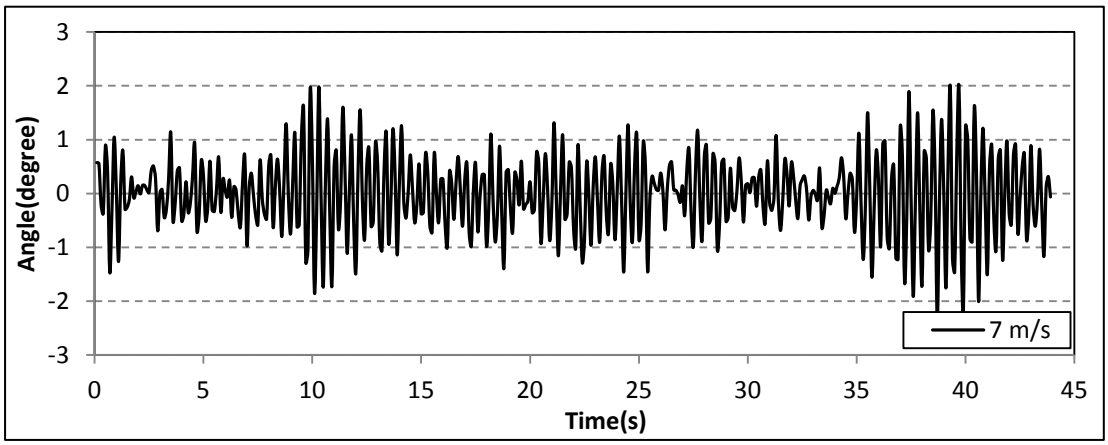

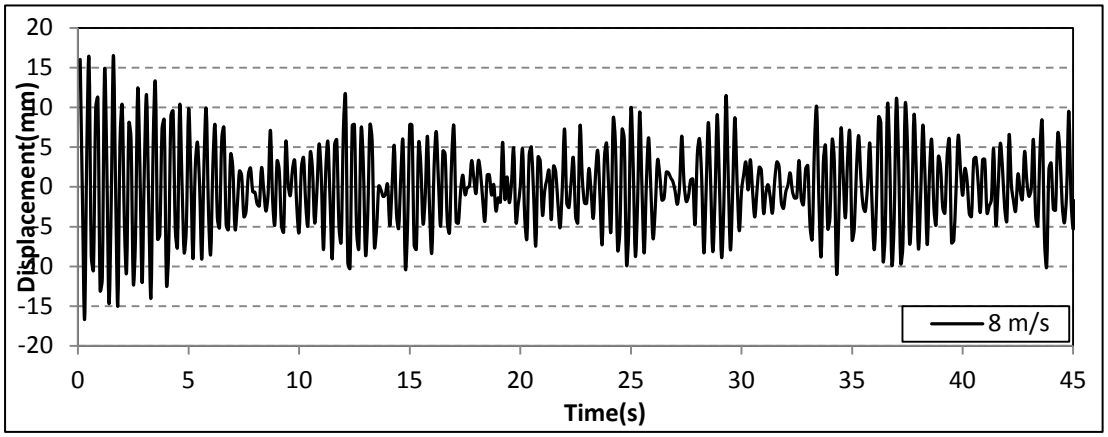
Displacement(mm)
Time(s)
8 m/s

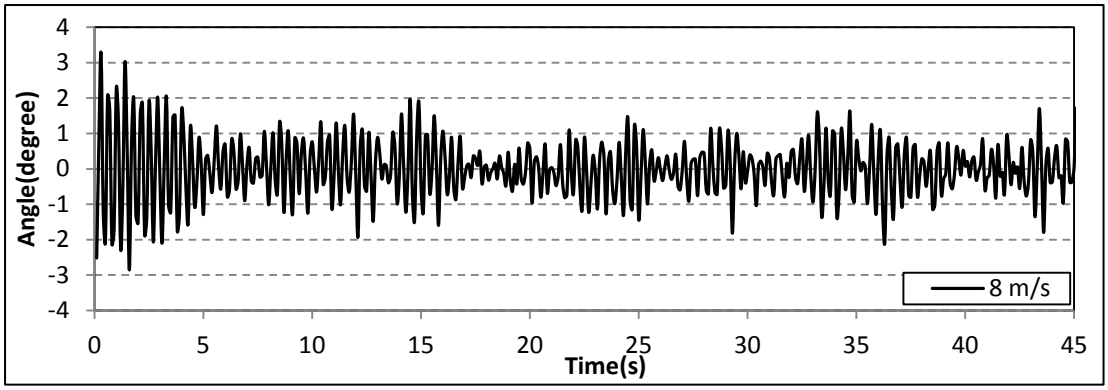
Angle(degree)
Time(s)
8 m/s

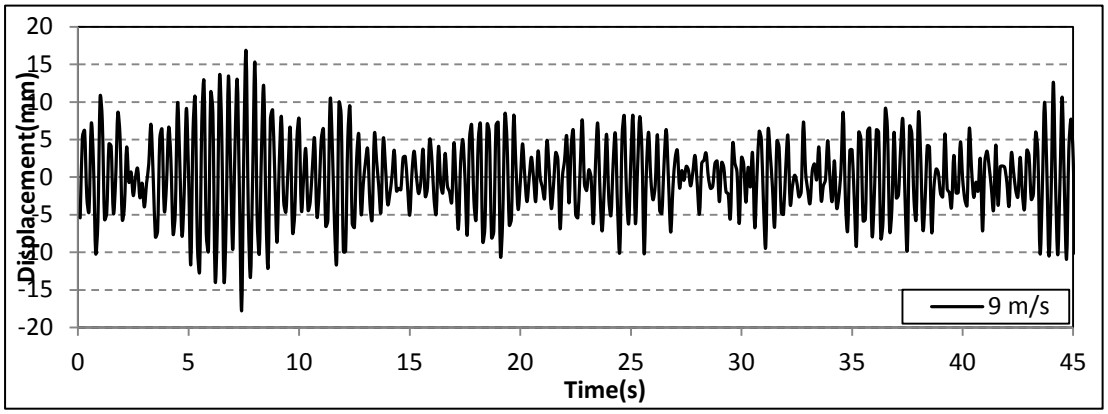
Displacement(mm)
Time(s)
9 m/s

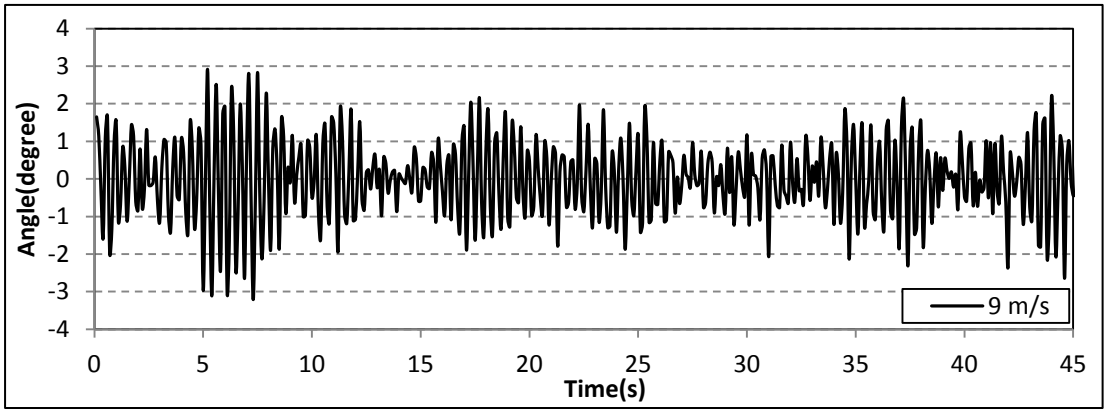
Angle(degree)
Time(s)
9 m/s

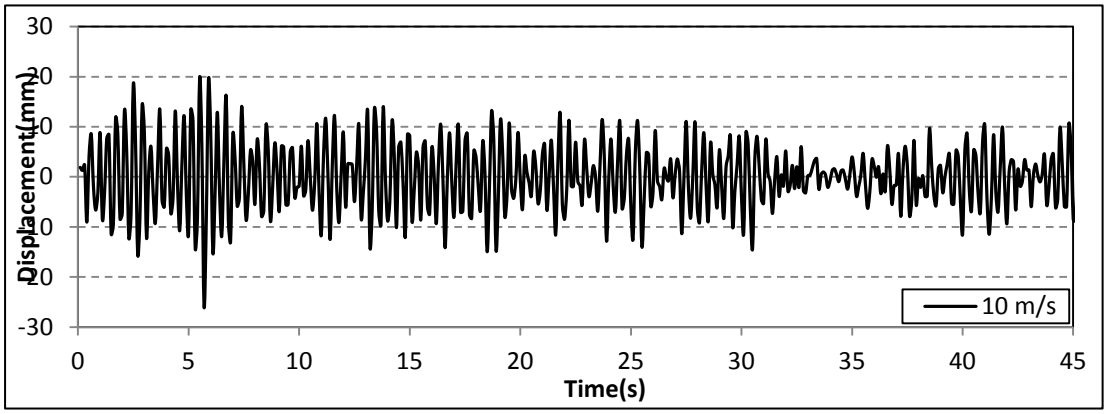

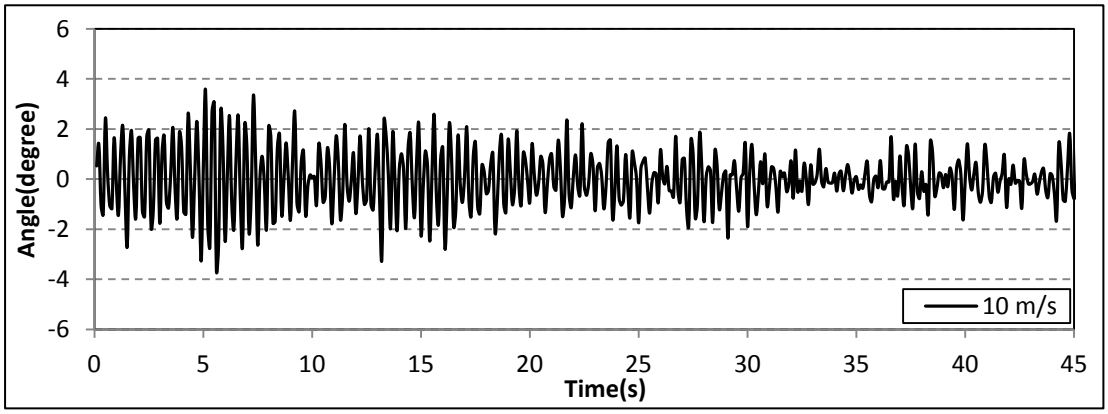

Vertical displacement and torsional angle time histories from 7 m/s to 10 m/s wind speed under 6 °attack angle (30 mm high edge wind barrier)

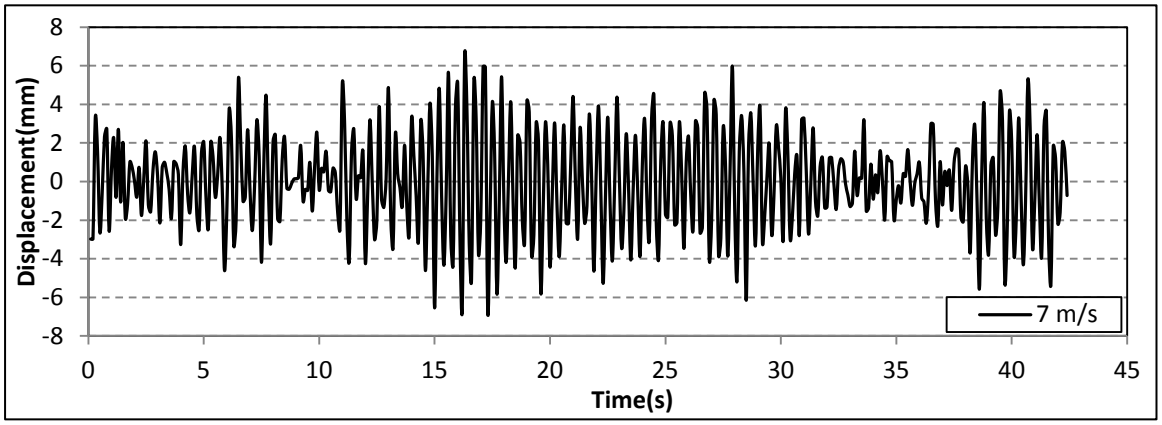

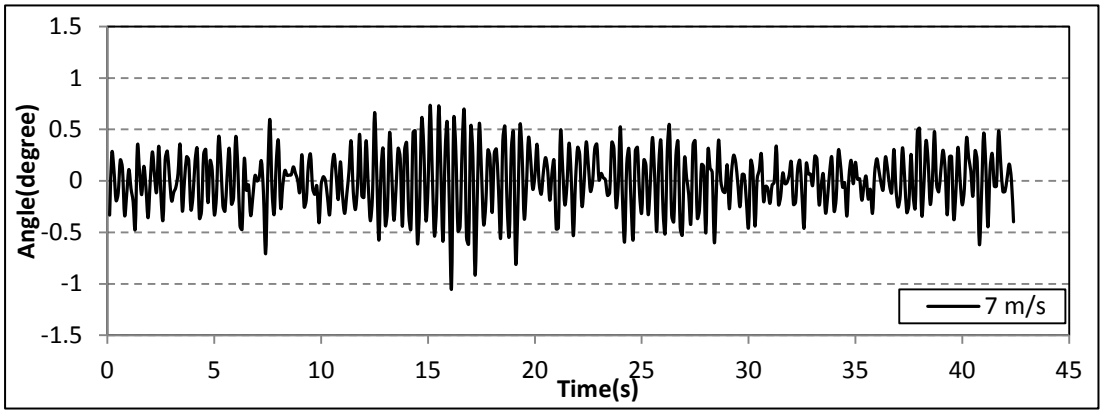
Angle(degree)
Time(s)
7 m/s

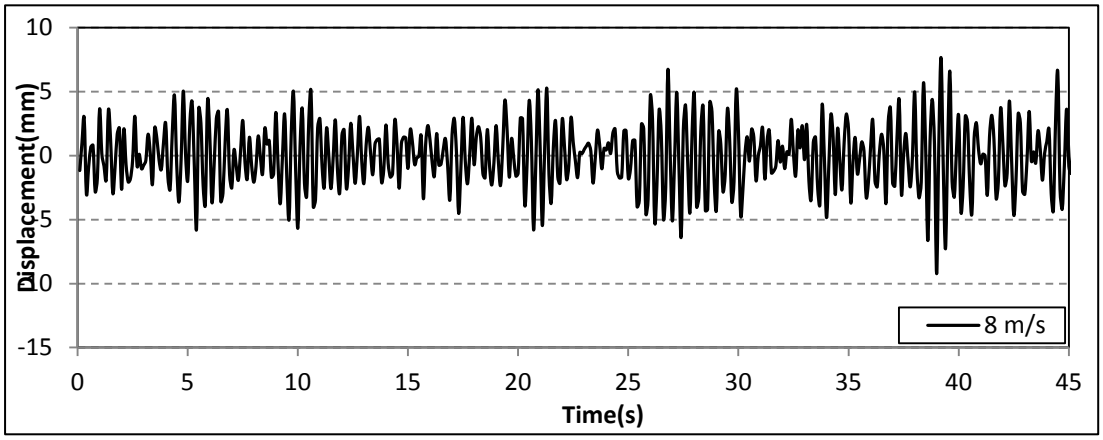
Displacement(mm)
Time(s)
8 m/s

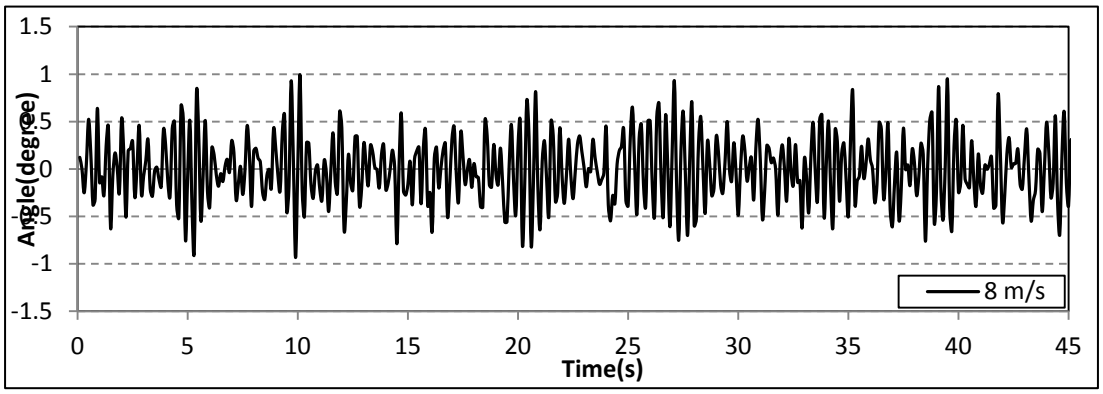
Angle(degree)
Time(s)
8 m/s

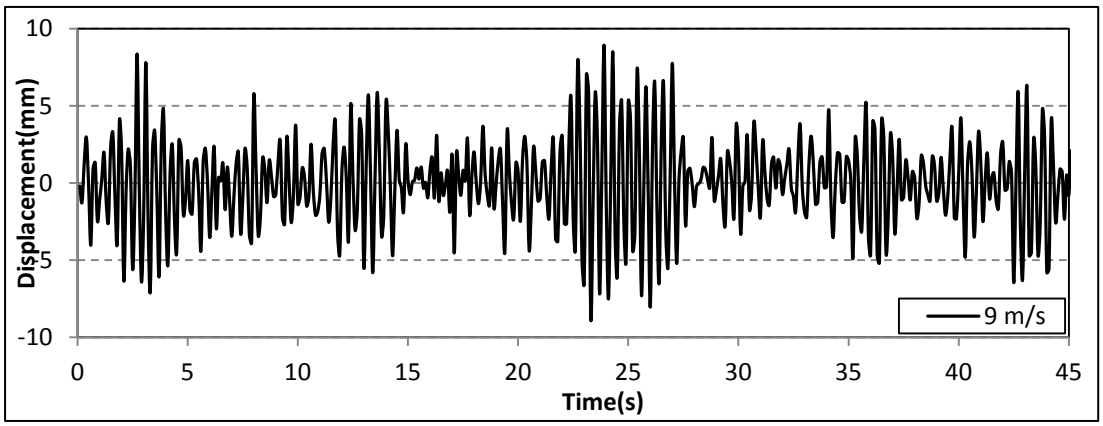
Displacement(mm)
Time(s)
9 m/s

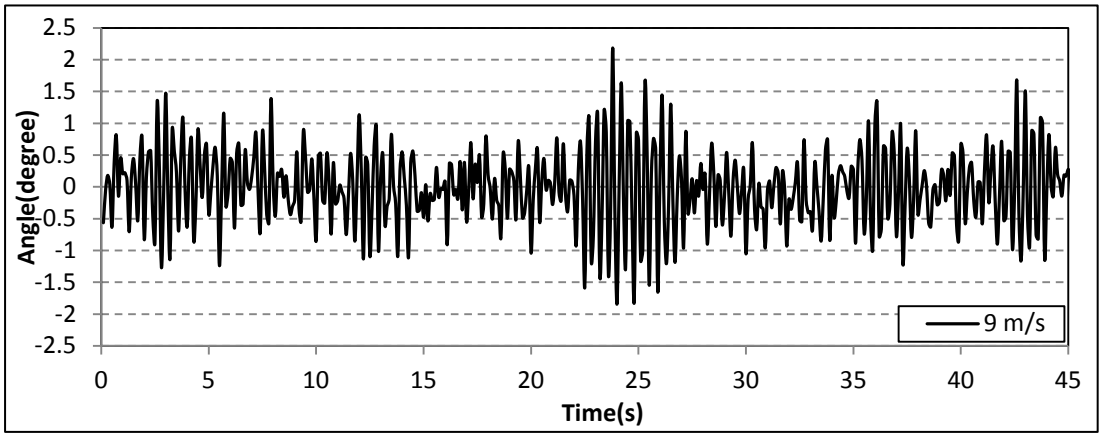

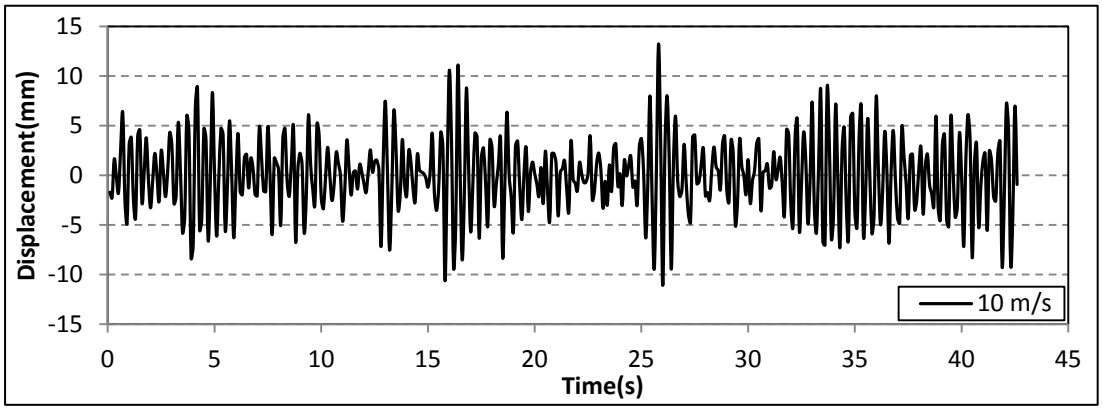

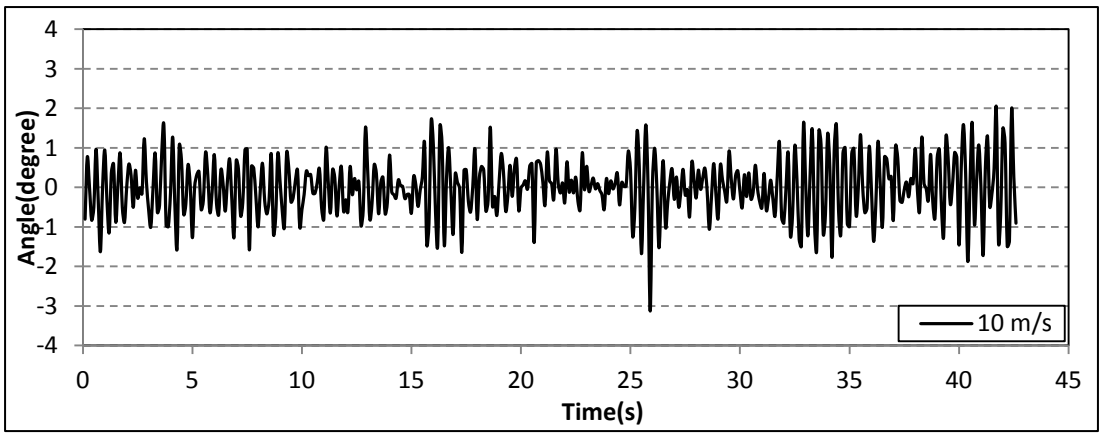

Vertical displacement and torsional angle time histories from 7 m/s to 10 m/s wind speed under 0 °attack angle (50 mm high edge wind barrier)

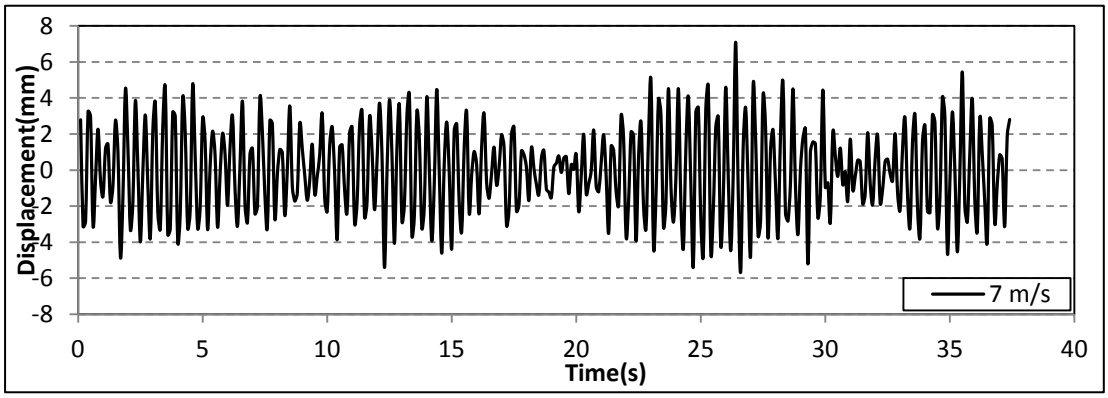
Displacement(mm)
8
6
4
2
0
-2
-4
-6
-8
0
5
10
15
20
25
30
35
40
Time(s)
7 m/s

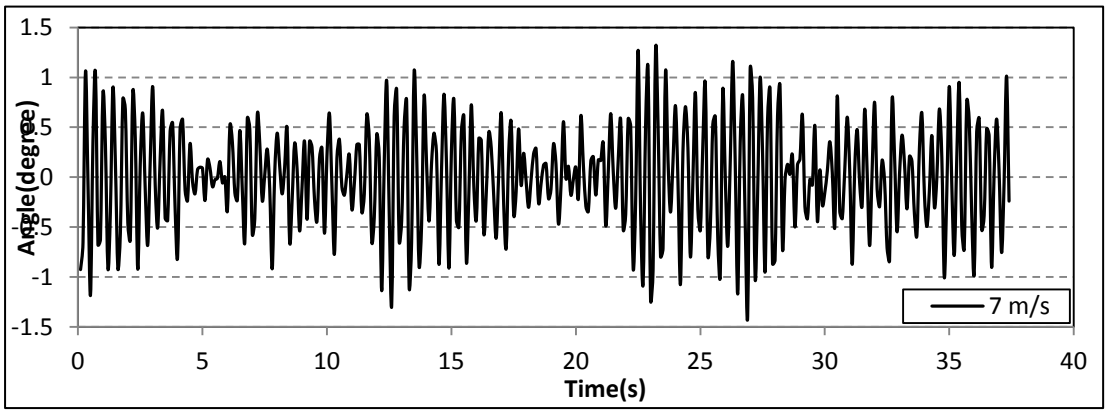
Angle(degree)
1.5
1
0.5
0
-0.5
-1
-1.5
0
5
10
15
20
25
30
35
40
Time(s)
7 m/s

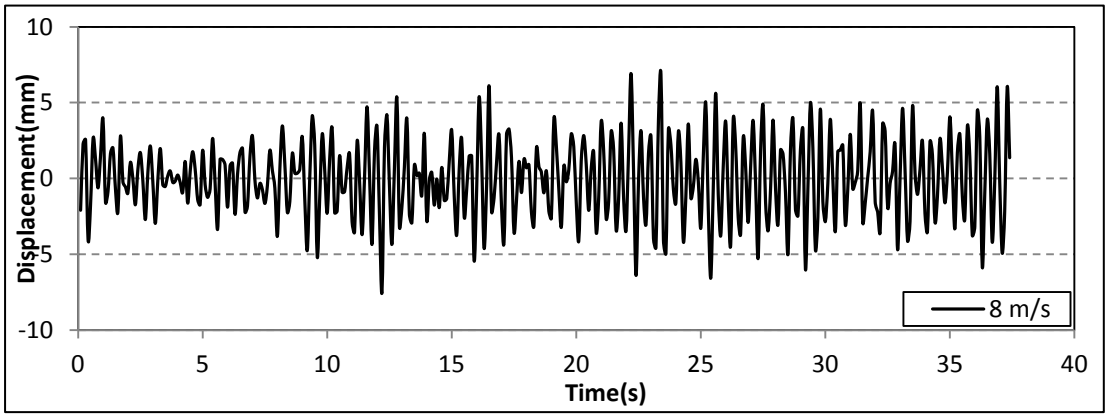
Displacement(mm)
10
5
0
-5
-10
0
5
10
15
20
25
30
35
40
Time(s)
8 m/s

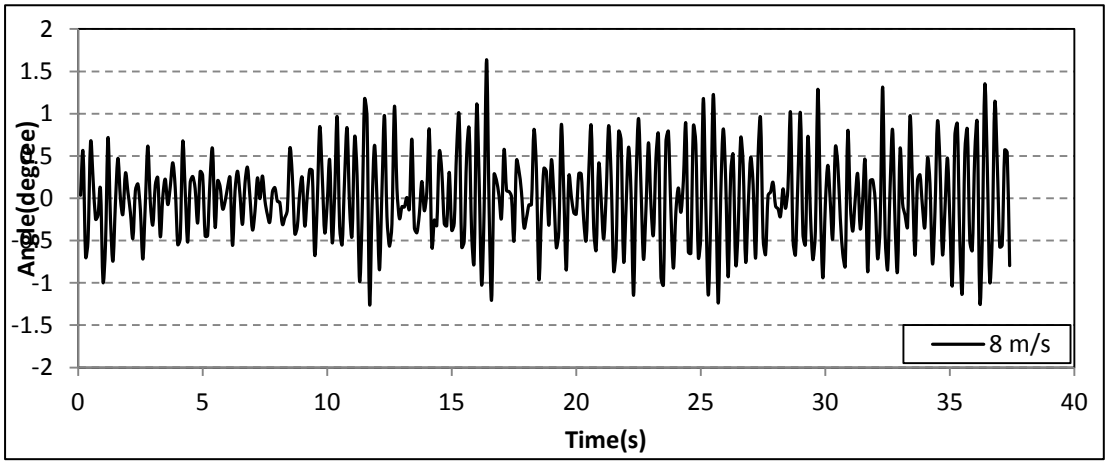
Angle(degree)
Time(s)
8 m/s

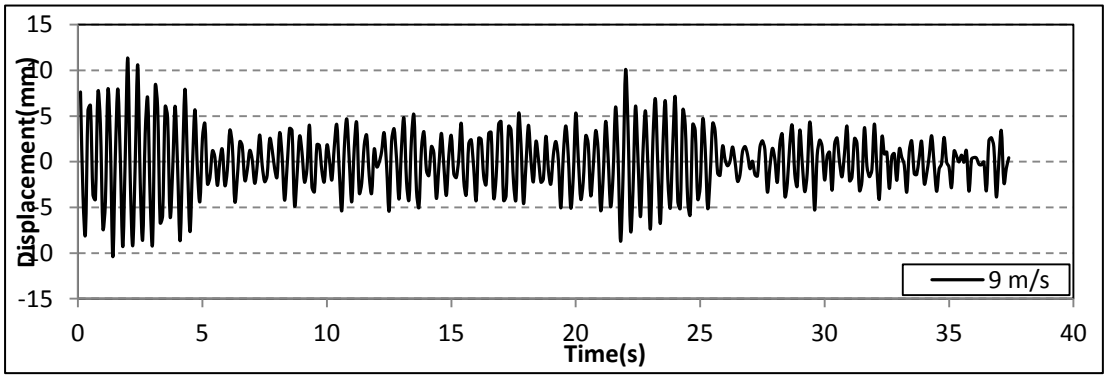
Displacement(mm)
Time(s)
9 m/s

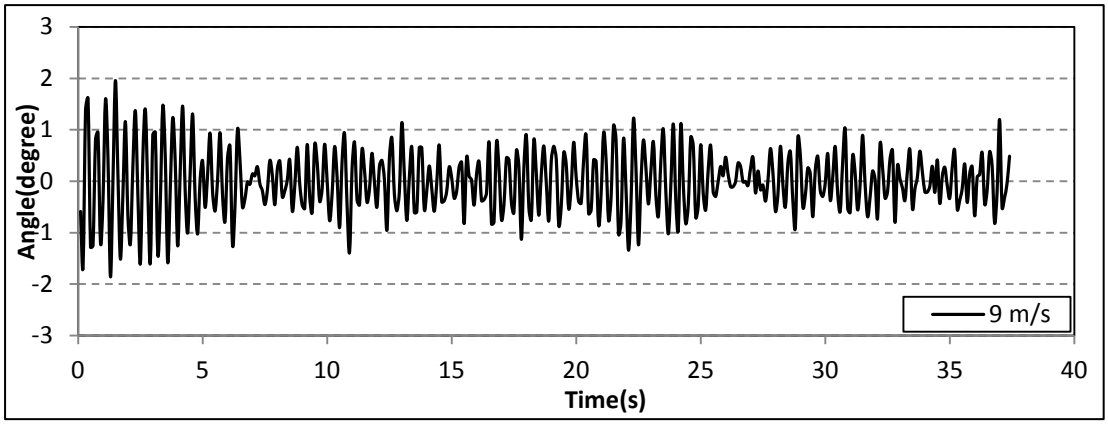
Angle(degree)
Time(s)
9 m/s

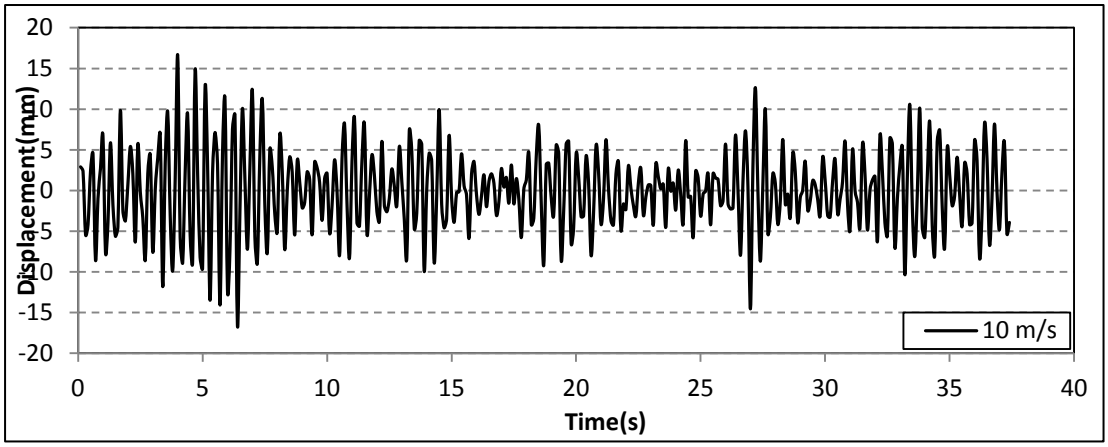
Displacement(mm)
Time(s)
10 m/s

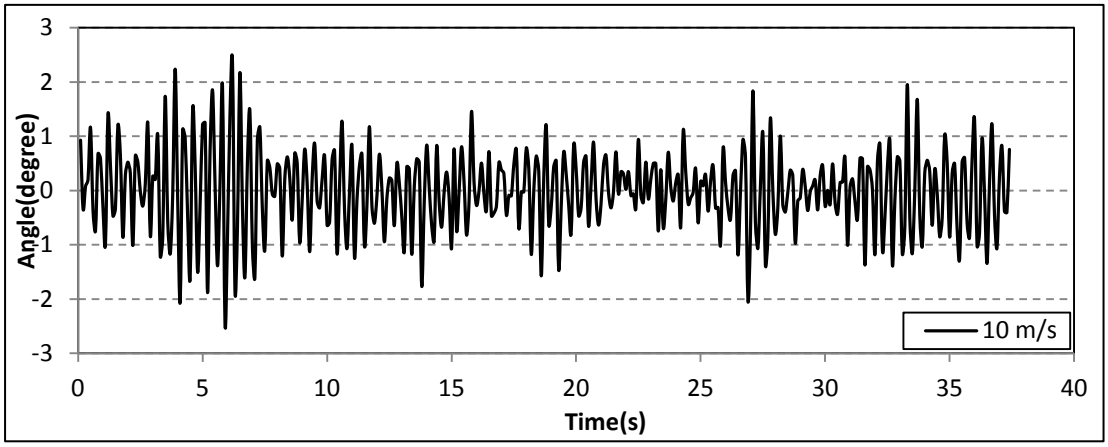
Angle(degree)
Time(s)
10 m/s

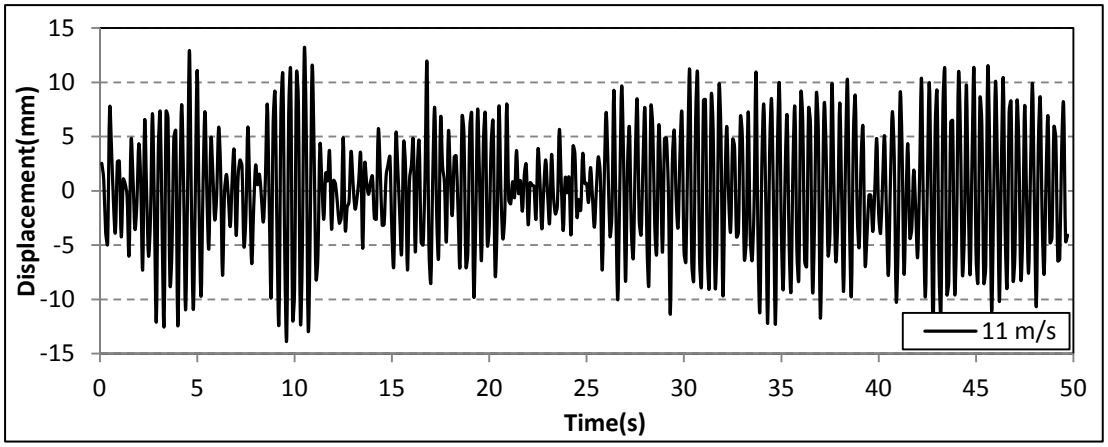
Displacement(mm)
Time(s)
11 m/s

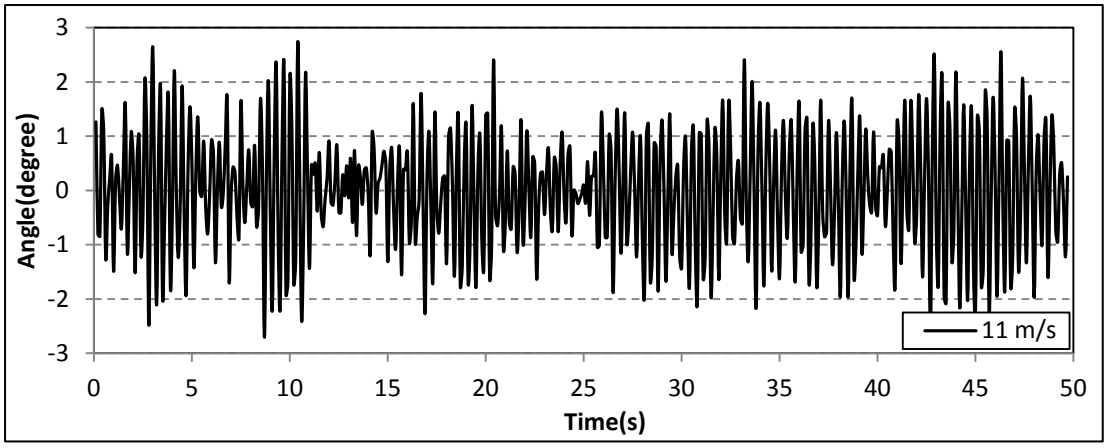

Vertical displacement and torsional angle time histories from 7 m/s to 11 m/s wind speed under -2 °attack angle (50 mm high edge wind barrier)

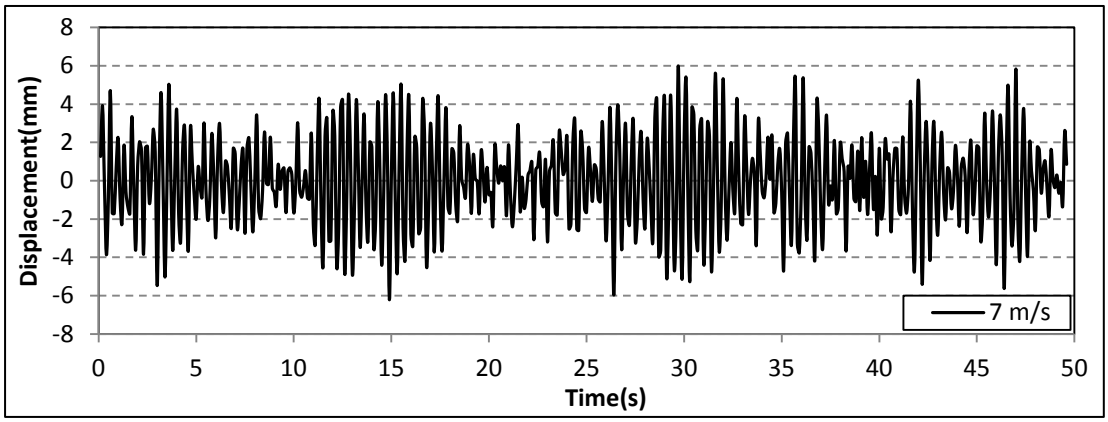

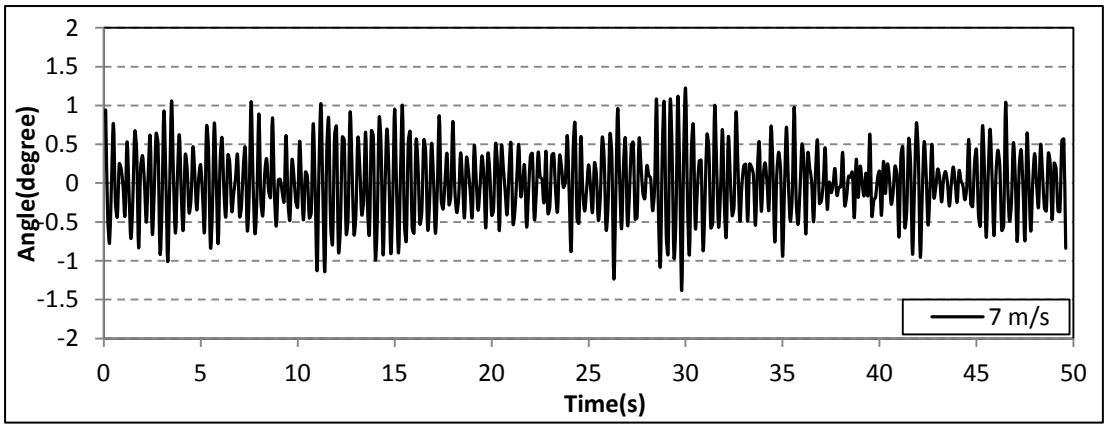

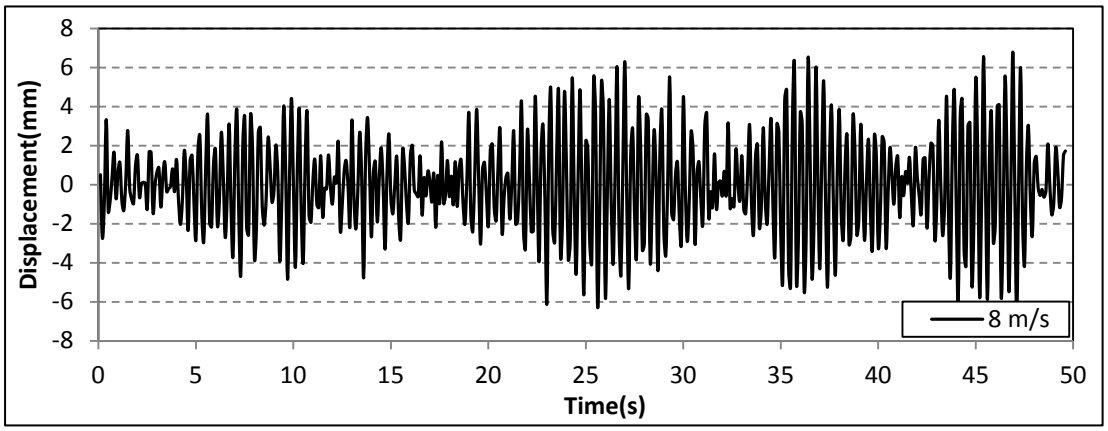
Displacement(mm)
8
6
4
2
0
-2
-4
-6
-8
0
5
10
15
20
25
30
35
40
45
50
Time(s)
8 m/s

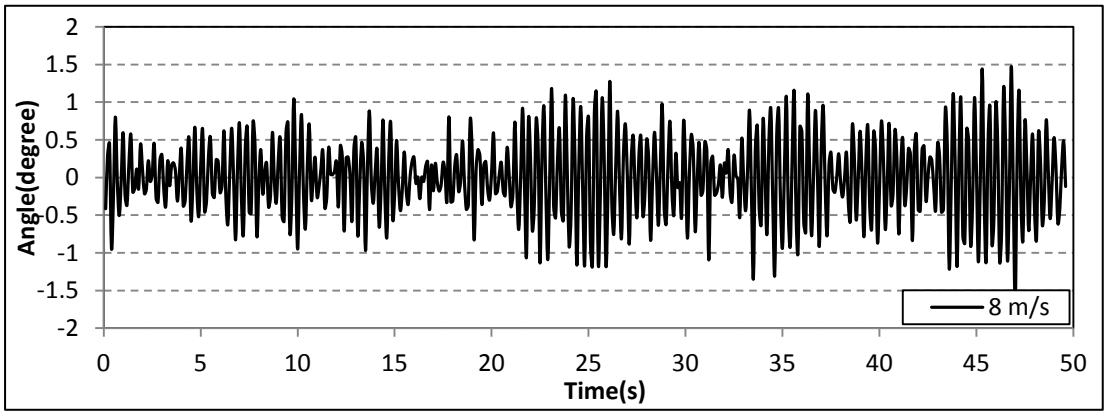
Angle(degree)
2
1.5
1
0.5
0
-0.5
-1
-1.5
-2
0
5
10
15
20
25
30
35
40
45
50
Time(s)
8 m/s

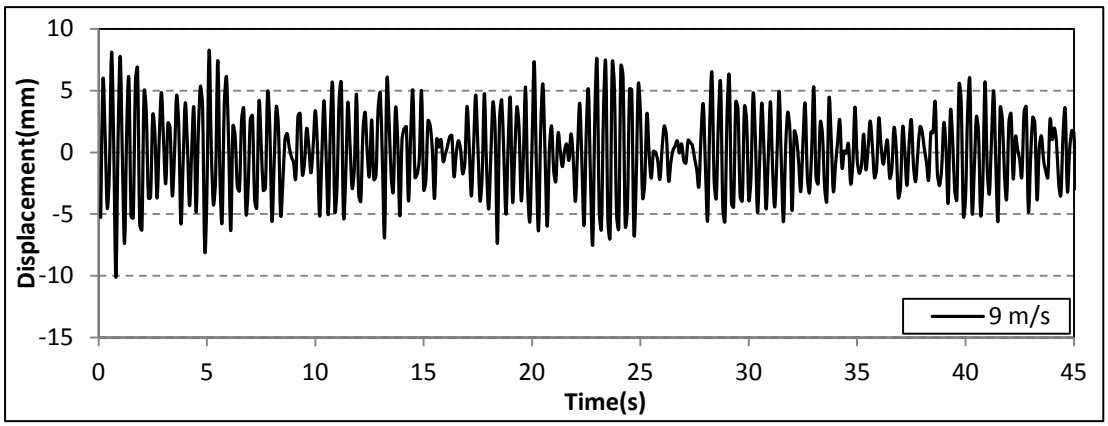
Displacement(mm)
10
5
0
-5
-10
-15
0
5
10
15
20
25
30
35
40
45
Time(s)
9 m/s

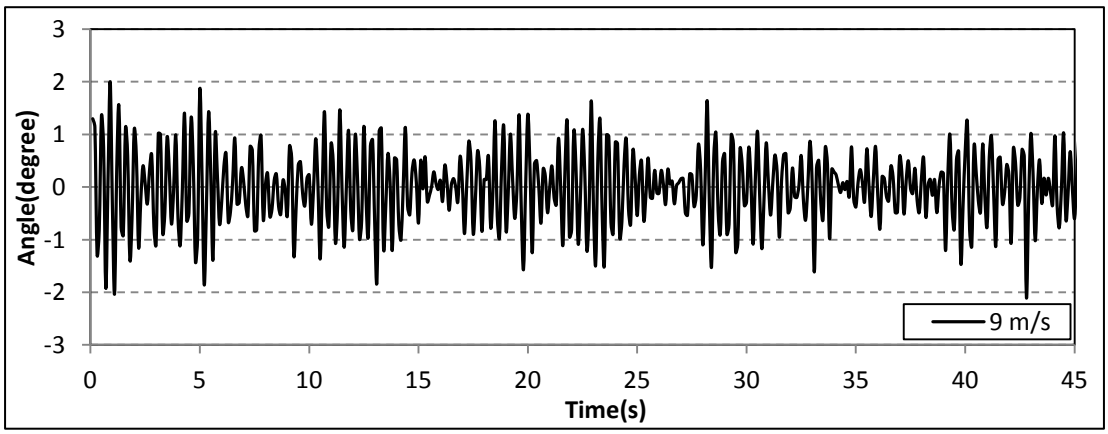
Angle(degree)
3
2
1
0
-1
-2
-3
0
5
10
15
20
25
30
35
40
45
Time(s)
9 m/s

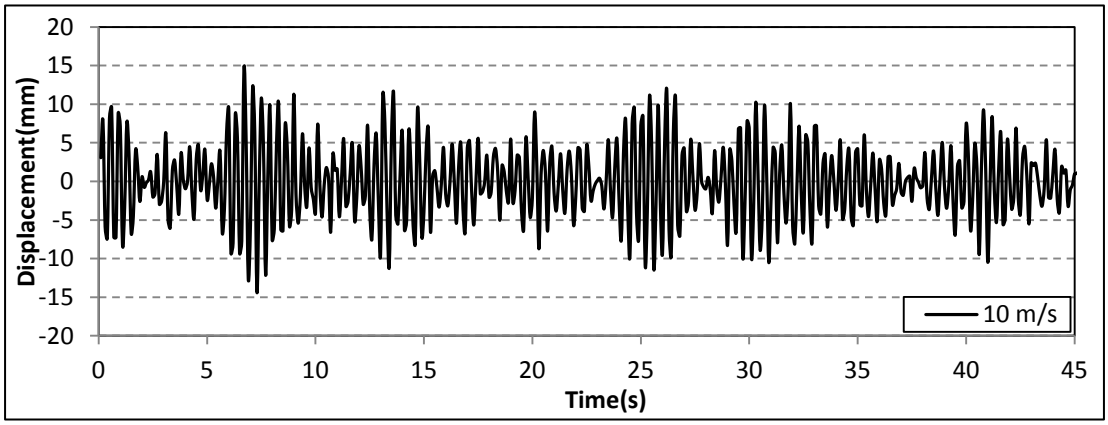
Displacement(mm)
20
15
10
5
0
-5
-10
-15
-20
0
5
10
15
20
25
30
35
40
45
Time(s)
10 m/s

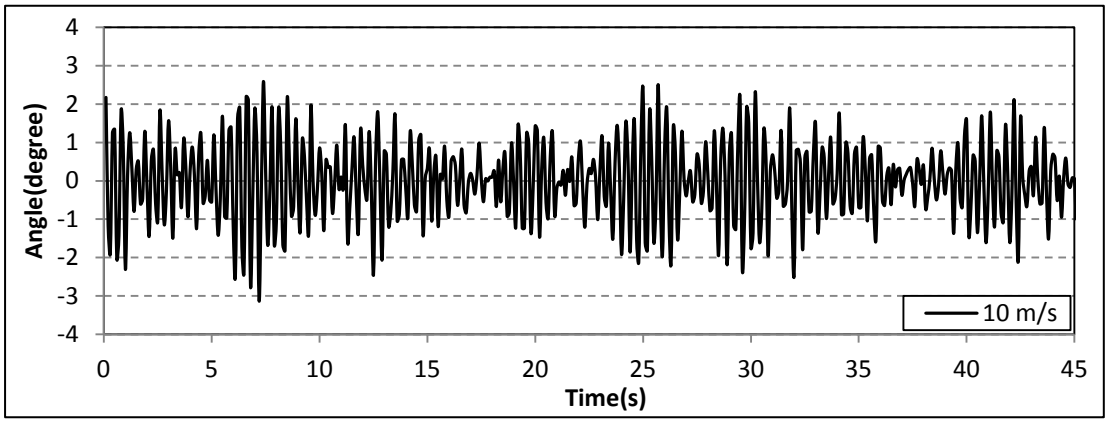
Angle(degree)
4
3
2
1
0
-1
-2
-3
-4
0
5
10
15
20
25
30
35
40
45
Time(s)
10 m/s

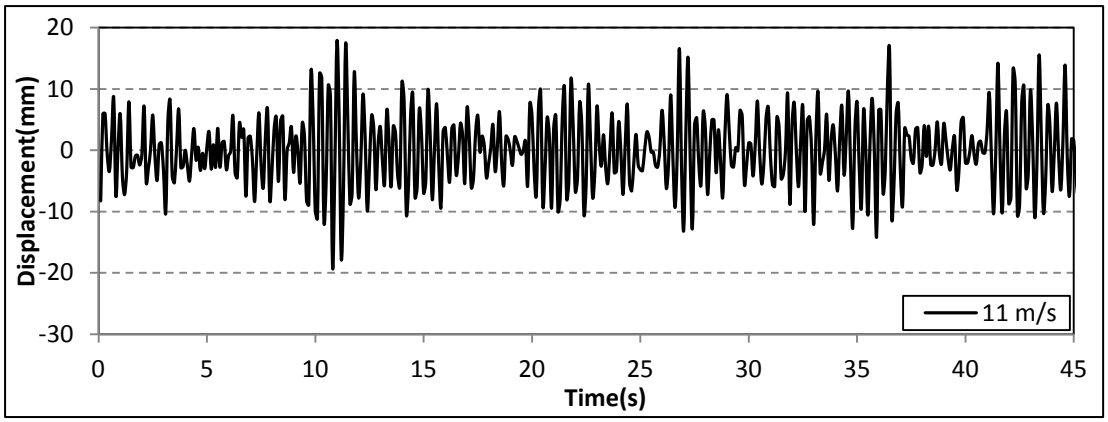
Displacement(mm)
20
10
0
-10
-20
-30
0
5
10
15
20
25
30
35
40
45
Time(s)
11 m/s

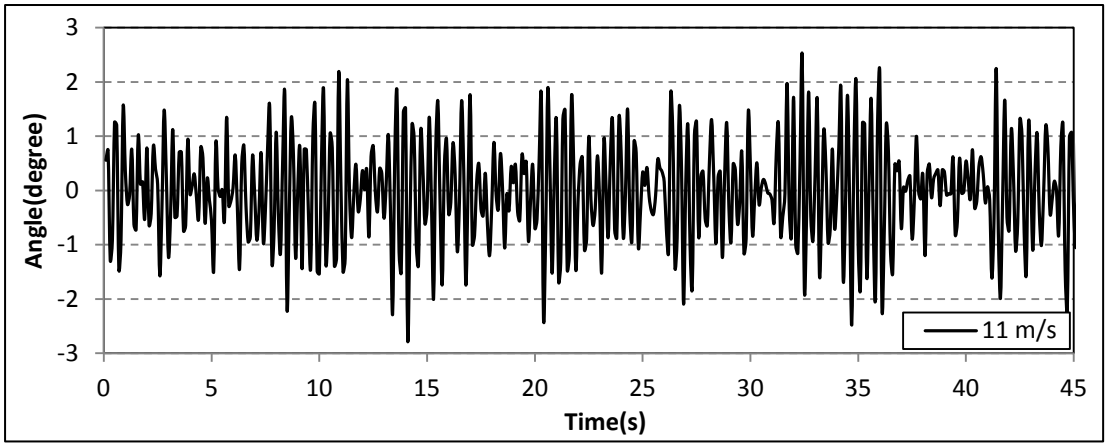

Vertical displacement and torsional angle time histories from 3 m/s to 11 m/s wind speed under -4 °attack angle (50 mm high edge wind barrier)

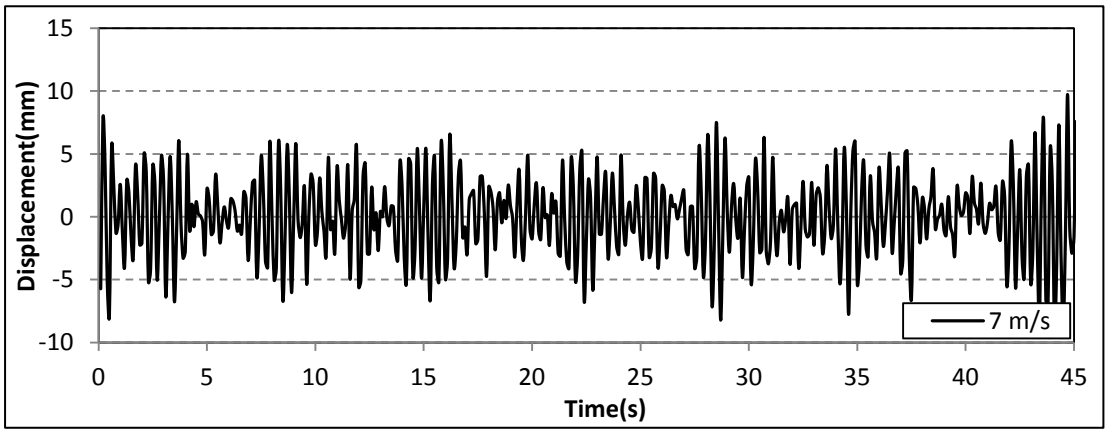

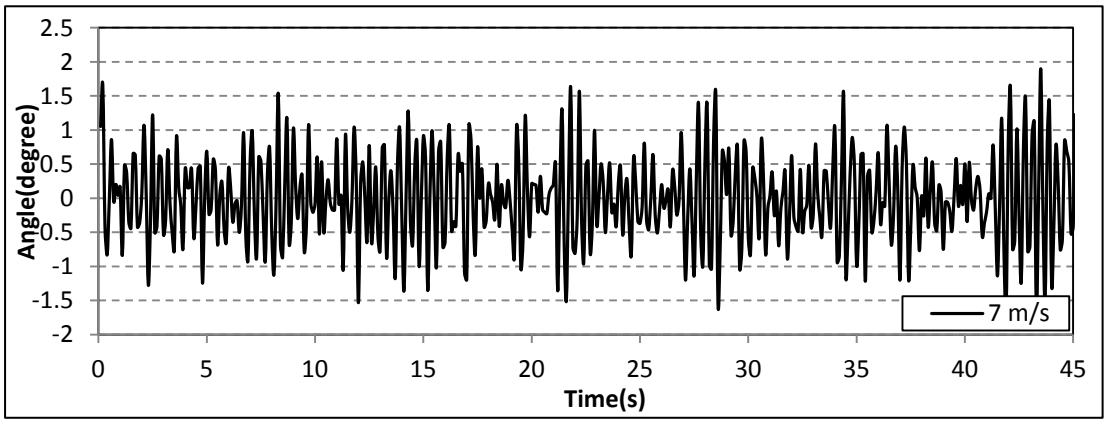

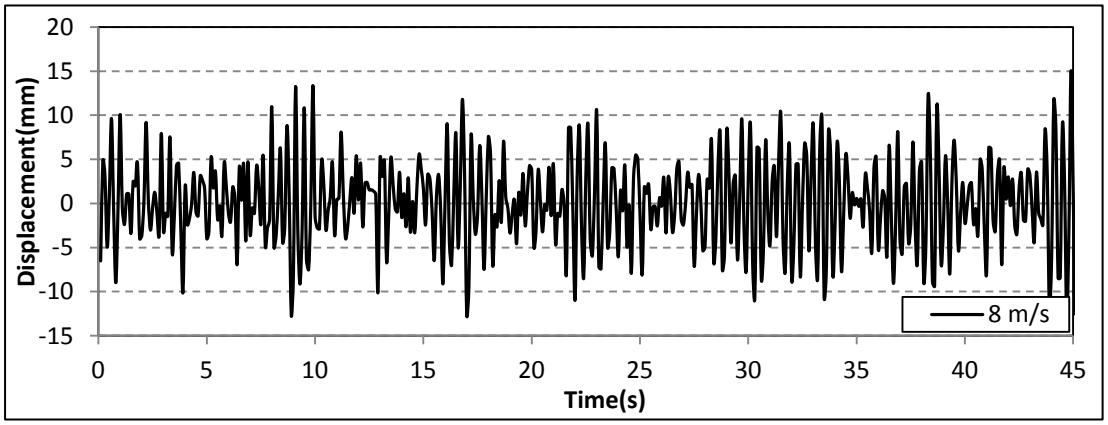
Displacement(mm)
Time(s)
8 m/s

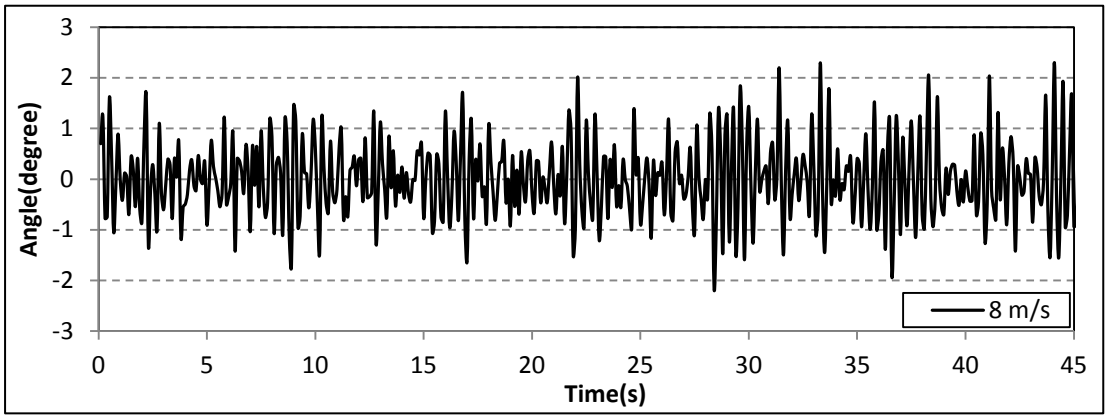
Angle(degree)
Time(s)
8 m/s

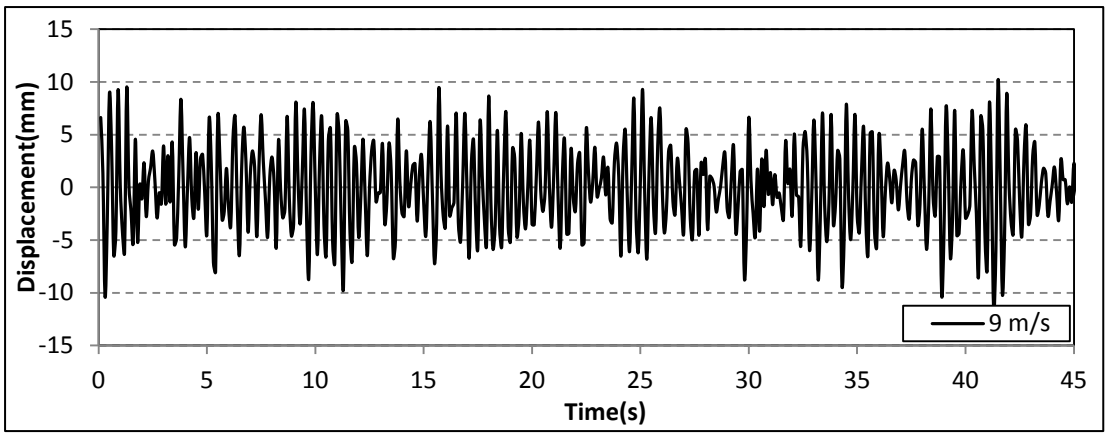
Displacement(mm)
Time(s)
9 m/s

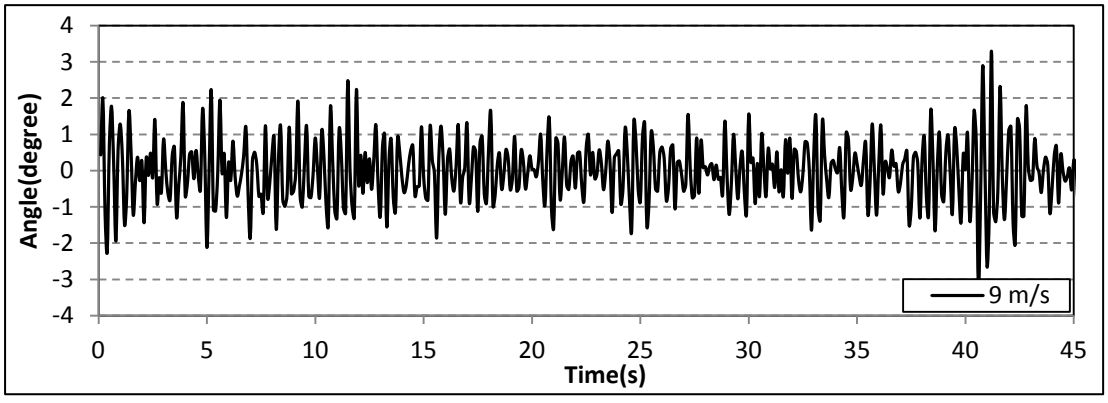
Angle(degree)
Time(s)
9 m/s

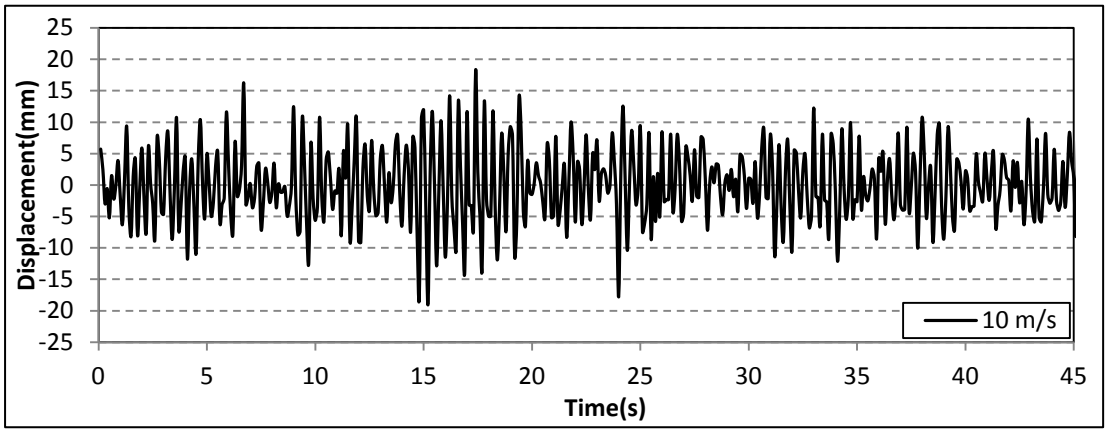

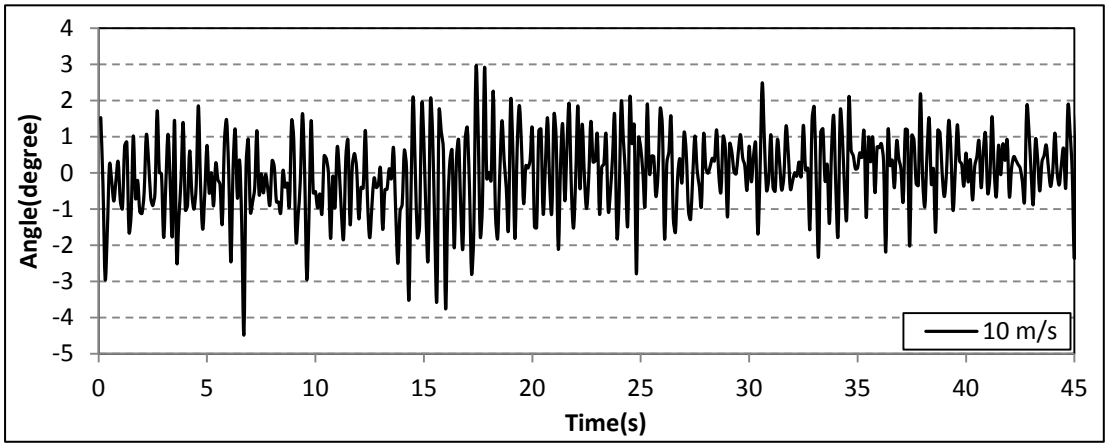

Vertical displacement and torsional angle time histories from 7 m/s to 10 m/s wind speed under -6 °attack angle (50 mm high edge wind barrier)

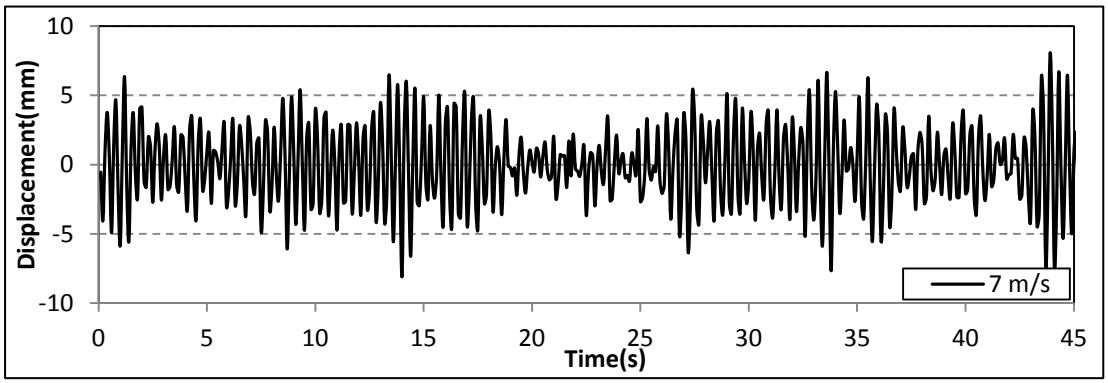

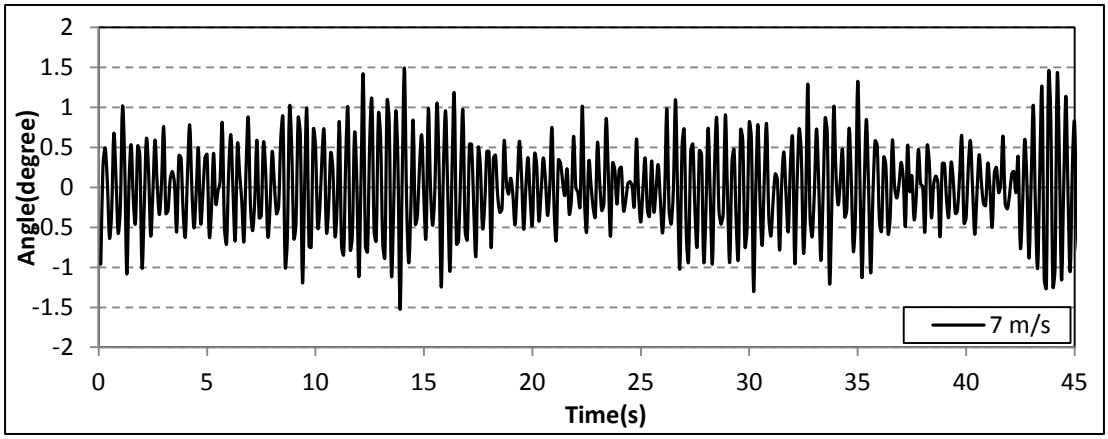
Angle(degree)
Time(s)
7 m/s

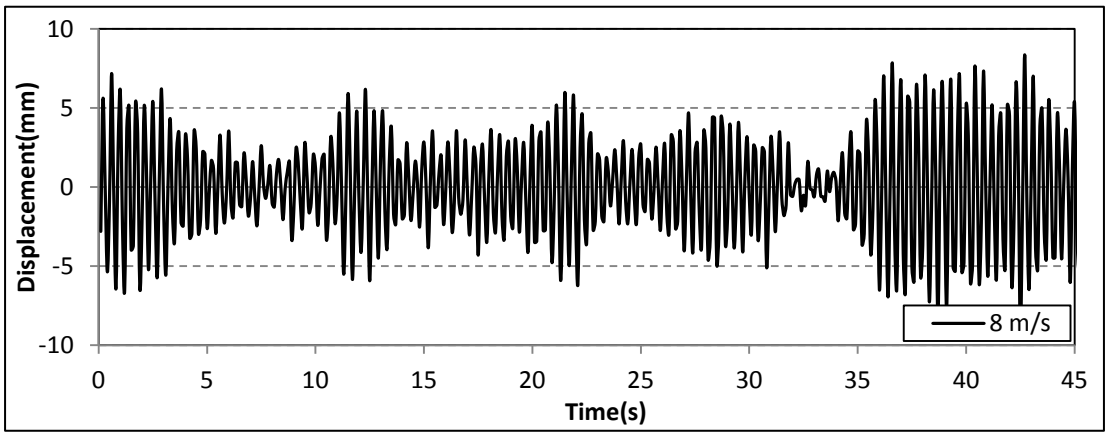
Displacement(mm)
Time(s)
8 m/s

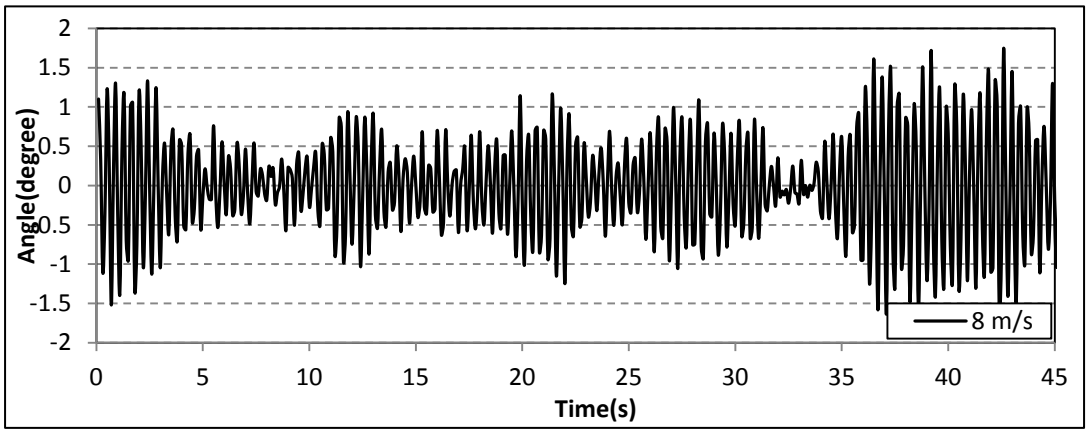
Angle(degree)
Time(s)
8 m/s

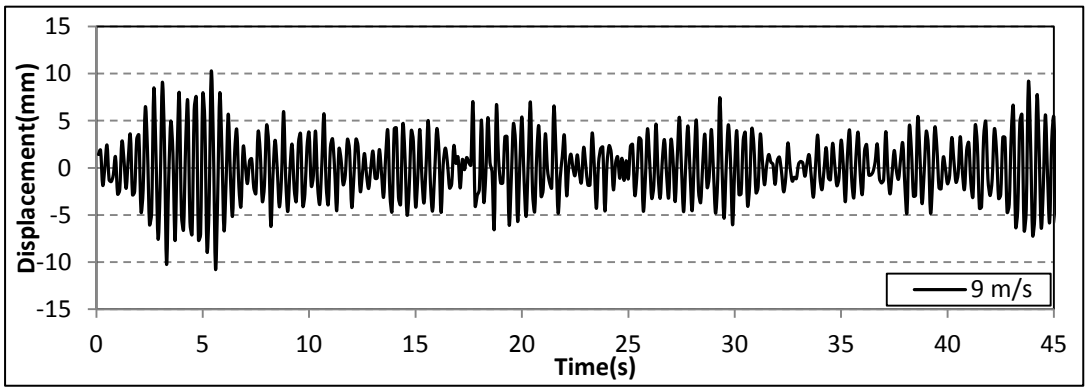
Displacement(mm)
Time(s)
9 m/s

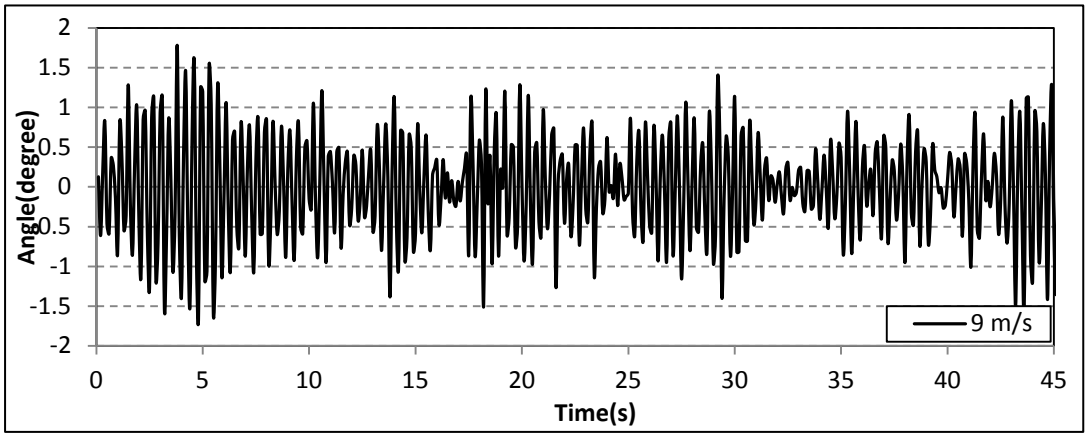
Angle(degree)
Time(s)
9 m/s

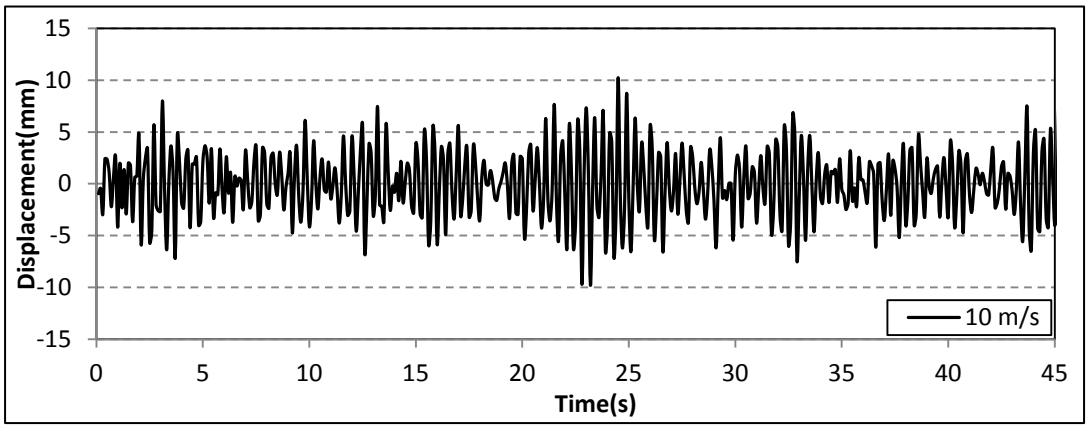
Displacement(mm)
Time(s)
10 m/s

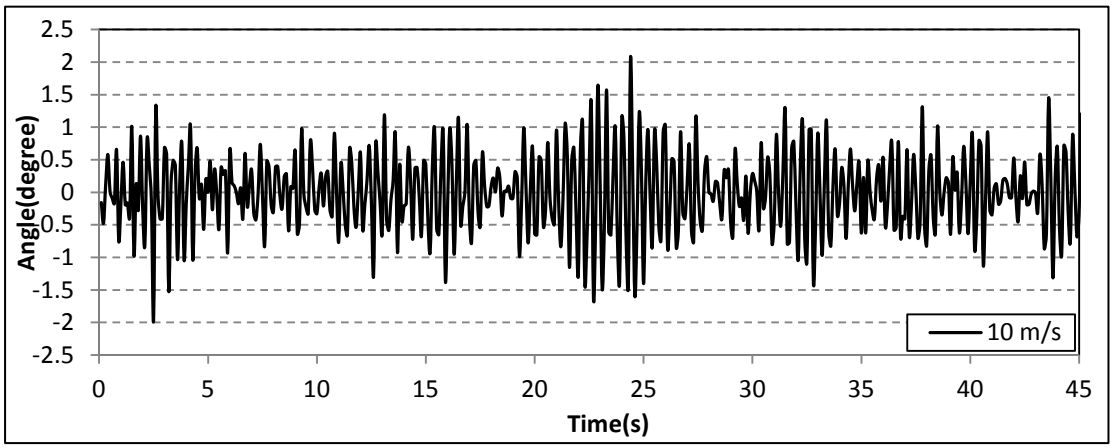
Angle(degree)
Time(s)
10 m/s

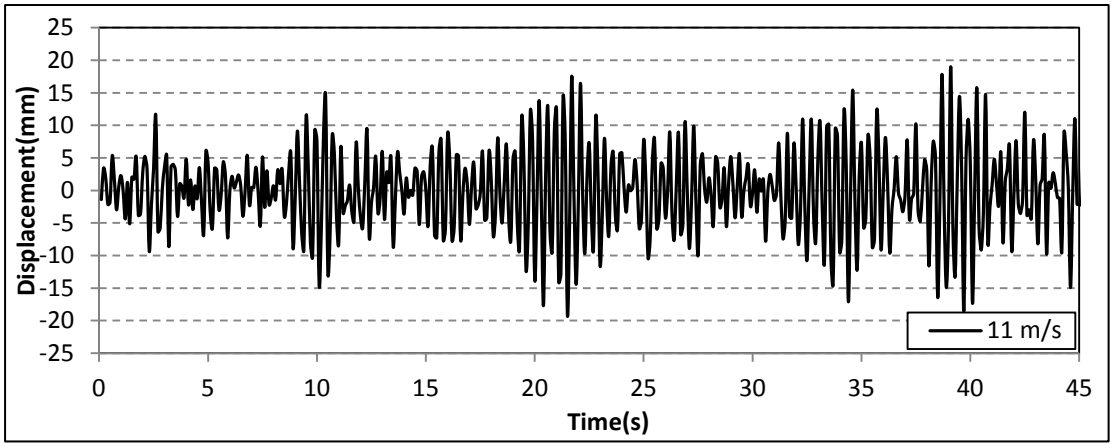

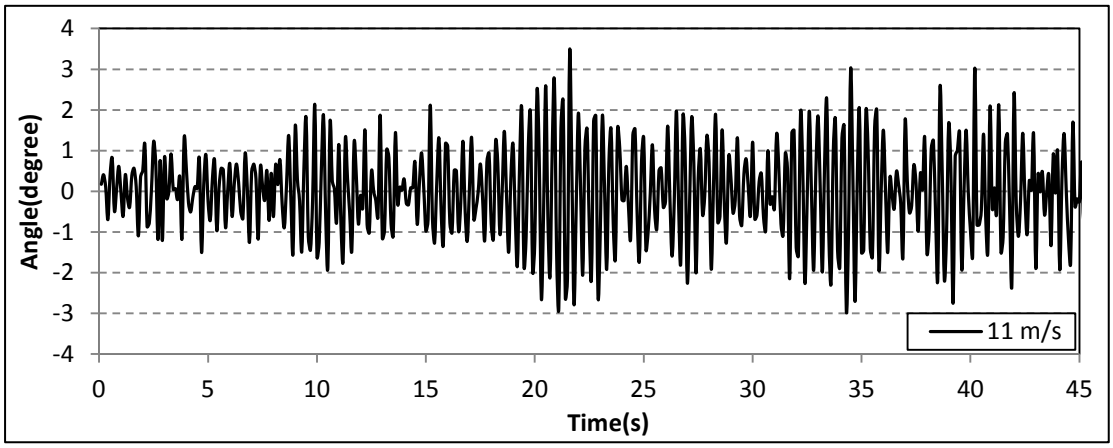

Vertical displacement and torsional angle time histories from 7 m/s to 11 m/s wind speed under 2 °attack angle (50 mm high edge wind barrier)

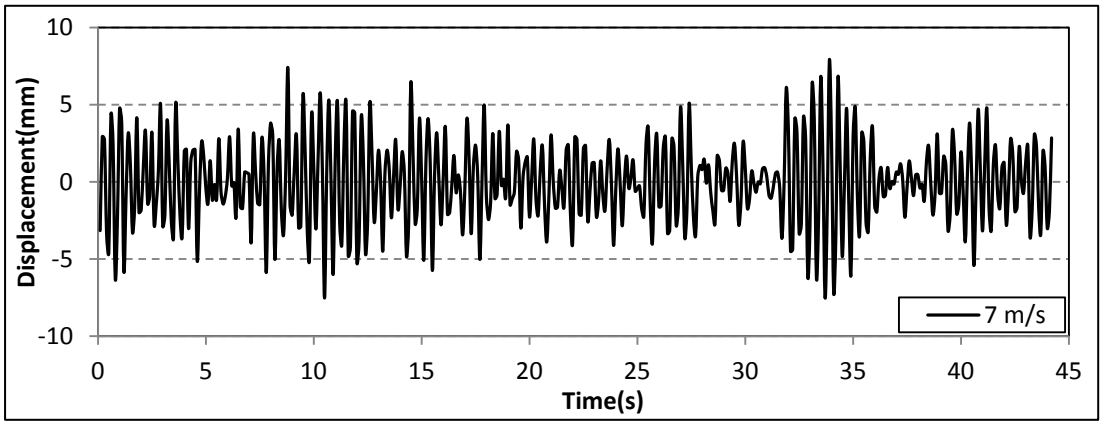

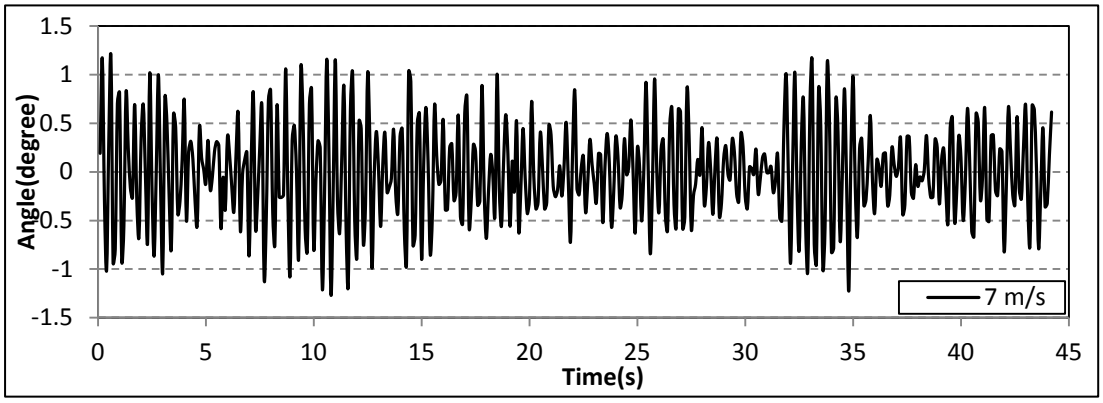
Angle(degree)
Time(s)
7 m/s

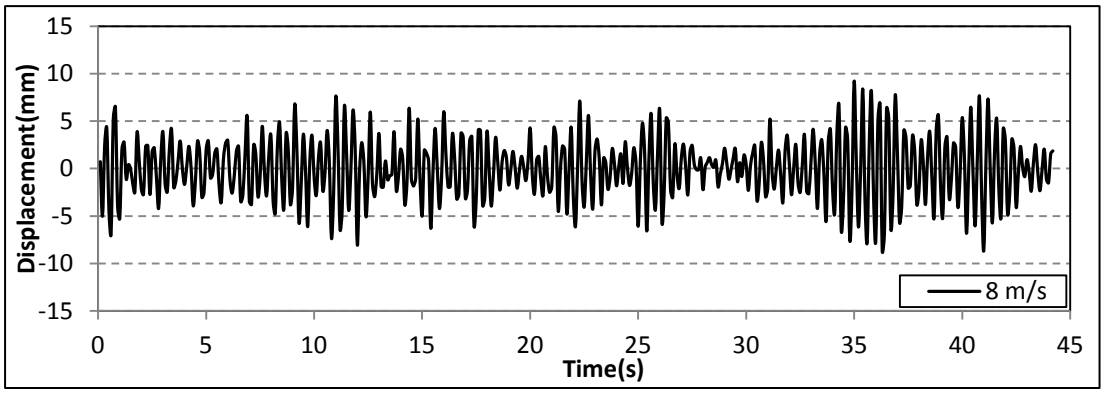
Displacement(mm)
Time(s)
8 m/s

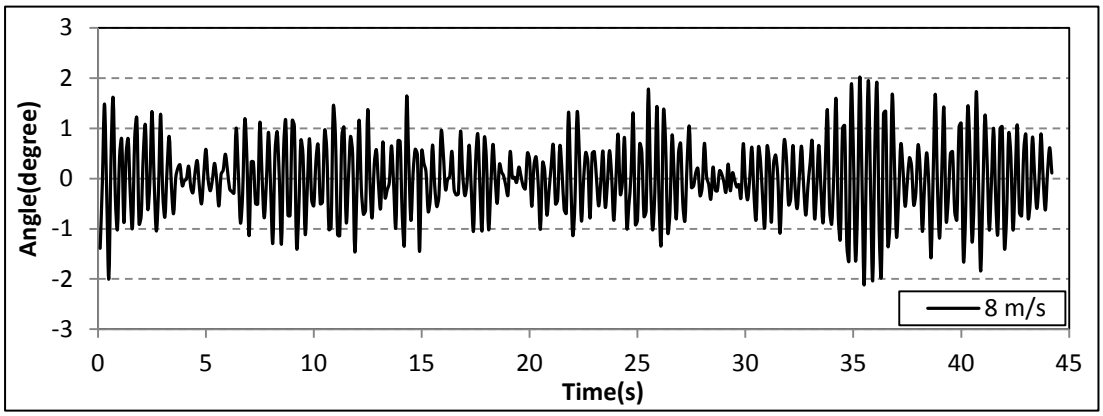
Angle(degree)
Time(s)
8 m/s

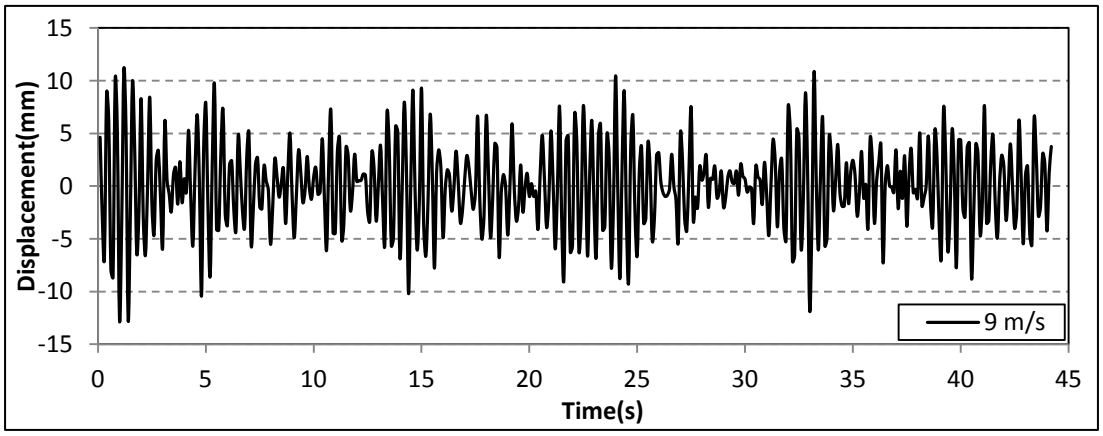
Displacement(mm)
Time(s)
9 m/s

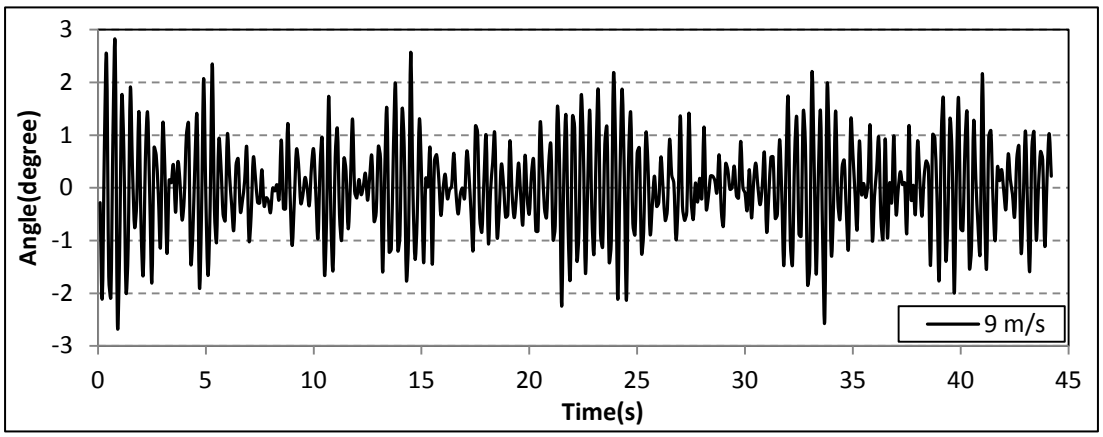
Angle(degree)
Time(s)
9 m/s

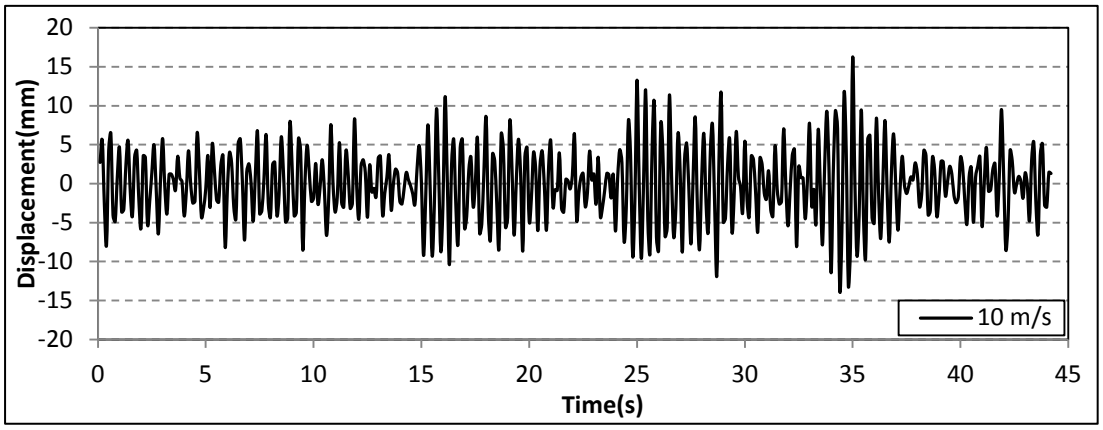
Displacement(mm)
Time(s)
10 m/s

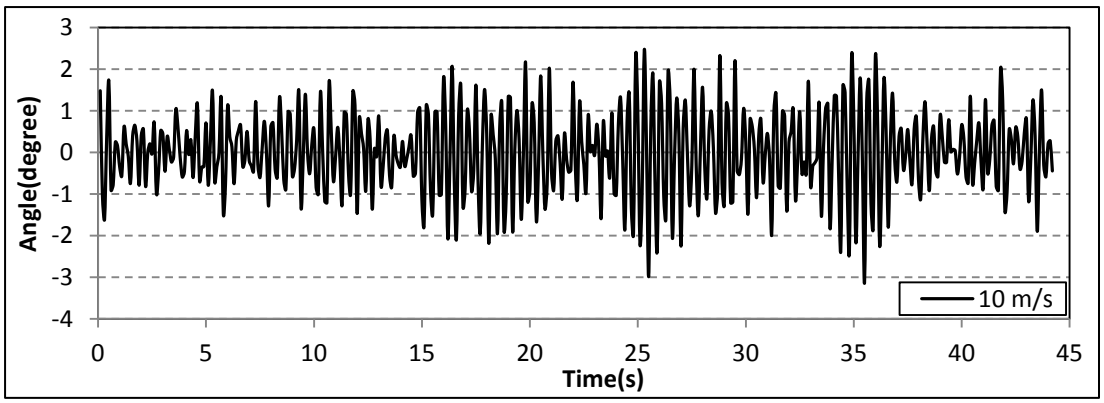
Angle(degree)
Time(s)
10 m/s

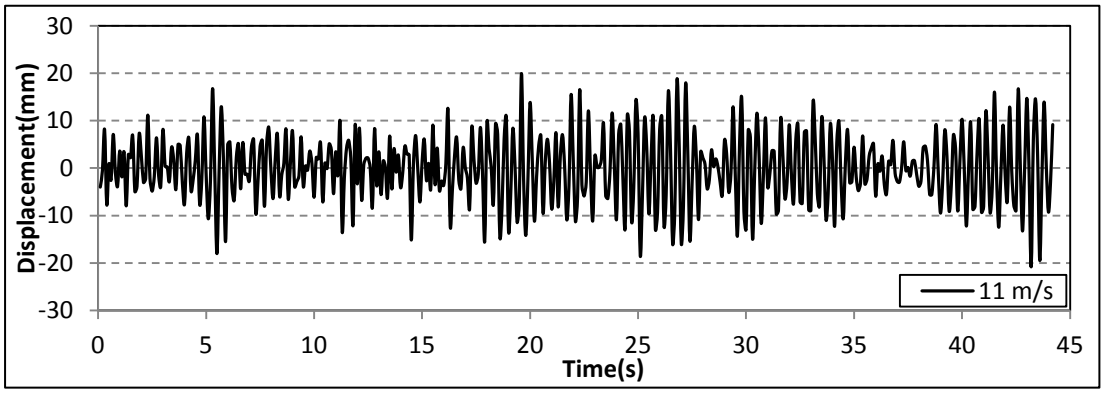
Displacement(mm)
Time(s)
11 m/s

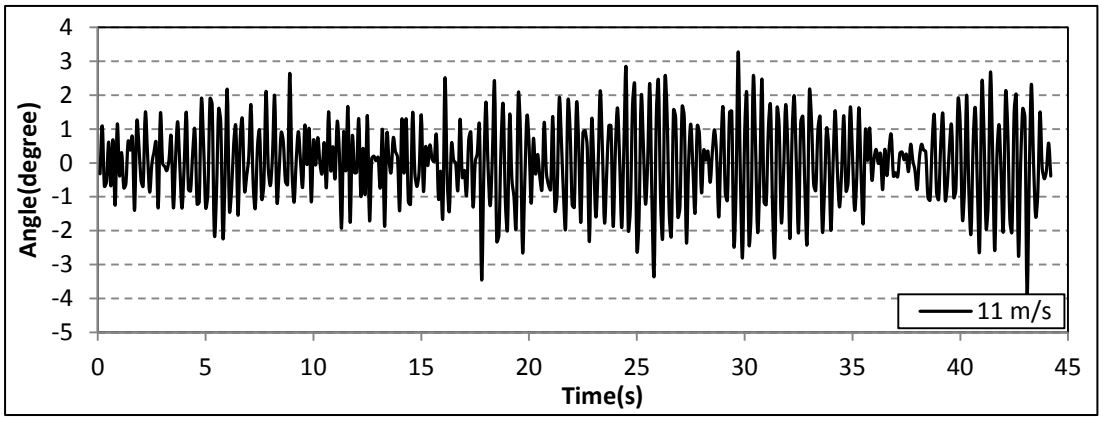

Vertical displacement and torsional angle time histories from 7 m/s to 11 m/s wind speed under 4 °attack angle (50 mm high edge wind barrier)

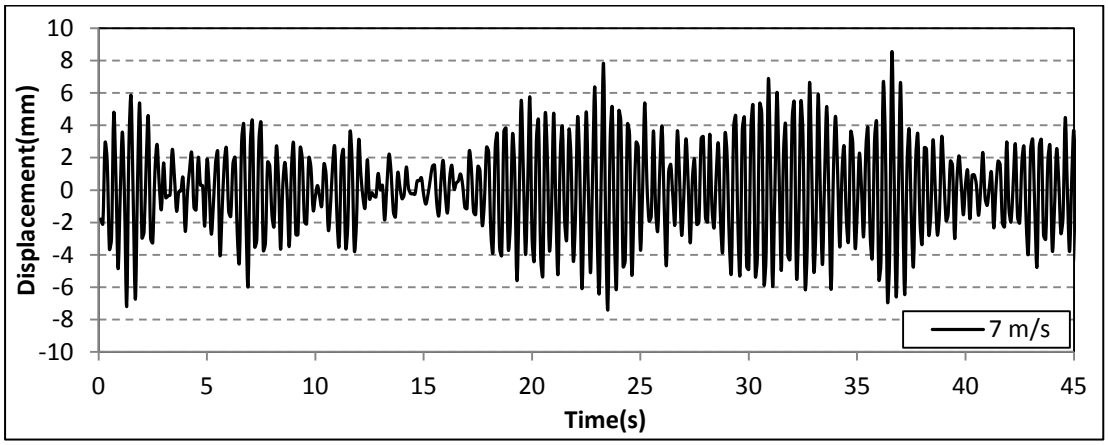

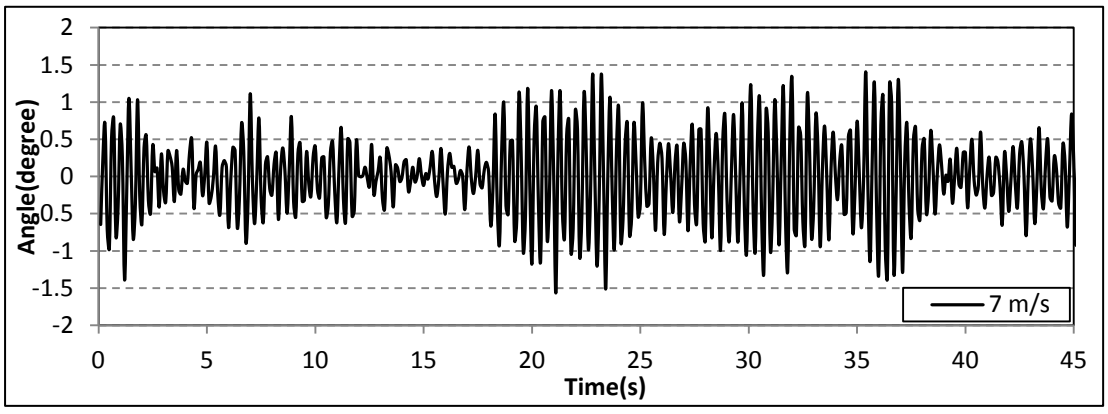

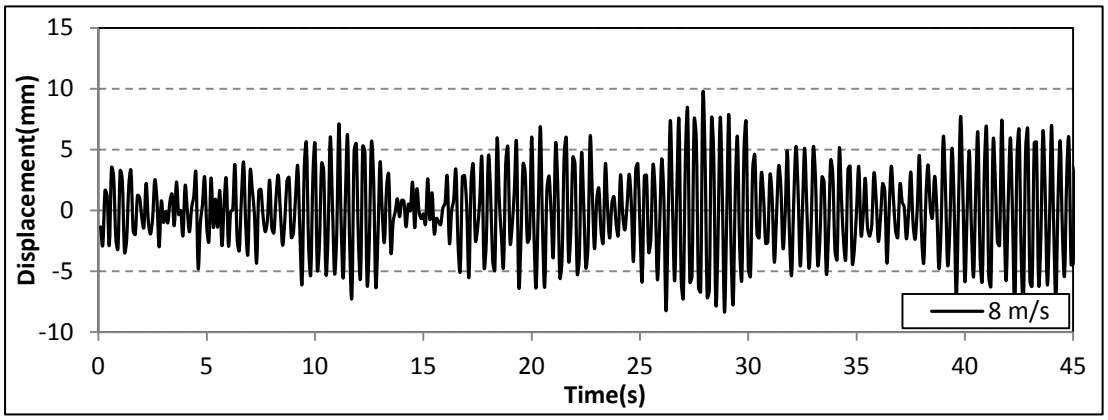
Displacement(mm)
15
10
5
0
-5
-10
0
5
10
15
20
25
30
35
40
45
Time(s)
8 m/s

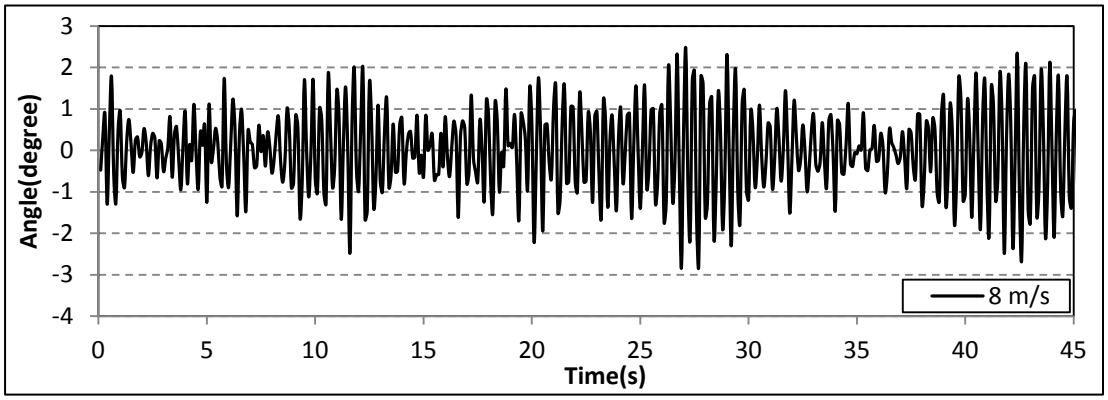
Angle(degree)
3
2
1
0
-1
-2
-3
-4
0
5
10
15
20
25
30
35
40
45
Time(s)
8 m/s

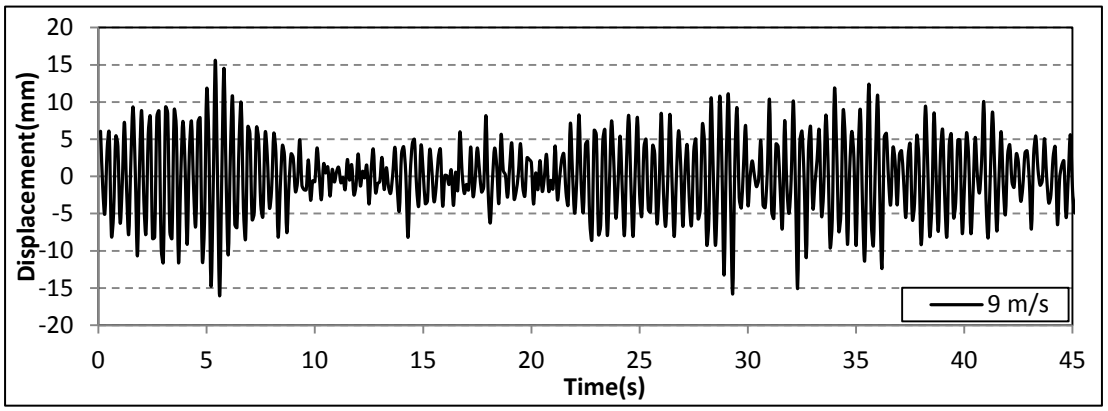
Displacement(mm)
20
15
10
5
0
-5
-10
-15
-20
0
5
10
15
20
25
30
35
40
45
Time(s)
9 m/s

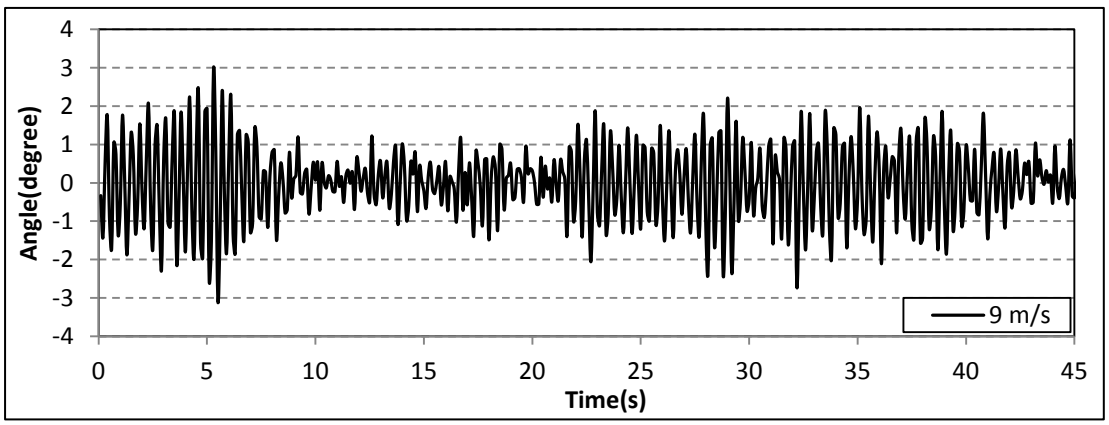
Angle(degree)
4
3
2
1
0
-1
-2
-3
-4
0
5
10
15
20
25
30
35
40
45
Time(s)
9 m/s

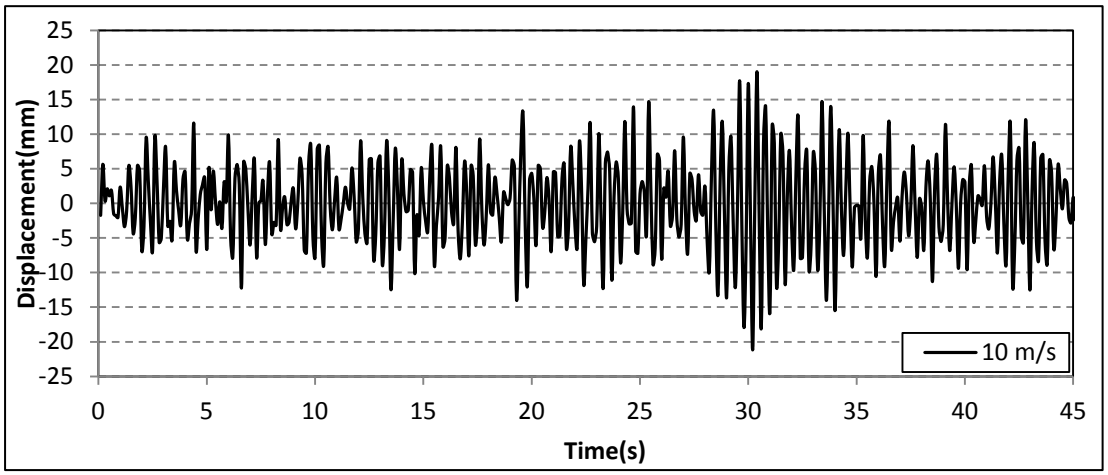
Displacement(mm)
25
20
15
10
5
0
-5
-10
-15
-20
-25
0
5
10
15
20
25
30
35
40
45
Time(s)
10 m/s

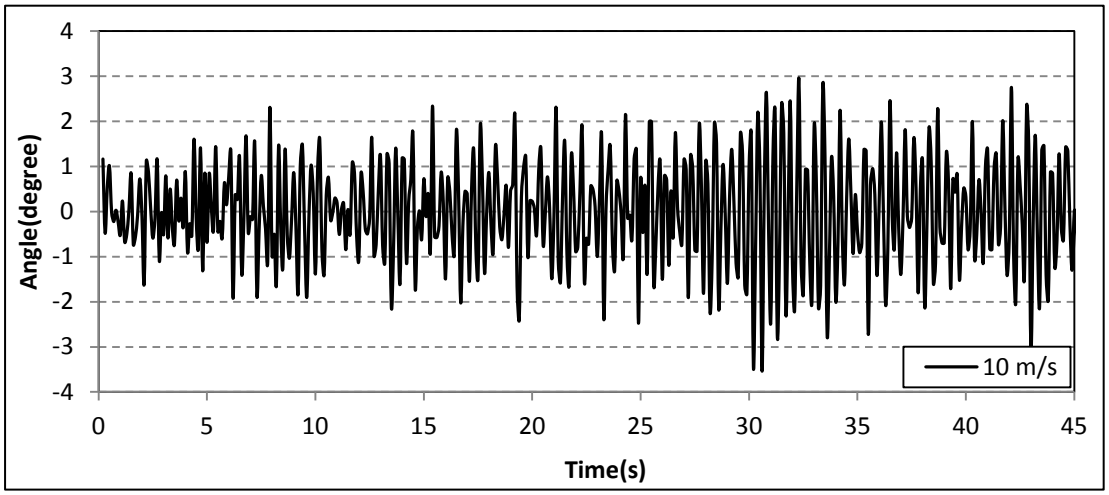
Angle(degree)
4
3
2
1
0
-1
-2
-3
-4
0
5
10
15
20
25
30
35
40
45
Time(s)
10 m/s

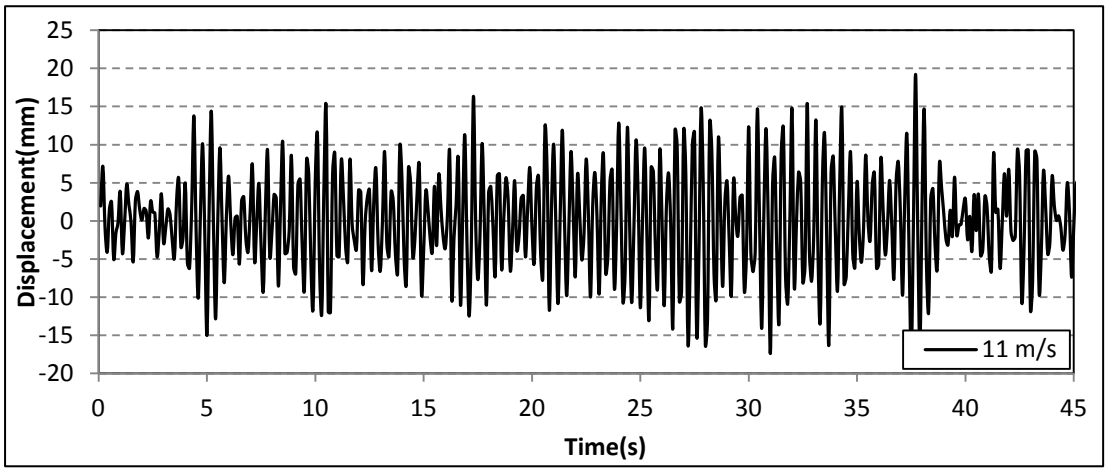
Displacement(mm)
25
20
15
10
5
0
-5
-10
-15
-20
0
5
10
15
20
25
30
35
40
45
Time(s)
11 m/s

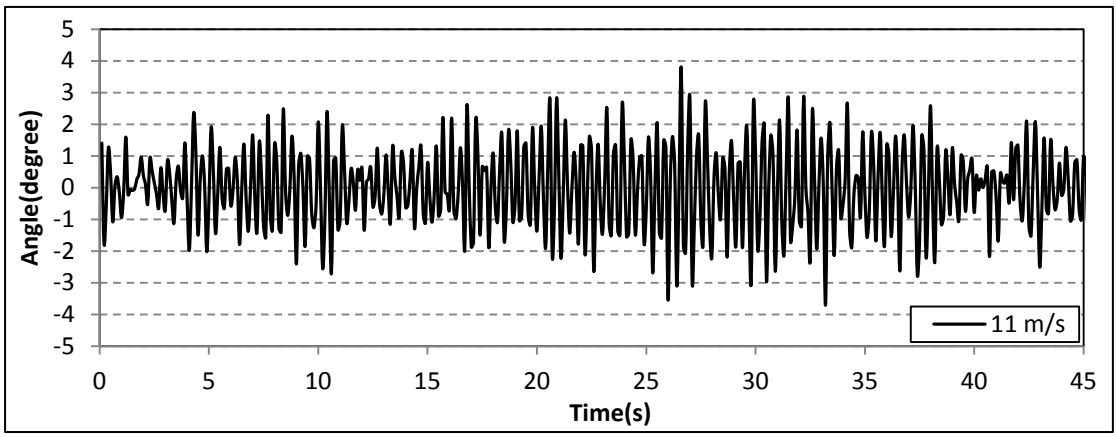

Vertical displacement and torsional angle time histories from 3 m/s to 11 m/s wind speed under 6 °attack angle (50 mm high edge wind barrier)